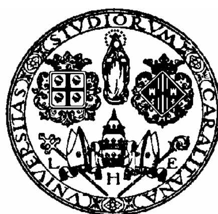

UNIVERSITÀ DEGLI STUDI DI CAGLIARI

FACOLTÀ DI SCIENZE MATEMATICHE, FISICHE E NATURALI

DIPARTIMENTO DI CHIMICA INORGANICA ED ANALITICA

DOTTORATO DI RICERCA IN SCIENZE E TECNOLOGIE CHIMICHE – XX CICLO

Concentration depth-profile reconstruction from angle-resolved XPS data using the maximum entropy method.

Characterization of surface film formed on Ni-18P alloy.

SUPERVISORE :
PROF. ANTONELLA ROSSI

TESI DI DOTTORATO :
MARIANO ANDREA SCORCIAPINO

2004 – 2007

"It is usually a good idea to visualize the structures
in an optimization as it progresses,
as every algorithm can sometimes
take a pathologically bad step,
and it's usually better to restart
the calculation with an improved guess
than it is to wait and hope that
the optimization ultimately returns to normalcy."

C.J. Cramer
"Computational Chemistry – Theories and Models"
Wiley and Sons, Ltd. (2004)

CONTENTS

CONTENTS **i**

List of Figures vi
List of Tables xviii

Abbreviations and Symbols xxiii

Abstract xxiv
Riassunto xxvi

1 INTRODUCTION 1
1.1 Ni-P ALLOYS 2
1.2 X-RAY PHOTOELECTRON SPECTROSCOPY IN-DEPTH PROFILING 2
1.3 AIM OF THE WORK 4
REFERENCES 5

2 LITERATURE REVIEW 7
2.1 PHYSICAL PROPERTIES AND APPLICATIONS OF NiP ALLOYS 8
2.1.1 Physical properties 9
2.1.1.1 *Microstructure and density* 9
2.1.1.2 *Deposit uniformity* 10
2.1.1.3 *Melting point* 11
2.1.1.4 *Electrical resistivity* 11
2.1.1.5 *Magnetic properties* 12
2.1.1.6 *Corrosion resistance* 12
2.1.1.7 *Hardness* 13
2.1.1.8 *Wear resistance* 13
2.1.1.9 *Solderability / Weldability* 14
2.1.2 Applications 14
2.1.2.1 *Automotive industry* 14
2.1.2.2 *Aerospace* 14
2.1.2.3 *Electronics* 15
2.1.2.4 *Oil, gas and chemical industries* 15
2.1.2.5 *Other applications* 16
2.2 CORROSION BEHAVIOUR OF NiP ALLOYS 16
2.2.1 Behaviour in acid solutions 17
2.2.2 Behaviour in neutral solutions 19

2.3 X-RAY PHOTOELECTRON SPECTROSCOPY ANALYSIS OF NiP ALLOYS SURFACE **19**
2.3.1 Corrosion films formed in acid and neutral solutions 19
2.3.2 Chemical state of phosphorus 21
2.3.3 The electronic structure of NiP alloys and features of the $Ni2p_{3/2}$ region 23
2.4 MODELS PROPOSED IN THE LITERATURE FOR EXPLAINING THE HIGH CORROSION RESISTANCE OF NiP ALLOYS **27**
2.5 OPEN QUESTIONS **29**
REFERENCES **31**

3 METHOD THEORY **34**
3.1 X-RAY PHOTOELECTRON SPECTROSCOPY **35**
3.1.1 Physical principle 35
3.1.2 Notation 36
3.1.3 Spectra 36
3.1.3.1 *Chemical shift* 37
3.1.3.2 *Spin-orbit coupling* 37
3.1.3.3 *Multiplet splitting* 38
3.1.3.4 *Satellite peaks* 38
3.1.3.5 *Energy scale correction for charging* 38
3.1.3.6 *Calibration* 38
3.1.4 Data processing 39
3.1.4.1 *X-ray source satellite subtraction* 39
3.1.4.2 *Peak fitting* 39
3.1.5 Auger parameter 40
3.1.6 The first principles method for quantitative surface analysis 43
3.1.7 Electron inelastic mean free path 46
3.1.7.1 *Seah and Dench* 48
3.1.7.2 *TPP-2M* 48
3.1.7.3 *G-1* 50
3.1.8 Tougaard's method for non destructive in-depth profiling 52
3.1.8.1 *The problem* 52
3.1.8.2 *Tougaard's approach* 53
3.1.8.3 *Path length distribution function Q* 54
3.1.8.4 *Energy distribution function G* 55
3.1.8.5 *Inelastic scattering cross-section* 55
3.1.9 Maximum entropy method for non destructive in-depth profiling from angular-resolved XPS data 57
3.1.9.1 *The problem* 57
3.1.9.2 *MEM approach* 58
3.1.9.3 *MEM theory* 59
3.2 THEORY OF CORROSION **63**
3.2.1 General background 63

3.2.2 Thermodynamics of corrosion 63
3.2.3 Pourbaix diagrams 64
3.2.4 Corrosion kinetics 65
3.2.5 Polarization curves 66
3.2.6 Pitting corrosion 67
REFERENCES **68**

4 EXPERIMENTAL **71**
4.1 MATERIALS **72**
4.1.1 NiP alloys 72
4.1.1.1 *Electrodeposited Ni-29P alloys* 72
4.1.1.2 *Electroless NiP alloys* 72
4.1.1.3 *Alloy surface preparation* 72
4.1.1.4 *Morphological and compositional characterization* 73
4.1.2 Reference materials 73
4.2 ELECTROCHEMISTRY **74**
4.2.1 Electrochemical cell 74
4.2.2 Electrochemical instrumentation and measurements 75
4.3 XPS SURFACE ANALYSIS **76**
4.3.1 VG ESCALAB 200 76
4.3.2 THETA PROBE 77
4.3.3 Energy scale calibration 77
4.3.4 Intensity/Energy response function determination 78
4.3.5 XPS measurements 79
4.3.6 Data processing 79
4.4 XPS QUANTITATIVE ANALYSIS AND DEPTH PROFILING **80**
4.4.1 Ion etching kinetics 80
4.4.2 First principles method 80
4.4.3 Tougaard's method 81
4.4.3.1 *QUASES-Analyze: quantification by background removal* 82
4.4.3.2 *QUASES-Generate: quantification by peak shape calculation* 83
4.4.4 Maximum Entropy Method 84
4.4.4.1 *First version of the MEM algorithm* 85
4.4.4.2 *New version of the MEM algorithm* 85
4.4.4.3 *Apparent concentration diagrams simulator* 85
4.4.4.4 *Synthetic structures for numerical experiments* 86
4.4.4.5 *Numerical experiments* 94
4.4.4.6 *Simulator routine* 96
4.4.4.7 *ARXPS experimental data processing* 97
4.4.4.8 *Electron inelastic mean free paths evaluation* 97

4.4.4.9 *MEM algorithms protocol application to ARXPS data* 99
REFERENCES **100**

5 RESULTS **101**
5.1 SPECIMENS MORPHOLOGY AND PREPARATION **102**
5.2 SAMPLES CHARACTERIZATION **103**
5.3 ELECTROCHEMICAL RESULTS **104**
5.3.1 Anodic potentiodynamic polarization 104
5.3.2 Potentiostatic polarization 105
5.4 XPS RESULTS **106**
5.4.1 Reference compounds spectra 106
5.4.1.1 *High resolution spectra of Ni2p$_{3/2}$ region* 106
5.4.1.2 *High resolution spectra of P2p and PKLL regions* 107
5.4.1.3 *High resolution spectra of O1s region* 111
5.4.2 NiP alloys spectra 112
5.4.2.1 *The survey spectra* 112
5.4.2.2 *High resolution spectra of Ni2p$_{3/2}$ region* 113
5.4.2.3 *High resolution spectra of P2p and PKLL regions* 114
5.4.2.4 *High resolution spectra of O1s region* 118
5.4.2.5 *High resolution spectra of C1s region* 120
5.4.3 Ion etching kinetics 122
5.4.3.1 *Kinetics 1* 122
5.4.3.2 *Kinetics 2* 123
5.4.3.3 *Kinetics 3* 124
5.4.4 First principles method of quantification 125
5.4.5 Tougaard's method of quantification and in-depth profiling 125
5.4.5.1 *The Analyze approach* 125
5.4.5.2 *The Generate approach* 126
5.4.6 Maximum Entropy Method 128
5.4.6.1 *Numerical experiments* 128
5.4.6.2 *Application to real samples* 155
5.4.6.3 *Summary of the MEM results obtained on the polarized samples* 165
REFERENCES **165**

6 DISCUSSION **166**
6.1 ELECTROCHEMICAL BEHAVIOUR **167**
6.1.1 Current arrest 167
6.1.2 Passivation vs. diffusion limitation 167
6.1.3 Localized corrosion of NiP alloys 168
6.2 CHEMICAL STATE OF ELEMENTS PRESENT ON SURFACE FILMS **168**
6.2.1 Ni2p$_{3/2}$ 168

6.2.2 P2p 169
6.2.3 Chemical state of intermediate P 170
6.2.4 O1s 171
6.2.5 C1s 172
6.2.6 Non-destructive depth profile 172
6.3 XPS QUANTITATIVE ANALYSIS OF SPUTTERED NiP ALLOYS SURFACE 173
6.3.1 Preferential ion sputtering of phosphorus 173
6.3.2 Comparison of different methods for quantitative XPS analysis 174
6.4 POLARIZED NiP ALLOYS IN-DEPTH PROFILING 175
6.4.1 Tougaard's Generate approach 175
6.4.2 MEM performance and accuracy : numerical experiments 177
6.4.2.1 *Apparent concentrations diagrams and Relative depth plots : influence of the IMFP* 177
6.4.2.2 *Accuracy of algorithms protocol for MEM application* 182
6.4.3 Application of MEM to real samples : polarized Ni-18P alloys 183
6.4.4 Comparison of Tougaard's and Maximum Entropy Method 185
6.5 DISSOLUTION MECHANISM OF NICKEL-PHOSPHORUS ALLOYS 187
REFERENCES 190

7 CONCLUSIONS AND OUTLOOK 193
7.1 CONCLUSIONS 194
7.2 OUTLOOK 195

Acknowledgements

A OTHER MEM NUMERICAL EXPERIMENTS RESULTS
B CURVE FITTING PARAMETERS FOR SPECTRA ACQUIRED WITH THETA PROBE

List of Figures

2.1	NiP alloy density vs P content	10
2.2	NiP alloys solid-liquid phases diagram	11
2.3	Example of a Computer Hard Disk	12
2.4	Cake diagram of NiP alloys application	16
2.5	Anodic polarization curves for Ni and Ni-20P in 0.1 N H_2SO_4	18
2.6	A schematic diagram showing the effects of a core hole potential on the valence and the conduction band	24
2.7	Generalized conduction band and valence band structure in Ni and conductor Ni compounds	24
3.1	Schematic picture of spectrometer analysis chamber: sample coordinated axis and spectrometer angles	45
3.2	Four widely different surface structure of copper in gold that give identical peak intensities	52
3.3	λ_i K(E,T) curves (theoretically calculated from the dielectric response function of the solid) for electrons of energy E in Cu, Ag and Au. For each metal, four primary energy values are considered (E = 300, 500, 1000 and 1500 eV). The thick solid line is the best two-parameter fit	56
3.4	Graphic illustration of the model used within the MEM	60
3.5	Pourbaix diagrams for **(a)** nickel and **(b)** phosphorus	65
3.6	Typical **(a)** anodic and **(b)** cathodic polarization curve	66

4.1	Electrochemical cell	74
4.2	XPS Spectrometer VG ESCALAB 200, Thermo Fisher Scientific Inc., East Grinstead, UK	76
4.3	XPS spectrometer THETA PROBE, Thermo Fisher Scientific Inc., East Grinstead, UK	77
4.4	Theta Probe intensity/energy response functions for the 4.7 mA 15 kV (70 W) and 300 μm spot size X-ray gun	78
4.5	Protocol for combining the first and new versions of the MEM algorithm	94
4.6	Simulator routine for apparent composition diagrams generation	96
4.7	Layered structure used in the simulator routine for the evaluation of the IMFP values	98

5.1	Surface of NiP alloys as received	102
5.2	Surface of a mechanical polished NiP alloy	102
5.3	XRD patterns of two NiP coatings on an iron substrate	103
5.4	EDX composition profile of a 10 μm thick NiP specimen	103
5.5	Anodic potentiodynamic polarization curves of unpolished and mechanically polished NiP samples in near-neutral and acidic solutions	104
5.6	Potentiostatic polarization curves of NiP samples at -0.1 V and +0.1 V SCE in 0.1 M Na_2SO_4	105
5.7	Surface of a NiP sample, polarized at +0.1 V SCE for 3 hours in 0.1 M Na_2SO_4	105
5.8	high resolution $Ni2p_{3/2}$ spectrum acquired with ESCALAB 200 from **(a)** pure metallic nickel foil, **(b)** one of the sputtered NiP specimens studied in this work, **(c)** $Ni_3(PO_4)_2 \cdot 5H_2O$ pellet on a conducting biadhesive tape, **(d)** lump of a pyrophosphate glass with composition $0.3NiO \cdot 0.35Na_2O \cdot 0.35P_2O_5$, **(e)** NiO lump	106

5.9	high resolution P2p spectrum acquired with ESCALAB 200 from **(a)** pure red phosphorus lump, **(b)** one of the sputtered NiP specimens studied in this work, **(c)** $Ni_3(PO_4)_2 \cdot 5H_2O$ pellet on a conducting biadhesive tape, **(d)** lump of a pyrophosphate glass with composition $0.3NiO \cdot 0.35Na_2O \cdot 0.35P_2O_5$, **(e)** Na_3PO_4 pellet on a conducting biadhesive tape, **(f)** NaH_2PO_4 pellet on a conducting biadhesive tape, **(g)** $NaH_2PO_2 \cdot H_2O$ pellet on a conducting biadhesive tape	107
5.10	high resolution PKLL spectrum acquired with ESCALAB 200 from **(a)** pure red phosphorus lump, **(b)** one of the sputtered NiP specimens studied in this work, **(c)** $Ni_3(PO_4)_2 \cdot$ 5H2O pellet on a conducting biadhesive tape, **(d)** lump of a pyrophosphate glass with composition $0.3NiO \cdot 0.35Na_2O \cdot 0.35P_2O_5$, **(e)** Na_3PO_4 pellet on a conducting biadhesive tape, **(f)** NaH_2PO_4 pellet on a conducting biadhesive tape, **(g)** $NaH_2PO_2 \cdot H_2O$ pellet on a conducting biadhesive tape	107
5.11	high resolution O1s spectrum acquired with ESCALAB 200 **(a)** (Al kα) from a $Ni_3(PO_4)_2 \cdot$ 5H2O pellet on a conducting biadhesive tape, **(b)** (Mg kα) from a lump of a pyrophosphate glass with composition $0.3NiO \cdot 0.35Na_2O \cdot 0.35P_2O_5$	111
5.12	Survey spectrum acquired with ESCALAB 200 from a NiP alloy after 1 hour polarization at +0.1 V SCE in 0.1 M Na_2SO_4	112
5.13	high resolution $Ni2p_{3/2}$ spectra acquired with ESCALAB 200 from a NiP specimen, polarized at +0.1 V SCE in 0.1 M Na_2SO_4 for **(a)** 1, **(b)** 3 and **(c)** 14 hours	113
5.14	**(a)** $Ni2p_{3/2}$ high resolution spectra acquired with Theta Probe in the ARXPS acquisition mode on a NiP specimen polarized at +0.1 V SCE in 0.1 M Na_2SO_4 for 1 hour. **(b)** Relative intensities vs. emission angle	114
5.15	high resolution P2p spectra acquired with ESCALAB 200 from a NiP specimen, polarized at +0.1 V SCE in 0.1 M Na_2SO_4 for **(a)** 1, **(b)** 3 and **(c)** 14 hours	115
5.16	high resolution PKLL spectra acquired with ESCALAB 200 from a NiP specimen, polarized at +0.1 V SCE in 0.1 M Na_2SO_4 for **(a)** 1, **(b)** 3 and **(c)** 14 hours	115
5.17	**(a)** high resolution P2p spectra acquired with Theta Probe in the ARXPS acquisition mode from a NiP specimen polarized at +0.1 V SCE in 0.1 M Na_2SO_4 for 1 hour. **(b)** Relative intensities vs. emission angle	117
5.18	high resolution O1s spectra acquired with ESCALAB 200 from a NiP specimen, polarized at +0.1 V SCE in 0.1 M Na_2SO_4 for **(a)** 1, **(b)** 3 and **(c)** 14 hours	119

5.19	**(a)** high resolution O1s spectra acquired with Theta Probe in the ARXPS acquisition mode from a NiP specimen polarized at +0.1 V SCE in 0.1 M Na_2SO_4 for 1 hour. **(b)** Relative intensities vs. emission angle	120
5.20	high resolution C1s spectra acquired with ESCALAB 200 from a NiP specimen, polarized at +0.1 V SCE in 0.1 M Na_2SO_4 for **(a)** 1, **(b)** 3 and **(c)** 14 hours	121
5.21	high resolution C1s spectra acquired with Theta Probe in the ARXPS acquisition mode from a NiP specimen polarized at +0.1 V SCE in 0.1 M Na_2SO_4 for 1 hour	121
5.22	high-resolution $Ni2p_{3/2}$ spectra from a Ni-29P alloy for 30 s etching time step, from 0 to 300 s, at 1 kV and 1 μA	122
5.23	high-resolution P2p spectra from a Ni-29P alloy for 30 s etching time step, from 0 to 300 s, at 1 kV and 1 μA	122
5.24	$Ni2p_{3/2}$ and P2p intensity of a Ni-29P alloy vs. etching time (30÷300 s), at 1 kV and 1 μA	123
5.25	Ni-29P alloy surface composition vs. etching time (30÷300 s), at 1 kV and 1 μA	123
5.26	$Ni2p_{3/2}$ high-resolution spectra of a Ni-29P alloy at 5 s etching time step, from 0 to 30 s, at 1 kV and 1 μA	123
5.27	P2p high-resolution spectra of a Ni-29P alloy at 5 s etching time step, from 0 to 30 s, at 1 kV and 1 μA	123
5.28	Ni2p3/2 and P2p intensity of a Ni-29P alloy vs. etching time (5÷30 s), at 1 kV and 1 μA	124
5.29	Ni-29P alloy surface composition vs. etching time (5÷30 s), at 1 kV and 1 μA	124
5.30	**(a)** Inelastic background analysis of Ni2p region, isolated from survey spectra from pure Ni foil. **(b)** Depth profile model of pure Ni sample	125
5.31	**(a)** Inelastic background analysis of Ni2p region, isolated from survey spectra from an electroless NiP specimen after ion etching. **(b)** Depth profile model	126
5.32	**(a)** Polarized NiP alloy spectrum simulation by Tougaard's "Generate" approach; **(b)** Depth profile model of polarized NiP alloy surface	127
5.33	Depth profile of synthetic structure 3_1+1+1 and MEM simulation (dotted lines)	129
5.34	Apparent Concentration Diagram of synthetic structure 3_1+1+1 (circles) and recalculated MEM data (dotted lines)	129

5.35 Relative Depth Plot of synthetic structure 3_1+1+1. **(a)** real-RDP and **(b)** trial-RDP 130

5.36 Depth profile of synthetic structure 3_1+2 and MEM simulation (dotted lines) 131

5.37 Apparent Concentration Diagram of synthetic structure 3_1+2 (circles) and recalculated MEM data (dotted lines) 131

5.38 Relative Depth Plot of synthetic structure 3_1+2. **(a)** real-RDP and **(b)** trial-RDP 132

5.39 Depth profile of synthetic structure 3_2+1 and MEM simulation (dotted lines) 133

5.40 Apparent Concentration Diagram of synthetic structure 3_2+1 (circles) and recalculated MEM data (dotted lines) 133

5.41 Relative Depth Plot of synthetic structure 3_2+1. **(a)** real-RDP and **(b)** trial-RDP 134

5.42 Depth profile of synthetic structure 4_1+1+1+1 and MEM simulation (dotted lines) 135

5.43 Apparent Concentration Diagram of synthetic structure 4_1+1+1+1 (circles) and recalculated MEM data (dotted lines) 135

5.44 Relative Depth Plot of synthetic structure 4_1+1+1+1. **(a)** real-RDP and **(b)** trial-RDP 136

5.45 Depth profile of synthetic structure 4_1+2+1 and MEM simulation (dotted lines) 137

5.46 Apparent Concentration Diagram of synthetic structure 4_1+2+1 (circles) and recalculated MEM data (dotted lines) 137

5.47 Relative Depth Plot of synthetic structure 4_1+2+1. **(a)** real-RDP and **(b)** trial-RDP 137

5.48 Depth profile of synthetic structure 5_1+1+1+1+1 and MEM simulation (dotted lines) 138

5.49 Apparent Concentration Diagram of synthetic structure 5_1+1+1+1+1 (circles) and recalculated MEM data (dotted lines) 138

5.50 Relative Depth Plot of synthetic structure 5_1+1+1+1+1. **(a)** real-RDP and **(b)** trial-RDP 139

5.51 Depth profile of synthetic structure 5_3+2 and MEM simulation (dotted lines) 140

5.52 Apparent Concentration Diagram of synthetic structure 5_3+2 (circles) and recalculated MEM data (dotted lines) 140

5.53 Relative Depth Plot of synthetic structure 5_3+2. **(a)** real-RDP and **(b)** trial-RDP 140

5.54	Depth profile of synthetic structure 6_1+1+1+1+1+1 and MEM simulation (dotted lines)	141
5.55	Apparent Concentration Diagram of synthetic structure 6_1+1+1+1+1+1 (circles) and recalculated MEM data (dotted lines)	141
5.56	Relative Depth Plot of synthetic structure 6_1+1+1+1+1+1. **(a)** real-RDP and **(b)** trial-RDP	142
5.57	Depth profile of synthetic structure 6_1+2+1+2 and MEM simulation (dotted lines)	143
5.58	Apparent Concentration Diagram of synthetic structure 6_1+2+1+2 (circles) and recalculated MEM data (dotted lines)	143
5.59	Relative Depth Plot of synthetic structure 6_1+2+1+2. **(a)** real-RDP and **(b)** trial-RDP	144
5.60	Depth profile of synthetic structure 6_1+3+2 and MEM simulation (dotted lines)	145
5.61	Apparent Concentration Diagram of synthetic structure 6_1+3+2 (circles) and recalculated MEM data (dotted lines)	145
5.62	Relative Depth Plot of synthetic structure 6_1+3+2. **(a)** real-RDP and **(b)** trial-RDP	145
5.63	Depth profile of synthetic structure 6_3+1+2 and MEM simulation (dotted lines)	146
5.64	Apparent Concentration Diagram of synthetic structure 6_3+1+2 (circles) and recalculated MEM data (dotted lines)	146
5.65	Relative Depth Plot of synthetic structure 6_3+1+2. **(a)** real-RDP and **(b)** trial-RDP	147
5.66	Depth profile of synthetic structure 6_3+3 and MEM simulation (dotted lines)	148
5.67	Apparent Concentration Diagram of synthetic structure 6_3+3 (circles) and recalculated MEM data (dotted lines)	148
5.68	Relative Depth Plot of synthetic structure 6_3+3. **(a)** real-RDP and **(b)** trial-RDP	149
5.69	Depth profile of synthetic structure 7_a and MEM simulation (dotted lines)	150
5.70	Apparent Concentration Diagram of synthetic structure 7_a (circles) and recalculated MEM data (dotted lines)	150
5.71	Depth profile of synthetic structure 7_a_{error} and MEM simulation (dotted lines)	151

5.72	Apparent Concentration Diagram of synthetic structure 7_a_{error} (circles) and recalculated MEM data (dotted lines)	151
5.73	Depth profile of synthetic structure 7_b and MEM simulation (dotted lines)	152
5.74	Apparent Concentration Diagram of synthetic structure 7_b (circles) and recalculated MEM data (dotted lines)	152
5.75	Depth profile of synthetic structure 7_b_{error} and MEM simulation (dotted lines)	152
5.76	Apparent Concentration Diagram of synthetic structure 7_b_{error} (circles) and recalculated MEM data (dotted lines)	152
5.77	Depth profile of synthetic structure 8 and MEM simulation (dotted lines)	154
5.78	Apparent Concentration Diagram of synthetic structure 8 (circles) and recalculated MEM data (dotted lines)	154
5.79	Depth profile of synthetic structure 8_{error} and MEM simulation (dotted lines)	154
5.80	Apparent Concentration Diagram of synthetic structure 8_{error} (circles) and recalculated MEM data (dotted lines)	154
5.81	Inelastic mean free path versus kinetic energy of photoelectrons travelling through the adventitious contamination layer, nickel (II) orthophosphate, red phosphorus and a Ni-18P alloy	156
5.82	**(a)** ACD and **(b)** RDP of a Ni-18P alloy after 1 hour polarization at +0.1 V SCE in 0.1 M Na_2SO_4	157
5.83	**(a)** The best layered structure for the Depth profile of a Ni-18P alloy after 1 hour polarization and **(b)** the ACD curves calculated correspondingly (dotted lines); experimental ACD data are shown too (circles)	158
5.84	Depth profile of a Ni-18P alloy after 1 hour polarization at +0.1 V SCE in 0.1 M Na_2SO_4	158
5.85	Apparent Concentration Diagram of a Ni-18P alloy after 1 hour polarization at +0.1 V SCE in 0.1 M Na_2SO_4 (circles) and recalculated MEM data (dotted lines)	159
5.86	**(a)** ACD and **(b)** RDP of a Ni-18P alloy after 3 hour polarization at +0.1 V SCE in 0.1 M Na_2SO_4	160
5.87	**(a)** The best layered structure for the Depth profile of a Ni-18P alloy after 3 hour polarization and **(b)** the ACD curves calculated correspondingly (dotted lines); experimental ACD data are shown too (circles)	160

5.88	Depth profile of a Ni-18P alloy after 3 hour polarization at +0.1 V SCE in 0.1 M Na_2SO_4	161
5.89	Apparent Concentration Diagram of a Ni-18P alloy after 3 hour polarization at +0.1 V SCE in 0.1 M Na_2SO_4 (circles) and recalculated MEM data (dotted lines)	161
5.90	**(a)** ACD and **(b)** RDP of a Ni-18P alloy after 14 hour polarization at +0.1 V SCE in 0.1 M Na_2SO_4	162
5.91	**(a)** The best layered structure for the Depth profile of a Ni-18P alloy after 14 hour polarization and **(b)** the ACD curves calculated correspondingly (dotted lines); experimental ACD data are shown too (circles)	163
5.92	Depth profile of a Ni-18P alloy after 14 hour polarization at +0.1 V SCE in 0.1 M Na_2SO_4	163
5.93	Apparent Concentration Diagram of a Ni-18P alloy after 14 hour polarization at +0.1 V SCE in 0.1 M Na_2SO_4 (circles) and recalculated MEM data (dotted lines)	164
6.1	Wagner chemical state plot of phosphorus, showing the different P species present on the surface of electroless deposited NiP alloys after 1, 3 and 14 hours polarization at +0.1 V SCE in 0.1 M Na_2SO_4 (full symbols). P-containing reference compounds analyzed in this work and others from the literature are given for comparison (open circles)	170
6.2	Comparison of high resolution spectra for O1s region acquired from NiP alloy **(a)** unpolished **(b)** after 1 hour polarization at +0.1 V SCE in 0.1 M Na_2SO_4	171
6.3	Schematic diagram of depth profile of a polarized Ni-18P alloy, reconstructed with Tougaard's generate approach	175
6.4	ACD of synthetic structure 3_2+1	177
6.5	ACD of synthetic structure 3_1+1+1	177
6.6	ACD of synthetic structure 7_a	178
6.7	RDP of synthetic structure **(a)** 3_1+1+1 and **(b)** 3_1+2	178

6.8	**(a)** ACD and **(b)** RDP of synthetic structure 4_1+2+1	179
6.9	**(a)** ACD and **(b)** RDP of modified synthetic structure 4_1+2+1. Intermediate layer composed of 50 at.% B and C, instead of 40 and 60 at.% respectively	181
6.10	**(a)** trial-ACD and **(b)** trial-RDP of synthetic structure 4_1+2+1	181
6.11	Maximum absolute deviation of the layers interfaces depth vs. depth	182
6.12	Maximum relative error of the species concentration vs. depth	182
6.13	Maximum **(a)** absolute deviation of the layers interfaces depth and **(b)** relative error of the species concentration vs. the number of the species involved in the structure	183
6.14	Schematic diagram of the depth profile of polarized Ni-18P alloy, reconstructed with MEM protocol	183
6.15	Schematic diagram of dissolution mechanism of NiP alloy upon immersion in the electrolyte solution	187
6.16	Schematic diagram of dissolution mechanism of NiP alloy at lower polarization times	188

A.1	Depth profile of synthetic structure 4_1+1+2 and MEM simulation (dotted lines)	A2
A.2	Apparent Concentration Diagram of synthetic structure 4_1+1+2 (circles) and recalculated MEM data (dotted lines)	A2
A.3	Relative Depth Plot of synthetic structure 4_1+1+2. **(a)** real-RDP and **(b)** trial-RDP	A2
A.4	Depth profile of synthetic structure 4_2+1+1 and MEM simulation (dotted lines)	A3
A.5	Apparent Concentration Diagram of synthetic structure 4_2+1+1 (circles) and recalculated MEM data (dotted lines)	A3
A.6	Relative Depth Plot of synthetic structure 4_2+1+1. **(a)** real-RDP and **(b)** trial-RDP	A3
A.7	Depth profile of synthetic structure 4_1+3 and MEM simulation (dotted lines)	A4

A.8	Apparent Concentration Diagram of synthetic structure 4_1+3 (circles) and recalculated MEM data (dotted lines)	A4
A.9	Relative Depth Plot of synthetic structure 4_1+3. **(a)** real-RDP and **(b)** trial-RDP	A4
A.10	Depth profile of synthetic structure 4_3+1 and MEM simulation (dotted lines)	A5
A.11	Apparent Concentration Diagram of synthetic structure 4_3+1 (circles) and recalculated MEM data (dotted lines)	A5
A.12	Relative Depth Plot of synthetic structure 4_3+1. **(a)** real-RDP and **(b)** trial-RDP	A5
A.13	Depth profile of synthetic structure 4_2+2 and MEM simulation (dotted lines)	A6
A.14	Apparent Concentration Diagram of synthetic structure 4_2+2 (circles) and recalculated MEM data (dotted lines)	A6
A.15	Relative Depth Plot of synthetic structure 4_2+2. **(a)** real-RDP and **(b)** trial-RDP	A6
A.16	Depth profile of synthetic structure 5_1+2+2 and MEM simulation (dotted lines)	A7
A.17	Apparent Concentration Diagram of synthetic structure 5_1+2+2 (circles) and recalculated MEM data (dotted lines)	A7
A.18	Relative Depth Plot of synthetic structure 5_1+2+2. **(a)** real-RDP and **(b)** trial-RDP	A7
A.19	Depth profile of synthetic structure 5_2+1+2 and MEM simulation (dotted lines)	A8
A.20	Apparent Concentration Diagram of synthetic structure 5_2+1+2 (circles) and recalculated MEM data (dotted lines)	A8
A.21	Relative Depth Plot of synthetic structure 5_2+1+2. **(a)** real-RDP and **(b)** trial-RDP	A8
A.22	Depth profile of synthetic structure 5_2+2+1 and MEM simulation (dotted lines)	A9
A.23	Apparent Concentration Diagram of synthetic structure 5_2+2+1 (circles) and recalculated MEM data (dotted lines)	A9
A.24	Relative Depth Plot of synthetic structure 5_2+2+1. **(a)** real-RDP and **(b)** trial-RDP	A9
A.25	Depth profile of synthetic structure 5_1+3+1 and MEM simulation (dotted lines)	A10
A.26	Apparent Concentration Diagram of synthetic structure 5_1+3+1 (circles) and recalculated MEM data (dotted lines)	A10

A.27	Relative Depth Plot of synthetic structure 5_1+3+1. **(a)** real-RDP and **(b)** trial-RDP	A10
A.28	Depth profile of synthetic structure 5_3+1+1 and MEM simulation (dotted lines)	A11
A.29	Apparent Concentration Diagram of synthetic structure 5_3+1+1 (circles) and recalculated MEM data (dotted lines)	A11
A.30	Relative Depth Plot of synthetic structure 5_3+1+1. **(a)** real-RDP and **(b)** trial-RDP	A11
A.31	Depth profile of synthetic structure 5_2+3 and MEM simulation (dotted lines)	A12
A.32	Apparent Concentration Diagram of synthetic structure 5_2+3 (circles) and recalculated MEM data (dotted lines)	A12
A.33	Relative Depth Plot of synthetic structure 5_2+3. **(a)** real-RDP and **(b)** trial-RDP	A12
A.34	Depth profile of synthetic structure 6_1+1+2+2 and MEM simulation (dotted lines)	A13
A.35	Apparent Concentration Diagram of synthetic structure 6_1+1+2+2 (circles) and recalculated MEM data (dotted lines)	A13
A.36	Relative Depth Plot of synthetic structure 6_1+1+2+2. **(a)** real-RDP and **(b)** trial-RDP	A13
A.37	Depth profile of synthetic structure 6_1+2+2+1 and MEM simulation (dotted lines)	A14
A.38	Apparent Concentration Diagram of synthetic structure 6_1+2+2+1 (circles) and recalculated MEM data (dotted lines)	A14
A.39	Relative Depth Plot of synthetic structure 6_1+2+2+1. **(a)** real-RDP and **(b)** trial-RDP	A14
A.40	Depth profile of synthetic structure 6_2+1+1+2 and MEM simulation (dotted lines)	A15
A.41	Apparent Concentration Diagram of synthetic structure 6_2+1+1+2 (circles) and recalculated MEM data (dotted lines)	A15
A.42	Relative Depth Plot of synthetic structure 6_2+1+1+2. **(a)** real-RDP and **(b)** trial-RDP	A15
A.43	Depth profile of synthetic structure 6_2+1+2+1 and MEM simulation (dotted lines)	A16
A.44	Apparent Concentration Diagram of synthetic structure 6_2+1+2+1 (circles) and recalculated MEM data (dotted lines)	A16
A.45	Relative Depth Plot of synthetic structure 6_2+1+2+1. **(a)** real-RDP and **(b)** trial-RDP	A16

A.46	Depth profile of synthetic structure 6_1+2+3 and MEM simulation (dotted lines)	A17
A.47	Apparent Concentration Diagram of synthetic structure 6_1+2+3 (circles) and recalculated MEM data (dotted lines)	A17
A.48	Relative Depth Plot of synthetic structure 6_1+2+3. **(a)** real-RDP and **(b)** trial-RDP	A17
A.49	Depth profile of synthetic structure 6_2+1+3 and MEM simulation (dotted lines)	A18
A.50	Apparent Concentration Diagram of synthetic structure 6_2+1+3 (circles) and recalculated MEM data (dotted lines)	A18
A.51	Relative Depth Plot of synthetic structure 6_2+1+3. **(a)** real-RDP and **(b)** trial-RDP	A18
A.52	Depth profile of synthetic structure 6_2+3+1 and MEM simulation (dotted lines)	A19
A.53	Apparent Concentration Diagram of synthetic structure 6_2+3+1 (circles) and recalculated MEM data (dotted lines)	A19
A.54	Relative Depth Plot of synthetic structure 6_2+3+1. **(a)** real-RDP and **(b)** trial-RDP	A19
A.55	Depth profile of synthetic structure 6_3+2+1 and MEM simulation (dotted lines)	A20
A.56	Apparent Concentration Diagram of synthetic structure 6_3+2+1 (circles) and recalculated MEM data (dotted lines)	A20
A.57	Relative Depth Plot of synthetic structure 6_3+2+1. **(a)** real-RDP and **(b)** trial-RDP	A20
A.58	Depth profile of synthetic structure 6_2+2+2 and MEM simulation (dotted lines)	A21
A.59	Apparent Concentration Diagram of synthetic structure 6_2+2+2 (circles) and recalculated MEM data (dotted lines)	A21
A.60	Relative Depth Plot of synthetic structure 6_2+2+2. **(a)** real-RDP and **(b)** trial-RDP	A21

LIST OF TABLES

2.1	Literature reported data of X-ray photoelectronic signals and X-ray induced Auger signals recorded on several NiP alloys, after different electrochemical tests carried out in different electrolytes	20
3.1	Relationship between spectroscopists' notation and X-ray notation	36
3.2	Empiric parameters of the Seah and Dench formula for IMFP calculation	48
3.3	Numerical fitting parameters k_1 and k_2 of the G-1 predictive formula	51
4.1	Main electroless deposition bath parameters	72
4.2	Mechanical polishing procedure parameters	73
4.3	List of spectral region binding energy ranges acquired	79
4.4	Synthetic profiles, on the basis of which numerical experiments were performed, are listed with their labels, layer thickness, components involved and their concentrations	87
5.1	Peak-fitting parameters of the $Ni2p_{3/2}$ region acquired from reference compounds with ESCALAB 200	107
5.2	Peak-fitting parameters of the P2p and PKLL regions acquired from reference compounds with ESCALAB 200	110
5.3	Peak-fitting parameters of the $Ni2p_{3/2}$ region acquired with ESCALAB 200 from the NiP alloys after 1, 3 and 14 hours polarization at +0.1 V SCE in 0.1 M Na_2SO_4	113

5.4	Peak-fitting parameters of the P2p and the PKLL region acquired with ESCALAB 200 from the NiP alloys after 1, 3 and 14 hours polarization at +0.1 V SCE in 0.1 M Na_2SO_4, together with the calculated modified Auger parameters	116
5.5	Peak-fitting parameters of the O1s region acquired with ESCALAB 200 from the NiP alloys after 1, 3 and 14 hours polarization at +0.1 V SCE in 0.1 M Na_2SO_4	118
5.6	Peak-fitting parameters of the C1s region acquired with ESCALAB 200 from the NiP alloys after 1, 3 and 14 hours polarization at +0.1 V SCE in 0.1 M Na_2SO_4	120
5.7	Tougaard's "Generate" results. NiP depth profile at three different polarization times	127
5.8	Depth profile parameters of synthetic structure 3_1+1+1 and results of MEM simulation	131
5.9	Depth profile parameters of synthetic structure 3_1+2 and results of MEM simulation	133
5.10	Depth profile parameters of synthetic structure 3_2+1 and results of MEM simulation	134
5.11	Depth profile parameters of synthetic structure 4_1+1+1+1 and results of MEM simulation	136
5.12	Depth profile parameters of synthetic structure 4_1+2+1 and results of MEM simulation	138
5.13	Depth profile parameters of synthetic structure 5_1+1+1+1+1 and results of MEM simulation	139
5.14	Depth profile parameters of synthetic structure 5_3+2 and results of MEM simulation	141
5.15	Depth profile parameters of synthetic structure 6_1+1+1+1+1+1 and results of MEM simulation	142
5.16	Depth profile parameters of synthetic structure 6_1+2+1+2 and results of MEM simulation	144
5.17	Depth profile parameters of synthetic structure 6_1+3+2 and results of MEM simulation	146
5.18	Depth profile parameters of synthetic structure 6_3+1+2 and results of MEM simulation	147
5.19	Depth profile parameters of synthetic structure 6_3+3 and results of MEM simulation	149

5.20 Depth profile parameters of synthetic structure 7_a and results of MEM simulation, both with and without random error in the ACD data 151

5.21 Depth profile parameters of synthetic structure 7_b and results of MEM simulation, both with and without random error in the ACD data 153

5.22 Depth profile parameters of synthetic structure 8 and results of MEM simulation, both with and without random error in the ACD data 155

5.23 Depth profile parameters of a Ni-18P alloy after 1 hour polarization at +0.1 V SCE in 0.1 M Na_2SO_4 159

5.24 Depth profile parameters of a Ni-18P alloy after 3 hour polarization at +0.1 V SCE in 0.1 M Na_2SO_4 162

5.25 Depth profile parameters of a Ni-18P alloy after 14 hour polarization at +0.1 V SCE in 0.1 M Na_2SO_4 164

5.26 Depth profile parameters of a Ni-18P alloy after 1, 3 and 14 hours polarization at +0.1 V SCE in 0.1 M Na_2SO_4 165

6.1 XPS and EDX results of quantitative surface analysis of the NiP alloys studied in this work 174

6.2 Depth profile parameters of a Ni-18P alloy after 1, 3 and 14 hours polarization in 0.1 M Na_2SO_4 at +0.1 V SCE, determined with Tougaard's generate approach 176

6.3 Depth profile parameters of Ni-18P alloy after 1, 3 and 14 hours polarization at +0.1 V SCE in 0.1 M Na_2SO_4, determined with MEM protocol 184

A.1 Depth profile parameters of synthetic structure 4_1+1+2 and results of MEM simulation A2

A.2 Depth profile parameters of synthetic structure 4_2+1+1 and results of MEM simulation A3

A.3 Depth profile parameters of synthetic structure 4_1+3 and results of MEM simulation A4

A.4	Depth profile parameters of synthetic structure 4_3+1 and results of MEM simulation	A5
A.5	Depth profile parameters of synthetic structure 4_2+2 and results of MEM simulation	A6
A.6	Depth profile parameters of synthetic structure 5_1+2+2 and results of MEM simulation	A7
A.7	Depth profile parameters of synthetic structure 5_2+1+2 and results of MEM simulation	A8
A.8	Depth profile parameters of synthetic structure 5_2+2+1 and results of MEM simulation	A9
A.9	Depth profile parameters of synthetic structure 5_1+3+1 and results of MEM simulation	A10
A.10	Depth profile parameters of synthetic structure 5_3+1+1 and results of MEM simulation	A11
A.11	Depth profile parameters of synthetic structure 5_2+3 and results of MEM simulation	A12
A.12	Depth profile parameters of synthetic structure 6_1+1+2+2 and results of MEM simulation	A13
A.13	Depth profile parameters of synthetic structure 6_1+2+2+1 and results of MEM simulation	A14
A.14	Depth profile parameters of synthetic structure 6_2+1+1+2 and results of MEM simulation	A15
A.15	Depth profile parameters of synthetic structure 6_2+1+2+1 and results of MEM simulation	A16
A.16	Depth profile parameters of synthetic structure 6_1+2+3 and results of MEM simulation	A17
A.17	Depth profile parameters of synthetic structure 6_2+1+3 and results of MEM simulation	A18
A.18	Depth profile parameters of synthetic structure 6_2+3+1 and results of MEM simulation	A19
A.19	Depth profile parameters of synthetic structure 6_3+2+1 and results of MEM simulation	A20
A.20	Depth profile parameters of synthetic structure 6_2+2+2 and results of MEM simulation	A21

B.1 Peak-fitting parameters of the $Ni2p_{3/2}$ region acquired with the Theta Probe on the NiP alloys after 1, 3 and 14 hours polarization at +0.1 V SCE in 0.1 M Na_2SO_4, in the angle-resolved mode B2

B.2 Peak-fitting parameters of the P2p region acquired with the Theta Probe on the NiP alloys after 1, 3 and 14 hours polarization at +0.1 V SCE in 0.1 M Na_2SO_4, in the angle-resolved mode B3

B.3 Peak-fitting parameters of the O1s region acquired with the Theta Probe on the NiP alloys after 1, 3 and 14 hours polarization at +0.1 V SCE in 0.1 M Na_2SO_4, in the angle-resolved mode B4

B.4 Peak-fitting parameters of the C1s region acquired with the Theta Probe on the NiP alloys after 1, 3 and 14 hours polarization at +0.1 V SCE in 0.1 M Na_2SO_4, in the angle-resolved mode B4

ABBREVIATIONS AND SYMBOLS

§	chapter - section
ACD	Apparent Concentration Diagram
AES	Auger Electron Spectroscopy
ARXPS	Angle Resolved X-ray Photoelectron Spectroscopy
ASTM	American Society for Testing and Materials
at.%	atomic percentage
bct	Body-Centered Tetragonal
BE	Binding Energy
CAE	Constant Analyzer Energy
CC	calculation cycle
CCD	Charge-Coupled Device
CD	Compact Disk
DoS	Density of States
EDX	Energy Dispersive X-ray
ELS	Energy Loss Spectroscopy
fcc	Fece-Centered Cubic
FEAL	Fast Entry Air Lock
FWHM	Full Width at Half Maximum
HV	Vikers Pyramid Number
IERF	Intensity/Energy Response Function
IMFP	Inelastic Mean Free Path
ISO	International Organization for Standardization
KE	Kinetic Energy
MEM	Maximum Entropy Method
NIST	National Institute of Standards and Technology
OC	Open Circuit
OCP	Open Circuit Potential
PE	Pass Energy
RDP	Relative Depth Plot
REELS	Reflection Electron Energy Loss Spectroscopy
RR	Retard Ratio
SCE	Saturated Calomel Electrode
wt.%	weight percentage
XAES	X-ray induced Auger Electron Spectroscopy
XPS	X-ray Photoelectron Spectroscopy
XRD	X-ray Diffraction

ABSTRACT

A knowledge of the depth concentration profile of thin layered surfaces a few nanometers thick is very important for research and applications in microelectronics, corrosion, wear and tribology. In-depth profiling methods reported in the literature are either destructive (ion sputtering), based on severe approximations (concentration gradients are not taken into account and electron IMFP are calculated for electrons travelling through pure elemental materials) or limited to relatively simple profiles (less than three components, constant IMFPs). A reconstructed depth-profile should be consistent with the ARXPS data acquired but transformation of XPS signal intensities vs. emission angle into chemical species concentrations vs. depth is an ill posed mathematical problem. The main goal of this work was thus to develop a new, iterative algorithm based on the maximum entropy method (MEM) that allows to obtain depth concentration profiles of layered surfaces from non-destructive ARXPS measurements.

In a first phase, numerical experiments were performed on a large series of computer generated, ideal and error containing, ARXPS data from model depth-profiles with up to four layers and up to eight components. The new algorithm allowed to reconstruct these depth profiles with a minimum accuracy of ± 20 % for the layer thickness and of ± 30 % for the composition of the individual layers.

In a second phase, the tested algorithm was implemented using real ARXPS data obtained from technologically important, highly corrosion and wear resistant Ni-P alloys. The choice of electroless deposited Ni-P alloys, electrochemically polarized in neutral solutions, was dictated by the fact that in the literature different and somewhat contrasting models are proposed for explaining the outstanding corrosion resistance of these alloys. Electrochemical data indicate a diffusion limited dissolution process of nickel through a phosphorus enriched layer – but both the nature of this layer and its composition are essentially unknown.

The results obtained implementing the new algorithm on ARXPS data show a depth profile with a complex layered structure at the solution / bulk alloy interface: 1) an uppermost hydrocarbon contamination layer (thickness ca. 1 nm) containing adsorbed water, 2) a thin (ca. 1 nm) nickel (poly)phosphate layer with composition gradient, 3) a highly phosphorus enriched (up to 70 at.%) surface zone (thickness ca. 0.7 nm), 4) a layer with a strong

phosphorus concentration gradient (from up to 70 at.% to ca. 20 at.% of phosphorus), 5) bulk of the alloy with the nominal composition.

The new algorithm involves an iterative procedure for calculating the IMFP values of the different components, taking into account the actual depth concentration profile of the sample surface under investigation. The new algorithm proved to be at least as accurate as Tougaard's method but more powerful than any of the existing algorithms as depth profiles with up to eight components can be reconstructed from ARXPS data.

Combining information on the chemical state of the different phosphorus compounds in the layered interface with the reconstructed in-depth profile it can be concluded that the high corrosion and wear resistance of Ni-P alloys is due to a thin, self-repairing nickel-(poly)phosphate film formed on a strongly phosphorus enriched surface.

RIASSUNTO

La conoscenza del profilo di composizione in funzione della profondità della regione superficiale di campioni che presentano strati di spessore dell'ordine di pochi nanometri, è di fondamentale importanza per la ricerca scientifica e lo sviluppo di applicazioni tecnologiche nei campi della microelettronica, della corrosione e della tribologia. I metodi di determinazione dei profili di concentrazione in funzione della profondità, riportati in letteratura, sono distruttivi, come nel caso dell'abrasione ionica, o sono basati su approssimazioni come ad esempio quella di trascurare la presenza di gradienti di concentrazione o quella di utilizzare i valori di libero cammino medio anelastico degli elettroni calcolati per sostanze pure invece che per i composti che vengono attraversati dopo la fotoemissione. In altri casi la ricostruzione dei profili di concentrazione in funzione della profondità è limitata a campioni aventi una struttura relativamente semplice costituita cioè da un numero di componenti ≤ 3 e usando valori di IMFP elettronici costanti.

Il profilo di concentrazione in funzione della profondità ricostruito dovrebbe essere coerente con i dati ARXPS acquisiti sul campione in studio. Tuttavia la conversione delle intensità dei segnali XPS (aree sottese ai segnali) in funzione dell'angolo di emissione in dati di concentrazione delle specie chimiche presenti in funzione della profondità è un problema matematicamente "mal posto", il che significa un piccolo errore nei dati può generare un grande errore nei risultati. In altre parole, date le intensità dei segnali XPS in funzione dell'angolo di emissione, possono esistere un gran numero di profili di composizione in funzione della profondità che soddisfano tali dati. L' obiettivo principale di questo lavoro è stato lo sviluppo di un nuovo algoritmo iterativo basato sul metodo della massima entropia (MEM) che permettesse la ricostruzione non distruttiva di profili di composizione in funzione della profondità da misure ARXPS.

Nella prima parte del lavoro sono stati condotti esperimenti numerici su un numero elevato di dati ARXPS generati al computer a partire da profili di composizione in funzione della profondità presi come modello. Sono stati considerati sia dati privi di rumore sia con errore casuale associato. I profili modello erano caratterizzati da un numero massimo di quattro strati e di otto componenti. Il nuovo algoritmo ha permesso la ricostruzione di questi profili con un'accuratezza minima dello spessore degli strati pari a $\pm$ 20 % e della composizione dei singoli strati pari a $\pm$ 30 %.

Nella seconda parte, l'algoritmo è stato applicato ai dati reali ARXPS acquisiti sulle leghe NiP che sono altamente resistenti alla corrosione ed all'usura e che presentano pertanto una notevole importanza tecnologica. Le superfici di campioni di Ni-18P depositate chimicamente senza passaggio di corrente in soluzione e poi polarizzate per via elettrochimica in soluzioni neutre, sono state scelte come esempio di applicazione del nuovo algoritmo ad un caso reale. E' da notare che in letteratura sono stati proposti diversi modelli per spiegare l'elevata resistenza alla corrosione di queste leghe, ma questi modelli sono tra loro discordanti. I dati elettrochimici indicano che il processo di dissoluzione è controllato dalla diffusione del nichel, presumibilmente attraverso uno strato arricchito di fosforo, ma sia la natura di questo strato che la sua composizione sono ancora sconosciute.
I risultati ottenuti applicando il nuovo algoritmo ai dati ARXPS ottenuti sulle leghe dopo polarizzazione potenziostatica suggeriscono la presenza di una struttura a strati all'interfaccia soluzione / lega piuttosto complessa: 1) uno strato superficiale di contaminazione idrocarburica (spessore ca. 1 nm) contenente anche acqua adsorbita, 2) uno strato sottile (ca. 1 nm) di (poli)fosfati di nichel con gradienti di composizione, 3) una regione superficiale della lega arricchita di fosforo (fino a 70 at.% ; spessore pari a ca. 0.7 nm), 4) uno strato con un elevato gradiente di concentrazione del fosforo (da ca. 70 at.% a ca. 20 at.%), 5) la lega di bulk con la sua composizione nominale.
Il nuovo algoritmo include anche una procedura iterativa per il calcolo dei valori di libero cammino medio anelastico degli elettroni che in questo modo sono calcolati tenendo in considerazione l'effettivo profilo di composizione in funzione della profondità della regione superficiale del campione in studio ossia tenendo conto del fatto che i fotoelettroni attraversano strati aventi diversa composizione. Il nuovo algoritmo garantisce un'accuratezza almeno pari a quella del metodo di Tougaard ma si è rivelato molto più potente di qualsiasi altro algoritmo esistente per la determinazione dei profili di composizione in funzione della profondità a partire da dati ARXPS, giacché consente la ricostruzione di profili con un numero di componenti almeno pari a 8.
L'insieme delle informazioni acquisite sullo stato chimico dei differenti composti del fosforo e sulla distribuzione delle specie in funzione della profondità ha permesso di concludere che l'elevata resistenza alla corrosione delle leghe NiP potrebbe essere dovuta ad un sottile strato auto-rigenerante di (poli)fosfati di nichel che si forma sulla superficie della lega fortemente arricchita di fosforo rispetto alla composizione media di massa della lega.

CHAPTER 1

INTRODUCTION

This chapter starts with a short introduction to the technological properties, especially corrosion resistance, and applications of NiP alloys. The main models reported in the literature describing the corrosion behaviour of these alloys are briefly summarized. Section 1.2 outlines the main issues in X-ray Photoelectron Spectroscopy depth profiling methods, instrumental calibration and electron inelastic mean free path calculation. Lastly, in Section 1.3 the open questions and goals of this thesis are presented.

1.1 Ni-P ALLOYS

The use of Ni-P alloys as corrosion protective coatings represents the earliest industrial application of nanocrystalline metals, and their preparation by electroless and electrodeposition has long been practised on a commercial scale [1,2]. These alloys have high hardness, wear resistance, low friction coefficient, non-magnetic behaviour and high electro-catalytic activity [3-7]. Today NiP alloys are widely used in the electronics industry as under-layer in thin film memory disks and in a broad range of other evolving technology applications [4-7].

One of the most important and appreciated properties of NiP alloys is their high corrosion resistance in acidic, neutral and alkaline environments. The corrosion resistance of NiP alloys strictly depends on the P content which, in turn, influences the the alloy's microstructure. High-P ($P \geq 17$ at.%) amorphous coatings are readily attacked in strong alkaline media where low-P ($P \leq 12$ at.%) crystalline alloys perform well [4,5]. On the contrary, in both acidic and neutral environments, NiP alloys with near eutectic composition of ca. 18-20 at.% P exhibit distinctly better corrosion resistance than pure Ni, exhibiting anodic dissolution suppression in the potential range where pure nickel dissolves actively [8-10]. On the other hand, the presence of even small amounts of phosphorus (0.5-1.6 at.%) leads to a loss of passivity and an increase in corrosion rate [11].

It is generally accepted that only amorphous high-P alloys show high corrosion resistance in acidic and neutral media, irrespective of production technique [8-10,12,13].

Several models have been proposed to explain this high corrosion resistance, but the issue is still under debate: a protective nickel phosphate film [14,15], the barrier action of hypophosphites (called "chemical passivity") [16,17], the presence of phosphides [18], a stable P-enriched amorphous phase [19-21].

1.2 X-RAY PHOTOELECTRON SPECTROSCOPY DEPTH PROFILING

Depth profiling with ion sputtering yields good in-depth resolution, but is destructive and can produce several artifacts including atom mixing at the sputter surface, preferential sputtering of some of the specimen components and implantation of sputtered species [22,23]. To avoid these artifacts, a non-destructive method is preferable. The three-layer model approach [24,25] requires the acquisition of XPS spectra at just one angle, but the information on film composition is averaged and not in-depth resolved. The Tougaard method provides a quantitative estimate of atom depth distribution within the outermost surface region of the

sample under investigation, but requires spectra acquisition of highly-pure reference compounds. Only a maximum of three reference spectra can be used to simulate the sample spectrum [26], few model structures can be verified [26] and a maximum of six structural parameters can be determined [27]. Otherwise, angle-resolved X-ray photoelectron spectroscopy (ARXPS) is, in principle, a suitable method for the nondestructive evaluation of in-depth composition profile of thin films [28,29], though reconstruction of the depth profile, based on the assumption of model structure, might be misleading because real data contain noise and a large number of very different model structures may match the experimental data within the measurement precision [30]. Consequently, simply minimizing the weighted sum-of-square differences between the simulated and measured data is not always adequate for determining the correct sample structure, especially if the sample has a large number of components. The maximum entropy method (MEM) has proven to be a powerful tool for reconstructing composition versus depth profiles from angle-resolved photoemission measurements [22,30-35] but a suitable algorithm has to be implemented to solve this ill-posed problem.

However, no matter what the method applied, to obtain accurate quantitative information from XPS analyses, a suitable calibration procedure must necessarily be performed to determine signal intensity versus electron kinetic energy response function (IERF) of the spectrometer being used. The calibration procedure is more complex when angle-resolved acquisition mode is used, since the signal intensity vs. energy function also depends on electron emission angle (i.e. the angle between the normal to the sample surface and emission direction). In this thesis the Theta Probe (Thermo Fisher Scientific Inc., East Grinstead, UK) XPS spectrometer was used to perform ARXPS analysis. Three years ago, when I began my PhD course, the Theta Probe had just been purchased by the research team conducting this work and no calibration procedures had yet been performed.

Lastly, another very important issue in XPS quantitative analysis is the determination of inelastic mean free path of electrons. The inelastic mean free path (IMFP) is defined as the mean distance travelled by the electron between two consecutive inelastic scattering events. However, despite the importance of IMFP, experimental values for a given material are generally available only over a narrow energy range and the measured values are affected by large uncertainties due to the experimental difficulties [36]. On the theoretical side, the most widely used IMFP predictive formulas are the *Seah and Dench* [37], the TPP-2M [38] and the G-1 [39], which for the same material and electron kinetic energy yield results often showing a large ($\gg$ 10%) relative difference. Thus, if the outermost surface region of the sample being

analyzed cannot be considered to have homogeneous composition versus depth profile, an IMFP predictive formula needs to be chosen that takes into account the differences in the material through which the photoemitted electrons travel along their escape path, but minimizing error introduced into the final quantitative result.

1.3 AIM OF THE WORK

The primary aim of this work is to study the corrosion surface film of electroless NiP alloys so as to gain a better understanding of the mechanism underlying protective film formation. Information on the phosphorus species present at the surface, on their chemical state and surface composition is pivotal to resolving the open question concerning the high stability of NiP alloys. The combined electrochemical and X-ray Photoelectron Spectroscopy (XPS) surface analytical study conducted here aims to provide a comprehensive explanation of the high corrosion resistance of NiP alloys.

However, in order to develop an exhaustive model for the corrosion behaviour of these alloys, an accurate method for the quantitative analysis of the in-depth composition profiles of surfaces with thickness in the order of a few nanometers is essential for investigating the formation conditions, growth kinetics and stability of thin-film systems with possible concentration gradients.

Thus, the other objective of this work is to test a new MEM algorithm on simulated ARXPS data and then to apply it to ARXPS experimental data for NiP alloy samples, so as to provide new insight into the composition and structure of the nano-sized protective film that forms on NiP alloy surfaces after exposure to corrosive acidic and neutral solutions. Only with this fundamental information will it be possible to gain a better understanding of the mechanism for the high corrosion resistance of NiP alloys and explain their high stability.

As a basis for developing this new MEM algorithm, firstly the XPS spectrometer was calibrated to determine the angular dependence of the IERF of our new Theta Probe, secondly a suitable IMFP predictive formula had to be chosen to account for the potential constituents of the corrosion film of NiP alloys.

REFERENCES

1. A.Brenner, E.G.Couch, E.K.Williams, *J. Res. NBS 44*, 109 (1950)
2. C.H.De Minjer, A.Brenner, *Plating 44*, 1297 (1957)
3. R.Parkinson, "Nickel Plating and Electroforming – Essential Industries for Today and the Future" - *NiDI Techn,. Series No.10088*, Toronto, (2001)
4. M. Sisti and A. Ruffini - Sirius Technology, Inc. – Oriskany, NY (http://www.pfonline.com/articles/pfd0507.html)
5. R. Bellemare and P. Vignati – OMG Fidelity, Inc. – Newark, New Jersey (http://www.pfonline.com/articles/pfd0024.html)
6. R. Taheri, PhD Thesis at University of Saskatchewan – Saskatoon - Canada, 2003
7. ASTM B733-04 : Standard Specification for Autocatalytic (Electroless) Nickel-Phosphorus Coatings on Metal
8. M.Ratzker, D.S.Lashmore, K.W.Pratt, *Plating and Surface Finishing 76*, 74 (1986)
9. A.Krolikowski, P.Butkiewicz, *Electrochimica Acta 38*, 1979 (1993)
10. J.Bielinski, A.Krolikowski, I.Kedzierska, W.Stokarski, *ACH-Models in Chemistry 132*, 685 (1995)
11. P.Marcus, O.Oda, *Mem. Sci. Rev. Metall. 76*, 715 (1979)
12. B.Bozzini, C.Lenardi, M.Serra, M.Fanigliulo, *Journal British Corrosion 37*, 173 (2002)
13. H.Ashassi-Sorkhabi, SH.Rafezadeh, *Surface and Coatings Technology 176*, 318 (2004)
14. G.T.Burstein, *Corrosion NACE 37*, 549 (1981)
15. A.Kawashima, K.Asami, K.Hashimoto, *Corrosion Science 24*, 807 (1984)
16. R.B.Diegle, N.R.Sorensen, G.C.Nelson, *Journal of the Electrochemical Society 133*, 1769 (1986)
17. R.B.Diegle, N.R.Sorensen, C.R.Clayton, M.A.Helfand, Y.C.Yu, *Journal of the Electrochemical Society 135*, 1085 (1988)
18. G.Salvago, G.Fumagalli, *Metal Finishing 85*, 31 (1987)
19. A.Krolikowski, *Material Science Forum 185*, 799 (1995)
20. A.Rossi, B.Elsener, "*Characterization of surface films on FeCrPC alloys by XPS and X-ray excited Auger peaks*" - *Surface Modifications of Passive films*, ed. P.Marcus, B.Baroux, M.Keddam, EFC Publication No. 12 (1994)
21. B.Elsener, A.Rossi, *Metallurgy and Foundry Engineering 23*, 157 (1997)

22. R.L.Opila, J.J.R.Eng *Progress in Surface Science* 69, 125 (2002)
23. D.Briggs, M.P.Seah, *"Practical Surface Analysis", 2nd ed. vol.1-2*, ed. J.Wiley & Sons, (1990)
24. A.Rossi, B.Elsener *Surface and Interface Analysis 18*, 499 (1992)
25. B.Elsener, A.Rossi, *Electrochimica Acta* 37, 2269 (1992)
26. http://www.quases.com/Downloads/QUASES-Tougaard/QUASES-Tougaard%20Ver5%20Manual.zip
27. S.Tougaard, *Surface and interface Analysis 26*, 249 (1998)
28. S.Haupt, H.H.Strehblow, *Corrosion Science 29*, 163 (1989)
29. H.W.Hoppe, S.Haupt, H.H.Strehblow, *Surface and Interface Analysis 21*, 514 (1994)
30. G.C.Smith, A.K.Livesey, *Surface and Interface Analysis 19*, 175 (1992)
31. A.K.Livesey, G.C.Smith, *Journal of Electron Spectroscopy and Related Phenomena 67*, 439 (1994)
32. J.P.Chang, M.L.Green, V.M.Donnelly, R.L.Opila, J.J.R.Eng, J.Sapjeta, P.J.Silverman, B.Weir, H.C.Lu, T.Gustafsson, E.Garfunkel, *Journal of Applied Physics 87*, 4449 (2000)
33. R.Champaneria, P.Mack, R.White, J.Wolstenholme, *Surface and Interface Analtsis 35*, 1028 (2003)
34. S.J.Splinter, N.S.McIntyre, *Surface and Interface Analysis 26*, 195 (1998)
35. M.Olla, G.Navarra, B.Elsener, A.Rossi, *Surface and Interface Analysis 38*, 964 (2006)
36. D.R.Penn, *Physical Review B. 35(2)*, 482 (1987)
37. M.P.Seah, W.A.Dench, *Surface and Interface Analysis 1(1)*, 2 (1979)
38. S.Tanuma, C.J.Powell, D.R.Penn, *Surface and interface Analysis 21*, 165 (1993)
39. W.H.Gries, *Surface and interface Analysis 24*, 38 (1996)

CHAPTER 2

LITERATURE REVIEW

ON FORMATION, STABILITY AND BREAKDOWN OF PASSIVE FILMS ON Ni-P ALLOYS AND THEIR XPS SURFACE ANALYSIS

This chapter provides an overview of the literature on Ni-P alloys and presents the state of art in XPS surface analysis of these alloy.. The chapter starts, in section 2.1, with a brief review of the most important physical properties of Ni-P alloys and their main technological applications. Then, in section 2.2 the corrosion behaviour of the Ni-P alloys is discussed in detail, especially in acidic and neutral environments. Section 2.3 provides a state of art review of XPS surface studies of the protective films that form on Ni-P alloys in acidic and neutral environments. Then, different models for explaining the high corrosion resistance of Ni-P alloys are reported and discussed in section 2.4. Lastly, in section 2.5, the open questions are underlined so as to focus on the reasons for conducting this research work.

2.1 PHYSICAL PROPERTIES AND APPLICATIONS OF NiP ALLOYS [1-4]

NiP alloys are primarily used as coatings because of their good corrosion resistance, both in acidic and alkaline environments, and excellent wear properties. NiP engineering applications include those where wear protection, corrosion prevention and/or aesthetics are important. Many tools are coated with an NiP alloy to increase their service life because of the hardness of NiP compared to pure nickel coatings. These alloys are also commonly used in catalysis and in electrical applications.

NiP coatings can be prepared using different procedures such as rapid quenching from a nickel and phosphorus containing melt, vapour deposition, electrolytic deposition and electroless deposition. Electrolytic and electroless deposition are the most widely used techniques.

The properties of the coatings obtained with these two deposition methods are similar and both fulfil the requirements for a variety of engineering applications. However, major differences do exist. Plating rates from an electroless nickel solution are very slow compared to electrolytic deposition, but electrolytic deposits are not as homogeneous as their electroless counterparts. Since cost is one of the most important aspects of industrial production, a slower and cheaper process will often be preferred to a faster but more expensive one. Unlike electroplating, electroless plating does not require electrical current. Deposition takes place in an aqueous solution containing metal ions, a reducing agent, complexing agents and stabilizers. Chemical reactions on the surface of the part being plated cause deposition of an NiP alloy. Since all surfaces wetted by the deposition bath are plated, deposit thickness is fairly uniform. These unique properties of the electroless deposition method make it possible to coat surfaces that are very difficult or impossible to be plated by other methods. Also it is quite impossible to achieve high thickness uniformity with other deposition methods.

For these reasons, electroless nickel technology has progressed considerably over the last fifteen years. In the early years, the electroless nickel plating manufacturers resorted to a

combination of trial and error approaches to their preparation and brave marketing campaigns. Today, electroless nickel technology requires a strong scientific explanation to meet the challenges of new applications and to uphold the reliability of existing ones. Over the last fifteen years, various international organizations have put major effort into developing reliable specifications. The purpose of these is to provide a consistent method for applying and testing electroless nickel deposits for proven and potential new applications.

One of the most appreciable advantages of electroless and electrodeposition of NiP alloys is the ability to obtain alloys of different composition by varying the deposition parameters. The resultant film composition can vary over a wide phosphorus atomic percent range and this variation has a significant effect on deposit microstructure and performance in general. Usually, NiP alloys are divided into three composition ranges: low (2-12 at.%), medium (13-16 at.%) and high ($\geq$17 at.%) phosphorus.

2.1.1 PHYSICAL PROPERTIES

2.1.1.1 MICROSTRUCTURE AND DENSITY

The influence of phosphorus content on the microstructure of NiP deposits has been investigated by means X-ray diffraction spectroscopy and scanning electronic microscopy studies. It has been shown that the typical crystalline structure of Ni deposits gradually transforms into an amorphous structure when P is introduced into the metal matrix. Deposits containing 4-12 at.% P exhibit a poor crystal structure (nanocrystalline) with porous morphology characterized by several intergranular cracks [5]. These deposits were represented as an fcc NiP solid solution of 5 to 10 nm crystallites [6].

On the other hand, for P content of 17 at.% or more, morphology was observed to be very smooth and devoid of nodules or cracks. High phosphorus deposits were accordingly expected to be amorphous, which was clearly supported by their XRD patterns.

Medium phosphorus deposits are not actually amorphous but a mixture of microcrystalline and amorphous phases with intermediate properties and performance [1,2].

The density of NiP alloys also depends upon phosphorus content as shown in Figure 2.1.

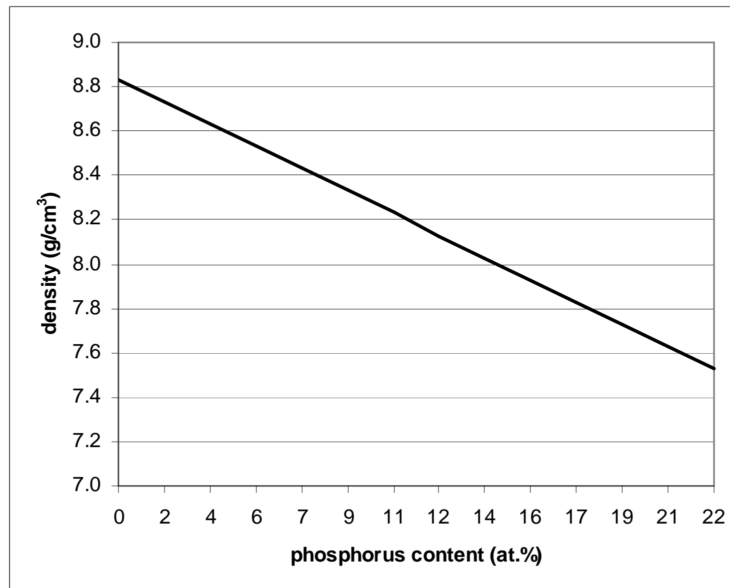

Figure 2.1 : NiP alloy density decreases with increasing phosphorus content due to P in nickel lattice. (http://www.pfonline.com/articles/pfd0507.html)

High phosphorus alloys have also been claimed to be amorphous, while some authors [7,8] maintain that high phosphorus alloys are actually a mixture of an amorphous NiP bulk phase and different quantities of nanocrystalline secondary phases (i.e. Ni and Ni_3P).

After annealing, the structure of NiP alloys becomes highly crystalline irrespective of phosphorus content [9,10] with the formation of fcc (face-centered cubic) Ni and bct (body-centered tetragonal) Ni_3P phases.

2.1.1.2 DEPOSIT UNIFORMITY [1-4]

One major advantage of electroless NiP plating, over electrodeposition, is its ability to produce a film of uniform thickness even on surfaces with complex geometries. Edges, deep and narrow holes as well as any surface roughness are easily plated. Current density is a

critical parameter in electrodeposition. Electroless deposition needs no electric current, hence as it is based upon a chemical reaction, any catalytic surface will plate uniformly. Bath solution agitation becomes a critical process parameter and the resultant film thickness is controlled by optimization of solution dynamics, immersion time and addition of additives.

2.1.1.3 MELTING POINT [1-3]

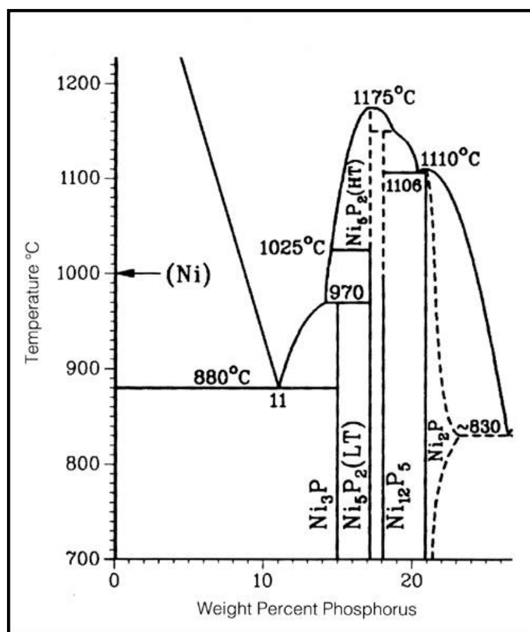

Figure 2.2 : NiP solid-liquid phases diagram (http://www.wallcolmonoy.com/TechServices/NicrobrazNewsArchives/WCC_Article_Nick_Based_Fill.htm).

Pure nickel has a melting point of 1455°C but the phosphorus containing alloys melt at lower temperatures (*Figure 2.2*). Melting point of NiP alloys decreases linearly with increasing phosphorus content. The lowest melting point for electroless NiP alloys is 880°C that occurs at the eutectic composition i.e. a phosphorus content of 11 wt% (19 at.%).

2.1.1.4 ELECTRICAL RESISTIVITY [1-3]

The electrical resistivity of NiP alloys is higher than that of pure nickel. Pure nickel has a specific resistivity of $7.8 \cdot 10^{-6}$ Ω cm. As the phosphorus content in the alloy increases, so too does its electrical resistivity. It ranges from 30 to $100 \cdot 10^{-6}$ Ω cm.

2.1.1.5 MAGNETIC PROPERTIES [1-3]

Figure 2.3 : Example of a Computer Hard Disk. (http://www.pfonline.com/articles/pfd0507.html)

One of the most important applications of electroless NiP alloys is in the data storage industry as substrate for computer hard disks (*Figure 2.3*). This is primarily due to their magnetic properties. The NiP substrate must remain non-magnetic after one hour bake cycles at 250-320°C. This requisite can only be satisfied by NiP alloys having a phosphorus content of at least 17 at.%.

2.1.1.6 CORROSION RESISTANCE [1,2]

The primary use of electroless NiP alloys is for preventing corrosion. Corrosion protection properties of NiP alloys vary with phosphorus content so that particular attention needs to be paid to choice of alloy composition depending on the specific application. This topic is discussed in detail in § 2.2.

For example, high phosphorus coatings are readily attacked in strong alkaline media while they perform very well in acid environments. To maximize corrosion protection the microstructure of NiP coatings must be devoid of microporosity, roughness, nodules and inhomogeneities. Phosphorus content alone does not guarantee specific performance. Factors affecting the corrosion protection performance of a NiP film, in a particular corrosive environment, are:

- phosphorus distribution throughout the coating
- volume fraction of micro-crystallinity within the film
- presence of phase boundaries and co-deposited impurities
- substrate pretreatment

- film surface structure and composition

In general, the following considerations hold:

- The rougher the surface, the lower the corrosion resistance
- The more porous the substrate material, the lower the corrosion resistance
- The higher the phosphorus content, the higher the corrosion resistance
- Post-deposition treatment such as low temperature baking or chromating, increases corrosion resistance
- Heat treatment reduces corrosion resistance

2.1.1.7 HARDNESS [10]

Another important tribological property of NiP deposits is their hardness. NiP coating hardness is mainly affected by P content and temperature and duration of heat treatment. As-plated electroless NiP films have a microhardness ranging from 500 to 720 HV N (Vickers Pyramid Number · Newton), while electrodeposited alloys have typical values of 150-400 HV N. Post-deposition heat treatment significantly enhances microhardness of the films and this increase is attributed to the phase transformations mentioned above. In general, hardness is inversely related to phosphorus content.

2.1.1.8 WEAR RESISTANCE [1]

Electroless NiP alloys have high wear resistance. This is due to their high hardness and natural lubricity but also to their excellent corrosion resistance that is strongly dependent upon deposit uniformity. Typically, as-plated low-phosphorus alloys tend to resist abrasive wear better than medium and high-phosphorus alloys. This is to be attributed to the greater microhardness of low-phosphorus alloys. However, after heat treatment the trend remains unchanged even if the microhardness becomes similar. This fact suggests that wear resistance is influenced by factors other than microhardness.

2.1.1.9 SOLDERABILITY / WELDABILITY [1]

One aspect that should not be neglected is the solderability of NiP alloys, particularly important for the electronics industry. As-plated low-phosphorus alloys are more solderable than medium and high-phosphorous ones but this difference disappears after 12-24 hours. Thus, it has been suggested that solderability depends upon the characteristics of the overlayer that forms on the deposit surface after air exposure.

2.1.2 APPLICATIONS [1-4]

2.1.2.1 AUTOMOTIVE INDUSTRY [1-3]

A large market segment of the automotive industry prefers the use of low cost materials plated with a NiP film. This choice is dictated by the need to satisfy stringent engineering requirements while maintaining market competitiveness. NiP alloys started to be used in the automotive industry about thirty years ago because of their properties such as corrosion and wear resistance, uniformity and lubricity and since then their use has been increasing. Examples of this NiP application, as a protective coating, are fuel filters, valves, differential shafts, brake pistons, etc…

Furthermore, the growth of fuel cell technology in the automotive industry will provide another potential application for NiP alloys. In any case, this market segment is growing continuously and NiP alloys are playing a very important role. This is due to the need for high quality and high performance components driven by the demand for longer warranty vehicles.

2.1.2.2 AEROSPACE [1,2]

Engineers have recognized the potential of the properties of NiP deposits for aerospace applications. A long term evaluation of these deposits has been and continues to performed. Various application tests resulted in the widespread use in engine parts such as valves,

undercarriages and turbine blades. Unlike the previously used materials such as hard chromium, compressive stresses on high phosphorus deposits do not significantly reduce their fatigue strength. For this reason, the continued use of NiP alloys in this area appears assured.

2.1.2.3 ELECTRONICS [1-3]

NiP alloys are increasingly used in the electronics industry. High phosphorus deposits are widely used as overcoats on aluminium substrates for magnetic data storage on computers. This is the largest single application of NiP alloys in electronics and can be attributed to their magnetic properties, solderability and corrosion resistance. Over the last 15 years several new technologies have been tested in an attempt to supersede the need for NiP coatings, but their uniformity, non-magnetic character and defect free nature have confirmed them as the most reliable and cost effective technology. Many different electronic components are plated with NiP to improve their corrosion and wear resistance. Also a variety of aluminium and zinc connectors are plated with NiP which ensures the uniformity, electrical conductivity and solderability required for these kinds of applications. Furthermore, new NiP technologies are emerging though certain technical and economic barriers still need to be overcome. Examples of these are the use of NiP alloys as floor grates for semiconductor packages and NiP/Au for circuit boards.

2.1.2.4 OIL, GAS AND CHEMICAL INDUSTRIES [1]

Components used in the oil, gas and chemical industries such as pumps, valves, flanges, pipes, etc., need to ensure long service life under severe conditions. Long life devices equate to low cost facility maintenance. These components are in contact with the final products so long life devices improve final products purity. These devices are usually plated with a 50-100 μm NiP film.

2.1.2.5 OTHER APPLICATIONS [1]

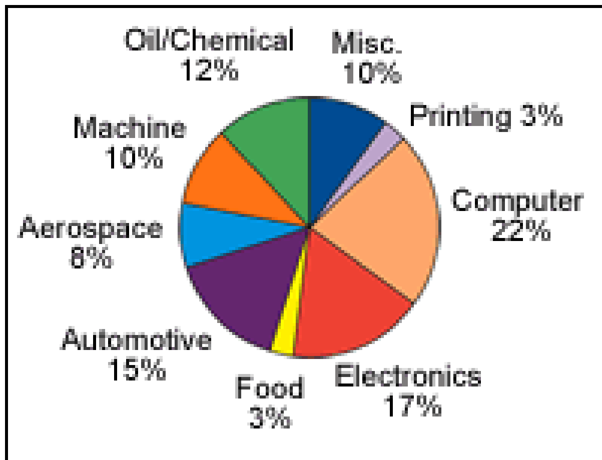

Fig. 2.4 : Cake diagram of NiP alloy applications (http://www.pfonline.com/articles/pfd0507.html).

Food, textile and printing industries are other important areas where NiP alloys are extensively used. The food industry bans the use of materials that are not legally approved. Steel was one of the most widely used materials; NiP alloys are now being used to coat the steel. NiP coatings are actually more versatile and corrosion resistant than steel ones, and ensure better food preservation during industrial processing. The textile industry takes full advantage of NiP alloys excellent wear resistance and lubricity. Shafts for ink-jet printers and large newspaper printing presses are two important examples of application of NiP alloys in the printing industry.

Note also, and this is not trivial, that electroless coating technology can be used on non-conductor materials.

2.2 CORROSION BEHAVIOUR OF NiP ALLOYS

Corrosion can be defined as damage to a material's surface, usually a metal or alloy, caused by a spontaneous redox reaction between the corroding material and its environment; the corroding material usually acting as anode. Corrosion always results in the deterioration of material properties with detrimental consequences on its performance. Therefore corrosion, especially in industrial facilities, can result in serious damage to devices, products and workers.

NiP alloys are widely used as corrosion protective coatings in many industrial applications (§ 2.1.2). Over the last thirty years, researchers have striven to understand the corrosion

behavior of NiP alloys. However, it is surprising how inconsistent the results and their interpretations are. Almost all the authors agree on the fact that small amounts of phosphorus in the alloy (0.5 - 1.6 at.%) lead to a decrease in corrosion resistance of nickel and to an increase in corrosion rate. But with respect to pure nickel increasing the phosphorus content enhances corrosion resistance.

On the contrary, there is no consensus on the nature of the anodic dissolution, “passivation” ability, susceptibility to pitting or on the nature of the film that forms on the alloy surface following exposure to a corrosive environment.

NiP alloys can be prepared using different methods such as rapid quenching, melt spinning, electrodeposition or electroless coating. However, how corrosion behaviour, as well as other properties or characteristics of NiP alloys, is influenced by the preparation method remains to be elucidated. It is generally accepted that only X-ray amorphous high-P alloys ($P \geq 17$ at.%) exhibit corrosion resistance clearly higher than pure crystalline nickel both in acidic and neutral environments, regardless of preparation technique. On the contrary, low-P alloys (2-12 at.%) perform better in alkaline environments than alloys with higher P content.

2.2.1 BEHAVIOUR IN ACID SOLUTIONS

In acid corrosive environments, the anodic behaviour of X-ray amorphous high-P alloys differs substantially from pure crystalline nickel (Figure 2.5). High-P alloys passivate at potentials at which Ni dissolves actively. At higher anodic potentials, the alloy undergoes transpassive dissolution while Ni passivates [11]. These differences in anodic behaviour were observed [11-13] both in the presence and absence of chloride ions in the electrolyte solution. The alloy surface remains shiny after polarization, while pure Ni becomes severely pitted [7,11,14,15].

However, some authors [12,16] failed to observe this sort of "passivation" for high-P alloys in practically identical acid environments. Others [12-14] reported that the NiP alloys suffered "pitting corrosion" by anodic polarization in acidic solutions containing chloride ions.

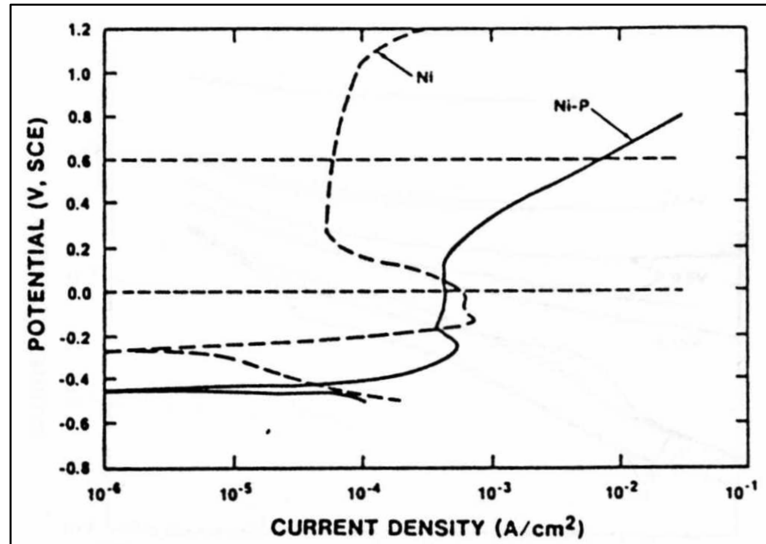

Fig. 2.5 [11]*: Anodic polarization curves for Ni and Ni-20P in 0.1 N H_2SO_4. Sweep rate = 1 mV/s.*

Regardless of the active/passive transition of NiP alloys, it is generally agreed that the corrosion film formed is P-enriched compared to Ni, suggesting that nickel is preferentially dissolved during anodic polarization [11,12,14-17].

Potentiostatic polarization, performed at potentials at which NiP alloy is "passivated" (ca. -0.2 ÷ +0.2 V SCE), showed a nearly logarithmic current decay suggesting a sort of kinetic limitation to alloy dissolution rather than an effective passivation [11,15,17].

Thus, the high corrosion resistance of high-P alloys may be explained by the formation of a P-enriched surface film which limits the diffusion rate of Ni from the bulk, slowing down dissolution of the alloy [15].

However, the chemical state of the P atoms in this enriched film it is still unclear. Several hypotheses have been advanced in the literature, including Diegle et al. [17] who proposed an adsorbed hypophosphite layer, Kawashima et al. [12] an orthophosphate layer, Salvago and Fumagalli [13] a phosphide layer, Rossi et al. [15] an elemental P interface between the bulk and a phosphate overlayer.

2.2.2 BEHAVIOUR IN NEUTRAL SOLUTIONS

Though little is reported about NiP alloys corrosion behaviour in neutral environments, the authors' findings concur. Under OC conditions, NiP alloys show a very low corrosion rate also in the presence of chloride ions [18]. The corrosion resistance of NiP alloys in neutral solutions is comparable, regardless of their structure and composition [19]. Anodic polarization, however, clearly gives rise to different dissolution mechanisms. Low-P crystalline alloys show active dissolution accompanied by the formation of a greyish-black non-protective film on the surface [19]. On the contrary, dissolution is suppressed in amorphous high-P alloys [20,21], and their passive properties are quite insensitive to the presence of chloride ions [19]. The high-P alloys remain bright and no pitting occurs [21]. Similarly to the acidic solutions, the excellent corrosion resistance of NiP alloys seems to be due to the formation of a P-enriched protective layer on the alloy surface [18,21,22] whose chemical state, as mentioned above, has not yet been conclusively identified.

2.3 X-RAY PHOTOELECTRON SPECTROSCOPY ANALYSIS OF NiP ALLOYS SURFACE

2.3.1 CORROSION FILMS FORMED IN ACID AND NEUTRAL SOLUTIONS

Notwithstanding the debate about the corrosion behaviour of Ni-P alloys, especially in acid environments, as well as about the chemical state of the phosphorus in the protective P-enriched layer, surprisingly the XPS results are consistent, both in acidic and neutral environments, and in the presence or absence of chloride ions in the test solutions.

NiP alloys show a current density vs. potential plateau range (ca. -0.2 ÷ 0.2 V SCE) both in acidic [12,15,16,23,24] and neutral [21,23,24] environments. After polarization, carried out at potentials within this plateau range, $Ni2p_{3/2}$, P2p, PKLL and O1s spectra show different

components (Table 2.1). The anodic polarization potential had no influence on the binding energy of either $Ni2p_{3/2}$ or P2p peaks [12,15].

Table 2.1 : Literature reported data of X-ray photoelectronic signals and X-ray induced Auger signals recorded on several NiP alloys, after different electrochemical tests carried out in different electrolytes.

Photoelectron Peak Attribution	Binding Energy (eV)	Literature Reference	C1s Binding Energy (eV)
$Ni2p_{3/2}$ bulk (main peak)	*852.9*	*[12]*	*/*
	852.7	*[16]*	*284.6*
$Ni2p_{3/2}$ phosphate (main peak)	*857.1*	*[12]*	*/*
	854 ÷ 856	*[16]*	*284.6*
$P2p_{3/2}$ bulk	*129.75*	*[12]*	*/*
	129.2	*[17]*	*284.6*
	129.9	*[16]*	*284.6*
	129.8	*[15]*	*285.0*
	130.0	*[21]*	*284.6*
$P2p_{3/2}$ “intermediate”	*132.2*	*[17]*	*284.6*
	132.2	*[16]*	*284.6*
	132.1	*[15]*	*285.0*
$P2p_{3/2}$ phosphate	*133.5*	*[12]*	*/*
	133.3	*[17]*	*284.6*
	133.3	*[16]*	*284.6*
	133.8	*[15]*	*285.0*
O1s phosphate	*531.7*	*[12]*	*/*
	531.9	*[17]*	*284.6*
O1s water	*533.0*	*[17]*	*284.6*
Induced Auger Peak Attribution	**Kinetic Energy (eV)**	**Literature Reference**	**C1s Binding Energy (eV)**
P KLL bulk	*1858.4*	*[15]*	*285.0*
P KLL “intermediate”	*1855.2*	*[15]*	*285.0*
P KLL phosphate	*1850.9*	*[15]*	*285.0*

$Ni2p_{3/2}$ spectra showed two peaks: a more intense peak at a BE (binding energy) of ~ 853 eV with a satellite at ~ 860 eV BE [12,16], and a second minor peak at ~ 856 eV BE with a satellite at ~ 863 eV BE [12,16]. The lower binding energy peak has been attributed unambiguously to the electrons photoemitted from the Ni in the bulk alloy [12,16]. The higher binding energy peak has been assigned to Ni^{2+} in the surface film formed after the corrosion tests [12,16].

P2p spectra consist of three different peaks [15]: a lower binding energy peak at ~ 129.7 eV BE attributed to P in the bulk [12,15-17,21], a higher binding energy peak at ~ 133.5 eV BE attributed to P^{5+} as phosphate [12,15,16], which according to some authors [12,17] may be dihydrogenated. Lastly, an intermediate peak at ~ 132.1 eV BE assigned by some authors [16,17] to P^{+} as hypophosphite. However, this assignment was based simply on comparison of the binding energy with several standard reference compounds, and assuming quite arbitrarily, the P present in the bulk to be in the elemental state. On the contrary, it is well known [25] that accurate chemical state information can rarely be obtained on the basis of BE alone, and that this might lead to XPS peaks being incorrectly assigned. As reported in the next subsection, Rossi et al. [15] based on the chemical state plot suggested the intermediate peak of phosphorus may be assigned to the elemental state.

As far as the O1s spectra are concerned, at least two superposed components have been found. One peak at ca. 532 eV has been definitively assigned to orthophosphate [12,17]. The peak at ca. 533 eV has been assigned to water molecules adsorbed on the samples surface [17]. A third peak at ca. 530 eV was observed by Kawashima et al. [12] but they were unable to assign it. On the other hand, Diegle et al. [17] did not observe this component at ca. 530 eV but a different peak at ca. 531 eV (not observed, on the contrary, by Kawashima et al. [12]), which they attributed to hypophosphate [17].

2.3.2 CHEMICAL STATE OF PHOSPHORUS

Sputtered NiP alloys are reported [15] to always exhibit a single P2p peak at 129.7 eV BE and a PKLL peak at 1858.5 eV KE. After mechanical polishing and/or anodic polarization [15] in acid solutions, three P2p components appeared with the following binding energy values: (1) 129.8 eV, (2) 132.1 eV and (3) 133.8 eV. The corresponding Auger induced KE (kinetic energy) values of the PKLL signal were (1) 1858.4 eV, (2) 1855.2 eV and (3) 1850.9 eV.

As reported in the previous subsection, from the chemical shifts of the $P2p_{3/2}$, the lower and higher binding energy peaks have been unambiguously attributed to the phosphorus in the bulk alloy and to the phosphate located in an outer surface layer, respectively [12,15-17].

As far as the peak at the intermediate BE value, it has been tentatively assigned to P^{+} or P^{3+} in an unidentified compound located in the inner part of the corrosion film [16], or to the hypophosphite [17] on the basis of the BE values alone.

However, more precise information on the chemical state of the phosphorus can be obtained from the so called modified Auger parameter α [25] :

$$\alpha = KE(PKLL) + BE\left(P2p_{3/2}\right)$$

Rossi et al. [15] calculated the α values for peaks detected in polarized NiP alloys as well as for several pure reference phosphorus compounds, so as to construct the so called *chemical state plot* [26,27].

The intermediate phosphorus of the mechanically polished and/or anodically polarized NiP alloys showed the same Auger parameter as those found for pure red P and black P, thus it was proposed [15] that this phosphorus might be present in the elemental state. The Auger parameter confirmed the assignments for the other two components of the P2p spectrum [15]: the one for the bulk at lower BE and the one for the phosphate at higher BE.

It should be pointed out that the Auger parameter of the phosphorus in the bulk was found to be similar to that of nickel phosphide [15]. The binding energy of the $P2p_{3/2}$ alloy was found to be about 0.3-0.4 eV lower than elemental red P [15] regardless of P content [28]. On the other hand, a very small shift (ca. 0.1 eV) to higher BE was found for the $Ni2p_{3/2}$ alloys peak compared to pure nickel, again, regardless of P content [28].

Comparing these results with those reported in the literature, it was concluded [15,28] that a small charge transfer (about 0.3-0.4 electrons per P atom) occurs from Ni to P in the NiP alloys [29] leading to a partially covalent bond [30]. This charge transfer corresponds to 0.1 electron per Ni atom [29]. In other words, P in the alloys shows a slightly negative formal charge compared to elemental red P.

2.3.3 THE ELECTRONIC STRUCTURE OF NIP ALLOYS AND FEATURES OF THE $Ni2p_{3/2}$ REGION

The XPS binding energies of core-level electrons commonly provide chemical state information about near surface atoms or ions. In other words, a change in chemical environment or oxidation state of an atom is usually accompanied by a change in its binding energy. Thus, evaluation of core-level photopeak binding energies of an uncharacterized sample should provide valuable insight into the oxidation state and bonding of its near-surface atoms. Unfortunately, nickel behaves anomalously. Ni core-level photopeak binding energies for pure metal nickel and its conductors alloys and compounds were found to be similar and within about 0.3 eV of 852.8 eV BE [31,32]. Apparently, electronegativity of the ligand and the presence and type of bonding orbitals of dominantly ligand character had little effect on e.g. $Ni2p_{3/2}$ main peak binding energy. However, the ligand electronic structure showed its influence upon overall alloy electronic structure separating the satellite and main peak of $Ni2p_{3/2}$ spectra as well as the other Ni core-level photopeaks [31,32]. In Ni compounds with a given element, satellite intensity tends to decrease with increasing partner concentration, at the same time satellite separation from the main peak tends to increase [32]. Furthermore, for a given stoichiometry, core-level satellite intensity tends to decrease with partner electronegativity and satellite separation from the main peak to increase [32]. Nesbitt and

coworkers [31] developed a model to explain these observations and for the time being this is the most widely accepted. In the following, Nesbitt's model is briefly discussed.

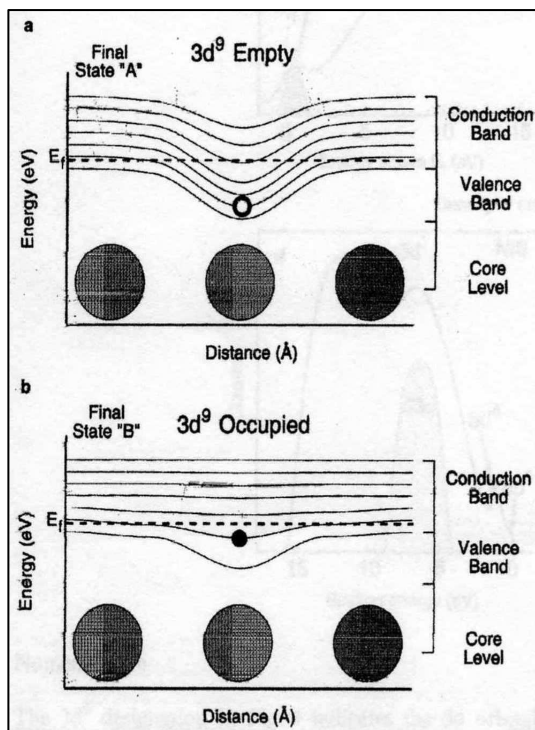

Figure 2.6 [31]*: (**a**) The Coulomb potential created by ejection of a photoelectron causes 3d^9 states (including empty states) to be temporarily localized over the photoion. (**b**) The effect of the core hole is enhanced by filling the 3d^9 state. The associated relaxation energy is transferred to the ejected photoelectron.*

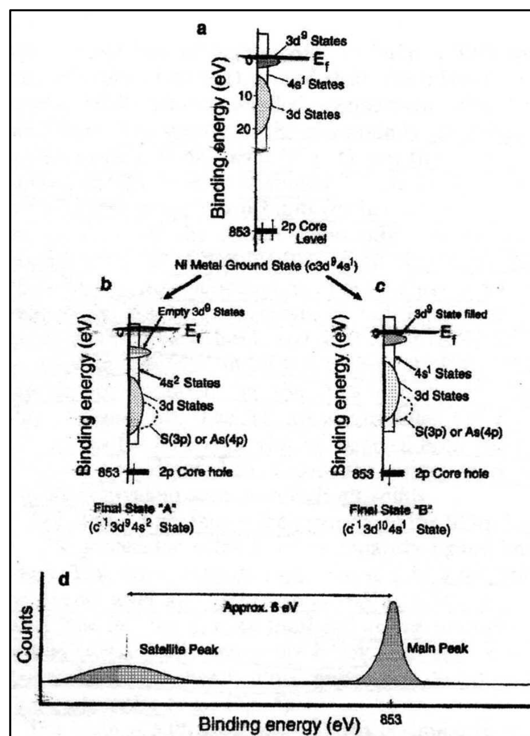

Figure 2.7 [31]*: Generalized conduction band and valence band structure in Ni and conductor Ni compounds. (a) Ground state. (b) Final state "A" resulting from 4s state filling. (c) Final state "B" resulting from 3d^9 state filling. (d) Relative binding energies of the main and satellite peaks.*

Photoejection of a core electron from an atom causes an instantaneous increase in Coulomb potential which attracts valence and conduction band orbitals towards the nucleus of the photoion. This potential is ephemeral and exists only for the life time of the core-hole (about 10^{-15} s). Unoccupied orbitals, initially energetically located just above the Fermi level, are drawn below it, as shown in Figure 2.6-a. These unoccupied orbitals, "localized" on the photoion, have a lower energy than the same orbitals unaffected by the core-hole potential. The possibility therefore exists that one or more empty orbitals within this potential well, will filled by Fermi sea electrons.

When Fermi sea electrons fill unoccupied orbitals in the core-hole potential well, they release energy and, in turn, the effect of the core-hole is partially attenuated by this relaxation energy being transferred to the outgoing photoelectron, as shown in Figure 2.6-b. Photoelectron kinetic energy is thus increased by an energy amount equal to this relaxation energy.

In the ground state (Figure 2.7-a), the conduction band of Ni includes $3d^9$ and 4s orbitals straddling the Fermi level, thus the electronic initial state of Ni is $c\,3d^9\,4s^1$. The photoemission of a core electron creates the core-hole, thus, both the $3d^9$ and 4s bands are drawn into the resulting potential well below the Fermi level. Whether a $3d^9$ or 4s orbital is filled first by one Fermi sea electron, the resulting screening of the core-hole decreases the probability of other empty orbitals within the same bands being filled during the life time of the same core-hole.

If an electron of the Fermi sea fills a 4s orbital, the final state $c^{-1}3d^9 4s^2$ is produced, referred to as final state A (Figure 2.7-b). Alternatively, if a Fermi sea electron fills a $3d^9$ orbital, during a separate photoemission event, the final state $c^{-1}3d^{10}4s^1$ is produced, referred to as final state B (Figure 2.7-c).

The effect of the potential well is attenuated whether a 4s or $3d^9$ state is filled first, but filling a $3d^9$ orbital provides greater core-hole screening, with the result that there is greater associated relaxation energy. The greater the relaxation energy, the greater the amount of energy acquired by the photoelectron, which in turn will be recorded at a lower BE in the XPS spectrum. In other words, the creation of the final state A (4s filled) gives rise to the satellite peak, the final state B (3d filled) to the main peak [31]. This argument was further substantiated by quantomechanical calculations based on electrical conductivity in metals [31] and by experimental measurement of the valence band density of states (DoS) of several Ni compounds [29,30,33-35].

The relative intensity of the main and satellite peaks should be determined by the relative probability of $3d^9$ and 4s holes being filled. Furthermore, Nesbitt's model [31] also provides a

plausible explanation for the different FWHM observed for the main $Ni2p_{3/2}$ peak and its satellite. As shown in Figure 2.7, the 4s band is energetically dispersed whereas the 3d band is more condensed. Thus, filling different 4s states will result in a wider range of relaxation energies and consequently in a broad satellite peak. On the contrary, filling 3d hole states results in a much narrower range of relaxation energies and thus in a narrower main peak [31].

But why does the ligand influence the satellite BE leaving the main peak position unaffected ?

Our research group carried out an XPS study to elucidate the effects of P concentration on the electronic structure of NiP alloys [28] with P content ranging from 6 to 29 at.% . A constant binding energy of the $Ni2p_{3/2}$ (852.7 ± 0.04 eV) and the $Ni2p_{1/2}$ signal (870.0 ± 0.05 eV) was found for the NiP alloys, irrespective of the P content. On the other hand, the distance of the satellite from the main peak increased, and its intensity decreased, with increasing P content in the alloy [28]. According to the results reported by Nesbitt et al. [31] (obtained, in particular, by the DoS study of NiS and NiAs), and to both XPS valence band measurement [33-35] and quantomechanical calculations [29,34,36], these observations were interpreted in terms of electron transfer from the P3p ligand band to Ni3d band. This charge transfer is not possible when the final state B (main peak) is formed since the energy difference between the ligand band and the Ni3d band is too high [31], i.e. the BE of $Ni2p_{3/2}$, as well as that of the other Ni core-peaks, is not affected by the phosphorus concentration. Thus, it has been hypothesized [28] that the number of bonding Ni3d electrons increases with phosphorus content in NiP alloys. Thus, less non-bonding electrons are available for shielding the core-hole [37]. Poorer core-hole screening leads to a deeper potential well and, thus, to a lower relaxation energy associated to the final state A formation ($c^{-1}3d^9 4s^2$). Hence, the photoelectrons responsible for satellite peak generation, gain a lower contribution to their KE as P concentration increases in the alloy while the main peak position remains unchanged.

However, even if Nesbitt's model seems to explain all the observed modifications of the $Ni2p_{3/2}$ features (as well as of the other Ni core-level peaks), the literature on the electronic

structure, theoretical models and energy loss spectroscopy (ELS) of Ni metal and its O containing compounds has been recently reviewed [38]. Nesbitt's model appears to be "too simple" and inadequate as it does not take into account all the photoelectron energy-loss processes.

It has been reported that the more intense feature of the Reflection Electron Energy Loss Spectroscopy (REELS) of metallic nickel at 6.0 and 9.5 eV are due to surface and bulk plasmon losses respectively, with weaker intra- and inter-band transitions at 3.7 and 7.1 eV [38]. The $Ni2p_{3/2}$ XPS spectrum from metallic nickel has been re-examined, on the basis of these REELS results, by other authors [39]. It may be possible to fit the $Ni2p_{3/2}$ XPS spectra with a set of five energy-loss peaks (satellites) at energy 3.5, 4.5, 5.5, 7.0 and 8.0 eV above the main emission line, and that these energy-loss features may be attributed to the REELS features observed by Hagelin-Weaver et al. [38]. However, the same authors [39] concluded that the $Ni2p_{3/2}$ is well fitted with only two satellites at 3.7 and 6.0 eV and that these "components" do not represent specific processes but are likely, on the basis of the REELS data, to represent both plasmon and some shake-up losses from the primary $Ni2p_{3/2}$ photoemission.

2.4 MODELS PROPOSED IN THE LITERATURE FOR EXPLAINING HIGH CORROSION RESISTANCE OF NiP ALLOYS

Several models have been proposed for explaining the high corrosion resistance of high-P alloys in acid environments. The most popular ones are briefly outlined in the following. As will be seen there are discrepancies between these models and all are questionable.

Diegle and coworkers [17] proposed the formation of an adsorbed film of hypophosphite through oxidation of the P present in the enriched surface layer formed as a consequence of the rapid and selective dissolution of Ni at the beginning of immersion in the test solution (pH ~ 1-2). This adsorbed hypophosphite film should prevent the water molecules from

interacting with Ni, inhibiting its further oxidation and dissolution. The successive breakdown of this protective film at higher potential (ca. > +0.2 V SCE) should be caused by its defective crystalline surface which facilitates further P oxidation from hypophosphite to "soluble" phosphate anions [16]. However, while nickel phosphate is readily soluble in acids (but insoluble in either cold or hot water), nickel hypophosphite is soluble even in cold water [40]. Furthermore, the most thermodynamically stable phosphorus species at pH ~ 1-2 and a potential of between -0.2 and +0.2 V SCE is orthophosphoric acid [41].

Kawashima and coworkers [12] proposed the formation of a nickel orthophosphate film on the NiP alloy surface, following polarization in acid solutions, and this is in agreement with the Pourbaix diagram for phosphorus [41]. It is also claimed [12] that this phosphate layer probably thickens with polarization time but it is not clear how film thickness is determined. However, the authors do not account for the fact that nickel orthophosphate is soluble in acids [40], even though it might be stabilized by interaction with the alloy surface.

However, the model proposed by Kawashima et al. [12] clearly contradicts that proposed by Diegle et al. [17] : the first proposed a protective *phosphate* layer, the second that the (hypophosphite) protective layer breaks down as a consequence of its oxidation to *phosphate*.

Another interesting model is the one proposed by Salvago and Fumagalli [13]. They claim that the differences in anodic behaviour between NiP alloys and elemental nickel cannot be attributed to superficial P oxidation products such as hypophosphites, phosphites or phosphates, since the presence of these anions in the electrolyte solution (i.e. added by the authors) did not alter the anodic behaviour of the alloys. Dissolution tests in hydrochloric acid, followed by a not well specified analysis, revealed the presence of Ni_2P residuals [13], thus, only on these bases, it was proposed [13] that NiP alloy "passivation" was due to a surficial nickel phosphide film, not taking into account the experimental evidence provided by XPS surface analysis [11,12,16,17,21].

Lastly, other authors [8] have discussed the anodic behaviour of NiP alloys focusing on the surface morphology instead of on the type of the P contained in the P-enriched layer. A model has been proposed [8] whereby the reduced atom coordination associated with the high volume fraction of grain boundaries and triple junctions of low-P crystalline alloys with respect to high-P X-ray amorphous alloys, results in an enhanced adsorption of oxygen from the solution which, in turn, facilitates oxidation and dissolution of the alloy. The most inhomogeneous alloys showed [8] reduced corrosion resistance suggesting that the main cause of the change in corrosion behaviour is the concentration of particular morphological features on the alloy surface. However this reasoning cannot explain why at higher potentials (ca. > +0.2 V SCE) NiP dissolves while Ni is passivated, since metallic Ni is highly crystalline.

In any case, some sort of contribution to the corrosion performance of NiP alloys, due to both their morphology and structure cannot be ruled out as it is well known [1] that these two aspects are closely related with the P content of the alloy.

2.5 OPEN QUESTIONS

NiP alloys are widely used in many industrial applications [1-4], especially because of their high corrosion and wear resistance [1].

There is general consensus in the literature that medium (13-16 at.% P) and high (≥17 at.% P) phosphorus alloys have higher corrosion resistance than pure Ni both in acid [7,11,12,15,17] and neutral [19-21] environments, irrespective of the presence of chloride ions in the test solution.

It is generally agreed that in both acid and neutral environments a P-enriched protective film forms [7,11,12,14,15,17,21], suggesting that nickel is preferentially dissolved during anodic polarization and that this P-enriched layer is responsible for the high corrosion resistance of NiP alloys. These hypotheses have been further confirmed by numerous XPS studies [12,15-

17,21] as well as by glow discharge optical spectroscopy [14] and Auger Electron Spectroscopy (AES) depth-profiling [11].

In particular, after anodic polarization, the P2p region shows three components. The lower BE peak (~ 130 eV) and higher BE peak (~ 133 eV) have been unambiguously assigned to phosphorus in the bulk alloy and in a phosphate layer, respectively. While the assignment of the third intermediate BE peak (~ 132 eV) is still under discussion.

Thus, the first important open question is to conclusively identify the chemical state of this "intermediate phosphorus".

The origin of this intermediate P2p component has been differently interpreted with the result that different contrasting models have been developed for explaining the high corrosion resistance of the NiP alloys. Diegle et al. [17] proposed an adsorbed hypophosphite layer, Kawashima et al. [12] an orthophosphate layer, Salvago and Fumagalli [13] a phosphide layer, while Rossi et al. [15] proposed an elemental P interface between the bulk and a phosphate overlayer.

It is clear, however, from the current literature review, that none of these models are fully satisfactory and actually contradict one another. An accurate study of the in-depth profile of the corrosion film formed on the NiP alloys has never been carried out, even though it it fundamental for gaining a deeper insight into the corrosion performance of NiP alloys. Furthermore, with an accurate and non-destructive reconstruction of the in-depth profile, it may be possible to advance a better-grounded hypothesis of the formation and breakdown mechanism of the corrosion film.

Indeed the corrosion behaviour of NiP alloys clearly does not depend on P concentration alone, since the P content strongly influences both alloy structure and morphology as well as its electronic structure. Thus, the high corrosion resistance of NiP alloys can probably be explained by all these aspects, but their influence on corrosion behaviour as a whole is not fully understood .

REFERENCES

1. M.Sisti, A.Ruffini - Sirius Technology, Inc. – Oriskany, NY (http://www.pfonline.com/articles/pfd0507.html)
2. R.Bellemare, P.Vignati – OMG Fidelity, Inc. – Newark, New Jersey (http://www.pfonline.com/articles/pfd0024.html)
3. R.Taheri, PhD Thesis at University of Saskatchewan – Saskatoon, Canada (2003)
4. ASTM B733-04 : *Standard Specification for Autocatalytic (Electroless) Nickel-Phosphorus Coatings on Metal*
5. C.Hu, A.Bai, *Materials Chemistry and Physics 77*, 215 (2002)
6. K.Hur, J.Jeong, D.N.Lee, *Journal of Materials Science 25*, 2573 (1990)
7. B.Bozzini, C.Lenardi, M.Serra, A.Fanigliulo, *British Corrosion Journal 37(2)*, 173 (2002)
8. L.Pèter, G.Làng, L.Kiss, J.Szalma, *Journal of Applied Electrochemistry 26*, 403 (1996)
9. T.S.N.Sankara Narayanan, I.Baskaran, K.Krishnaveni, S.Parthiban, *Surface & Coatings Technology 200*, 3438 (2006)
10. H.Ashassi-Sorkhabi, S.H.Rafizadeh, *Surface & Coatings Technology 176*, 318 (2004)
11. R.B.Diegle, N.R.Sorensen, G.C.Nelson, *Journal of the Electrochemical Society 133(9)*, 1769 (1986)
12. A.Kawashima, K.Asami, K.Hashimoto, *Corrosion Science 24(9)*, 807 (1984)
13. G.Salvago, G.Fumagalli, *Metal Finishing 85*, 31 (1987)
14. E.T.Van der Kouwe, *Electrochimica Acta 38(14)*, 2093 (1993)
15. A.Rossi, D.Atzei, B.Elsener, A.Krolikowski, *EUROCORR (on CD)*, (2001)
16. S.J.Splinter, R.Rofagha, N.S.McIntyre, U.Erb, *Surface and Interface Analysis 24*, 181 (1996)

17. R.B.Diegle, N.R.Sorensen, C.R.Clayton, M.A.Helfand, Y.C.Yu, *Journal of the Electrochemical Society 135(5)*, 1085 (1988)

18. R.L.Zeller, *Corrosion 47(9)*, 692 (1991)

19. A.Krolikowski, P.Butkiewicz, *Electrochimica Acta 38(14)*, 1979 (1993)

20. M.M.V.Parente, O.R.Mattos, S.L.Diaz, P.Lima Neto, F.J.Fabri Miranda, *Journal of Applied Electrochemistry 31*, 677 (2001)

21. P.Lo, W.Tsai, J.Lee, M.Hung, *Surface and Coatings Technology 67*, 27 (1994)

22. J.N.Balaraju, T.S.N.Sankara Nayanan, S.K.Seshadri, *Journal of Solid State Electrochemistry 5*, 334 (2001)

23. M.Crobu, Master Thesis - University of Cagliari, Italy (2007)

24. M.Crobu, M.A.Scorciapino, B.Elsener, A.Rossi, *"The corrosion resistance of electroless deposited nano-crystalline Ni-P alloys"* , Electrochimica Acta in press, Accepted Manuscript, Available online 5 December 2007 (http://www.sciencedirect.com/science/article/B6TG0-4R8WK1H-1/2/a4a9ab51d212b7a398c70873b28fc3b2)

25. C.D.Wagner, *Analytical Chemistry 44*, 967 (1972)

26. C.D.Wagner, A.Joshi, *Journal of Electron Spectroscopy and Related Phenomena 47*, 283 (1991)

27. G.Moretti, *Journal of Electron Spectroscopy and Related Phenomena 95*, 95 (1998)

28. B.Elsener, A.Krolikowski, D.Atzei, A.Rossi, "*Effect of phosphorus concentration on the electronic structure of NiP nanocrystalline electrodeposited alloys: an XPS and X-AES investigation*", accepted for publication on *Surface and Interface Analysis*

29. J.Kojnok, A.Szasz, W.Krasser, G.Mark, V.S.Stepanjuk, A.A.Katsnelson, *Journal of Physics of Condensed Matter 4*, 2487 (1992)

30. E.Belin, A.Traverse, A.Szàsz, F.Machizaud, *J. Phys. F.: Met. Phys. 17*, 1913 (1987)

31. H.W.Nesbitt, D.Legrand, G.M.Bancroft, *Physical Chemistry Minerals 27*, 357 (2000)

32. F.U.Hillebrecht, J.C.Fuggle, P.A.Bennett, Z.Zolnierek, *Physical Review B 27(4)*, 2179 (1983)

33. H.Yang, J.C.Swihart, D.M.Nicholson, R.H.Brown, *Physical Review B 47(1)*, 107 (1993)

34. A.Jezierski, *Solid State Communications 69(11)*, 1023 (1989)

35. J.C.Fuggle, F.U.Hillebrecht, R.Zeller, Z.Zolnierek, P.A.Bennett, C.Freiburg, *Physical Review B 27(4)*, 2145 (1982)

36. R.P.Messmer, *Physical Review B 23(4)*, 1616 (1981)

37. S.Diplas, S.Jørgensen, J.Taftø, T.Tønnessen, T.Knutsen, J.Lehrmann, T.Våland, M.-L.Abel, J.F.Watts, *Surface and Interface Analysis 38*, 238 (2006)

38. H.A.E.Hagelin-Weaver, J.F.Weaver, G.B.Hoflund, G.N.Salaita, *Journal of Electron Spectroscopy and Related Phenomena 134*, 139 (2004)

39. A.P.Grosvenor, M.C.Biesinger, R.S.Smart, N.S.McIntyre, *Surface Science 600*, 1771 (2006)

40. *CRC Handbook of Chemistry and Physics*, ed. D.R.Lide – CRC Press, 75th edition (1995)

41. M.Pourbaix, *“Atlas of Electrochemical Equilibria in aqueous solutions”* Pergamon Press Ltd. (1966)

CHAPTER 3

METHOD THEORY

In this chapter the theoretical foundations underlying the techniques used in this work are described in detail. In section 3.1 the principles of X-ray Photoelectron Spectroscopy (XPS) are summarized together with the most important information to be gleaned from the spectra (from subsections 3.1.1 to 3.1.5).

In subsection 3.1.6 the First Principles method for quantitative surface analysis is discussed in detail and its limitations underlined. Then, subsection 3.1.7 presents the problem of electron Inelastic Mean Free Path (IMFP) evaluation. Three of the most important IMFP predictive formulas found in the literature: the Seah&Dench, the TPP-2M and the G-1, are described in detail underlining their advantages and limitations. In subsection 3.1.8 the Tougaard method for quantitative and non-destructive in-depth profiling is presented together with its advantages and limitations. Subsection 3.1.9 presents the theory of the Maximum Entropy Method for the non-destructive reconstruction of compositional depth profiles from angle-resolved XPS data.

Finally, section 3.2 deals with the theory of the corrosion process, in both thermodynamic and kinetic terms. Information that can be gleaned from the polarization curves is discussed in some detail.

3.1 X-RAY PHOTOELECTRON SPECTROSCOPY (XPS)

3.1.1 PHYSICAL PRINCIPLE [1]

The XPS technique is based on the photoelectric effect, i.e. the ejection of an electron from an atomic level by an X-ray photon of energy hν. The energy of the emitted photoelectrons is then analyzed by the electron spectrometer and the data presented as a graph of intensity (usually expressed as counts or counts/s) versus electron energy.

The kinetic energy (KE) of the electron is the experimental quantity measured by the spectrometer, but this is dependent on the photon energy of the X-rays employed and is therefore not an intrinsic property of the materials being studied. On the other hand, the binding energy (BE) is a parameter that identifies the electron specifically, both in terms of its parent element and atomic energy level from which it was photoemitted. The fundamental relationship between the parameters involved in a XPS experiment is:

$$KE = h\nu - BE - \Phi$$

where Φ is the spectrometer work function. The photon energy hν must be greater than BE in order to obtain electron photoemission. Once the electron is emitted, all energies are permitted and selection rules do not apply.

The photoelectron can come from the valence band levels or, more interestingly for XPS, from core levels. The electron binding energies differ from element to element and elemental identification is almost straightforward. The above equation shows that if the BE of an electron in an element changes due to a different chemical environment (e.g. the same element in two different compounds) the KE also changes. Thus, valuable information on the chemical state of the elements can be obtained from XPS.

Once a photoelectron has been emitted, the ionized atom must relax. This can be achieved by emission of an X-ray photon (X-ray fluorescence) or ejection of an Auger secondary electron. Thus, Auger electrons are produced as a consequence of the XPS primary process, and this secondary phenomenon is often referred to as XAES (X-ray induced Auger electron spectroscopy). Auger peaks can yield valuable chemical information about an atom but they can also interfere with photoelectronic peaks. Signal superposition can be avoided by changing the X-ray source.

Hydrogen and helium cross sections using Al kα or Mg kα radiations are too small, so these two elements cannot be detected by XPS.

The sampling depth of the XPS technique varies with the KE of the electrons being examined. It is determined by a quantity $\Lambda = \lambda \cos\theta$ known as electron attenuation length (AL). It

depends on the inelastic mean free path λ (IMFP), which depends firstly on the KE of the electron and density of the solid being passed through by the electron, and on the emission angle θ, i.e. the angle at which particles leave a specimen measured relative to the normal to the specimen surface. Typical sampling depth is ca. 3Λ. In the energy range of interest in electron spectroscopy, i.e. 200-2000 eV, Λ is equal to very few nanometers (< 10 nm). This is the reason why XPS is a surface sensitive technique.

3.1.2 NOTATION [1]

The formalism used for XPS differs from that used for Auger electron spectroscopy (AES) to describe which electrons are involved in each of the observed transitions: XPS uses the so called spectroscopists' notation whereas Auger electrons are identified by the equivalent X-ray notation.

In the former, the transitions are labelled according to the scheme nl_j where n is the principal quantum number, l is the electron angular momentum quantum number and j is the so called total angular momentum quantum number and it is given by |l+s| (s is the spin angular momentum quantum number).

In X-ray notation, the principal quantum numbers are identified with the letters K, L, M, etc. whereas subscript numbers refer to the j values. The relationship between the two notations is given in Table 3.1.

Table 3.1 : Relationship between spectroscopists' notation and X-ray notation.

quantum numbers			**spectroscopists' notation**	**X-ray subscript**	**X-ray notation**
n	**l**	**j**			
1	*0*	*1/2*	*1s*	*1*	*K*
2	*0*	*1/2*	*2s*	*1*	L_1
2	*1*	*1/2*	$2p_{1/2}$	*2*	L_2
2	*1*	*3/2*	$2p_{3/2}$	*3*	L_3
3	*0*	*1/2*	*3s*	*1*	M_1
3	*1*	*1/2*	$3p_{1/2}$	*2*	M_2
3	*1*	*3/2*	$3p_{3/2}$	*3*	M_3
3	*2*	*3/2*	$3d_{3/2}$	*4*	M_4
3	*2*	*5/2*	$3d_{5/2}$	*5*	M_5
…	…	…	…	…	…

3.1.3 SPECTRA [1]

It has been seen that an XPS spectrum is a plot of intensity (number of electrons counted) vs. electron energy (either BE or KE). Those electrons that are excited and escape without energy

loss, contribute to the characteristic peaks in the spectrum; those that undergo inelastic scattering and suffer energy loss, contribute to the spectrum background.

The first step in characterizing the surface chemistry of the specimen under investigation is to identify the elements present on its surface. To achieve this, a survey, or wide scan, is recorded over a region that provides the peaks that the different elements can emit after irradiation with the source. Usually, the range 0-1200 eV is sufficient. Peak identification is achieved by means of electron energy reference tables.

The survey spectrum will generally be followed by the acquisition of spectra around the element peaks of interest with a higher resolution. Curve fitting routine applied to these spectra allows to resolve peak overlap thus providing chemical information on the specimen and making quantitative analysis possible.

XPS peaks have a mixed Gaussian-Lorentzian shape. The main contributions to their width can originate from the sample or the instrument. The mean lifetime of a core vacancy following photoemission (Lorentzian contribution) and the peak overlap are the main sample contributions to peak width. The source line-width, spectrometer resolution and uneven sample charging are the main instrumental contributions (Gaussian contribution).

3.1.3.1 CHEMICAL SHIFT

If an atom is bonded to another atom its valence electron density will be altered with respect to its elemental state. The electrostatic potential of the core electrons will be modified as well as a change of the BE of the signal (chemical shift) will be observed in the spectrum. The chemical shift can vary from a fraction up to several electronvolts. Due to line width of the X-ray source used in XPS (0.25-0.9 eV) data processing is often required to extract information from a spectrum. Tables of the chemical shift of an element in several of its compounds enable to identify its chemical state [2].

3.1.3.2 SPIN-ORBIT COUPLING

The peaks in XPS spectra, derived from orbitals whose angular momentum quantum number l is greater than 0, are usually split into two. This is the result of the interaction of the electron angular momentum due to the spin (s) with that due to the orbital angular momentum (l). The value of s can be either +1/2 or -1/2. The two resulting states have a different j value equal to $|l \pm ½|$. The relative intensity of the components of the doublets formed is dependent upon their relative populations (degeneracies) which are given by 2j+1. The spacing between the components of the doublets depends upon the strength of the spin-orbit coupling. For a given

value of n and l, separation increases with the atomic number of the element. For a given element, it decreases with both increasing n and increasing l.

3.1.3.3 MULTIPLET SPLITTING

Multiplet splitting of a photoelectron peak may occur in a compound that has unpaired electrons in the valence band, and arises from different spin distributions of the electrons band structure. This results in a doublet of the core level peak. Multiplet splitting effects are observed for several transition metals.

3.1.3.4 SATELLITE PEAKS

The initial-state energy changes are mainly due to the chemical bond formed by the atom. Final-state effects that occur after photoemission, such as core-hole screening, relaxation of electron orbitals and polarization of surrounding ions cause other peaks to appear in the XPS spectrum, known as satellites.

One of the most important satellite peaks is the shake-up satellite. This spectral feature may occur when the outgoing photoelectron simultaneously interacts with a valence electron and excites it (shakes it up) to a higher energy level. The energy of the core photoelectron is then slightly reduced giving a satellite structure a few electronvolts below (above on a binding energy scale) the core level position on the kinetic energy scale.

Another important feature is the shake-off satellite, where the valence electron is ejected from the ion completely.

3.1.3.5 ENERGY SCALE CORRECTION FOR CHARGING

Photoemission from an insulating sample causes electrostatic charging to occur in the positive direction. This results in a shift in the peaks position towards higher BE values. Energy scale correction is usually performed by referring all peaks to that of the aliphatic C1s at 285.0 eV. This is the most widely used charging correction and is generally accepted. Other methods are however reported in the literature [3].

3.1.3.6 CALIBRATION

Accurate spectrometer calibration is required to extract chemical shift information by comparing the measured BE with literature data or databases enhancing experimental data interpretation and providing a qualified analysis.

The linearity of the BE scale is checked by comparing the $Au4f_{7/2}$, $Ag3d_{5/2}$, $Cu2p_{3/2}$ and the CuLMM (this is required only for non-monochromatic sources) positions with their expected values. The most common guidelines for the calibration procedure and for the references peaks can be found in the ISO15472:2001 norm [4].

3.1.4 DATA PROCESSING

Data processing is required to extract the maximum amount of information from an XPS spectrum. Several commercial software packages are available for rapidly and easily implementing curve fitting routines. CASA XPS (Casasoftware Ltd., UK) has been used in this work.

Data manipulation is a multi-step process and involves the following:

- spectra inspection
- X-ray source satellite removal (only for non-monochromatic sources)
- background subtraction
- peak fitting

3.1.4.1 X-RAY SOURCE SATELLITE SUBTRACTION

Subtraction of the satellites due to the use of a non-monochromatic X-ray source must be carried out carefully as spectral distortion may result in incorrect removal. Some authors [5] [6] suggest keeping all the satellites to preserve all the data.

3.1.4.2 PEAK FITTING

In many cases the information provided by XPS is contained in a spectrum that consists of a number of overlapping peaks. This happens when the full width at half maximum (FWHM) of a photoelectron line is wider than the same parameter in a standard acquired under the same experimental conditions. Some accepted criteria, that are based on statistic observations, can be useful for establishing the number of component peaks:

- visual inspection of the peak shape to check for asymmetry and the presence of shoulders;
- calculation of the FWHM ratio between the test spectrum and a reference one. If the ratio is < 1.05, one peak is assigned. If it is close to 1.15 and no valley appears or the test spectrum peak is 20% wider than that of the reference spectrum, two peaks are assigned;

- visual inspection of the first and second derivative spectra.

Experimentally it is best to employ a monochromatic X-ray source but this may lead to substantial loss of intensity. The two main techniques used for spectra interpretation are deconvolution and curve fitting. The second approach has been used in this work and will be briefly described hereafter.

A spectrum can be synthesized by summing a series of functions representing individual peaks in order to produce a final function that closely represents the experimental spectrum. The peak function is generally designed to be a function of appropriate peak variables such as position, intensity, width, function type and peak tail characteristics. This curve synthesis provides a useful initial estimate for the refining process of non-linear least squares curve fitting.

A number of function types have been used for this purpose. A core level photoemission peak inherently has a Lorentzian shape whose width is proportional to the inverse of the core hole lifetime. The phonons, i.e. the vibrational energy distribution of the host lattice, produce a broadening of the photoemission peak which has essentially a Gaussian character. The Voigt function is the convolution of these two contributions and is sometimes approximated by the sum or the product of a mixed Gaussian/Lorentzian function. The product approximation has been used in this work.

Tail parameters may be included in the Gaussian/Lorentzian function to take into account the asymmetric line shape. Curve fitting of this function assumes that a particular peak profile is uniquely characterized once its FWHM has been fixed, and cannot be resolved into subcomponents. This is done by acquiring a series of standard materials in the same experimental conditions of the samples under investigation.

Many non-linear least squares algorithm for optimization of the curve synthesis process have been proposed. The one used in this work is based on Marquardt’s method [7]. More details can be found in [5] and in the CASA XPS on-line software user’s manual.

3.1.5 AUGER PARAMETER [8] [9]

In 1971 Charles Wagner introduced the Auger parameter concept that increases the usefulness of XPS for identifying chemical states. He noted that the difference in two kinetic energies (Auger and photoelectron), which is accurately measurable in the presence of static charging, can be very useful for characterizing insulators and semiconductor materials.

The original Auger parameter was defined as the difference in the kinetic energies of prominent and conveniently situated Auger and photoelectron peaks from the same elements recorded in the same spectrum, i.e.

$$\alpha = KE(C'C''C''') - KE(C)$$

where KE(C'C''C''') is the kinetic energy of the Auger transition involving electrons from C', C'' and C''' core levels, and KE(C) is the kinetic energy of the photoelectron from the core level C. However, this definition of the Auger parameter could produce negative values for α but, as KE(photoelectron) = hν - BE(photoelectron), it is possible to define α', the modified Auger parameter:

$$\alpha' = KE(C'C''C''') + BE(C)$$

The so defined modified Auger parameter α' is then independent of hν and always positive and it is the sum of the kinetic energy of the Auger signal and the binding energy of the photoelectron signal.

The Auger parameter concept was based on the following ideas:

- There is a fixed difference between two line energies (Auger and photoelectron) of the same element in the same sample.
- Charge corrections due to individual peak measurements are unnecessary because they simply cancel out during estimation of the Auger parameter.
- Work function corrections are also unnecessary, and vacuum level data can be compared directly with Fermi level data.

The concept of the Auger parameter is of considerable analytical value, because it is independent of charging effects and changes with the chemical environment of the element being examined.

The Auger parameter is still a one-dimensional quantity, like the photoelectron BE or the Auger KE alone. Actually, a more useful general approach than the Auger parameter alone is the representation of photoelectron and Auger data in the form of a scatter plot. In a two-dimensional plot, the position of the sharpest Auger line and the most intense photoelectron line, recorded for a series of compounds of a given element, form the basis for a

new approach to chemical state identification. In this plot, called *Wagner plot* or *chemical state plot*, the Auger KE lies along the y-axis and the photoelectron BE along the negative x-axis.

In the Wagner plot, the position of the different chemical states depends on both initial and final state effects. The initial state effects include the contribution to the chemical shift of both the valence charge and the Madelung potential (which takes into account the charges of all the other atoms in a compound) at the core-ionized atom. The final state effects include information about the extra-atomic polarization energy, which is measured directly by the modified Auger parameter $\alpha' = KE + BE$.

In the final state of the photoemission process an atom is left with a core-hole and this positive charge will polarize the surrounding atoms and the valence electrons. The system is thus in an excited state and will tend to relax; the corresponding relaxation energy, in turn, will lower the BE values. This relaxation energy can be divided into two parts: an atomic contribution, that depends on the atomic number and the core orbital involved in the process, and an extra-atomic contribution which is the relaxation energy associated with the rest of the system (with the flow of electron density from the surrounding toward the core –ionized atom) [10].

In a simplest approximation, assuming that the intra-atomic relaxation energy is independent of the chemical environment, the shifts in the core ionization energy ΔBE, and in the kinetic energy of an Auger transition ΔKE, are given by the following equations [11]:

$$\Delta BE = \Delta V - \Delta R^{ea}$$

$$\Delta KE = - \Delta V + 3\ \Delta R^{ea}$$

ΔV reflects differences in the orbital energy of the electron in the initial un-ionized state, ΔR^{ea} reflects differences in the final-state extra-atomic relaxation energy. The shift in the Auger parameter $\Delta\alpha'$ thus provides a direct measurement of the shifts in the extra-atomic relaxation energy [11], according to

$$\Delta\alpha' = \Delta KE + \Delta BE = 2\ \Delta R^{ea}$$

Summarizing, three different situations can be found in the Wagner state plot:

1) Identical Auger parameter.

The individual data point of different compounds or samples are found on a diagonal line with equation KE = α' – BE with a slope $\Delta KE/\Delta BE = -1$ in the Wagner plot (actually the line shows a positive slope in the graph due to the negative x-axis). These compounds show the same modified Auger parameter α' and identical chemical state.

2) Initial and final state effects have similar values.

The BE for an element in different compounds or samples is similar: $\Delta BE = \Delta V - \Delta R^{ea} = 0$, so $\Delta V = \Delta R^{ea}$ (initial and final state have similar values). Differences in α' are due to differences in the bond nature: the more positive the Auger parameter shifts, the more covalent the bond; the more negative the Auger parameter shifts, the more ionic the bond.

3) Similar initial state effect.

The data point for an element in different compounds or samples lie along a line with slope $\Delta KE/\Delta BE = -3$.

3.1.6 THE FIRST PRINCIPLES METHOD FOR QUANTITATIVE SURFACE ANALYSIS [3]

In order to quantify spectra from XPS, one must convert peak intensities (usually peak areas) to atomic concentrations. The easiest case concerns homogeneous samples. The situation is more complicated for samples with surface films that are either thinner than the information depth of the technique or discontinuous.

As will be shown in the following, experimental peak intensities depend upon several parameters, which are dependent on the photoemitting element, the matrix, the physics of the X-ray photoemission phenomenon, the mechanics and dynamics of the electron travelling through the sample, spectrometer geometry, experimental design, etc Thus, the experimental peak intensities can be considered “raw” data which have to be corrected in order to obtain comparable quantities. The peak intensity correction factors are usually referred to as *sensitivity factors*. There are three main approaches for evaluating the sensitivity factors. They can be found in the literature or experimentally determined in-house. Alternatively, sensitivity factors can be calculated taking into account all the physical parameters involved in XPS peak “generation”. The last approach is known as the first principles method. This method has been used here and will be described in some detail.

The most generic expression used in XPS quantitative analysis is

$$A\ at.\% = \frac{I_A / S_A}{\sum_i I_i / S_i} \cdot 100$$

where A is the element or the chemical species, I_i is the experimental intensity of the chosen XPS peak generated from the species i, S_i is the sensitivity factor for that particular XPS peak generated from the species i.

In the first principles method, the intensity I_i of a particular peak of the generic species i, is given by the following expression

$$I_i = \sigma_i(h\upsilon)\, D(E_i) \int_0^{\pi} d\gamma \int_0^{2\pi} d\Phi\ L_i(\gamma) \int_{-\infty}^{+\infty} dx \int_{-\infty}^{+\infty} dy\ J_0(xy) \sec\delta\, T(xyz\Phi E_i) \int_0^{\infty} dz\ N_i(xyz)\, e^{-z/\lambda_M(E_i)\cos\theta}$$

whose resolution for the atomic density N_i could be used in the above expression for the atomic concentration. It may be rewritten as

$$A\ at.\% = \frac{N_A}{\sum_i N_i} \cdot 100$$

σ is the *photoionization cross-section* which is defined as the "effective area" of the collision between an incident X-ray photon and an atom of the species i in the sample. σ depends upon the photon energy hν, the element of i and the quantic numbers n, l, s and j describing the initial state of the photoemitted electron [12].

D is the *detector efficiency function* which describes the efficiency of the spectrometer detector versus the electronic kinetic energy E_i, i.e. the ratio of the electrons actually counted and the total number of electrons arrived at the detector.

L is the *angular asymmetry function* which takes into account the non-isotropic nature of the electronic photoemission phenomenon. It depends upon the X-ray source and the quantic numbers n, l, s and j describing the initial state of the photoemitted electron [13].

J_0 is the X-ray photon flux versus the x and y coordinates as shown in Figure 3.1.

T is the so called *transmission function* of the spectrometer. It can be defined as the spectrometer lens-analyzer-detector system efficiency, since it represents the ratio of the number of electrons actually counted and the number of electrons entering the detection system of the spectrometer. It depends upon the instrument devices and design.

λ is the inelastic mean free path of the electrons, which depends firstly upon the electron KE and the density of the material M (i.e. the sample).

Figure 3.1 shows both the x,y,z coordinates with respect to sample position in the spectrometer analysis chamber, and the spectrometer angles γ, Φ, δ and θ.

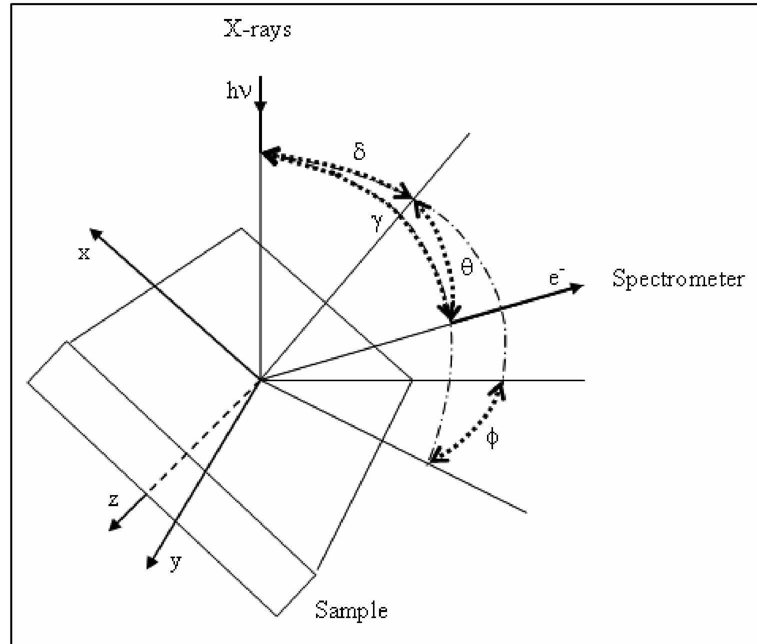

Figure 3.1 : Schematic picture of spectrometer analysis chamber: sample coordinated axis and spectrometer angles.

The above rigorous expression for peak intensity I_i is indeed very complex, but can be simplified with certain assumptions. First of all, under the hypothesis that the sample is homogeneous down to a depth greater than the sampling depth of the XPS technique:

$$\int_0^{\infty} dz\, N_i(xyz)\, e^{-z/\lambda_M(E_i)\cos\theta} = N_i\, \lambda_M(E_i)\cos\theta = N_i\, \Lambda_{Mi}$$

Thus, the above expression for intensity of a photoelectron line I_i can be rewritten as

$$I_i = \sigma_i(h\upsilon)\, D(E_i) \int_0^{\pi} d\gamma \int_0^{2\pi} d\Phi\, L_i(\gamma) \int_{-\infty}^{+\infty} dx \int_{-\infty}^{+\infty} dy\, J_0(xy) \sec\delta\, T(xyz\Phi E_i)\, N_i\, \Lambda_{Mi}$$

where $\Lambda = \lambda \cos\theta$ is the so called *attenuation length* and is defined as the pathway length travelled by the electron with kinetic energy E_i through the material M, which causes the electron itself to loose all its energy. In other words, the attenuation length is the maximum

path length which can be travelled by the electron (with a certain KE) in the sample (i.e. the material M).

However, this last expression for peak intensity I_i can be further simplified. As stated at the beginning of this section, the aim is to convert the raw peak areas to atomic concentrations. As mentioned above, the atomic concentration is calculated by the ratio between corrected intensities. Thus, in the expression for peak intensity I_i, all of the functions and quantities which are either independent of the particular peak being considered or constant with respect to the performed experiment, will be deleted. First of all, if the analyzed surface area of the sample does not vary during spectra acquisition, the X-ray flux J_0 is constant. The efficiency of the detector $D(E_i)$ does not have to be explicitly taken into account since it is determined together with the spectrometer transmission function during experimental determination of the so called *Intensity/Energy Response Function* (IERF) of the spectrometer [14]. Furthermore, if the experiment is performed without changing any of the spectrometer angles (Figure 3.1), the following expression for atomic density can be written:

$$N_i = \frac{I_i}{\sigma_i(h\nu)\,L(\gamma)\,[IERF(E_i)]\,\Lambda_M(E_i)} = \frac{I_i}{S_i}$$

Finally, the sensitivity factor of each of the interesting photoelectron peaks is calculated as the product of the photoemission cross-section σ [12], the asymmetry function $L(\gamma)$ [13], the experimentally determined IERF(KE) [14] and the attenuation length Λ, which depends on the material M and the electron kinetic energy.

3.1.7 ELECTRON INELASTIC MEAN FREE PATH

An electron, moving through a solid, may undergo two different types of scattering phenomena: elastic and inelastic. Scattering is defined as a phenomenon where the direction, frequency and polarization of an electromagnetic wave are modified by some discontinuity of the media through which the wave itself is passing. As far as an electron moving through a solid is concerned, the main affected quantity is linear momentum. The elastic scattering causes the electron to deviate from its initial straight pathway without almost any loss of its kinetic energy. The angular deviation from the electron pathway can be very large but elastic scattering does not have to be taken into account if the emission angles is $\leq 60°$ [15]. On the contrary, inelastic scattering causes the electron to loose some of its initial kinetic energy without almost any deviation from its initial pathway [16].

While elastic scattering is essentially a coulomb interaction between the travelling electron and an atomic nucleus (shielded by its electrons), inelastic scattering results from the interaction between the travelling electron and the atomic electrons of a certain nucleus. While travelling through the solid, the photoelectron may undergo different types of inelastic scattering. A different excitation phenomenon corresponds to each type of inelastic scattering. The energy needed for excitation is given by the travelling and interacting photoelectron which, thus, looses an equal amount of its kinetic energy. The most important excitation processes are:

- *Plasmon excitation*: the excitation of a quantum of energy associated to the waves of the solid conduction band. These waves correspond to the collective oscillation of a large number of conduction electrons.
- *Phonon excitation*: the excitation of a quantum of vibrational energy of the crystalline lattice. In other words, phonon excitation is the temperature increase caused by inelastic scattering.
- Ejection of a core electron from the target atom.
- Ejection of a valence electron from the target atom.
- Excitation of an electron in the valence band.

The inelastic mean free path (IMFP) is defined as the mean distance travelled by the electron between two consecutive inelastic scattering events. The IMFP of the electrons plays an important role in surface physics. It is required for quantitative surface analysis both by AES and XPS and determines the surface sensitivity of these two techniques. Moreover, the IMFP plays a fundamental role in the interpretation of almost any experiment in which an excited electron moves through a solid material. However, despite the importance of the IMFP, experimental values for a given material are generally available only over a limited energy range and the measured values can be affected by large uncertainties due to the inherent experimental difficulties [16]. On the theoretical side the situation does not improve. With the exception of the so called *free-electron materials*, the IMFP cannot be calculated from the first principles. Thus several formulas exist for calculating the IMFP values, which are all semiphenomenological and, because of experimental difficulties, it is difficult to assess how well the models actually perform [16].
The most widely used IMFP predictive formulas are the *Seah and Dench* [17], the TPP-2M [18] and the G-1 [19].

3.1.7.1 SEAH AND DENCH

In 1979, Seah and Dench proposed a universal formula for calculating the IMFP of electrons travelling within solids [17]. Their predictive formula is empiric and was derived by fitting several IMFP values which were experimentally determined in previous works [20] [21]. Seah and Dench divide the solids into three classes: elemental, inorganic and organic materials. Their universal formula for calculating the IMFP is the following:

$$\lambda_i = \left(\frac{A}{E^2}\right) + B \cdot E^{1/2}$$

where λ is the IMFP in nanometers, E is the kinetic energy of the travelling electron, A and B are two empiric parameters whose values vary with the solid class as reported in Table 3.2.

Table 3.2 : Empiric parameters of the Seah and Dench formula for IMFP calculation.

solid class	A	B
elemental material	*143*	*0.054*
organic material	*31*	*0.087*
inorganic material	*641*	*0.096*

The Seah and Dench formula is simple and fast to use but it is empirical and does not take into account the difference between materials belonging to the same class of solids. It has been reported that it can lead to large errors in the quantification of an XPS spectrum [22].

3.1.7.2 TPP-2M

The TPP-2M predictive formula for IMFP calculation of electrons in solids is the results of studies conducted by Tanuma, Powell and Penn [18]. Starting from the Penn algorithm [16] they developed the TPP-2M formula on a theoretically rigorous physical basis. For about 6 years (1987-1993), they continuously revised and improved their formula by comparing the calculated IMFP values with the most accurate empiric data available. The most recent version of the TPP-2M predictive formula is the following:

$$\lambda_i = \frac{E}{\left\{E_p^2 \left[\beta \ln(\gamma E) - \frac{C}{E} + \frac{D}{E^2}\right]\right\}}$$

where λ is the IMFP in Angstroms and E is the kinetic energy of the electron. E_p is the plasmon excitation energy, and β, γ, C and D are parameters. Both E_p and all the parameters have their own mathematical expression:

$$\beta = -0.1 + 0.944\left(E_p^2 - E_g^2\right)^{-1/2} + 0.069\,\rho^{0.1}$$

$$\gamma = 0.191\,\rho^{-1/2}$$

$$C = 1.97 - 0.91\,U$$

$$D = 53.4 - 20.8\,U$$

$$E_p = 28.8\left(\frac{N_V\,\rho}{M}\right)^{1/2}$$

E_g is the *energy gap* between the valence band and the conduction band of the solid. ρ is the solid density in g cm^{-3}. N_V is the number of valence electrond of the element, or the molecule, or corresponding to the minimum formula, depending on solid type. M is the atomic, or the molecular, or the formula weight, depending on solid type. Finally, U is another parameter with its own expression:

$$U = \frac{N_V\,\rho}{M}$$

The TPP-2M predictive formula allows to calculate the IMFP values taking into account the particular solid through which the photoelectrons pass. It is quite tedious to use since several quantities have to be evaluated. But the main problem with applying the TPP-2M is, in our experience, the availability of energy gap values. Energy gaps can be found in the literature, determined from quantum-mechanics calculations or experimentally determined. However, it has to be stressed that both plasmon excitation energy and energy gap can be determined only for stoichiometric materials, and not for the non-standard materials which are often found in

and on solid surfaces. This places a severe limitation on the applicability of the TPP-2M to technological surfaces [19].

3.1.7.3 G-1

In 1996, Gries published his new universal IMFP predictive equation called the G-1 formula. It has been formulated for use in analytical electron XPS and AES spectroscopy. The G-1 essentially states that the IMFP of an electron traversing matter is inversely proportional to the matter density. The formula is based on an atomistic model in which matter is described as consisting of clusters of interacting regions (identified with the orbitals of an atom). The energy dependence of the IMFP and the best values for two fitting parameters were obtained from a large set of IMFP values derived from the TPP-2M for stoichiometric solids. However, the main difference between the G-1 and the TPP-2M predictive formulas is that the first can be applied to any arrangement of atoms both stoichiometric and non-stoichiometric. Local atomic composition, atomic density, photoelectron energy and some knowledge of the chemical state of the atoms suffice for the IMFP to be calculated using the G-1 equation. This is the main difference between the G-1 and the TPP-2M predictive formulas. Another important aspect is that, on average, the TPP-2M predicted IMFP values are no closer to the experimental optical IMFP than are the G-1 predicted values. In conclusion, because of its simplicity, the G-1 equation is much more widely applicable than the TPP-2M, for equal reliability. For these reasons, in this work the G-1 predictive equation was used to calculate the electron IMFP values.

The formula, which yields units of nm for the IMFP, is

$$\lambda_i = k_1 \left(\frac{V_a}{Z^*} \right) \frac{E}{\log_{10} \left(E - k_2 \right)}$$

where V_a is the atomic volume in $cm^3\ mol^{-1}$, E is the kinetic energy of the photoelectron in eV, k_1 and k_2 are parameters (the former magnitude-adaptive and the energy-adaptive respectively), and Z* is a real number which can be regarded as the number of the “actual” interaction-prone electrons per atom.

V_a can be calculated with the following expression:

$$V_a = \frac{p\,M_A + q\,M_B + \cdots + r\,M_C}{\rho\,(p + q + \cdots + r)}$$

where ρ is the density of the compound in g cm^{-3}, M_A M_B … M_C are the atomic masses of the elements present, p q … r are the "stoichiometric" coefficients in the minimum formula of the compound.

Z* can be calculated with the following expression:

$$Z^* = \frac{p\,\sqrt{Z_A} + q\,\sqrt{Z_B} + \cdots + r\,\sqrt{Z_C}}{p + q + \cdots + r}$$

where Z_A Z_B … Z_C are the atomic numbers of the elements present.

Finally, the numerical fitting parameters k_1 and k_2 have been determined by Gries over the electron kinetic energy range 200-2000 eV. Within this energy range the materials were found to be classifiable into six categories, according to a common energy dependence of their either experimentally determined or TPP-2M calculated IMFP values. In other words, each of the six categories has its own value of the energy-adaptive parameter k_2. On the other hand, the magnitude-adapter parameter k_1 was found to vary from one element to another and from one compound to another. Rather than giving the value of k_1 for every element and compound separately, Gries decided to give an average value of k_1 for each of the six categories of materials. Table 3.3 reports the value of k_1 and k_2 for all six categories.

Table 3.3 : Numerical fitting parameters k_1 and k_2 of the G-1 predictive formula.

category	**k_1**	**k_2**
main group elements	*0.0014*	*1.10*
transition elements of the 4th period	*0.0020*	*1.30*
transition elements of the 5th period	*0.0019*	*1.35*
transition elements of the 6th period	*0.0019*	*1.45*
inorganic compounds	*0.0019*	*1.30*
organic compounds	*0.0018*	*1.00*

3.1.8 TOUGAARD'S METHOD FOR NON-DESTRUCTIVE IN-DEPTH PROFILING

3.1.8.1 THE PROBLEM [23]

Quantification by XPS relies on several factors such as knowledge of photoionization cross-section, electron IMFP, influence of electron elastic scattering and energy dependence of the spectrometer transmission function [24] [25]. The most serious problem that contributes to the greatest extent errors is, however, a knowledge of the in-depth distribution of atoms [26] [27]. For a meaningful quantification, assumptions on the depth profile have to be made since the measured peak intensity depends critically thereon. Now, in practice the depth profile is never known and usually, the solid composition is for convenience, but quite arbitrarily, assumed to be homogeneous down to a depth of several nanometers. This assumption may result in enormous errors in quantification [26] [27]. In fact, it is precisely because samples are inhomogeneous on the nanometer depth scale that they are analyzed using XPS rather that with other well established but less surface sensitive techniques. To illustrate the fundamental problem with the assumption of homogeneous composition with depth, Tougaard reported [23] a clear example of model spectra calculated for different depth distributions of Cu in Au (Figure 3.2).

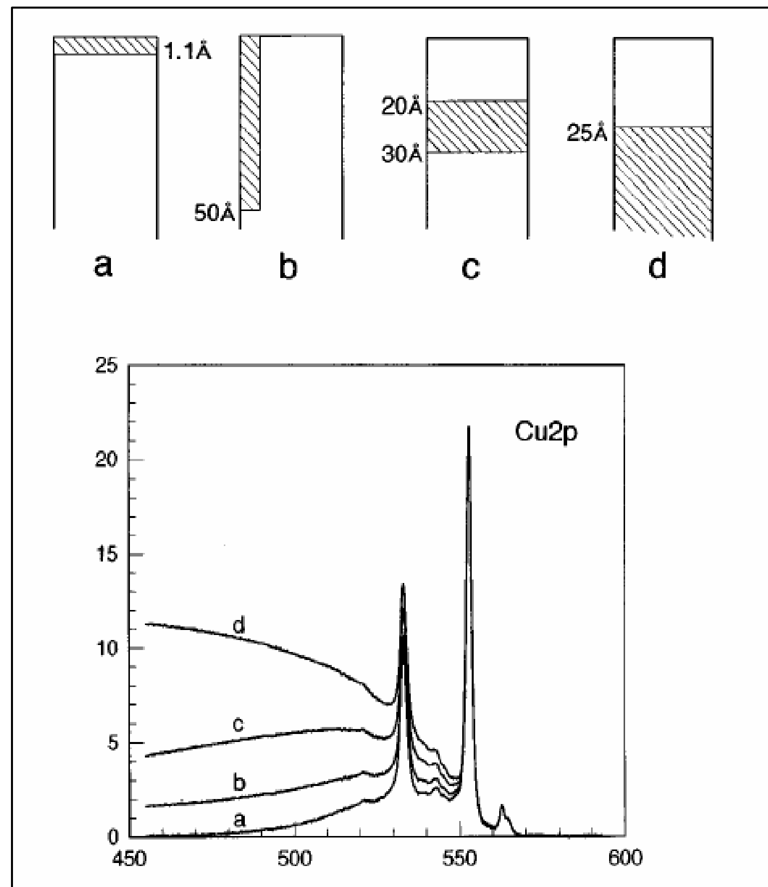

Figure 3.2 [23]*: Four widely different surface structure of copper in gold that give identical peak intensities.*

Figure 3.2 shows spectra of the Cu2p peaks corresponding to four different surface morphologies of copper in a gold matrix. The XPS peak intensity from all four solids is identical although the surface compositions differ substantially. Analysis of these spectra with e.g. the first principles method i.e. under the assumption that surface concentration is proportional to peak intensity would give an identical result for all four samples, while the true

concentration at the surface could be anywhere from 0% (as in d) to 100% (as in a) and the true total amount of copper within the surface region could be anywhere between the equivalent of 1.1 Å (as in a) or 10 Å (as in c) or even higher (as in d). Thus, quantification based on peak intensities alone is clearly affected by large uncertainty which may be of several hundred percent [23].

From figure 3.2 it is, however, clear that the peak shape in a broader kinetic energy range below the peak maximum (~ 100 eV) depends critically on the in-depth distribution of the element. Much more accurate quantification can therefore be achieved if the dependence of peak shape on surface in-depth profile can be taken into account in the analysis.

3.1.8.2 TOUGAARD'S APPROACH

When an electron travels in a solid, it will experience inelastic scattering events and as a result, the original electron energy distribution is changed. On the other hand, when an electron travels in a solid, it will experience elastic scattering events too. Angular deflection associated to elastic scattering will cause deviations from the original straight path motion of the electron and thus increase the total path length travelled by the electron itself. Therefore, elastic electron scattering can also be of importance for "distorting" an electron energy spectrum [28].

However, angular deflection in a typical inelastic scattering event is small. On the other hand, in a typical elastic scattering event energy loss is small. It is therefore a reasonable approximation to assume that elastic and inelastic scattering can be treated as separate effects [29].

Let $F(E_0,\Omega_0,x)\, dE_0\, d^2\Omega_0\, dx$ be the average number of electrons excited at depth x dx, over the energy range E_0 dE_0, into the solid angle Ω_0 $d^2\Omega_0$. Then, the flux of electrons $J(E,\Omega)\, dE\, d^2\Omega$ emitted from the solid surface with energy E dE into the solid angle Ω $d^2\Omega$ is given by [30]

$$J(E,\Omega)=\int dE_0 \int d^2\Omega_0 \int dx\; F(E_0,\Omega_0,x)\int dR\; Q(E_0,\Omega_0,x\,;R,\Omega)\,G(E_0,R\,;E)$$

where $Q(E_0,\Omega_0,x\ ;\ R,\Omega)\, dR\, d^2\Omega$ is the so called *path length distribution* function, i.e. the probability that the electron will arrive at the surface in direction Ω $d^2\Omega$ after having travelled the path length R dR.

$G(E_0,R\ ;\ E)\, dE$ is the so called *energy distribution* function, i.e. the probability that the electron has energy E dE after having travelled the path length R dR.

For an isotropic photoemission $F(E_0,x)$, we have [30]

$$J(E,\Omega)=\int dE_0 \int dx\ F(E_0,x)\int dR\ Q(E_0,\Omega_0,x\,;R,\Omega)\,G(E_0,R\,;E)$$

3.1.8.3 PATH LENGTH DISTRIBUTION FUNCTION Q

Based on the Boltzmann transport equation, it has been shown [29] that the characteristic length determinant for the shape of the path length distribution function of emitted electrons is the *transport mean free path* λ_{tr} for elastic electron scattering:

$$\lambda_{tr}=\int d\sigma(\theta)\,(1-\cos\theta)$$

where $d\sigma(\theta)$ is the differential cross-section for elastic scattering by the emission angle θ.
Then, on the basis of several works about the importance of elastic scattering in surface analysis, Tougaard reported that for a homogeneous solid [30]

$$\int_0^{\infty} dx\ Q(E_0,x\,;R,\eta)\approx A(\eta)\,e^{-R/L_x}$$

where $L_x \approx 5\lambda_{tr}$ and $A(\eta)$ is a function of the directional $\cos\theta$.
Thus, for homogeneously distributed isotropic electron emitters

$$J(E,\Omega)=A(\eta)\int dE_0\ F(E_0)\int dR\ e^{-R/L_x}\ G(E_0,R\,;E)$$

Actually, the range of R values which is decisive for the energy spectrum is of the order of only a few times the IMFP λ_i [30]. Since in general $\lambda_{tr} >> \lambda_i$, the effect of angular electron deflection on $J(E,\Omega)$ is minor [30]. This implies, in turn, that an accurate description of inelastic scattering (the function G) is far more important for determining energy distribution of the emitted electrons than the effects of angular deflection (the function Q) [30].
If angular deflection is neglected assuming that the electron moves along straight lines, and R is substituted with $x/\cos\theta$

$$J(E,\Omega)=\int dE_0 \int dx\ F(E_0,x)\,G\left(E_0,{x}/{\cos\theta}\,;E\right)$$

If it is further assumed that the concentration of the electron emitters f(x) may vary with depth x, but that the energy distribution of the emitted electrons $F(E_0)$ is independent of depth, i.e.

$$F(E_0, x) = f(x)\, F(E_0)$$

then

$$J(E, \Omega) = \int dE_0\; F(E_0) \int dx\; f(x)\, G\left(E_0, \frac{x}{\cos\theta}; E\right)$$

3.1.8.4 ENERGY DISTRIBUTION FUNCTION G

Let K(E,T) be the differential inelastic-scattering cross-section, i.e. the probability that an electron of energy E shall lose an amount of energy T per unit energy loss and per unit path length travelled in the solid [30]. Since in an inelastic scattering event the energy loss T is small with respect to the primary photoelectron energy, K(E,T) will be ≈ K(T) independent of E. Then, the energy distribution function $G(E_0,R\ ;\ E)$ is given by the Landau formula [31] [30]:

$$G(E_0, R\,;\,E) = \frac{1}{2\pi} \int_{-\infty}^{+\infty} ds\; e^{is(E_0 - E) - R\Sigma(s)}$$

with

$$\Sigma(s) = \int_0^{\infty} dT\; K(T)\left(1 - e^{-isT}\right)$$

Thus, it is mandatory to have an expression for K(T).

3.1.8.5 INELASTIC SCATTERING CROSS-SECTION

The electrons in the solid respond to the presence of the moving electron with a charge redistribution. This in turn gives rise to a local electric field induced in a small volume around the moving electron. In a dielectric response model of the energy-loss process, it is the interaction of the moving electron with this field that is responsible for inelastic scattering [32]. The induced electric field may be calculated from the dielectric response function of the solid. However, this approach uses a complex algorithm and also involves the use of optical diffraction data for solids [32] and may be very tedious and time-consuming.

On the contrary, Sven Tougaard proposed [32] a *universal inelastic-scattering cross-section*. In order to determine this cross-section of general applicability, Tougaard started from the definition of the IMFP:

$$\lambda_i = \frac{1}{\int dE\; dT\; K(E,T)}$$

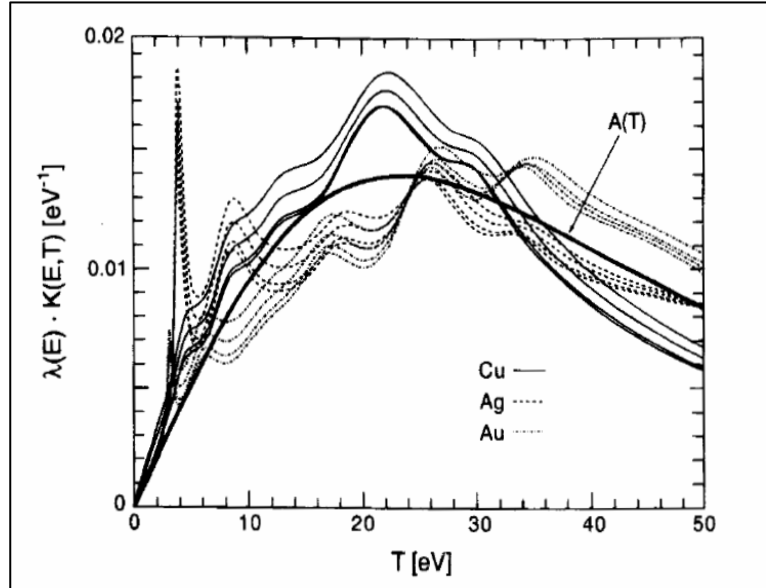

Figure 3.3 [32]*: λ_i K(E,T) curves (theoretically calculated from the dielectric response function of the solid) for electrons of energy E in Cu, Ag and Au. For each metal, four primary energy values are considered (E = 300, 500, 1000 and 1500 eV). The thick solid line is the best two-parameter fit (see the text).*

Since an inelastic scattering event leads to an electron energy loss T that is small compared to the primary photoelectron energy, K(E,T) ≈ K(T) independent of E. Thus

$$\lambda_i \approx \frac{1}{\int dT\; K(T)}$$

This relationship between the inelastic mean free path λ_i and the inelastic-scattering cross-section K(E,T), implies that the product λ_i K(E,T) is less influenced by energy variations than K(E,T) [32]. This idea was further supported by the observation that the shape of K(E,T) versus T (Figure 3.3), is almost identical at different energy values and is characteristic of solids [32]. However, λ_i K(E,T) was found to have some general properties regardless of the solid examined, i.e.

- λ_i K(E,T) → 0 when T → 0
- λ_i K(E,T) increases with increasing T and shows a broad maximum at T ≈ 20-30 eV
- λ_i K(E,T) decreases at higher T values

Tougaard reported [32] these λ_i K(E,T) properties for all the noble and many transition metals. On this basis, he proposed his *universal inelastic-scattering cross-section*:

$$\lambda(E)\,K(E,T) \cong A(T) = \frac{BT}{\left(C + T^2\right)^2}$$

where B = 2900 eV^2 and C = 1643 eV^2.

Tougaard concluded [32] that the detailed structure of λ_i K(E,T) is not reproduced by the universal function A(T) (Figure 3.3). However, to judge the validity of the proposed universal inelastic-scattering cross-section, one must consider the specific physical problem to which this approximation has to be applied. For electron path lengths exceeding a few times the IMFP, as in XPS, only the overall behaviour of the inelastic cross-section is of importance. This is so because these electrons will typically have undergone several inelastic scattering events, thus all finer details in the cross-section will be smeared out. Furthermore, the width of the original emission spectrum (which would be recorded if any one scattering event occurred) is larger than the width of the finer features in λ_i K(E,T) [32].

In this work, the fundamental Tougaard's equation

$$J(E,\Omega)=\int dE_0\ F(E_0)\int dx\ f(x)\,G\left(E_0, x/\cos\theta\,; E\right)$$

was numerically resolved and iteratively applied with QUASES-software v.4.4 (Quantification Analysis of Surfaces by Electron Spectroscopy – Sven Tougaard – Odense, DK) to analyze the experimental spectra. Numerical resolutions of the equation and the application of the QUASES iterative procedure allows to determine both the depth profile and composition of the sample under investigation.

3.1.9 MAXIMUM ENTROPY METHOD FOR NON-DESTRUCTIVE IN-DEPTH PROFILING FROM ANGULAR-RESOLVED XPS DATA

3.1.9.1 THE PROBLEM

Tougaard's method is quite simple to apply and allows to quantitatively determine in-depth distribution of the atoms within the outermost surface region of the sample under investigation. However it requires the spectra acquisition of highly-pure reference compounds in order to simulate the spectrum of the sample under investigation. This implies the assumption that the elements are present in the sample in exactly the same chemical states as those in the reference compounds. Only three reference spectra can be use at the most [33]. A few model structures can be used [33] and a maximum of six structural parameters can be determined [34].

Angle-resolved X-ray photoelectron spectroscopy (ARXPS) is in principle a suitable method for non-destructive evaluation of the composition depth profile of material surface with thickness in the order of a few nanometers [15] [35]. However, the reconstruction of a depth profile based on the assumption of model structures might be misleading because

experimental ARXPS data contain noise and, thus, a large number of very different model structures may exist that match the experimental data [36]. Consequently, simply minimizing the weighted sum-of-square differences between the calculated (on the basis of a model structure) and measured (ARXPS) data is not always adequate for determining the correct sample depth profile, especially if the sample contains a large number of components.

A depth profile that satisfies experimental data has to be found but it must contain the minimum amount of structural parameters necessary to do so (since the details of the noise must not be fitted).

3.1.9.2 THE MEM APPROACH

The Maximum Entropy Method (MEM), which became popular after its successful use for restoring astronomical images [37] [38], has proven to be a powerful tool for reconstructing composition versus depth profiles from ARXPS measurements [36] [39] [40] [41] [42] [43]. The aim of the MEM, as mentioned above, is to find a depth profile that satisfies the experimental ARXPS data but contains the minimum "amount of structure" necessary to do so. In the following two examples are given to clarify this concept and to illustrate the idea upon which the MEM is based.

Firstly, let us consider the depth profile of a homogeneous sample, comprising number n components. Each of the components has a certain concentration which is equal at all depths from 0 (the surface) to $+\infty$. Thus, the depth profile is determined by a number of structural parameters equal to $n-1$, i.e. the concentration of $n-1$ components (the "last" component concentration is determined by that of the other n-1 components since the sum of all the n components is necessarily equal to 100%). This homogenous depth profile can be described using a certain number of variables which correspond to the concentration of all the n components at each of the depth values. How many different combinations of variable values exist that equally describe this homogenous sample? Quite intuitively, there will be a very large number of combinations corresponding to the entropy of the system.

Let us now consider another example starting from the homogenous sample described above. Let one of the n components be located alone at the surface, in the depth range from 0 to 1 nm. The other $n-1$ components constitute a homogeneous bulk in the depth range from 1 nm to $+\infty$. This new depth profile is defined by a larger number of structural parameters: the depth value of the interface between the overlayer and the bulk, the concentration of n-1 components within the overlayer, and the concentration of n-1 components within the bulk. The same number of variables used to describe the previously considered homogeneous

sample, now has to describe this new depth profile. How many different combinations of values for the variables exist to equally describe this system? It is clear that the entropy is now lower than in the case of the homogenous sample described above.

Thus, it can be stated that the higher the number of structural parameters needed to define the system, the lower the corresponding entropy associated to the variables used to describe it. In other words, the entropy can be used to evaluate the amount of information carried by the random variables which are used to describe the depth profile of the sample.

The reconstruction of a depth profile from ARXPS data is an ill-posed mathematical problem [15]. Thus, in an attempt to solve this problem, the entropy can be used as a regularizing function (which has to be maximized) to constrain the solution in order to obtain the simplest possible depth profile that matches the experimental data.

3.1.9.3 MEM THEORY [43]

As discussed in this chapter, because photoelectrons interact strongly with the atoms and electrons in the sample, they usually travel only a small distance (few nanometers) before undergoing inelastic scattering. A signal I(z) generated at a depth z in the sample will contribute to the overall intensity of the photoelectronic peak according to the Beer-Lambert law [36]:

$$I = I(z)\, e^{-\frac{z}{\lambda \cos\theta}}$$

where λ is the characteristic IMFP of the photoelectrons and θ is the emission angle.

Deviation from the Beer-Lambert law occurs at large emission angles owing to the effects of elastic scattering [44] [45].

Signal intensities depend on sample composition and its variation with depth. Attenuation of the intensity of the outgoing photoelectron weights the signals towards the outermost surface layers. Variation of the emission angle, therefore, results in a change of sampling depth of the XPS technique [15] [35]. Spectra acquired at near-normal emission angles will be representative of the average composition of the inner layers, while spectra acquired at near-grazing emission angles will characterize the outermost layers of the surface region of the sample [15] [35]. The objective of the MEM is to use this measured angle dependence to reconstruct the composition depth profile of the sample. A quantitative relationship that is of general validity in XPS practice is the following:

$$X_A = \frac{I_A / I_A^{\infty}}{\sum_{j=1}^{N} I_j / I_j^{\infty}}$$

where X_A is the atomic percent concentration of the element A in a sample containing N components, I_A is the measured intensity of the photoelectronic peak of A examined and I^{∞}_A is the intensity of the same photoelectronic peak that is measured from a pure material of A under the same experimental conditions.

To evaluate how compositional variations within sample depth affect the measured XPS intensities, let us consider a solid divided into an arbitrary number of *p+1* layers of equal thickness *t*, as shown in Figure 3.4.

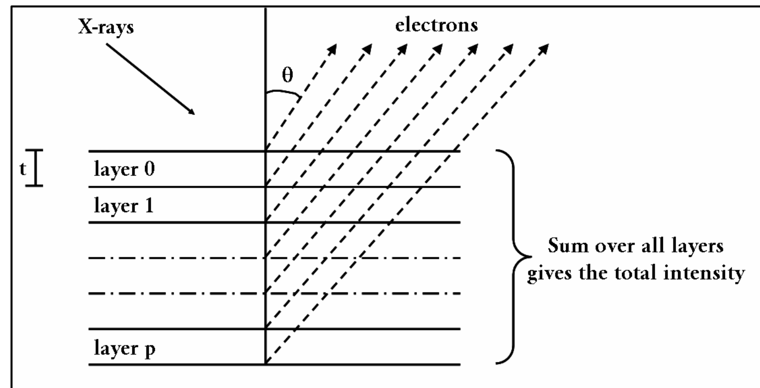

Figure 3.4 : Graphic illustration of the model used within the MEM.

Each layer contains any number of the N elements A, B, C, etc. with concentration $n_{A,i}$, $n_{B,i}$, $n_{C,i}$, etc., such that $n_{j,i}$ represents the atomic fraction of the element j in the ith layer. It is assumed that the layers are thin enough for its composition to be considered homogeneous.

Then, the so called *layer transmission function* $T_A(\theta)$ for the element A at a certain photoemission angle θ, is defined by:

$$T_A(\theta) = e^{-\frac{t}{\lambda_A \cos\theta}}$$

where λ_A is the IMFP for the photoelectrons generating the peak of element A. The intensities generated by photoelectrons of the element A from each of the layers, are then summed over all layers (Figure 3.4) to obtain the total intensity of the measured peak $I_A(\theta)$ at a given emission angle θ:

$$I_A(\theta) = k_A \left[n_{A,0} + n_{A,1}\, e^{-\frac{t}{\lambda_A \cos\theta}} + n_{A,2}\, e^{-\frac{2t}{\lambda_A \cos\theta}} + n_{A,3}\, e^{-\frac{3t}{\lambda_A \cos\theta}} + \cdots \right]$$

i.e.:

$$I_A(\theta) = k_A \left[n_{A,0} + n_{A,1} \left(e^{-\frac{t}{\lambda_A \cos\theta}} \right) + n_{A,2} \left(e^{-\frac{t}{\lambda_A \cos\theta}} \right)^2 + n_{A,3} \left(e^{-\frac{t}{\lambda_A \cos\theta}} \right)^3 + \cdots \right]$$

Substituting the expression of the layer transmission function, one obtains

$$I_A(\theta) = k_A \left\{ n_{A,0} + n_{A,1} \left[T_A(\theta)\right] + n_{A,2} \left[T_A(\theta)\right]^2 + n_{A,3} \left[T_A(\theta)\right]^3 + \cdots \right\}$$

i.e.:

$$I_A(\theta) = k_A \sum_{i=0}^{p} n_{A,i} \left[T_A(\theta)\right]^i$$

The element-specified terms, such as photoelectron cross-section, asymmetry function, etc., are included in the constant of proportionality k_A.

If all the n_A are equal to 1, the analogous expression for the pure material of element A is obtained:

$$I_A(\theta) = k_A \sum_{i=0}^{p} \left[T_A(\theta)\right]^i$$

Finally, the apparent concentration $X_A(\theta)$ of element A at the emission angle θ can be written as

$$X_A(\theta) = \frac{\sum_{i=0}^{p} n_{A,i} \left[T_A(\theta)\right]^i \Big/ \sum_{i=0}^{p} \left[T_A(\theta)\right]^i}{\sum_{j=1}^{N} \left\{ \sum_{i=0}^{p} n_{j,i} \left[T_j(\theta)\right]^i \Big/ \sum_{i=0}^{p} \left[T_j(\theta)\right]^i \right\}}$$

where the constants k_j for each of the elements are cancelled out in each term. In this treatment it is implicitly assumed that the photoelectron IMFP are independent of composition [46] and thus that the sample density is uniform with respect to depth [47].

These are critical assumptions and in this work an iterative procedure was used to determine the best set of IMFP values for each of the studied samples. This procedure was applied so as to take into account the fact that photoelectron IMFPs actually vary with varying composition of the layer being traversed, and hence with varying material density. This procedure is described in detail in Chapter 4.

The last expression is used to calculate the expected apparent concentration of the elements present in a sample for a given depth profile.

If entropy is defined as [48]:

$$S = \sum_{j=1}^{N} \sum_{i=0}^{p} \left[n_{j,i} - m_{j,i} - n_{j,i} \log\left(\frac{n_{j,i}}{m_{j,i}} \right) \right]$$

where $n_{j,i}$ is the atomic fraction of the element j in the ith layer and $m_{j,i}$ is its initial estimate and the deviation of the calculated intensities versus emission angle from the experimental ARXPS data is defined by the chi-squared statistic misfit, as

$$C = \chi^2 = \sum_{j=1}^{N} \sum_{k=1}^{N^{th}} \frac{\left(X_{j,k}^{calc.} - X_{j,k}^{obs.} \right)^2}{\sigma_{j,k}^2}$$

where $X_{j,k}^{calc.}$ and $X_{j,k}^{obs.}$ are, respectively, the calculated and observed apparent concentration of the jth element at the kth emission angle and $\sigma_{j,k}^2$ is the variance of the kth measurements for the jth elements.

Finally, a depth profile that satisfies the experimental ARXPS data can be calculated by minimizing C. However, this profile must contain the minimum "amount of structure" necessary to do so, correspondingly a maximum of S has to be found.

These two necessary conditions can be satisfied simultaneously by maximizing the so called *probability function*:

$$Q = \alpha \cdot S - \frac{C}{2}$$

where α is a Lagrange multiplier (also called the *regularizing parameter*). A large value for α will result in an over-smoothed solution that, thus, will not agree with the data, while a small value for α will lead to an over-fitting of the data, the depth profile reconstruction attempting to fit and reproduce the noise in the data.

3.2 THEORY OF CORROSION

3.2.1 GENERAL BACKGROUND

Because of their good mechanical properties and reasonably low cost, metallic materials are used for a very wide variety of technological products and engineering constructions. Metals and their alloys, especially copper, iron, chromium, nickel, bronze, stainless steel and NiP alloys are also used because of their aesthetic appeal.

When exposed to the environment, corrosion may occur on the surface of the metals and their alloys, leading to tarnishing (detrimental to appearance), rust formation and loss in cross section (affecting the mechanical properties of the structure).

Corrosion can generally be defined as the reaction of a metal or alloy with its environment with the formation of corrosion products [49]. The (detrimental) effects of corrosion, its rate and extent depend upon material composition and structure and upon the environmental conditions to which it will be exposed during its service life.

3.2.2 THERMODYNAMICS OF CORROSION [50] [51]

The corrosion process of a metal can be represented by the following reaction:

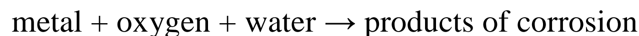

metal + oxygen + water → products of corrosion

This generic reaction is an electrochemical process and can be regarded as the sum of a cathodic and an anodic reaction.

The anodic reaction is the metal dissolution (oxidation reaction):

$$M \leftrightarrows M^{n+} + n\,e^-$$

whose equilibrium potential is, according to Nernst's law:

$$E_{eq.,a} = E^0 + \frac{RT}{nF} \ln a_{M^{n+}}$$

where E^0 is the standard reduction potential in volts, F is the Faraday constant (96486 C/mol), R is the universal gas constant (8.314 J K^{-1} mol), T is the absolute temperature in Kelvin, n is the number of exchanged electrons.

The most common cathodic process (reduction reaction) in acid environments is hydrogen reduction:

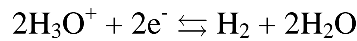

$$2H_3O^+ + 2e^- \leftrightarrows H_2 + 2H_2O$$

$$E_{eq.,c} = E^0 + \frac{RT}{2F} \ln \frac{a_{H^+}^2}{P_{H_2}}$$

while in neutral or alkaline environments, it is the oxygen reduction:

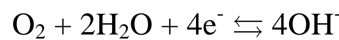

$$O_2 + 2H_2O + 4e^- \leftrightarrows 4OH^-$$

$$E_{eq.,c} = E^0 + \frac{RT}{4F} \ln \frac{P_{O_2}}{a_{OH^-}^4}$$

where P_{H2} and P_{O2} are the partial pressure of hydrogen and oxygen respectively.

From a thermodynamic point of view, corrosion occurs only if the free energy of the system decreases, i.e. $\Delta G<0$. Since $\Delta G = -nF\,\Delta E$ and $\Delta E = E_{eq.,c} - E_{eq.,a}$, it follows that a metal can corrode if:

$$E_{eq.,c} > E_{eq.,a}$$

On the other hand, if the potential of the cathodic reaction is lower than that of the anodic reaction, corrosion is thermodynamically prevented and the metal is thus immune.

3.2.3 POURBAIX DIAGRAMS

The Pourbaix diagrams [52] are a series of lines representing the potential and pH equilibrium values among the compounds formed by reaction between an element and water. The lines bound the stability fields of the element, its ions and its oxygenated compounds.

Figure 3.5 shows the Pourbaix diagrams for both nickel and phosphorus.

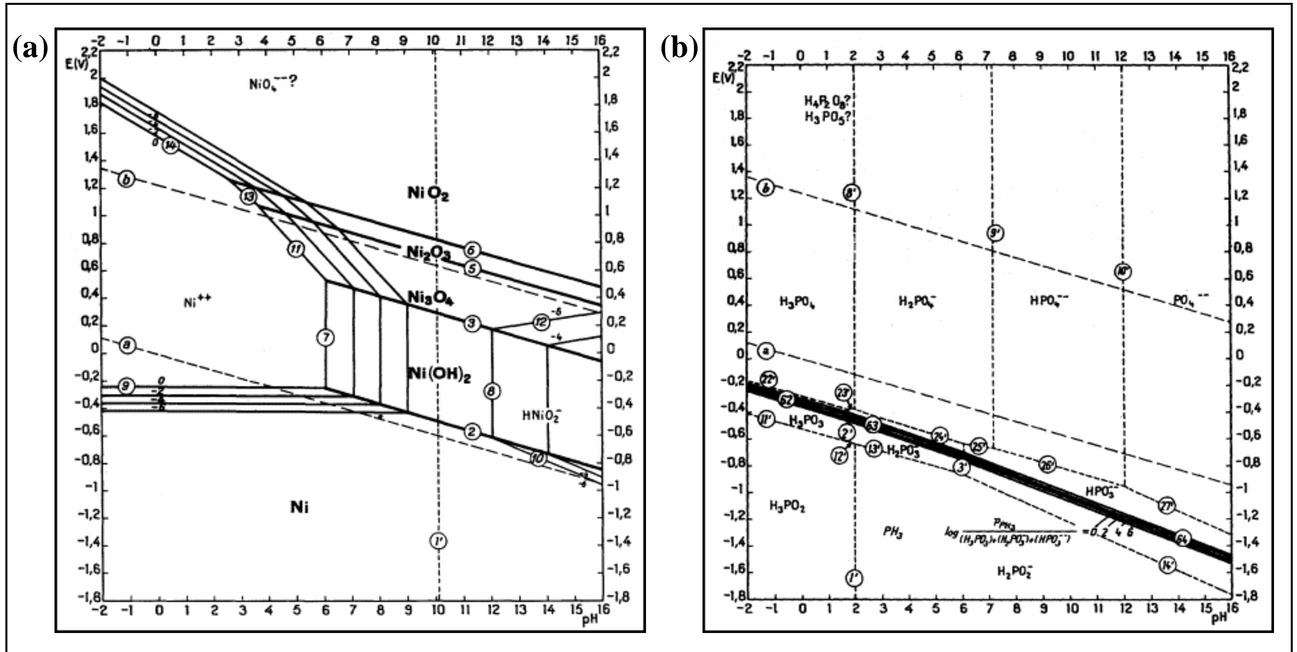

*Figure 3.5 [52]: Pourbaix diagrams for **(a)** nickel and **(b)** phosphorus.*

The dashed lines labelled “a” and “b” refer to the cathodic reaction of H^+ and O_2 respectively. If the element line lies below line “a”, the element can be oxidized for both hydrogen and oxygen reduction. If it lies between line “a” and line “b”, the only possible cathodic process will be oxygen reduction. If it lies above line “b” the element will not be oxidized even in the presence of oxygen.

3.2.4 CORROSION KINETICS

Corrosion processes are thermodynamically possible but the rate at which they occur depends on the reaction kinetics.

All the electrons produced by the anodic process have to be consumed simultaneously by a cathodic reaction. The current flow causes a shift in the electrode potential from its equilibrium value; this shift is called *electrode polarization* and is measured experimentally as overpotential η.

According to Tafel’s law the overpotential η is defined as:

$$\eta_c = E_c - E_{eq.,c} = -\beta_c \ln \frac{i_c}{i_{0,c}} \qquad (cathode)$$

$$\eta_a = E_a - E_{eq.,a} = \beta_a \ln \frac{i_a}{i_{0,a}} \qquad (anode)$$

where E is the actual electrode potential, $E_{eq.}$ is the electrode equilibrium potential, β is the Tafel constant, I is the current density, i_0 is the exchange current density i.e. the current flowing when $E = E_{eq.}$. Cathodic overpotential is always negative and, according to European sign convention, cathodic current is negative. Note that in a corrosion process the current i_a and i_c must be identical.

3.2.5 POLARIZATION CURVES

The corrosion rate of a metal or an alloy in a given environment can be monitored by means of the potential-current density diagram, i.e. a polarization curve.

A typical anodic polarization curve for a metal undergoing an active-passive transition is shown in Figure 3.6a.

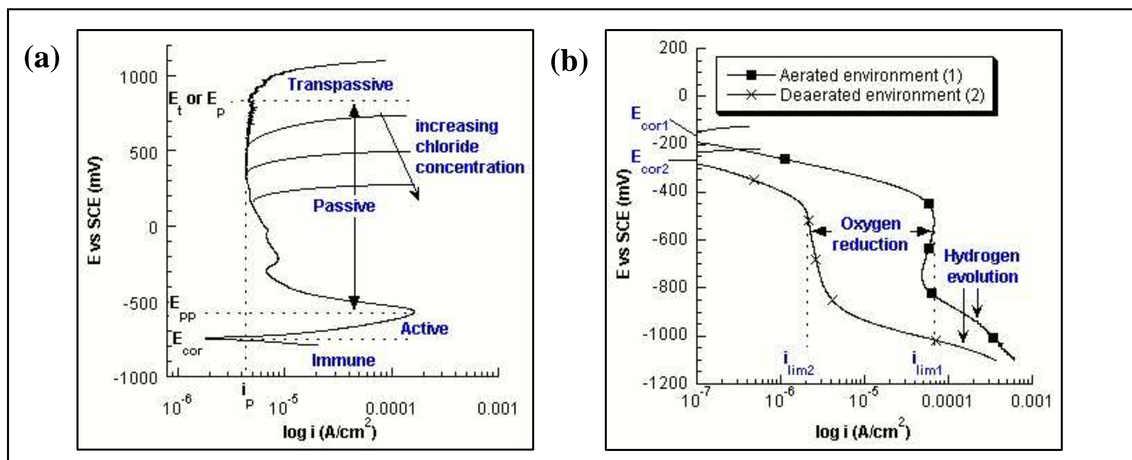

Figure 3.6 [56]*: Typical* ***(a)*** *anodic and* ***(b)*** *cathodic polarization curve.*

Between the corrosion potential E_{cor} and E_{pp} , the *primary passivation potential*, the metal is actively corroding, the current density increases exponentially with increasing potential. At E_{pp} the current density reaches a peak (i.e. the critical current density for passivation) and starts to decrease. This behaviour is known as active-passive transition indicating a progressive film formation on the metal surface. The current density reaches a very low value i_p , the *passive current density*, and remains at a low but not necessarily constant value over a range of potentials, called the *passive range*. Due to film formation kinetics, i_p depends upon scan rate [53], metal or alloy composition, solution pH and composition, and temperature. The very low passive current can be seen as the rate of chemical dissolution of the passive film (or, in a more dynamic view of the passive film, as the result of a huge number of single dissolution/reformation events).

At more positive potentials the current density starts to increase again. In a chloride free solution, this current increase is due to the onset of gaseous oxygen evolution by water electrolysis [54] and the correspondent potential is known as E_t , the *transpassive potential*. The anodic oxygen evolution produces acidity. If these conditions persist the passive film will be destroyed and corrosion will initiate.

If a metal or an alloy is vulnerable to chloride pitting corrosion (see below), a sudden current increase can occur below the transpassive potential (Figure 3.6a). This current increase is accompanied by the formation of corrosion pits on the sample surface, and the potential where it occurs is known as the *pitting potential* E_p. The pitting potential depends for a given metal or alloy on the chloride content of the solution.

Figure 3.6b shows, on the other hand, a typical cathodic polarization curve. The first current increase is due to the oxygen reduction reaction. After an initial exponential increase of current density with decreasing potential, a limiting current density (current arrest) is reached. The limiting current density observed is due to the slow transport of oxygen in solution and depends on oxygen availability on the specimen’s surface. At more anodic potentials current density increases exponentially again as the hydrogen evolution starts.

3.2.6 PITTING CORROSION

The passive films formed can be attacked (but not all metals and alloys are vulnerable to pitting corrosion) and destroyed by the presence of chloride ions and pitting corrosion occurs. The characteristic potential, the *pitting potential* E_p , is influenced both by alloy composition and by the environment (mainly the chloride content). For a given alloy the pitting potential shifts towards more negative potentials as chloride concentration increases. For constant chloride concentration the pitting potential decreases with decreasing solution pH. The pitting potential, in general, decreases with increasing temperature [55]. The *critical chloride concentration* for a given potential is the maximum chloride concentration that does not destroy the passive film.

Pitting corrosion is basically a two-step process: initiation and propagation. The exact mechanism of pit initiation is not yet fully understood. Pit initiation can occur at weak points (structural or chemical inhomogeneities) in the passive film, mainly associated with inclusions.

Propagation of pitting corrosion is favoured by the acidity produced in the pit (anodic zone) due to metal hydrolysis. Furthermore, the acidic pit environment hinders repassivation of the metal surface. The accumulation of positively charged ions (protons, metal ions) in the pit

requires negative ions (chlorides) to migrate into the pit environment. Chlorides accumulate inside the pit, where acidity is produced and the whole mechanism is self-sustaining.
The pit repassivates if these transport and diffusion processes cease and no longer promote this self-sustaining mechanism.

REFERENCES

1. J.F.Watts, J.Wolstenholme, *"An Introduction to Surface Anlysis by XPS and AES"*, ed. J.Wiley & Sons Ltd. (2003)
2. J.F.Moulder, W.F.Stickle, P.E.Sobol, K.D.Bomben, "*Handbook of X-ray Photoelectron Spectroscopy*", ed. J.Chastain – Perkin-Elmer Corporation (1992)
3. M.P.Seah, D.Briggs in D.Briggs, M.P.Seah, *"Practical Surface Analysis", 2nd ed. vol.1*, ed. J.Wiley & Sons, (1990)
4. ISO 15472:2001 – "*Surface Chemical Anlaysis – X-ray Photoelectron Spectrometers – Calibration of Energy Scales*". M.P.Seah, *Surface and Interface Analysis 31*, 721 (2001)
5. P.M.A.Sherwood in D.Briggs, M.P.Seah, *"Practical Surface Analysis", 1st ed. vol.1*, ed. J.Wiley & Sons Ltd. (1983)
6. A.M.Salvi, J.E.Castle, J.F.Watts, E.Desimoni, *Applied Surface Science 90*, 333 (1995)
7. P.R.Bevington, D.K.Robinson, *Data Reduction and Error Analysis for the Physical Science*, 2nd ed. McGraw Hill (1992)
8. C.D.Wagner, A.Joshi, *Journal of Electron Spectroscopy and Related Phenomena 47*, 283 (1991) and references quoted therein
9. G.Moretti, *Journal of Electron Spectroscopy and Related Phenomena 95*, 95 (1998)
10. G.Moretti, *Journal of Electron Spectroscopy and Related Phenomena 76*, 365 (1995)
11. C.D.Wagner, *Faraday Discussions of Chemical Society 60*, 291 (1975)
12. J.H.Scofield, *Journal of Electron Spectroscopy 8,* 129 (1976)
13. R.F.Reilman, A.Msezane, S.T.Manson, *Journal of Electron Spectroscopy 8*, 389 (1976)
14. P.J.Cumpson, M.P.Seah, S.J.Spencer, *Spectroscopy Europe 10(3)*, 2 (1998)

15. P.J.Cumpson, *"Angle-Resolved X-Ray Photoelectron Spectroscopy"* in *Surface Analysis by Auger and X-Ray Photoelectron Spectroscopy*, ed. D.Briggs and J.T.Grant, Surface Spectra and IM Pubblications (2003)
16. D.R.Penn, *Physical Review B. 35(2)*, 482 (1987)
17. M.P.Seah, W.A.Dench, *Surface and Interface Analysis 1(1)*, 2 (1979)
18. S.Tanuma, C.J.Powell, D.R.Penn, *Surface and interface Analysis 21*, 165 (1993)
19. W.H.Gries, *Surface and interface Analysis 24*, 38 (1996)
20. I.Lindau, W.E.Spicer, *Journal of Electron Spectroscopy and Related Phenomena 3*, 409 (1974)
21. C.J.Powell, *Surface Science 44*, 29 (1974)
22. S.Tanuma, C.J.Powell, D.R.Penn, *Surface and Interface Anlaysis 11*, 577 (1988)
23. S.Tougaard, *Journal of Vacuum Science and Technology A14(3)*, 1415 (1996)
24. D.Briggs and M.P.Seah, in *Practical Surface Anlysis vol.1*, ed. Wiley & Sons Ltd. (1990)
25. M.P.Seah, *Surface and Interface Analysis 2*, 222 (1980)
26. S.Tougaard, *Journal of Electron Spectroscopy and Related Phenomena 52*, 243 (1990)
27. S.Tougaard, *Journal of Vacuum Science and Technology A8*, 2197 (1990)
28. S.Tougaard, A.Jablonski, *Surface and Interface Analysis 25*, 404 (1997)
29. S.Tougaard, P.Sigmund, *Physical Review B. 25*, 4452 (1982)
30. S.Tougaard, *Surface and Interface Analysis 11*, 453 (1988) and references therein
31. L.Landau, *Journal of Physics (Moscow) 8*, 201 (1944)
32. S.Tougaard, *Surface and Interface Analysis 25*, 137 (1997) and references therein
33. http://www.quases.com/Downloads/QUASES-Tougaard/QUASES-Tougaard %20Ver5%20Manual.zip
34. S.Tougaard, *Surface and interface Analysis 26*, 249 (1998)
35. S.Haupt, H.Strehblow, *Corrosion Science 29*, 163 (1989)
36. G.C.Smith, A.K.Livesey, *Surface and Interface Analysis 19*, 175 (1992)
37. S.F.Gull, G.J.Daniel, *Nature 272*, 686 (1978)
38. T.J.Cornwell, K.F.Evans, *Astronomic Astrophysics 143*, 77 (1985)
39. A.K.Livesey, G.C.Smith, *Journal of Electron Spectroscopy and Related Phenomena 67*, 439 (1994)
40. R.L.Opila, J.J.R.Eng, *Prog. Surface Science 69*, 125 (2002)

41. J.P.Chang, M.L.Green, V.M.Donnelly, R.L.Opila, J.J.R.Eng, J.Sapjeta, P.J.Silverman, B.Weir, H.C.Lu, T.Gustafsson, E.Garfunkel, *Journal of Applied Physics 87,* 4449 (2000)
42. R.Champaneria, P.Mack, R.White, J.Wolstenholme, *Surface and Interface Analysis 35*, 1028 (2003)
43. M.Olla, G.Navarra, B.Elsener, A.Rossi, *Surface and interface Analysis 38*, 964 (2006)
44. W.S.M.Werner, W.H.Gries, H.Störi, *Journal of Vacuum Science and Technology 9*, 21 (1991)
45. A.Jablonski, J.Zemek, *Journal of Surface Science 387*, 288 (1997)
46. P.J.Cumpson, *Journal of Electron Spectroscopy and Related Phenomena 73*, 25 (1995)
47. P.W.Paynter, *Surface and Interface Analysis 3*, 186 (1981)
48. J.Skilling, S.F.Gull, *IEE Proc. 131*, 646 (1984)
49. V.E.Carter, *"Metallic coatings for corrosion control"*, ed. Newnes-Butterworths (1977)
50. G.Bianchi, F.Mazza, *"Fondamenti di corrosione e protezione dei metalli"*, ed. Masson (1989)
51. L.Bertolini, B.Elsener, P.Pedeferri, R.Polder, *"Corrosion of steel in concrete"*, ed. Wiley and Sons Ltd. (2004)
52. M.Pourbaix, *"Atlas of Electrochemical Equilibria in aqueous solution"*, ed. Pergamon Press (1966)
53. D.Landolt, *Surface and Interface Analysis 15*, 395 (1990)
54. N.Hara, K.Sugimoto, *Journal of the Electrochemical Society 6*, 138 (1991)
55. L.Bertolini, F.Bolzoni, T.Pastore, P.Pedeferri, *British Corrosion Journal 31(3)*, 218 (1996)
56. D.Addari, PhD Thesis at University of Cagliari, Italy (2005)

CHAPTER 4

EXPERIMENTAL

This chapter is concerned with the materials used and the experimental methods applied in this study. In section 4.1, the alloy samples and their preparation methods are reported, then the reference materials are listed. In section 4.2, the electrochemical cell and the potentiostat/galvanostat used in this study are described together with the experimental setup for the electrochemical tests. Then, in section 4.3, the two XPS spectrometers used are described together with the experimental setup for both standard and ARXPS spectra acquisition modes. At the end of this chapter, in section 4.4, a detailed description is provided of the ion etching kinetics performed in this work (§ 4.4.1), of the application of the First Principles Method of quantification (§ 4.4.2), as well as of Tougaard's (§4.4.3) and MEM (§ 4.4.4) application procedures.

4.1 MATERIALS

4.1.1 NiP ALLOYS

Two differently prepared NiP alloys were studied in this work.

An electrodeposited Ni-29P alloy was used as “probe” to determine whether preferential sputtering occurred during ion etching of the NiP alloy surface.

Electroless NiP coatings were the actual specimens studied by both electrochemical tests and XPS surface analysis as described in the following.

4.1.1.1 ELECTRODEPOSITED Ni-29P ALLOYS

These Ni-29P alloys were prepared by electrodeposition and their composition was determined by both XPS surface analysis and wet analysis performed after dissolution in nitric acid. Details of both the preparation and characterization of these NiP coatings are reported in [1].

4.1.1.2 ELECTROLESS NiP ALLOYS

NiP coatings were prepared by electroless deposition using a commercial bath (Galvanic, Wädenswil, CH). Table 4.1 gives the main bath deposition parameters. Deposition was performed on 300 x 300 x 2 mm copper or iron foil after mechanical polishing with 4000 SiC grit paper. The substrates were then pickled with hydrochloric acid and coated with a 1 µm thick nickel layer to facilitate electroless deposition. Phosphorus content as well as properties of the resultant NiP deposit depends on bath parameters. Bath formulation was chosen so as to obtain a phosphorus content of 18-24 at.% and a coating thickness of 15-20 µm. As received samples were examined under the optical microscope.

Table 4.1 : Main electroless deposition bath parameters.

Ni^{2+} concentration	6 g/L
NaH_2PO_2 concentration	20 g/L
pH	4.8
Temperature	88 °C

4.1.1.3 ALLOY SURFACE PREPARATION

To obtain a reproducible surface condition, sample surfaces were usually mechanically polished. following the procedure described in Struers online “Metalog Guide” [2]. The procedure is divided into grinding and polishing phases, in turn divided into two steps. Table 4.2 shows the main parameters of the mechanical polishing procedure.

Table 4.2 : parameters of the mechanical polishing procedure

	GRINDING		POLISHING	
	I step	II step	I step	II step
Surface	2400 SiC-paper	4000 SiC-paper	MD-Dac (Struers)	MD-Nap (Struers)
Abrasive	-	-	1 µm diamond paste	¼ µm diamond paste
Lubricant	distilled water	distilled water	ethanol	ethanol
Rotation Speed (rpm)	180	180	150	150
Time (min)	3	5	3	5

Because of its surface flatness, the grinding phase was not applied to the NiP alloy-coated copper. After each polishing step, the samples were examined under an optical microscope to check surface uniformity.

4.1.1.4 MORPHOLOGICAL AND COMPOSITIONAL CHARACTERIZATION

Optical microscopy images of the as received samples, and of the mechanically polished and potentiostatically polarized samples, were taken using an Axiolab A (Zeiss, Oberkochen, Germany) microscope equipped with a charge-coupled device (CCD) camera. Every sample was examined using 20x and 100x objective lens and fixed camera magnification of 55x.

Crystal structure of the NiP coatings was determined by X-ray Diffraction Spectroscopy (XRD) and chemical composition by Energy Dispersive X-ray analysis (EDX).

4.1.2 REFERENCE MATERIALS

Reagent	**Chemical formula**		**Supplier**
Nickel	*Ni*	*foil*	*Good-Fellow*
Red Phosphorus	P_4	*lump*	*ABCR GmbH & Co.*
Nickel (II) Oxide	NiO	*lump*	*Alfa Aesar*
penta-hydrated Nickel (II) Orthophosphate	$Ni_3(PO_4)_2 \cdot 5H_2O$	*lump*	*Alfa Aesar*

Sodium Orthophosphate	$Na_3PO_4 \cdot 12H_2O$	*powder on biadhesive tape*	*Merck*
Sodium dihydrogen Orthophosphate	NaH_2PO_4	*powder on biadhesive tape*	*Carlo Erba*
mono-hydrated Sodium Hypophosphite	$NaH_2PO_2 \cdot H_2O$	*powder on biadhesive tape*	*Fluka*
Nickel (II) Sodium Pyrophosphate	$0.3NiO \cdot 0.35NaO_2 \cdot 0.35P_2O_5$	*glass*	*synthesized at University of Cagliari* [3]
Ar^+ *ion etched NiP alloy*	*Ni-18P*	*electroless deposited on Cu (17 μm thick)*	*Galvanic*

Pure nickel and red phosphorus were ion etched before spectra acquisition.

4.2 ELECTROCHEMISTRY

4.2.1 ELECTROCHEMICAL CELL

The electrochemical cell (Figure 4.1) consisted of a plexiglass cylinder with a 0.865 cm^2 lateral porthole close to the base. The sample, referred to as *working electrode*, was pressed against the o-ring sealing the hole. The cell was filled with 200 mL test solution. The plexiglass cell lid was provided with openings for inserting the working electrode, the Haber-Luggin capillary, the counter electrode and an argon bubbler. A saturated

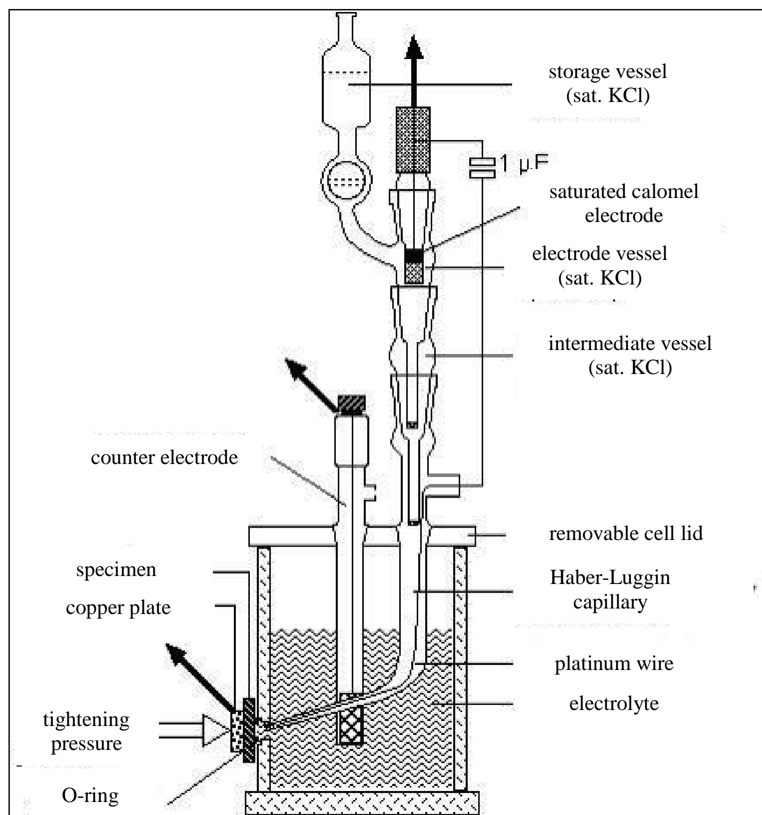

Figure 4.1 : electrochemical cell

calomel electrode (SCE) was used as reference electrode:

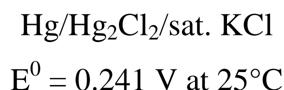

$$Hg/Hg_2Cl_2/\text{sat. } KCl$$
$$E^0 = 0.241 \text{ V at } 25°C$$

The Haber-Luggin capillary, its tip 3 mm away from the working electrode, was filled with test solution. An intermediate vessel was filled with a saturated KCl solution and placed between the Haber-Luggin capillary and the reference electrode. This set-up prevented the SCE electrode from undergoing ion exchange with the test solution. A platinum net was used as counter electrode. The test solution was de-aerated by argon bubbling for at least 1 hour before measurement and argon flow was maintained throughout the experiment. All experiments were performed at 25 °C.

4.2.2 ELECTROCHEMICAL INSTRUMENTATION AND MEASUREMENTS

All the electrochemical measurements were performed using a Model 273A Eg&G Parc potentiostat/galvanostat. The instrument was remotely controlled using Model 352 SoftCorr II software run on an IBM-compatible personal computer.

The specimens were cleaned with ethanol and then dried out argon before measurements.

Potentiodynamic polarization curves (sweep rate 0.2 mV/s) were measured in deaerated near-neutral 0.1 M NaCl, 0.1 M Na_2SO_4, 0.1 M Na_2SO_4 + 0.1 M NaCl and 0.1 M H_2SO_4 solutions. The specimens were kept at open circuit potential (OCP) for 15 minutes before polarization was initiated.

Potentiostatic polarizations were carried out using the following procedure:

1) The Na_2SO_4 0.1 N solution was de-aerated by argon bubbling for at least 1 hour.
2) The specimen was fitted onto the cell O-ring and left at OCP for at least 15 minutes.
3) Potentiostatic polarizations were recorded at +0.1 V SCE for 1 hour, 3 hours and 14 hours.

4.3 XPS SURFACE ANALYSIS

Surface analysis was performed using two different XPS spectrometers: a VG ESCALAB 200 and a Theta Probe, both manufactured by Thermo Fisher Scientific Inc., East Grinstead, UK. The non-monochromatic Al source of the VG ESCALAB 200 made it possible to record the PKLL region on the specimens using Bremsstrahlung radiation. Electrons were collected at 16 different emission angles simultaneously using the innovative Theta Probe lens system, combined with a 2D detector. Emission angle is defined as the angle between the normal to the sample surface and the direction of the emitted electrons [4].

4.3.1 VG ESCALAB 200

The main part of the instrument is the Mu-metal analysis chamber where residual pressure is usually maintained around 10^{-9} mbar (10^{-7} Pa) by a turbomolecular pump and a titanium sublimation pump. The sample is rapidly introduced through a forechamber where a rotary pump keeps residual pressure at 10^{-3} mbar.

Pressure in the analysis chamber during measurements was always lower than $5 \cdot 10^{-7}$ mbar.

Figure 4.2 : VG ESCALAB 200, Thermo Fisher Scientific Inc., East Grinstead, UK.

The X-ray source is a twin anode: a copper anode with two angled end faces. A 10 µm thick aluminium film is deposited on one of the faces, a 10 µm thick magnesium film on the other. A 1 µm aluminium window shields the sample from stray electrons from the source. Spectra were collected with the Al $k\alpha_{1,2}$ (1486.6 eV) operated at 20 mA and 15 kV (300 W). The analyzer was operated in Constant Analyzer Energy (CAE) mode, at 20 eV Pass Energy (PE) for high resolution spectra, and at 50 eV PE for survey spectra. The Full Width at Half Maximum (FWHM) of the $Ag3d_{5/2}$ line, at 20 eV CAE, was 1.1 eV.

Sample etching was performed with an Ar^+ ion gun operated at 5 kV, 0.2 mA current. Electron collection was always carried out at 0° emission angle.

THETA PROBE

Again, the main part of the instrument is the Mu-metal analysis chamber where residual pressure is usually maintained around 10^{-10} mbar (10^{-8} Pa) by a turbomolecular pump and a titanium sublimation pump. The sample is rapidly introduced through the Fast Entry Air Lock (FEAL) where a second turbomolecular pump keeps residual pressure at 10^{-3} mbar.

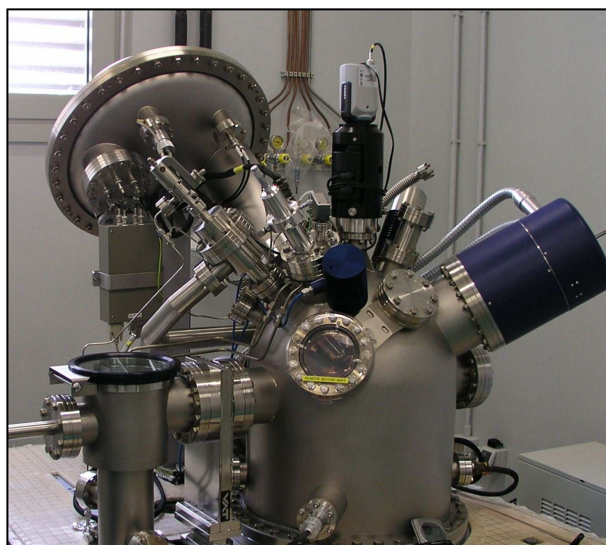

Figure 4.3 : THETA PROBE, Thermo Fisher Scientific Inc., East Grinstead, UK.

Pressure in the analysis chamber during measurements was always lower than $5 \cdot 10^{-8}$ mbar.

The X-ray source is a MXR1 monochromator system and consists of a resistively heated LaB_6 emitter (cathode), an extractor electrode, an asymmetric electrostatic lens, a water cooled aluminium anode and a monochromator crystal. The monochromator is a single thin crystal quartz wafer bonded to the surface of a appropriately shaped substrate.

Spectra were collected with the Al kα_1 (1486.6 eV) operated at 4.7 mA and 15 kV (70 W), 300 μm spot size. The analyzer was operated in CAE mode at 100 eV pass energy for both high resolution and survey spectra. The FWHM of the Ag3$d_{5/2}$ line, under these experimental conditions, was 0.83 eV.

Sample etching was performed with an Ar^+ ion gun operated at 3 kV, 1 μA current. A dual beam (electron and ions) neutralizer was used to compensate for the charge build up on the surface of insulating samples. Electrons were collected at 53° emission angle for the standard acquisition mode, at 16 different emission angles ranging from 24.88 to 81.13 simultaneously, for the Angle-Resolved XPS (ARXPS) acquisition mode.

4.3.2 ENERGY SCALE CALIBRATION

A periodic calibration was performed to verify the linear response of both XPS spectrometers over the whole energy scale. Both instruments were calibrated using the inert-gas-sputter-cleaned reference materials SCAA90 of Cu, Ag and Au [5]. The Au4$f_{7/2}$ line at 83.98 eV, the Ag3$d_{5/2}$ line at 368.26 eV and the Cu2$p_{3/2}$ line at 932.67 eV were taken for

instrument calibration. For the VG ESCALAB 200 the CuLMM line at 334.94 eV was also taken [6]. Accuracy for both instruments was ±0.05 eV.

4.3.3 INTENSITY/ENERGY RESPONSE FUNCTION (IERF) DETERMINATION

VG ESCALAB 200 IERF was determined at $KE^{-0.5}$ [7].

Theta Probe IERF (Figure 4.4) was calculated following the operating instructions provided in the on-line manual [8]. IERF was determined for the X-ray source operating at 4.7 mA and 15 kV (70 W), 300 μm spot size. High resolution Ag3d spectra were acquired from 350 eV BE to 395 eV BE on pure silver foil after mechanical polishing and ion etching. Spectra acquisition was carried out with the lens in the standard acquisition mode (53° emission angle) and in the ARXPS mode (16 different emission angles). Three scans were recorded for each spectral region with 0.05 eV step size and 100 ms dwell time. Spectra acquisition was carried at nine different PE values ranging from 10 eV to 400 eV both in the standard and the ARXPS lens mode. The resultant 153 spectra were fitted with a Gaussian-Lorentzian product function, after Shirley background subtraction [9]. Theta Probe IERF was finally calculated using a polynomial fit to a Log_{10} ($Ag3d_{5/2}$ peak area / PE) versus Log_{10} (RR) plot, where RR is the retard ratio defined as KE/PE. Figure 4.4 shows the Theta Probe IERF for the X-ray gun operated at 4.7 mA and 15 kV (70 W), 300 μm spot size.

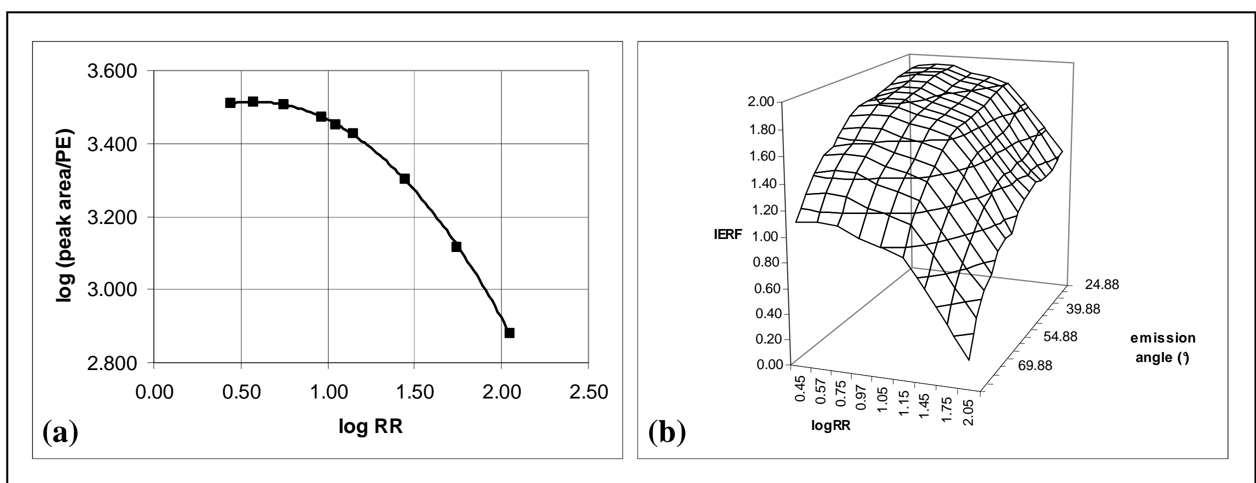

*Figure 4.4 : Theta Probe intensity/energy response functions for the 4.7 mA 15 kV (70 W) and 300 μm spot size X-ray gun with lens in **(a)** standard mode and **(b)** ARXPS mode.*

4.3.4 XPS MEASUREMENTS

Table 4.3 : List of spectral region binding energy ranges acquired with VG ESCALAB 200 and Theta Probe.

Region name	VG ESCALAB 200	Theta Probe
	Binding energy range (eV)	
Survey	0 ÷ 1400	0 ÷ 1400
$Ni2p_{3/2}$	845 ÷ 868	848 ÷ 865
P2p	120 ÷ 140	125 ÷ 138
PKLL	-385 ÷ -355	-
O1s	525 ÷ 545	525 ÷ 539
C1s	275 ÷ 295	280 ÷ 293

Spectra of the above listed pure samples were acquired as reference spectra.
Spectra of the NiP alloy-coated copper were acquired after different treatments:

A) Polarized at +0.1 V SCE in 0.1 M Na_2SO_4 for 1 hour

B) Polarized at +0.1 V SCE in 0.1 M Na_2SO_4 for 3 hours

C) Polarized at +0.1 V SCE in 0.1 M Na_2SO_4 for 14 hours

4.3.5 DATA PROCESSING

All the spectra were processed with CASA XPS software (Casasoftware Ltd., UK). An iterated Shirley-Sherwood background subtraction was applied prior to curve fitting with a Gaussian-Lorentzian product function. The Gaussian-Lorentzian ratio was determined, for each peak, from measurements on pure reference compounds, which were analyzed under the same experimental conditions.

Phosphorus modified Auger parameters were calculated for both reference compounds and polarized NiP alloys. The Wagner chemical state plot of phosphorus was then constructed.

Ion etching kinetics were performed on the Theta Probe to check whether preferential sputtering occurred. Then, XPS quantitative analysis of the etched NiP coatings was performed using both the First Principle and Tougaard's method.

Non-destructive depth profile reconstruction of the polarized NiP alloys surface was carried out using Tougaard's and the Maximum Entropy Method (MEM). Tougaard's method was applied to the survey spectra of the polarized NiP alloys, acquired with the VG ESCALAB 200 and using survey spectra for pure nickel, red phosphorus and $Ni_3(PO_4)_2 \cdot 5H_2O$ as

references. The MEM was applied to the apparent concentration diagram (ACD) data which were calculated from ARXPS spectra collected using the Theta Probe.

4.4 XPS QUANTITATIVE ANALYSIS AND DEPTH PROFILING

4.4.1 ION ETCHING KINETICS

In order to evaluate the possibility of preferential sputtering occurring during ion etching of NiP alloy surface, three ion etching kinetics were tested.

Kinetics n.1 : An electrodeposited Ni-29P specimen was mechanically polished and immediately transferred to the Theta Probe analysis chamber. Ion etching was performed as described above for an etch-time of 300 s. Survey and high-resolution spectra were recorded at time intervals of 30 s; lens was operated in the standard mode.

Kinetics n.2 : A second surface point was chosen on the same specimen used above at an appropriate distance from the first, so as to perform etch rate 2 on a fresh surface area. Ion etching was performed as described above for an etch-time of 30 s. Survey and high-resolution spectra were recorded at time intervals of 5 s; lens was operated in the standard mode.

Kinetics n.3 : Another electrodeposited Ni-29P specimen was mechanically polished and immediately transferred to the Theta Probe analysis chamber. Ion etching was performed as described above for an etch-time of 30 s. Survey and high-resolution spectra were recorded at time intervals of 5 s; lens were operated in the standard mode.

4.4.2 FIRST PRINCIPLES METHOD

The First Principles method was applied for the quantitative analysis of the etched NiP alloys and to monitor changes in NiP coatings composition during the ion etching kinetics. Application of the First Principle Method is firstly based upon the assumption that the sample has a homogeneous composition using the formula:

$$A\ at.\% = \frac{I_A / S_A}{\sum_i I_i / S_i} \cdot 100$$

where I is the peak area of the i_{th} element and S is the sensitivity factor.
The sensitivity factor is calculated, for each element, using the formula:

$$S_i = \sigma_i \cdot L_i(\gamma) \cdot T(KE) \cdot \Lambda_i$$

where:

σ_i is the photoionization cross-section [10];

$L_i(\gamma) = 1 + \frac{1}{2}\beta_i\left(\frac{3}{2}sen^2\gamma - 1\right)$ is the angular asymmetry function;

γ is the angle between the X-ray source and the lens axis (49.1° for the VG ESCALAB 200; 67.38° for the Theta Probe with lens in standard acquisition mode);
β_i is the asymmetry parameter [11];

$T(KE)$ is the Intensity/Energy Response Function (IERF);

$\Lambda_i = \lambda_i \cos\theta$ is the attenuation length;

λ_i is the inelastic mean free path (IMFP) which was calculated using the G-1 equation [12];
θ is the emission angle i.e. the angle between the normal to the sample surface and the lens axis (0° for the VG ESCALAB 200; 53° for the Theta Probe with lens in standard acquisition mode).

4.4.3 TOUGAARD'S METHOD

To apply Tougaard's method for quantification and in-depth profiling of sample surfaces, QUASES-software v.4.4 (Quantification Analysis of Surfaces by Electron Spectroscopy – Sven Tougaard – Odense, DK) was used to process survey spectra. In the following, the principles used in QUASES are summarized.
The measured spectrum is

$$J(E,\Omega) = \int dE\ F(E,\Omega) \int dx\ f(x)\, G\left(E, \frac{x}{\cos\theta}\right)$$

where

E is the electron kinetic energy

Ω is the detector solid angle

F(E,Ω) is the primary excitation spectrum i.e. the spectrum that would be observed in the absence of electron elastic and inelastic scattering

f(x) is the concentration of atoms at depth *x* i.e. the in-depth concentration profile

G(E, x/cosθ) is the energy distribution of an electron as a function of the path length *x/cosθ* travelled in the solid

θ is the emission angle i.e. the angle between the normal to the sample surface and the lens axis

QUASES software uses two different approaches for applying Tougaard's method, described in detail in the user's guide [13]. One is the so called QUASES-Analyze; the other QUASES-Generate.

4.4.3.1 QUASES-ANALYZE : QUANTIFICATION BY BACKGROUND REMOVAL

In this approach the primary excitation spectrum is calculated by

$$F(E,\Omega)=\frac{1}{P_1}\left[J(E,\Omega)-\int dE'\, J(E,\Omega)\quad \int ds\, e^{i2\pi s(E'-E)}\left(1-\frac{P_1}{P(s)}\right)\right]$$

where

$$P(s)=\int dx\, f(x)\, e^{-\frac{x}{\cos\theta}\Sigma(s)}$$

$$P_1=\int dx\, f(x)\, e^{-\frac{x}{\lambda_i\cos\theta}}$$

$$\Sigma(s)=\frac{1}{\lambda_i}-\int_0^\infty dT\; K(T)\, e^{-isT}$$

λ_i is the IMFP

K(T) is, in XPS practice, the inelastic electron scattering cross section.

To apply Tougaard's method using QUASES, the inelastic electron scattering cross section is substituted by Tougaard's *Universal cross section* [14]

$$\lambda_i(E)\, K(T)=\frac{B\,T}{\left(C+T^2\right)^2}$$

where T is the energy loss, B ≈ 3000 eV^2 and C = 1643 eV^2.

The Analyze approach was used to analyze etched NiP survey to determine coatings composition.

Survey spectrum of etched pure elemental Ni foil was used as reference. Reference survey spectrum as well as NiP coatings survey spectra were first corrected for the spectrometer IERF.

The Ni2p peak was isolated from all spectra. A straight line was subtracted from each of the isolated Ni2p peaks. The IMFP of the Ni2p electrons (~ 634 eV KE) in pure elemental Ni was calculated, using the G-1 predictive equation [12], to be equal to 10.57 Å. The inelastic background of the reference Ni2p peak was calculated using a *buried layer* depth-profile extended from 0 Å to 1000 Å and the universal scattering cross-section scale-factor was correspondingly calculated as 1.13. The calculated background was then subtracted from the reference Ni2p peak and F(E,Ω) was determined.

So, the IMFP of 10.57 Å and the universal scattering cross-section scale-factor of 1.13, were used to analyze the inelastic background of the Ni2p peak isolated from the etched NiP survey spectrum. The background was iteratively calculated and subtracted from the peak, using both these quantities and a hypothetical depth profile f(x). The depth-profile f(x) was varied until a good match to both shape and intensity of the primary excitation spectrum F(E,Ω) was obtained. Phosphorus concentration was then calculated by difference.

Results were compared with those obtained using the First Principle Method and EDX data.

4.4.3.2 QUASES-GENERATE : QUANTIFICATION BY PEAK SHAPE CALCULATION

If it is not possible to locate peaks from each element that are free from interfering peaks within ~ 30 eV on the high kinetic energy side and ~ 50-100 eV on the low kinetic energy side, a larger energy region has to be chosen. In this case, the Generate approach is the most suitable. Indeed, if some peaks are actually the convolution of different signals from different chemical states of the same element, then again the Generate approach has to be chosen.

In this approach, the experimental spectrum is calculated by

$$J(E,\Omega) = \int dE_0 \; F(E_0,\Omega) \quad \int ds \; e^{-i2\pi s(E-E_0)} \quad \int dx \; f(x) \, e^{-x\Sigma(s)/\cos\theta}$$

The Generate approach was used to analyze NiP survey spectra (recorded with VG EscaLab 200) after polarization of the alloys, so as to determine their depth profiles.

Survey spectra of pure Ni foil, the lump of red P and of $Ni_3(PO_4)_2\cdot 5H_2O$ were used as references. Reference as well as NiP specimens survey spectra were first corrected for spectrometer IERF. The 300÷1486 eV KE region was isolated from all spectra. A straight line was subtracted from each of the isolated regions.

The IMFP values of Ni2p electrons (~ 634 eV KE) in pure elemental Ni and in the nickel phosphate were calculated using the G-1 predictive equation [12] as 10.57 Å and 32.37 Å respectively. The IMFP of P2p electrons (~ 1357 eV KE) in the red phosphorus obtained using the same equation was 34.61 Å.

The inelastic backgrounds of the reference regions were calculated using the *buried layer* depth-profile extended from 0 Å to 1000 Å and the universal scattering cross-section scale-factors were calculated correspondingly (0.83 for pure Ni ; 0.97 for red P ; 0.93 for nickel phosphate). The calculated backgrounds were subtracted from the corresponding reference region and then the $F_i(E,\Omega)$ were determined. The depth-profiles $f_i(x)$ of the three reference compounds were varied iteratively, the three corresponding model spectra $J_i(E,\Omega)$ were then determined and the sum of the three model spectra $J_i(E,\Omega)$ calculated, i.e. the simulated spectrum.

The three depth-profiles $f_i(x)$ were varied until a good match with both shape and intensity of the experimental spectrum was obtained.

4.4.4 MAXIMUM ENTROPY METHOD

The basic feature of the MEM theory consists in finding the depth-profile that satisfies the experimental data but contains the minimum “amount of structure” necessary to do so (since we do not want to fit noise).

The theory leads to the possibility of simultaneously meeting this two conditions by maximizing the so called *probability function*

$$Q = \alpha S - \frac{C}{2}$$

where

α is the regularizing parameter

S is the entropy

C is the chi-squared calculated data deviation from the experimental data

Two different versions of one algorithm were implemented to apply the MEM theory to the ACD data derived from ARXPS data. Since minimization algorithms are, in general, easier to implement than maximization ones, the above equation was changed into

$$Q = \frac{C}{2} - \alpha S$$

so as to satisfy the above two conditions by minimizing the probability function Q.

4.4.4.1 FIRST VERSION OF THE MEM ALGORITHM

The first version of the algorithm [15] was based on a number of variables given by the product of the "mathematical layers" (*mem-layer*) into which the depth profile is divided and the component number, i.e. the number of chemical species. Each component had an individual concentration value for each of the mem-layers. The sum of all component concentrations within each mem-layer was normalized to 1. Mem-layers thickness was taken as 1 Å. This version of the MEM algorithm had already been successfully applied to solve a 5-component depth-profile [15].

4.4.4.2 NEW VERSION OF THE MEM ALGORITHM

In the second version of the MEM algorithm each of the n-variables components (where n is the number of mem-layers) is substituted with a 4-parameter-pseudo-Gaussian function, so as to reduce the overall number of variables. The sum of all component concentrations within each mem-layer was normalized to 1 and mem-layer thickness was taken as 1 Å.

4.4.4.3 APPARENT CONCENTRATIONS DIAGRAMS SIMULATOR

Using the MEM theory equations, a computer code was implemented to calculate the theoretically expected ACD data for a given depth profile. This code is hereinafter referred to as *the simulator*.

4.4.4.4 SYNTHETIC STRUCTURES FOR NUMERICAL EXPERIMENTS

First of all, note that mem-layers do actually differ from real layers. In the MEM theory, the specimen surface region (i.e. the surface region down to a depth equal to XPS sampling depth) is divided into parallel and identical numerical layers. These numerical layers do not necessarily coincide with real atomic planes but they are simply mathematical “entities”. These numerical layers are referred to as *mem-layers*, since they are involved in the MEM theory. On the other hand, if a specimen has a layered structure e.g. iron oxide formed on a pure metallic iron surface, these physically existing layers are simply referred to as *layers*, possibly accompanied by a distinguishing “name”, e.g. oxide layer, phosphate layer, intermediate layer, overlayer, sublayer, etc…

A series of numerical experiments was carried out to assess the performance of the two versions of our MEM algorithm. The two versions were evaluated both singularly (only on 7 and 8 synthetic components structures) and combined into a single protocol (see next subsection).

Various numerical structures (Table 4.4) were introduced into the simulator as input, in order to obtain the corresponding ACD data as output. The numerical structures were composed of 3 to 8 components labelled A, B, C, D, E, F, G and H. The IMFP values of the components were arbitrarily chosen as 40, 30, 20, 10, 45, 35, 25 and 27 Å respectively. As the number of components in the numerical structures increased from 3 to 8, the “new” component was labelled in the alphabetical order. In other words, all the 3-component structures were composed of A, B and C pseudo-species, all the 4-component structures of A, B, C and D pseudo-species, and so on. The mem-layers were taken as 1 Å thick. All profiles were composed of 151 mem-layers. The maximum number of components in one layer was 3. Numerical structures were unambiguously labelled as reported in Table 4.4.

As an example, let us consider the label “5_2+3”. The first digit, i.e. 5 in this example, indicates the total number of components throughout the entire depth profile of the synthetic structure. After the underscored blank, a series of digits are reported, all of which are separated by the sign “+”. Each digit indicates the number of components that together constitute one layer, going from the surface to the bulk respectively. Species were always included in alphabetical order. So, the label “5_2+3” indicates a 5-component profile in which species A and B form an overlayer while the bulk is composed of species C, D and E.

Table 4.4 : synthetic profiles, on the basis of which numerical experiments were performed, are listed with their labels, layer thickness, components involved and their concentrations.

Synthetic Profile	***Layer***	***Thickness (Å)***	***Species***	***Concentration (at%)***
3_1+1+1	overlayer	21	A	100
	intermediate	20	B	100
	bulk	/	C	100
3_1+2	overlayer	21	A	100
	bulk	/	B C	20 80
3_2+1	overlayer	21	A B	80 20
	bulk	/	C	100
4_1+1+1+1	overlayer	11	A	100
	1st intermediate	10	B	100
	2nd intermediate	10	C	100
	bulk	/	D	100
4_1+1+2	overlayer	11	A	100
	intermediate	10	B	100
	bulk	/	C D	30 70
4_1+2+1	overlayer	11	A	100
	intermediate	20	B C	40 60
	bulk	/	D	100

4_2+1+1	overlayer	16	A	40
			B	60
	intermediate	15	C	100
	bulk	/	D	100
4_2+2	overlayer	16	A	20
			B	80
	bulk	/	C	40
			D	60
4_1+3	overlayer	16	A	100
	bulk	/	B	20
			C	30
			D	50
4_3+1	overlayer	16	A	20
			B	30
			C	50
	bulk	/	D	100
5_1+1+1+1+1	overlayer	7	A	100
	1st intermediate	7	B	100
	2nd intermediate	7	C	100
	3rd intermediate	7	D	100
	bulk	/	E	100
5_1+2+2	overlayer	11	A	100
	intermediate	10	B	40
			C	60
	bulk	/	D	80
			E	20
5_2+1+2	overlayer	11	A	40
			B	60
	intermediate	10	C	100
	bulk	/	D	80
			E	20

5_2+2+1	overlayer	16	A	40
			B	60
	intermediate	25	C	30
			D	70
	bulk	/	E	100
5_1+3+1	overlayer	11	A	100
	intermediate	30	B	20
			C	35
			D	45
	bulk	/	E	100
5_3+1+1	overlayer	16	A	20
			B	35
			C	45
	intermediate	15	D	100
	bulk	/	E	100
5_3+2	overlayer	16	A	35
			B	45
			C	20
	bulk	/	D	80
			E	20
5_2+3	overlayer	16	A	20
			B	80
	bulk	/	C	35
			D	45
			E	20
6_1+1+1+1+1+1	overlayer	5	A	100
	1st intermediate	5	B	100
	2nd intermediate	5	C	100
	3rd intermediate	5	D	100
	4th intermediate	5	E	100
	bulk	/	F	100

6_1+1+2+2	overlayer	7	A	100
	1st intermediate	7	B	100
	2nd intermediate	17	C	40
			D	60
	bulk	/	E	25
			F	75
6_1+2+1+2	overlayer	7	A	100
	1st intermediate	7	B	40
			C	60
	2nd intermediate	17	D	100
	bulk	/	E	25
			F	75
6_2+1+1+2	overlayer	16	A	40
			B	60
	1st intermediate	10	C	100
	2nd intermediate	15	D	100
	bulk	/	E	25
			F	75
6_2+1+2+1	overlayer	16	A	40
			B	60
	1st intermediate	10	C	100
	2nd intermediate	15	D	75
			E	25
	bulk	/	F	100
6_1+2+2+1	overlayer	7	A	100
	1st intermediate	19	B	40
			C	60
	2nd intermediate	15	D	75
			E	25
	bulk	/	F	100
6_2+2+2	overlayer	11	A	40
			B	60
	intermediate	15	C	30
			D	70
	bulk	/	E	20
			F	80

6_1+2+3	overlayer	6	A	100
	intermediate	10	B	40
			C	60
	bulk	/	D	60
			E	15
			F	25
6_1+3+2	overlayer	6	A	100
	intermediate	10	B	15
			C	25
			D	60
	bulk	/	E	35
			F	65
6_2+1+3	overlayer	6	A	30
			B	70
	intermediate	10	C	100
	bulk	/	D	65
			E	10
			F	25
6_2+3+1	overlayer	11	A	30
			B	70
	intermediate	10	C	25
			D	70
			E	15
	bulk	/	F	100
6_3+1+2	overlayer	11	A	20
			B	30
			C	50
	intermediate	10	D	100
	bulk	/	E	35
			F	65
6_3+2+1	overlayer	11	A	20
			B	30
			C	50
	intermediate	10	D	80
			E	20
	bulk	/	F	100

6_3+3	overlayer	21	A	20
			B	30
			C	50
	bulk	/	D	60
			E	15
			F	25
7_a *and* 7_a_{error} (*see text*)	overlayer	7	B	80
			G	20
	1st intermediate	12	D	23
			F	15
			G	62
	2nd intermediate	6	A	100
	bulk	/	C	82
			E	18
7_b *and* 7_b_{error} (*see text*)	overlayer	7	B	80
			G	20
	1st intermediate	12	D	23
			F	15
			G	62
	2nd intermediate	6	A	100
	1st bulk	16	C	65
			E	35
	2nd bulk	/	C	82
			E	18
8 *and* 8_{error} (*see text*)	overlayer	7	B	80
			H	20
	intermediate	12	D	23
			F	15
			G	62
	intermediate/bulk	12	A	40
			C	36
			E	24
	bulk	/	C	82
			E	18

As shown in Table 4.4, this means of labeling synthetic structures was applied to all the profiles having from 3 to 6 components. On the other hand, 7 and 8 component profiles were built based on assumptions about polarized NiP alloys depth profile i.e. literature indications and the results of Tougaard's method. Structure *7_a* was built in order to verify the algorithms ability to solve a profile in which one species (i.e. *G*) was present in two consecutive layers. Another complexing feature was introduced into structure *7_b* by generating an outer *E*-enriched bulk layer. Lastly, also the 8-component structure had an *E*-enriched outer bulk

layer, but was mixed with the non-bulk species *A*. When a structure was introduced in the simulator, the output was the corresponding theoretical ACD i.e. the ACD spots were calculated by the simulator without taking experimental error into account. All the numerical experiments were performed introducing these theoretical ACD spots as MEM algorithm input. However, all the 7 and 8 component ACD data sets (i.e. theoretical) were modified adding a random error to each of the theoretical ACD spots, ranging from -10 to +10%. All the 7 and 8 component numerical experiments were performed both on theoretical and error simulated ACD data sets. Then, 38 different ACD data sets were calculated and 38 relative depth plots (RDP) were correspondingly generated. Finally, 38 numerical experiments were carried out.

In addition, for all the structures listed in Table 4.4, the 38 ACD and corresponding 38 RDP were also re-calculated using the same IMFP value (e.g. 10 Å) for all the components, in order to evaluate the effect of IMFP on the ACD and RDP data.

4.4.4.5 NUMERICAL EXPERIMENTS

The first and the new algorithms were independently checked for all the 7 and 8 component structures. First, checks were performed by setting the starting profile with the same concentration for all the components within each mem-layer. Further checks were performed by basing the starting profile on the *simulator routine* results (see next subsections).

Furthermore, a protocol was established for the combined use of the first and new MEM algorithms, referred to as *the protocol* and this was applied to all the structures listed in Table 4.4. The protocol was not computer-based but performed step by step as shown by the flow diagram in Figure 4.5. The starting profile was always based on simulator routine results. For the first calculation cycle (CC), quantitative data were always disregarded when constructing the starting profile for the new version of the MEM algorithm i.e. only

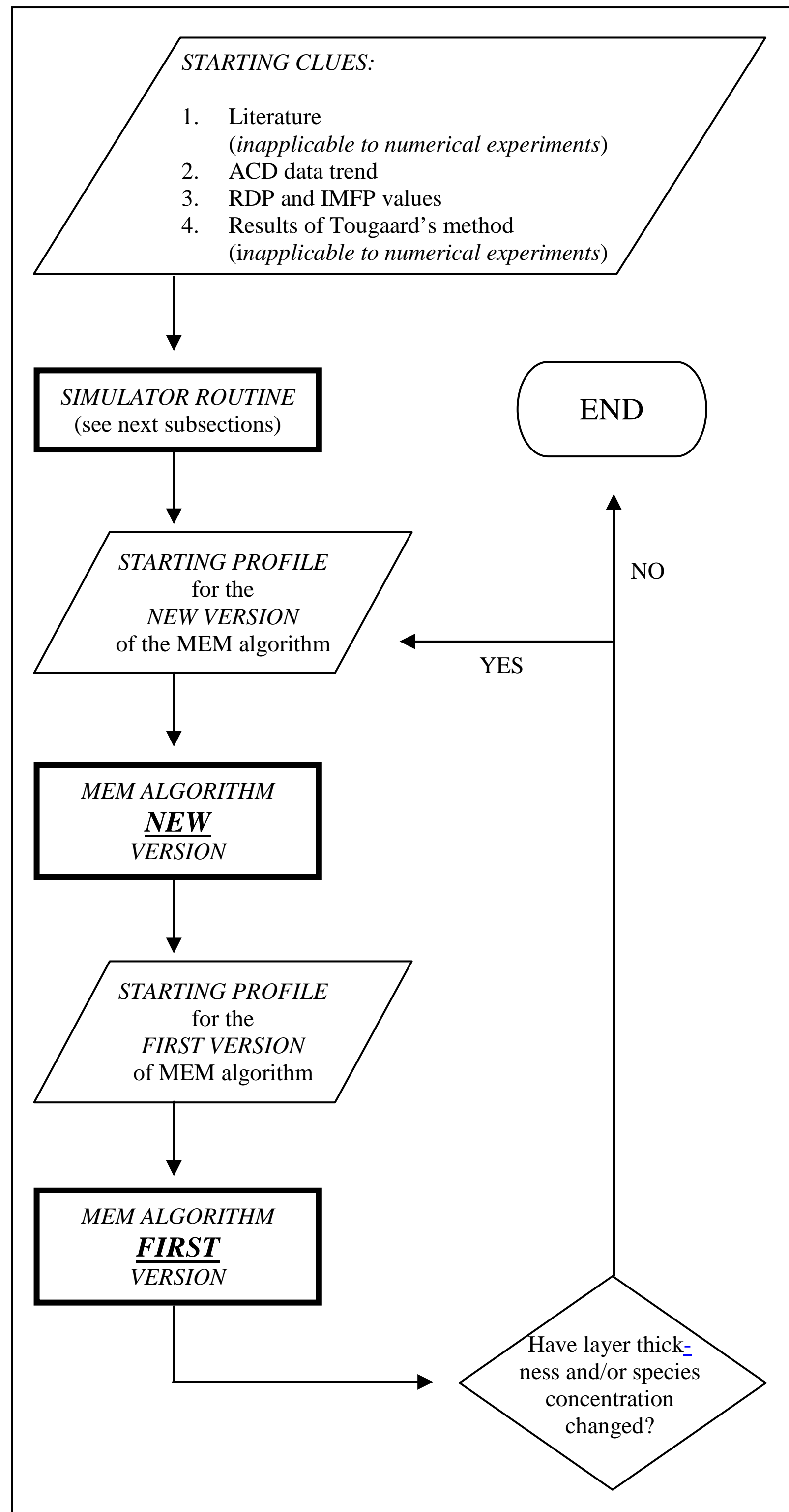

Figure 4.5 : Protocol for combining the first and new versions of the MEM algorithm.

layer thickness was taken into account. At the end of each CC i.e. when the first version of the MEM algorithm generated its output, the difference was calculated between these output results (i.e. ACD data fitting, layer thickness, component concentration and depth profile curves trend) and the analogous output generated at the end of the previous CC. A 1% threshold was chosen as criterion for deciding whether a new CC had to be started up.

Regarding the new version of the MEM algorithm, neither the starting nor the final depth of each component were constrained at the estimated values, but were allowed to range over a closed symmetric 6 Å interval. Once the probability function Q had attained a local minimum, parameter ranges were extended for all components with values exceeding an extreme. Then, minimization of Q was allowed to continue.

During processing of both algorithms the regularizing parameter α was changed so as to keep the entropic αS term and the chi-squared C/2 within same order of magnitude.

4.4.4.6 SIMULATOR ROUTINE

A simulator of apparent concentration diagrams was implemented using the MEM theory equations. A layered depth-profile (referred to as the simulator profile) was used as input, the corresponding ACD being the output. A simulation routine (Figure 4.6) was used to search for the best layered depth-profile whose ACD reproduced the numerical or experimental ACD data, depending on the case studied (i.e. numerical or real). The routine was not computer-based but performed step by step as shown by the flow diagram in Figure 4.6. Mem-layer thickness was taken as 1 Å. Mem-layer number was set to 151. For the numerical experiments, IMFP values were assumed to be correctly known.

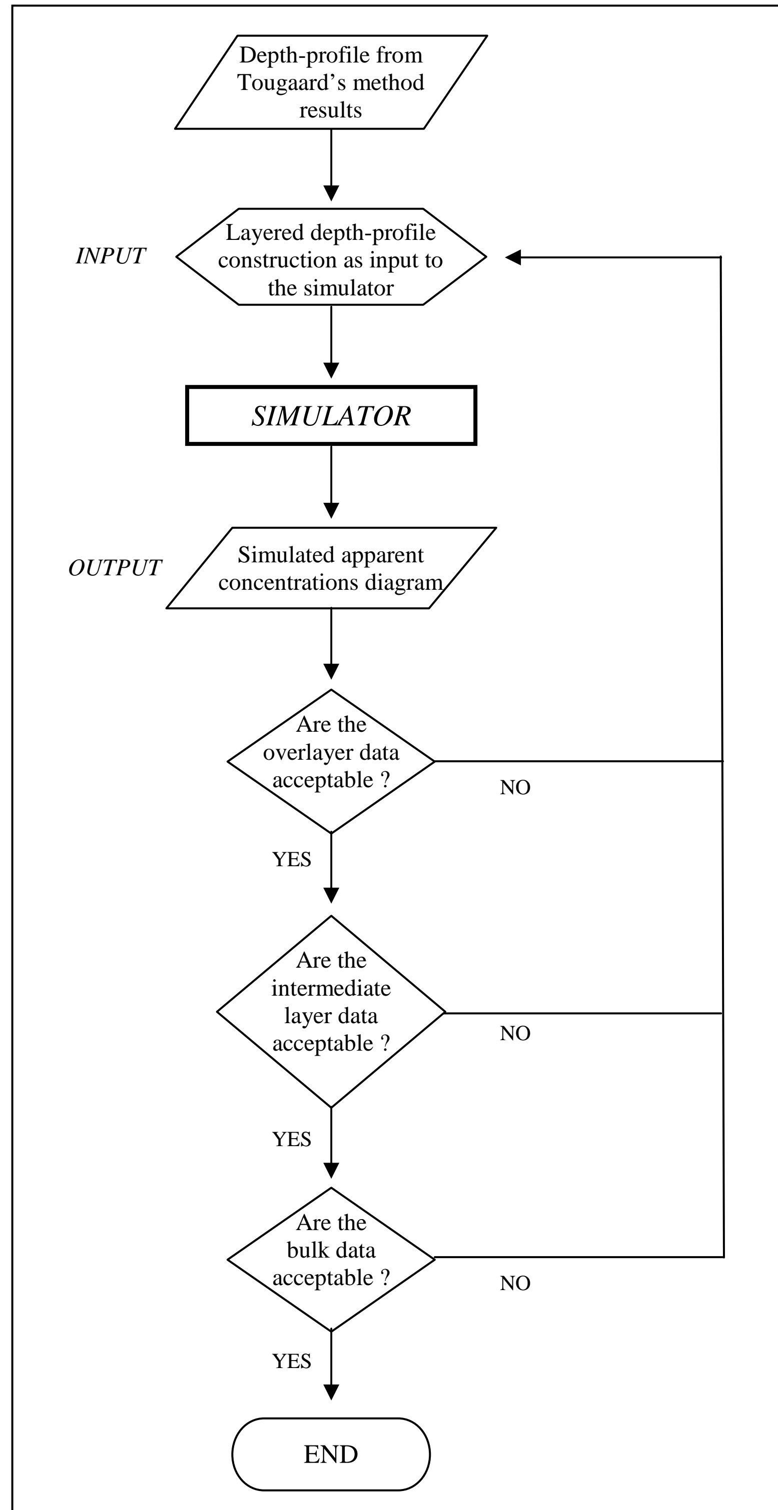

Figure 4.6 : Simulator routine for apparent composition diagrams generation. This simulation routine was used to simultaneously search for the best layered depth-profile (see text) and the best IMFP data set.

Regarding the simulations of experimental data (i.e. acquired on real NiP specimens), the number of mem-layers was taken as ten times the maximum IMFP value of the bulk components, considering the electrons to travel only through the bulk (i.e. overlayer

and intermediate layers were not taken into account). However, as described in the next subsections, whenever the simulator profile was modified, a new set of IMFP values was evaluated accordingly i.e. an IMFP value for each component. At the end of the simulator routine, the "minimum considerable depth" of the simulator profile was investigated by gradually decreasing the number of mem-layers. As this total depth decreased, the ACD data and the difference with respect to their initial values (i.e. ACD data calculated before decreasing mem-layers) were calculated. The minimum number of mem-layers was chosen so that ACD data difference with respect to their initial values was no more than 1%.

Finally, the ultimate IMFP values set was determined in agreement with the best simulator profile and the minimum considerable depth. This set of IMFP values was used in the protocol application to the experimental data of the real NiP samples; the best layered structure with the minimum considerable depth was used for the starting profile.

4.4.4.7 ARXPS EXPERIMENTAL DATA PROCESSING

MEM algorithms protocol was applied to ARXPS data recorded on the polarized NiP samples. ARXPS spectra were recorded with the Theta Probe, as described above, at 16 different emission angles ranging from 24.88° to 81.13°. Spectra at emission angles of more than 60° were not considered owing to the increasing effect of elastic scattering [16,17].

Data were processed using CASA XPS software (Casasoftware Ltd., UK). An iterated Shirley-Sherwood background subtraction was applied prior to curve fitting with a Gaussian-Lorentzian product function. The Gaussian-Lorentian ratio for each peak was determined from measurements on pure reference compounds.

Thus, the high resolution spectra of C1s, O1s, Ni2$p_{3/2}$ and P2p regions were resolved into their components and their intensity determined. Intensities were then corrected for the photoionization cross-section [10], angular asymmetry function and the Theta Probe IERF. Regarding angular asymmetry function, it should be noted that for the Theta Probe ARXPS acquisition mode, γ angle was not constant since data collection was done without tilting the specimen but utilizing the radians lens [18]. Finally, corrected intensities were normalized to 1 for each emission angle. Corrected and normalized intensities were plotted against emission angle i.e. the ACD.

4.4.4.8 ELECTRONIC INELASTIC MEAN FREE PATHS EVALUATION

IMFP calculations were performed with the G-1 predictive equation [12]. The G-1 equation was applied using NIST software "Standard Reference Database 71" [19]. IMFP values were

plotted versus electronic KE, ranging from 200 to 2000 eV, considering an electron travelling through four different materials:

mat. 1) homogeneous organic material composed of O (α at.%) and C (β at.%) with density assumed equal to 1 g cm^{-3} to simulate adventitious surface contamination

mat. 2) $Ni_3(PO_4)_2$ with density of 1.6 g cm^{-3} determined by the immersion method

mat. 3) pure red phosphorus [12]

mat. 4) NiP alloy with phosphorus content of 18 at.% and density of 7.75 g cm^{-3} [20]

The electron IMFPs were then calculated for all chemical species in the NiP specimens (i.e. for photoelectrons which generated the corresponding components of the XPS signals) as the photoelectrons travelled through each of the materials considered separately (i.e. four different IMFP values for each signal electron).

Furthermore, IMFP values were determined for each chemical species in the NiP specimens, as they traveled through a fifth material:

mat. 5) homogeneous mixture of pure red phosphorus (x at.%) and Ni-18P (y at.%)

using the formula

$$IMFP_{mat.5}(KE) = \frac{x \cdot IMFP_{mat.3}(KE) + y \cdot IMFP_{mat.4}(KE)}{x + y}$$

Starting from these values, the actual IMFP values were calculated with the simulator routine. A 4-layer structure was built as shown in Figure 4.7. A formula was used for each of the four layers to calculate the IMFP of the chemical species located in that specific layer.

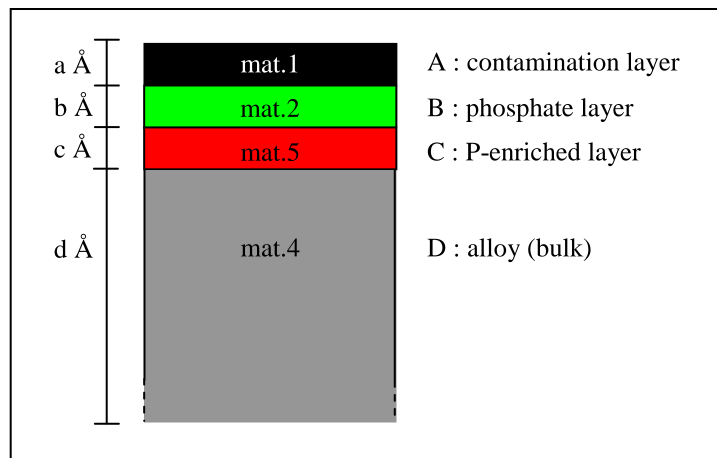

Figure 4.7 : layered structure used in simulator routine for calculating IMFP.

$$_{layer\ A}IMFP(KE) = IMFP_{mat.1}(KE)$$

$$_{layer\ B}IMFP(KE) = \frac{a \cdot IMFP_{mat.1}(KE) + b \cdot IMFP_{mat.2}(KE)}{a+b}$$

$$_{layer\ C}IMFP(KE) = \frac{a \cdot IMFP_{mat.1}(KE) + b \cdot IMFP_{mat.2}(KE) + c \cdot IMFP_{mat.5}(KE)}{a+b+c}$$

$$_{layer\ D}IMFP(KE) = \frac{a \cdot IMFP_{mat.1}(KE) + b \cdot IMFP_{mat.2}(KE) + c \cdot IMFP_{mat.5}(KE) + d \cdot IMFP_{mat.4}(KE)}{a+b+c+d}$$

In the simulator routine, whenever the thickness of the 4 layers and/or the red P/NiP alloy ratio of layer C (i.e. material n.5) were modified, a new set of IMFP values was estimated.

4.4.4.9 MEM ALGORITHMS PROTOCOL APPLICATION TO ARXPS DATA

The protocol was applied to the ARXPS data after processing as previously described. Seven chemical species were examined. The starting depth profile was determined by applying the simulator routine. A set of suitable IMFP values was determined, using the same simulator routine (see previous subsections).

Regarding the new version of the MEM algorithm, neither the starting nor the final depth of each of the eight components was constrained at the estimated values, but they were allowed to range over a closed symmetric 6 Å interval. Once the probability function Q had attained a local minimum, parameter ranges were extended for all components whose values exceeded an extreme. Then, minimization of Q was allowed to continue.

During processing of both algorithms, the regularizing parameter α was changed in order to keep the entropic αS term and the chi-squared C/2 within the same order of magnitude.

REFERENCES

1. A.Krolikowski, *Material Science Forum 799*, 185 (1995)
2. http://www.struers.com/modules/emetalog/login.asp
3. A.Musinu, G.Piccaluga, Journal of Non-Crystalline Solids 192&193, 32 (1995)
4. *"Standard Terminology Relating to Surface Analysis"* in *Annual Book of ASTM Standards* E673-97, 903 (2000)
5. M.P.Seah, *Surface and Interface Analysis 14*, 488 (1989)
6. M.P.Seah, *Surface and interface Analysis 17*, 855 (1991)
7. M.P.Seah, *Surface and Interface Analysis 20*, 243 (1993)
8. Avantage software v3.45, Thermo Fisher Scientific Inc. – Micro Focus Ltd.
9. D.A.Shirley, *Physical Review B. 5(12)*, 4709 (1972)
10. J.H.Scofield, *Journal of Electron Spectroscopy and Related Phenomena 8*, 129 (1976)
11. R.F.Reilman et al., *Journal of Electron Spectroscopy and Related Phenomena 8*, 389 (1976)
12. W.H.Gries, *Surface and Interface Analysis 24*, 38 (1996)
13. http://www.quases.com/Downloads/QUASES-Tougaard/QUASES-Tougaard%20Ver5%20 Manual.zip
14. S.Tougaard, *Surface and Interface Analysis 25*, 137 (1997)
15. M.Olla, G.Navarra, B.Elsener, A.Rossi, *Surface and Interface Analysis 38*, 964 (2006)
16. P.J.Cumpson, in "*Angle-resolved X-Ray Photoelectron Spectroscopy* in *Surface Analysis by Auger and X-Ray Photoelectron Spectroscopy"* - Briggs D, Grant JT (eds) - Surface Spectra and IM Publications (2003)
17. P.J.Cumpson, M.P.Seah, *Surface and Interface Analysis 25*, 430 (1997)
18. Theta Probe Operative Manual – Thermo Fischer Scientific Inc.
19. C.J.Powell, A.Jablonski, NIST Electron Inelastic-Mean-Free-Path Database v.1.1 (2000)
20. R.Taheri PhD thesis: *"Evaluation of Electroless Nickel-Phosphorus (EN) Coatings"* - University of Saskatchevan, Saskatoon, CDN (2002)

CHAPTER 5

RESULTS

In this chapter the experimental results are described. The first two sections, 5.1 and 5.2, deal with samples characterization. Section 5.3 presents the electrochemical results while the XPS spectra for both the reference compounds and the polarized NiP alloys together with the fitting parameters are shown in Section 5.4. Ion etching kinetics are presented in subsection 5.4.3 while the results of sputtered electroless NiP quantitative surface analysis are described in subsection 5.4.4. The results of depth profiling of polarized NiP alloys obtained using Tougaard's method are reported in Section 5.4.5: the Analyze approach is adopted for the quantitative analysis of sputtered NiP alloy surfaces, while the Generate approach is applied for in-depth profiling of the polarized NiP alloys. In the last section 5.4.6 the results of the Maximum Entropy Method are presented. The MEM protocol developed during this thesis work was first verified for numerical synthetic structures in order to validate the method and evaluate its accuracy (§ 5.4.6.1), and then applied for in-depth profiling of the polarized NiP alloys.

5.1 SPECIMENS MORPHOLOGY AND PREPARATION

NiP coatings were prepared by electroless deposition. A commercial bath was used (Galvanic, Wädenswil, CH). Bath formulation was chosen so as to obtain a phosphorus content of 18-24 at.% and a coating thickness of 15-20 µm. Unpolished samples were examined under an optical microscope. Figure 5.1 shows some examples of the morphology of the NiP coatings, deposited on both iron and copper foil.

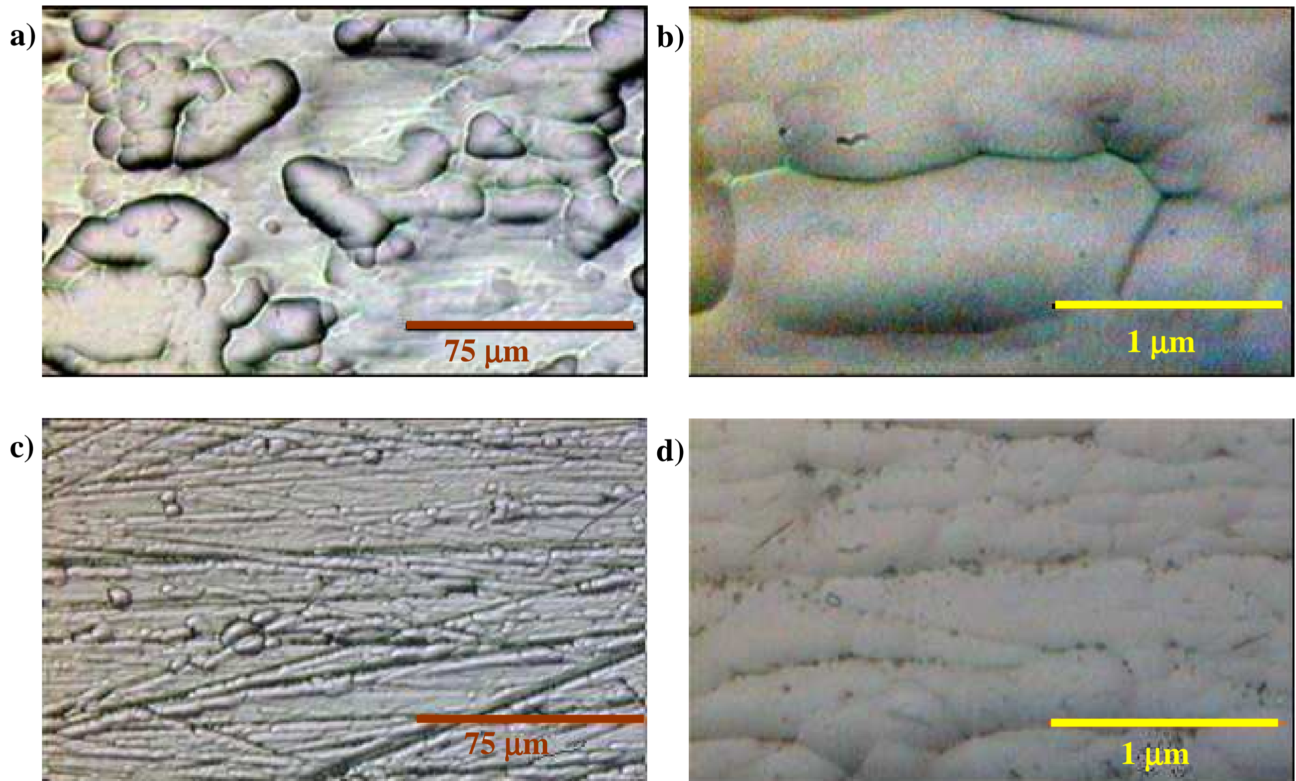

*Figure 5.1 : Surface of NiP coatings as received. **a)** NiP alloy deposited on iron foil, objective magnification 20x, camera magnification 55x ; **b)** NiP alloy deposited on iron foil, objective magnification 100x, camera magnification 55x ; **c)** NiP alloy deposited on a copper foil, objective magnification 20x, camera magnification 55x ; **d)** NiP alloy deposited on copper foil, objective magnification 100x, camera magnification 55x.*

The surface of all the specimens appeared irregular with several semicircular protuberances. Surface irregularities of NiP alloys deposited on copper appeared to be less prominent than those on iron. To obtain a reproducible surface condition, the samples' surface was mechanically polished. After each polishing step, the

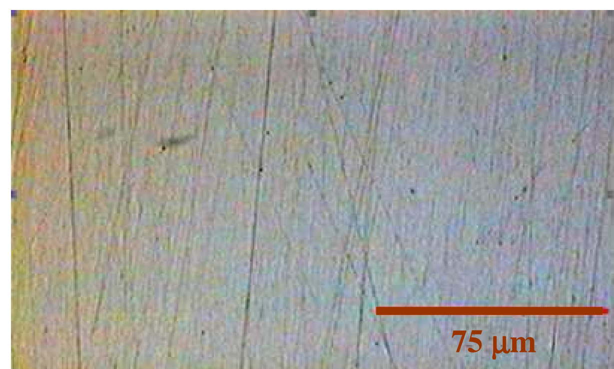

Figure 5.2 : Surface of a mechanically polished NiP alloy deposited on iron foil, objective magnification 20x, camera magnification 55x.

samples were examined under the optical microscope. After mechanical polishing, all the specimens were shiny and highly reflective.

5.2 SAMPLES CHARACTERIZATION

Crystal structure of the NiP coatings was determined by XRD spectroscopy. Irrespective of the substrate material i.e iron or copper, NiP alloys showed a large diffraction peak at about 45° (2 θ), confirming the amorphous/nanocrystalline structure of all deposits. The XRD patterns also exhibited the characteristic diffraction peaks of the substrate (Fe 45°, 65°, 82° ; Cu 42°, 51°, 74°, 90°, 95°), intensity decreasing with increasing deposit thickness. As an example, Figure 5.3 shows the XRD patterns recorded for two alloys of different thickness deposited on iron.

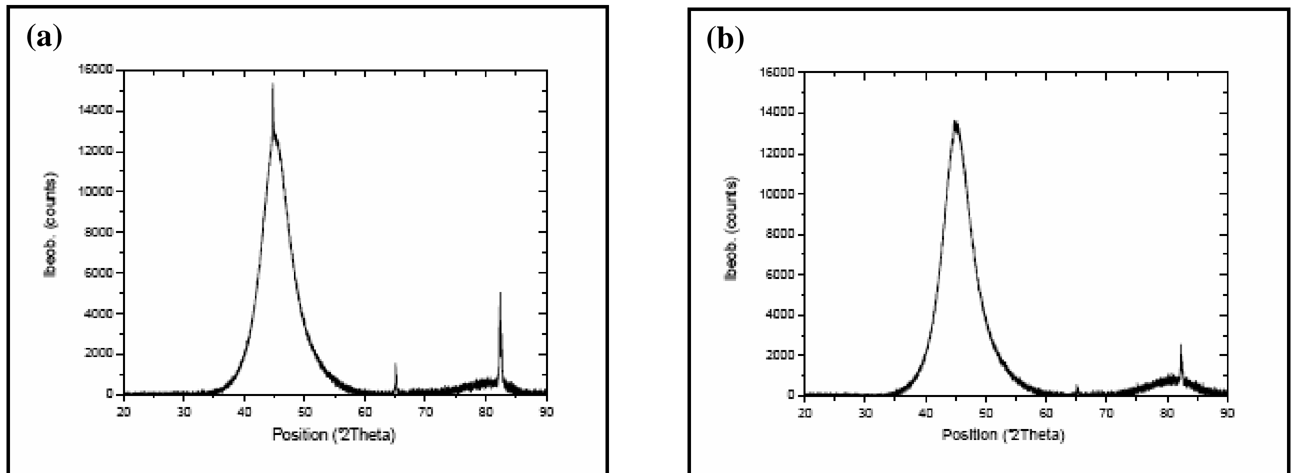

*Figure 5.3 : X-ray diffraction pattern of a **(a)** 10 µm and **(b)** 20 µm thick NiP coating, deposited on an iron substrate.*

Chemical composition of the NiP coatings was determined by EDX analysis. Phosphorus concentration was 10.6 – 11.0 wt% for all specimens, corresponding to a phosphorus content of 18.4 – 19.0 at%.

A line scan over the coating thickness provided evidence of homogeneous chemical composition, as shown in Figure 5.4 for a 10 µm thick deposit.

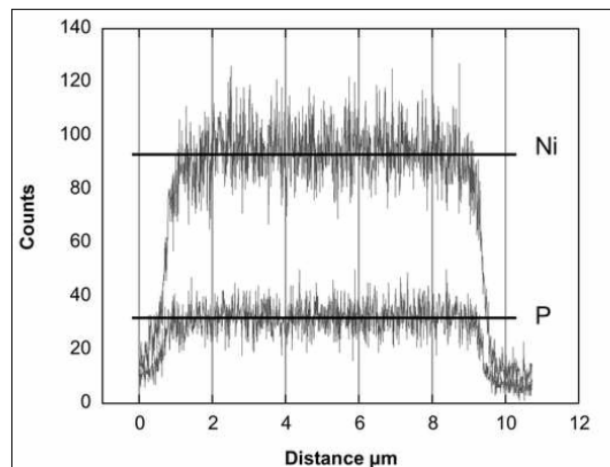

Figure 5.4 : EDX composition profile of a 10 µm thick NiP coating.

5.3 ELECTROCHEMICAL RESULTS

Potentiodynamic polarization curves (sweep rate 0.2 mV/s) were measured in deaerated near-neutral 0.1 M NaCl, 0.1 M Na_2SO_4, 0.1 M Na_2SO_4 + 0.1 M NaCl and 0.1 M H_2SO_4 solutions.

Potentiostatic polarizations were carried out adopting the following procedure:

4) The 0.1 M Na_2SO_4 solution was de-aerated by argon bubbling for at least 1 hour.

5) The specimen was fitted on the cell O-ring and left at the OCP for at least 15 minutes.

6) Potentiostatic polarizations were recorded at +0.1 V and -0.1 V SCE for 1 hour, 3 hours and 14 hours.

After potentiostatic polarization, the specimens were examined under the optical microscope.

5.3.1 ANODIC POTENTIODYNAMIC POLARIZATION

The anodic potentiodynamic polarization curves of unpolished and mechanically polished NiP samples in near-neutral (pH 6-6.5) and acid (pH 1) solutions are shown in Figure 5.5. Three distinct potential ranges were observed. In the potential range from the OCP to about +0.2 V SCE, current density increased. A current arrest was observed in the -0.2 V to +0.2 V SCE potential range. Above +0.2 V SCE current density increased with increasing potential. No

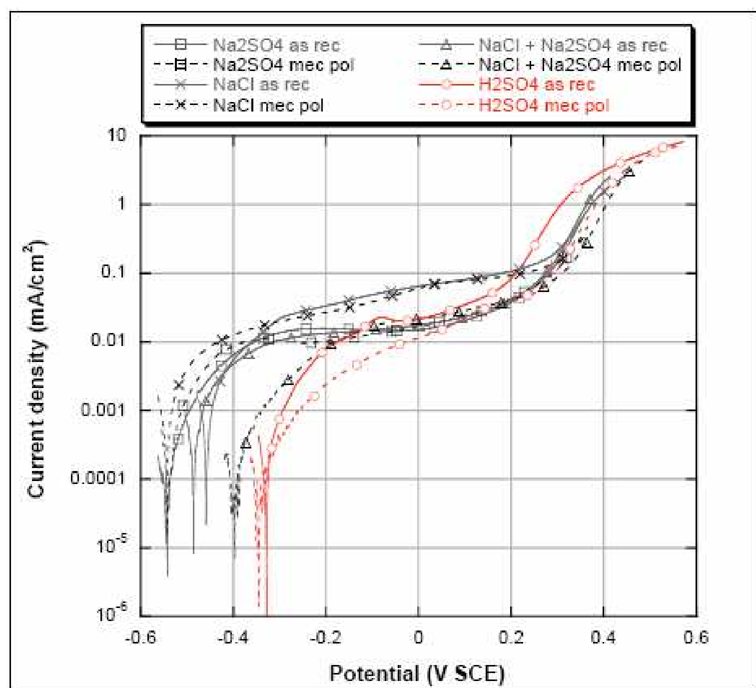

Figure 5.5 : Anodic potentiodynamic polarization curves of unpolished and mechanically polished NiP samples in near-neutral and acidic solutions.

significant difference was observed between unpolished and mechanically polished samples and between acid and near-neutral solutions. All the samples maintained their shiny appearance up to +0.2 V SCE, irrespective of solution pH and sample pre-treatment.

5.3.2 POTENTIOSTATIC POLARIZATION

Potentiostatic polarization curves of NiP specimens at -0.1 V and +0.1 V SCE in 0.1 M Na_2SO_4 are shown in Figure 5.6. Current decayed with a power law exponent ca.-0.5, indicating a diffusion controlled process. Current density increased slightly with polarization times. This behaviour was attributed to a kind of localized corrosion attack.

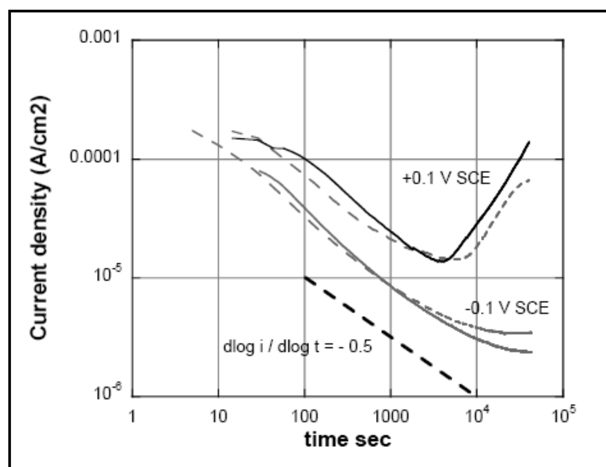

Figure 5.6 : Potentiostatic polarization curves of NiP samples at -0.1 V and +0.1 V SCE in 0.1 M Na_2SO_4.

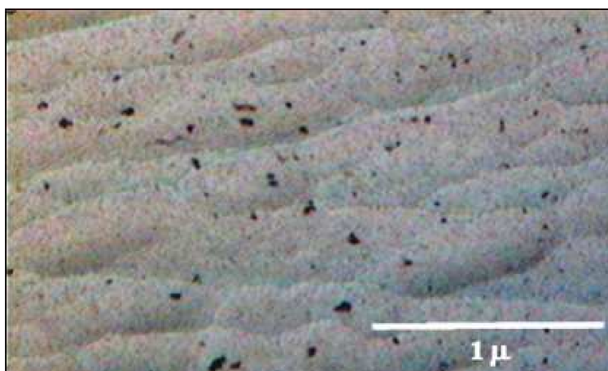

Figure 5.7 : Surface of a NiP sample, polarized at +0.1 V SCE for 3 hours in 0.1 M Na_2SO_4.

Specimen surface appeared morphologically unchanged at polarization times lower than that of the current density minimum. For longer polarization times, many corrosion spots appeared on the sample surface as shown in Figure 5.7, indeed their number increased with increasing polarization time.

5.4 XPS RESULTS

5.4.1 REFERENCE COMPOUNDS SPECTRA

5.4.1.1 HIGH-RESOLUTION SPECTRA OF THE $Ni2p_{3/2}$ REGION

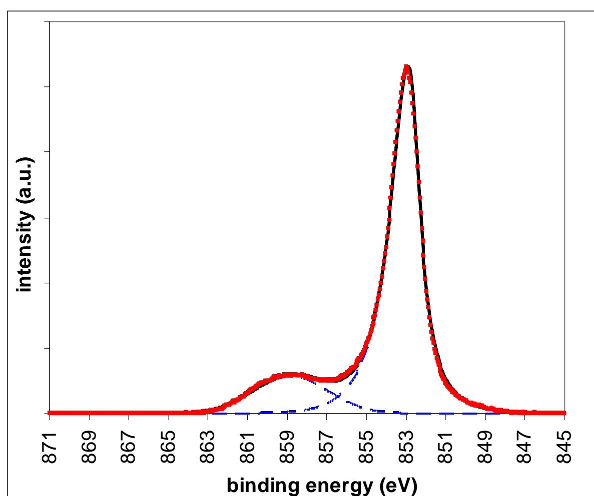

*Figure 5.8(**a**): high resolution $Ni2p_{3/2}$ spectrum acquired with ESCALAB 200 from pure metallic nickel foil.*

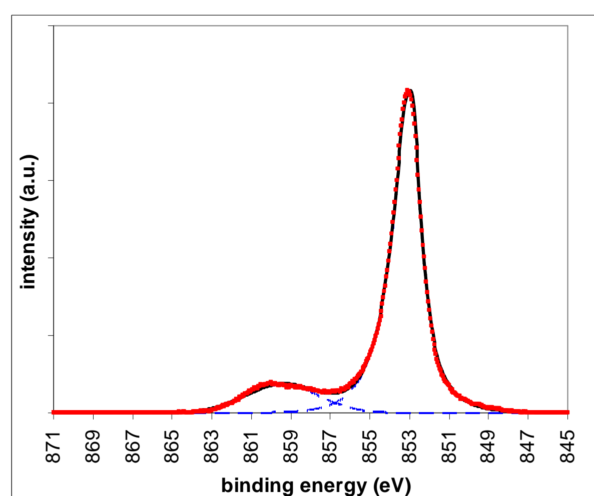

*Figure 5.8(**b**) : high resolution $Ni2p_{3/2}$ spectrum acquired with ESCALAB 200 from one of the sputtered NiP specimens studied in this work.*

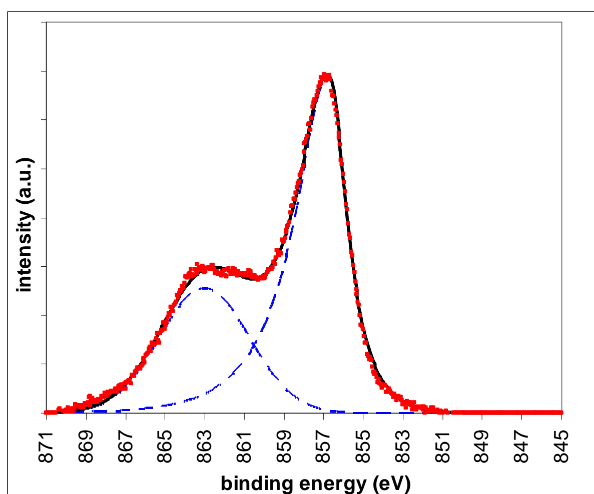

*Figure 5.8(**c**) : high resolution $Ni2p_{3/2}$ spectrum acquired with ESCALAB 200 from $Ni_3(PO_4)_2 \cdot 5H_2O$ pellet on conducting biadhesive tape.*

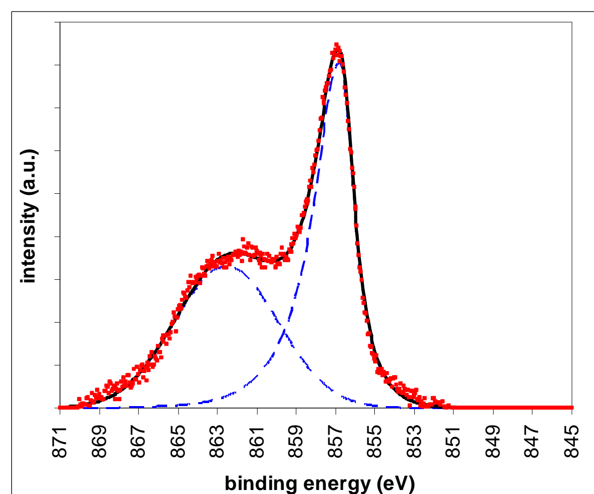

*Figure 5.8(**d**) : high resolution $Ni2p_{3/2}$ spectrum acquired with ESCALAB 200 from lump of pyrophosphate glass with composition $0.3NiO \cdot 0.35Na_2O \cdot 0.35P_2O_5$.*

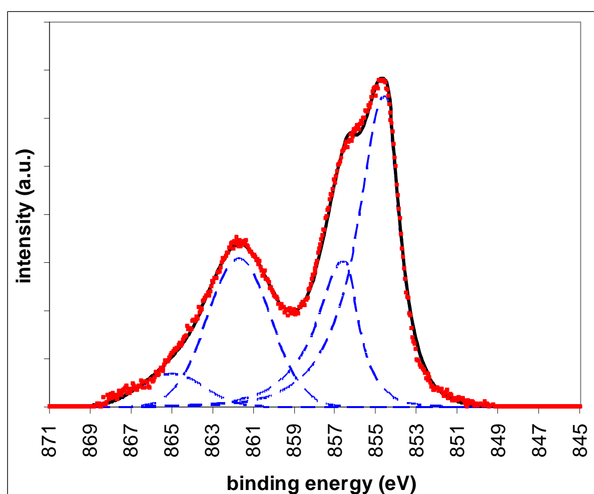

*Figure 5.8(**e**) : $Ni2p_{3/2}$ high resolution spectrum acquired with ESCALAB 200 on NiO lump.*

The $Ni2p_{3/2}$ spectrum of all the reference compounds, except the NiO, is the convolution of a main peak and a satellite at higher BE. The $Ni2p_{3/2}$ spectrum of the NiO is more complex. It is the convolution of four signals: the main peak (854.53 eV BE), a second

"main peak" due to multiplet splitting (856.55 eV BE), and two satellites (861.72 and 864.99 eV BE). Table 5.1 gives the fitting parameters of the Ni2p$_{3/2}$ spectral region of all the reference compounds examined.

Table 5.1 : Peak-fitting parameters of the Ni2p$_{3/2}$ region acquired from reference compounds with ESCALAB 200.

compound	component	BE (eV)	$BE_{sat.} - BE_{main\ peak}$ (eV)	FWHM (eV)	line shape	$A_{sat.}/A_{main\ peak}$
metallic nickel	*main peak*	*852.8$_5$*		*1.4*	*GL(97)T(1.3)*	
	satellite	*858.8$_4$*	*5.9$_9$*	*4.4*	*GL(0)*	*0.22*
etched NiP alloy	*main peak*	*852.9$_4$*		*1.3*	*GL(97)T(1.4)*	
	satellite	*859.4$_5$*	*6.5$_1$*	*4.4*	*GL(0)*	*0.18*
$Ni_3(PO_4)_2 \cdot 5H_2O$	*main peak*	*856.7$_0$*		*2.2*	*GL(89)T(1)*	
	satellite	*863.0$_0$*	*6.3$_0$*	*5.3*	*GL(0)*	*0.53*
Ni(II) Na pyrophosphate glass	*main peak*	*856.7$_7$*		*1.7*	*GL(92)T(1)*	
	satellite	*862.5$_6$*	*5.7$_9$*	*6.2*	*GL(0)*	*0.86*
NiO	*main peak*	*854.5$_3$*		*1.7*	*GL(90)T(1)*	
	multiplet splitting	*856.5$_5$*	*2.0$_2$*	*1.7*	*GL(90)T(1)*	*0.47*
	satellite 1	*861.7$_2$*	*7.1$_9$*	*3.6*	*GL(0)*	*0.60*
	satellite 2	*864.9$_9$*	*10.4$_6$*	*3.6*	*GL(0)*	*0.13*

5.4.1.2 HIGH RESOLUTION SPECTRA OF THE P2p AND THE PKLL REGIONS

Figure 5.9 shows the high resolution P2p spectra of the reference compounds acquired in this work with the ESCALAB 200. Figure 5.10 shows the corresponding high resolution PKLL spectra. P2p region of all the reference compounds is a doublet, due to spin-orbit coupling. The most intense component at the lower BE, corresponds to the quantic number of total angular momentum j = 3/2, while the least intense component at the higher binding energy, corresponds to j = 1/2. The area of the least intense peak was always constrained to be 1/2 of the most intense one, as stated by theoretical multiplicity of a 2p doublet.

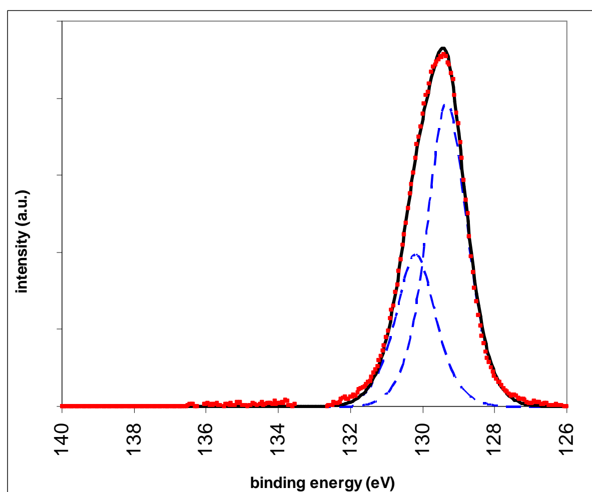

*Figure 5.9(**a**) : high resolution P2p spectrum acquired with ESCALAB 200 from red P lump.*

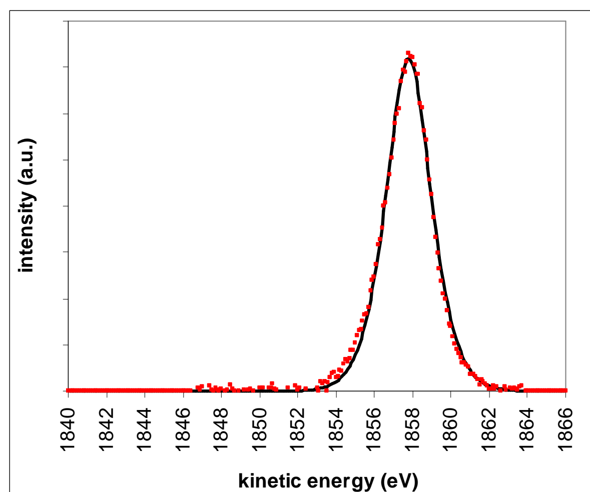

*Figure 5.10(**a**) : high resolution PKLL spectrum acquired with ESCALAB 200 from red P lump.*

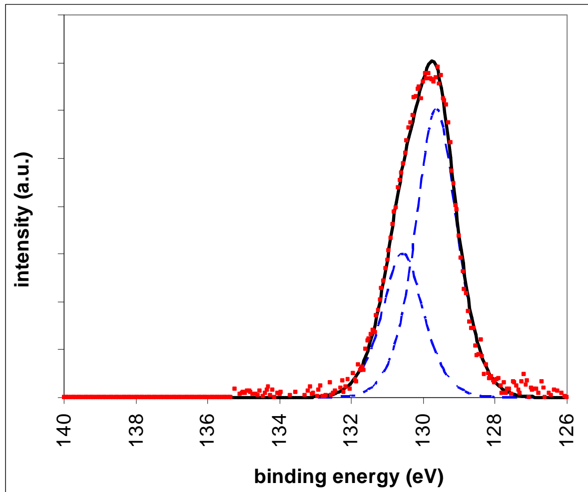

*Figure 5.9(**b**) : high resolution P2p spectrum acquired with ESCALAB 200 from one of the sputtered NiP specimens studied in this work.*

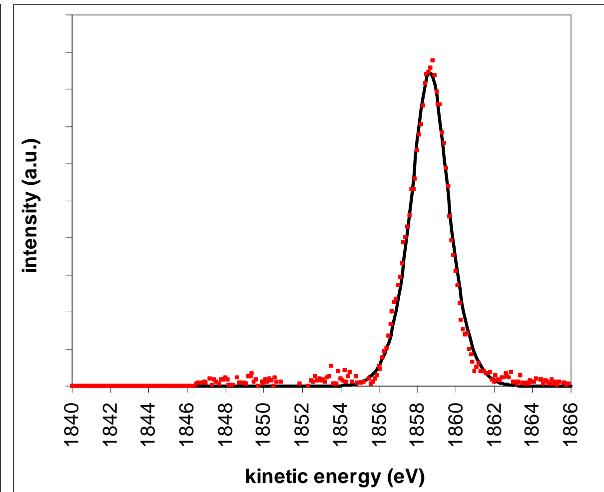

*Figure 5.10(**b**) : high resolution PKLL spectrum acquired with ESCALAB 200 from one of the sputtered NiP specimens studied in this work.*

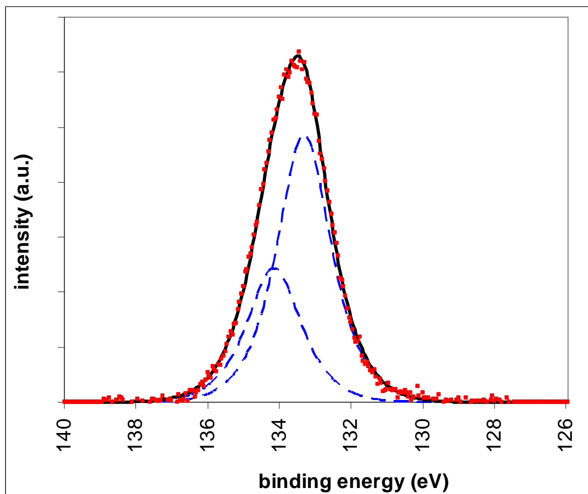

*Figure 5.9(**c**) : high resolution P2p spectrum acquired with ESCALAB 200 from $Ni_3(PO_4)_2 \cdot 5H_2O$ pellet on conducting biadhesive tape.*

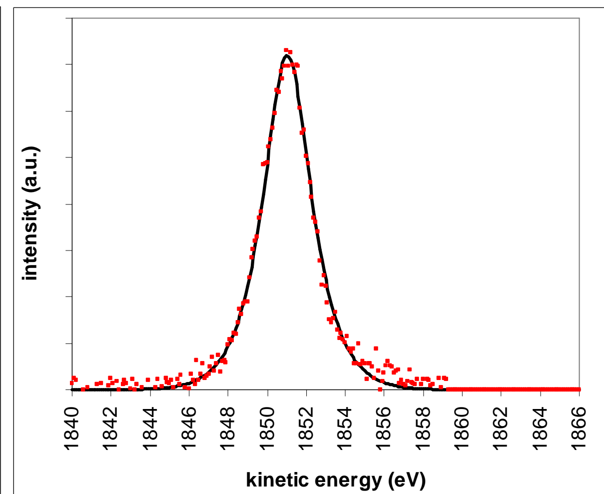

*Figure 5.10(**c**) : high resolution PKLL spectrum acquired with ESCALAB 200 from $Ni_3(PO_4)_2 \cdot 5H_2O$ pellet on conducting biadhesive tape.*

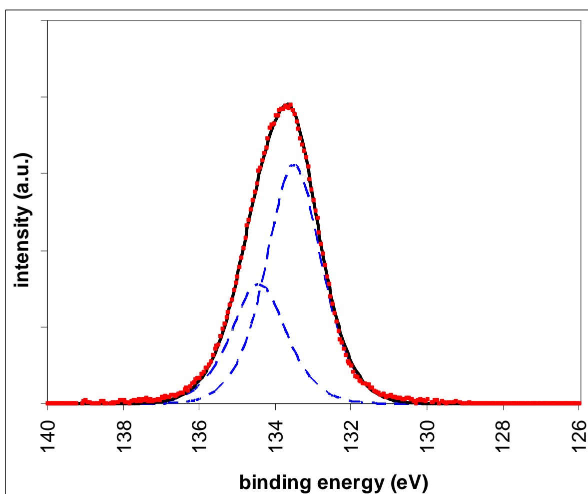

*Figure 5.9(**d**) : high resolution P2p spectrum acquired with ESCALAB 200 from lump of pyrophosphate glass with composition $0.3NiO \cdot 0.35Na_2O \cdot 0.35P_2O_5$.*

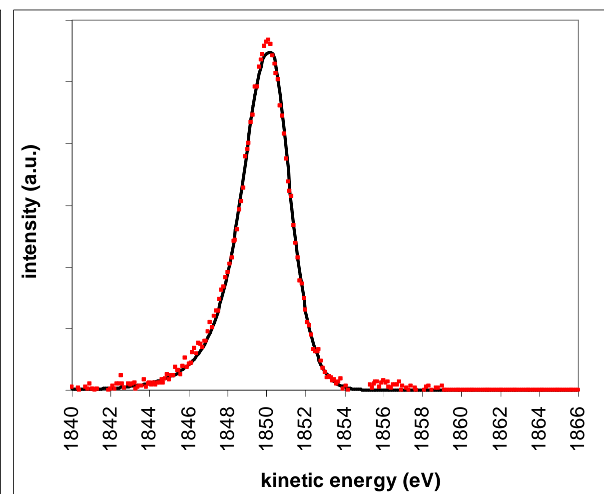

*Figure 5.10(**d**) : high resolution PKLL spectrum acquired with ESCALAB 200 from lump of pyrophosphate glass with composition $0.3NiO \cdot 0.35Na_2O \cdot 0.35P_2O_5$.*

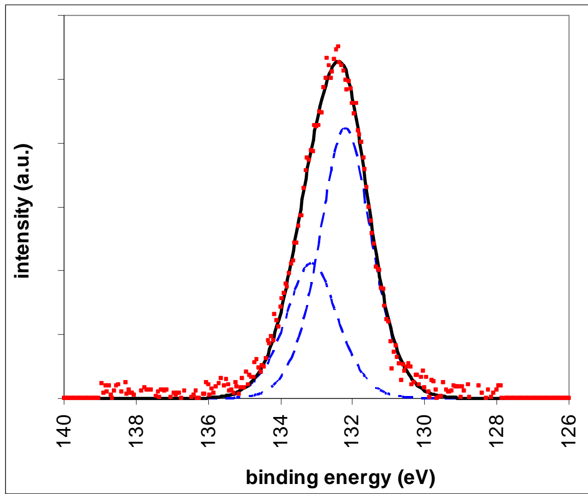

Figure 5.9(e) : P2p high resolution spectrum acquired with the ESCALAB 200 on a Na_3PO_4 pellet on a conducting biadhesive tape.

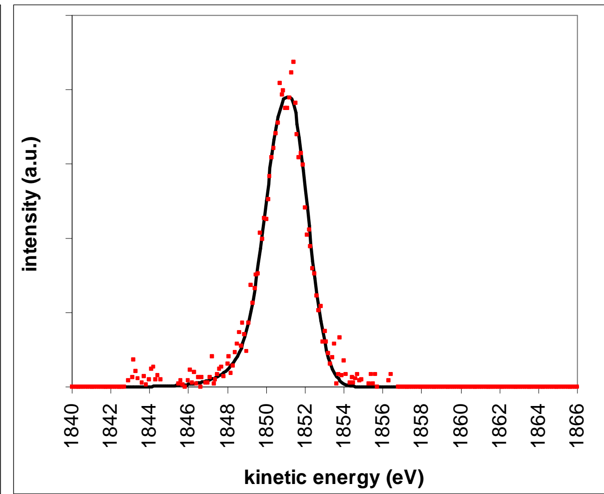

Figure 5.10(e) : high resolution PKLL spectrum acquired with ESCALAB 200 from Na_3PO_4 pellet on conducting biadhesive tape.

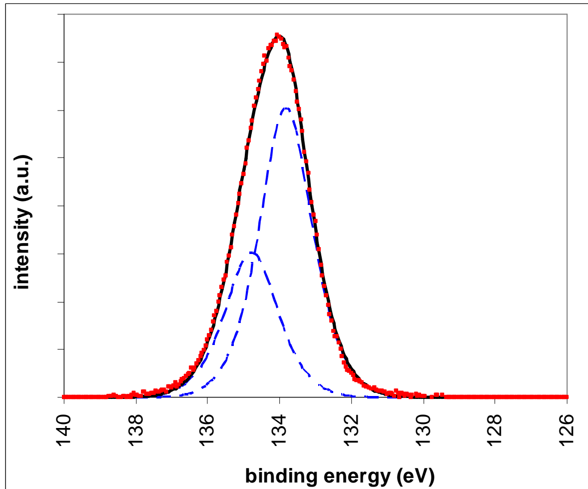

Figure 5.9(f) : high resolution P2p spectrum acquired with ESCALAB 200 from NaH_2PO_4 pellet on conducting biadhesive tape.

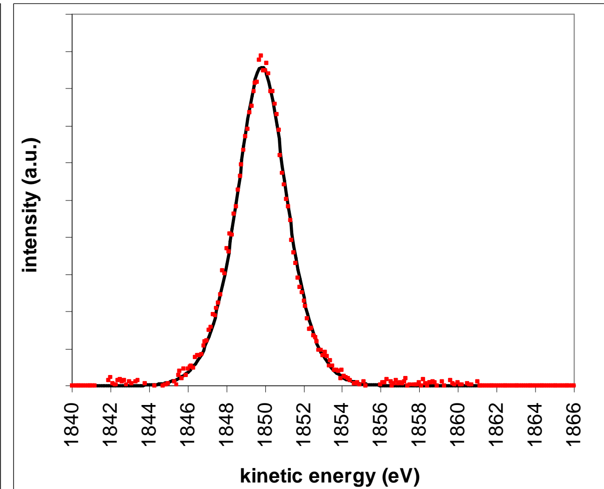

Figure 5.10(f) : high resolution PKLL spectrum acquired with ESCALAB 200 from NaH_2PO_4 pellet on conducting biadhesive tape.

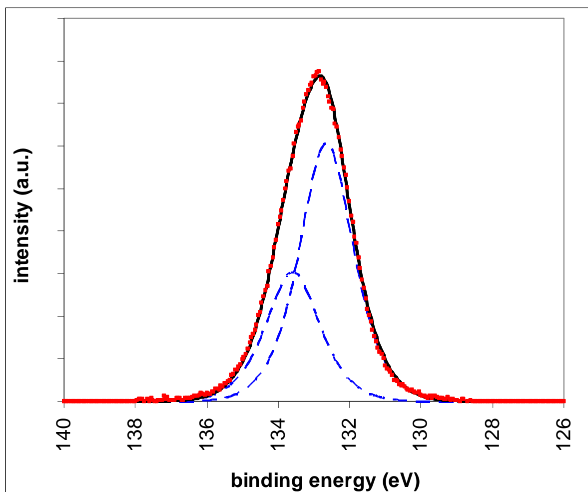

Figure 5.9(g) : P2p high resolution spectrum acquired with the ESCALAB 200 on a $NaH_2PO_2 \cdot H_2O$ pellet on a conducting biadhesive tape.

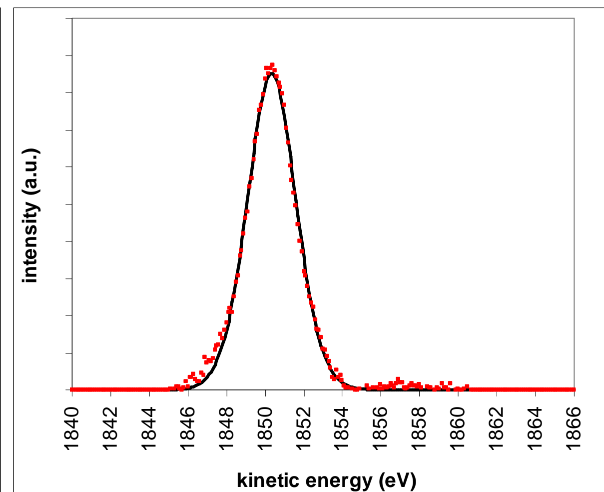

Figure 5.10(g) : PKLL high resolution spectrum acquired with the ESCALAB 200 on a $NaH_2PO_2 \cdot H_2O$ pellet on a conducting biadhesive tape.

Table 5.2 shows the fitting parameters of the P2p and PKLL spectral region of all the examined reference compounds together with the modified Auger parameters. The Auger parameter was calculated, for all the reference compounds, as the sum of $P2p_{3/2}$ BE and PKLL KE.

Table 5.2 : Peak-fitting parameters of P2p and PKLL regions acquired from reference compounds with the ESCALAB 200.

compound	peak	BE (eV)	KE(eV)	Δ BE ($P2p_{1/2}$ - $P2p_{3/2}$) (eV)	FWHM (eV)	line shape	α' (eV)
red P	$P2p_{3/2}$	129.3_1	1357.3_7	0.8_7	1.3	GL(60)	1987
	$P2p_{1/2}$	130.1_7	1356.5_0		1.3	GL(60)	
	PKLL	-371.1_6	1857.8_3		2.8	GL(60)	
etched NiP alloy	$P2p_{3/2}$	129.3_7	1357.3_0	0.8_4	1.5	GL(55)	1988
	$P2p_{1/2}$	130.2_1	1356.4_6		1.5	GL(55)	
	PKLL	-372.0_5	1858.7_2		2.3	GL(55)	
$Ni_3(PO_4)_2 \cdot 5H_2O$	$P2p_{3/2}$	133.3_4	1353.3_3	0.8_4	1.8	GL(75)	1984
	$P2p_{1/2}$	134.1_8	1352.4_9		1.8	GL(75)	
	PKLL	-364.4_1	1851.0_8		2.9	GL(80)	
Ni(II) Na pyrophosphate glass	$P2p_{3/2}$	133.5_5	1353.1_2	0.9_3	1.7	GL(60)	1984
	$P2p_{1/2}$	134.4_8	1352.1_9		1.7	GL(60)	
	PKLL	-363.6_0	1850.2_7		2.4	GL(60)T(1.5)	
Na_3PO_4	$P2p_{3/2}$	132.1_9	1354.4_8	0.9_4	1.7	GL(50)	1984
	$P2p_{1/2}$	133.1_3	1353.5_4		1.7	GL(50)	
	PKLL	-364.6_4	1851.3_1		2.3	GL(0)T(2)	
NaH_2PO_4	$P2p_{3/2}$	133.8_1	1352.8_6	0.9_5	1.7	GL(60)	1984
	$P2p_{1/2}$	134.7_6	1351.9_1		1.7	GL(60)	
	PKLL	-363.2_0	1849.8_7		3.0	GL(60)	
$NaH_2PO_2 \cdot H_2O$	$P2p_{3/2}$	132.6_6	1354.0_1	0.9_4	1.8	GL(65)	1983
	$P2p_{1/2}$	133.6_0	1353.0_7		1.8	GL(65)	
	PKLL	-363.7_3	1850.4_0		3.0	GL(30)	

5.4.1.3 HIGH RESOLUTION SPECTRA OF THE O1S REGION

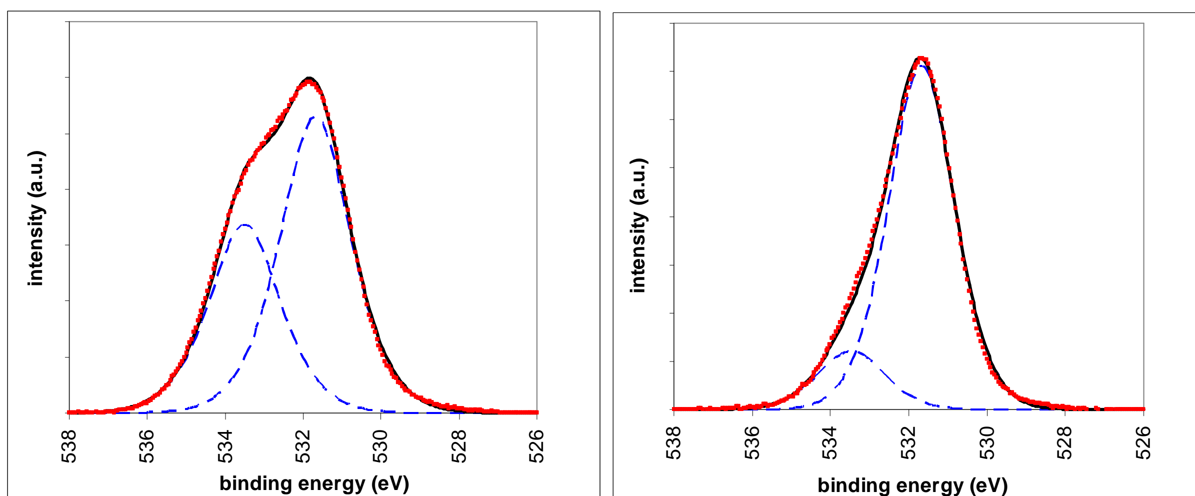

*Figure 5.11(**a**) : high resolution O1s spectrum acquired with ESCALAB 200 (Al kα) from $Ni_3(PO_4)_2 \cdot 5H_2O$ pellet on conducting biadhesive tape.*

*Figure 5.11(**b**) : high resolution O1s spectrum acquired with ESCALAB 200 (Mg kα) from lump of pyrophosphate glass with composition $0.3NiO \cdot 0.35Na_2O \cdot 0.35P_2O_5$.*

Figure 5.11(a) shows the high resolution spectrum of the O1s region acquired with Al kα radiation of the ESCALAB X-ray source on a $Ni_3(PO_4)_2 \cdot 5H_2O$ pellet. The most intense component at 531.7 eV was assigned to the oxygen of the phosphate, while the least intense component at 533.5 eV was assigned to the oxygen of the water. The intensity ratio of the most and the least intense component was found to be 1.6, as expected from the stoichiometry of this compound.

Figure 5.11(b) shows the high resolution spectrum of the O1s region acquired with Mg kα radiation of the ESCALAB X-ray source on a lump of a pyrophosphate glass with composition $0.3NiO \cdot 0.35Na_2O \cdot 0.35P_2O_5$. The most intense component at 531.6 eV was assigned to the non-bridging oxygen of the pyrophosphate chains, while the least intense component at 533.4 eV was assigned to the bridging oxygen of the pyrophosphate chains. The intensity ratio of the most and the least intense component was found to be 6.0. The line shape of all the components of both spectra was a product of the Gaussian and the Lorentzian function with a mixing ratio of 60; FWHM was 2.2.

5.4.2 POLARIZED NiP ALLOYS SPECTRA

The spectra acquisition was carried out on the NiP specimens, after different treatments:

A) Polarization at +0.1 V SCE in deaerated 0.1 M Na_2SO_4 for 1 hour

B) Polarization at +0.1 V SCE in deaerated 0.1 M Na_2SO_4 for 3 hours

C) Polarization at +0.1 V SCE in deaerated 0.1 M Na_2SO_4 for 14 hours

5.4.2.1 THE SURVEY SPECTRA

Figure 5.12 shows the survey spectrum of a NiP alloy after 1 hour polarization at +0.1 V SCE in 0.1 M Na_2SO_4 acquired with the ESCALAB 200. The characteristic signals of Ni, P, C and O with traces of Na were detected. Small Cu signals were also detected their intensity increasing with polarization time. No other significant difference was observed after 3 and 14 hours polarization.

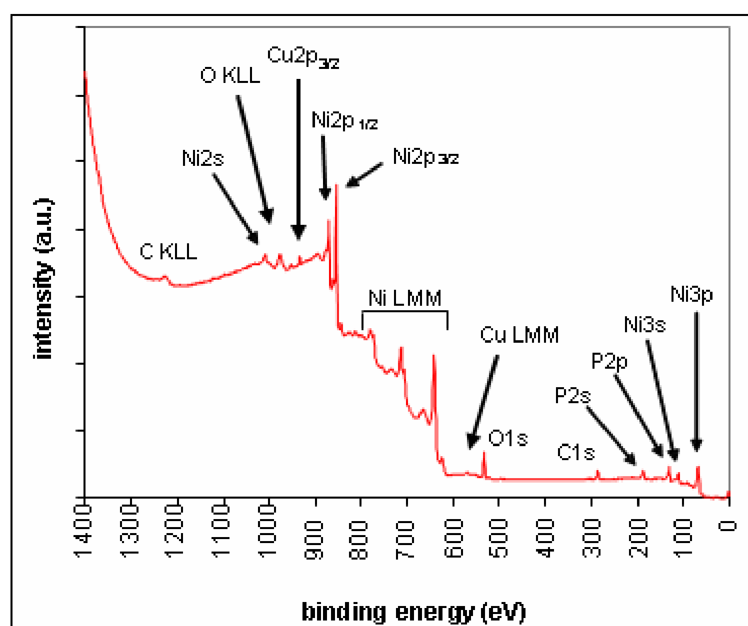

Figure 5.12 : Survey spectrum acquired with ESCALAB 200 from NiP alloy after 1 hour polarization at +0.1 V SCE in 0.1 M Na_2SO_4.

5.4.2.2 HIGH-RESOLUTION SPECTRA OF THE $Ni2p_{3/2}$ REGION

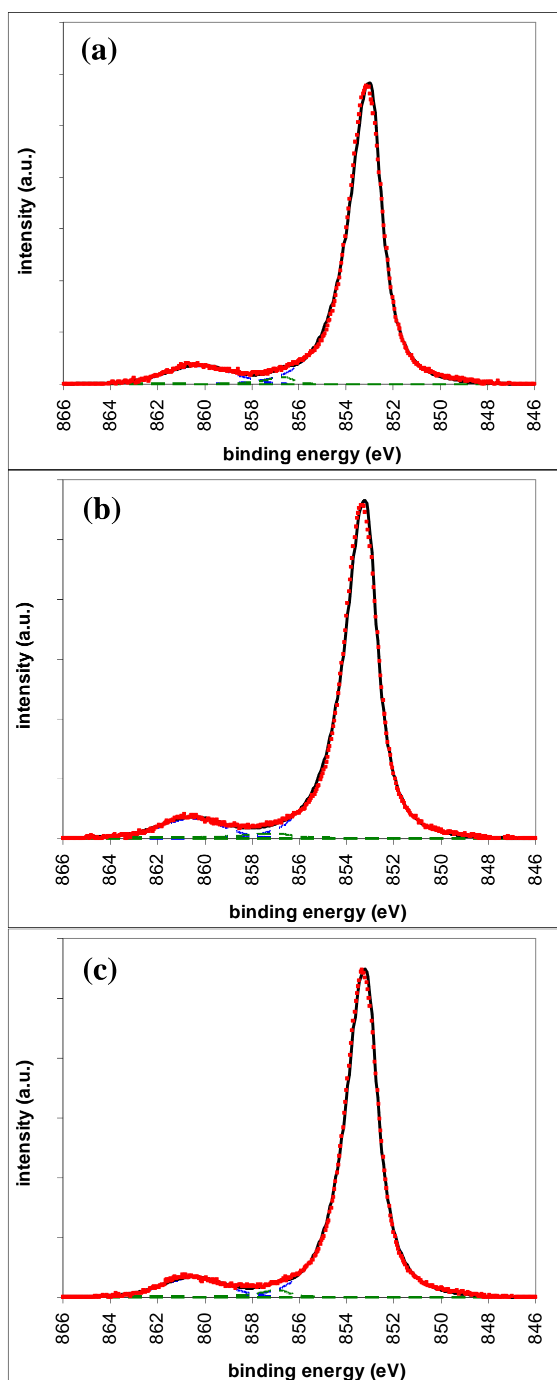

*Figure 5.13 : high resolution $Ni2p_{3/2}$ spectra acquired with ESCALAB 200 from NiP specimen polarized at +0.1 V SCE in 0.1 M Na_2SO_4 for **(a)** 1, **(b)** 3 and **(c)** 14 hours.*

Table 5.3 : Peak-fitting parameters of the $Ni2p_{3/2}$ region acquired with ESCALAB 200 from NiP alloys after 1, 3 and 14 hours polarization at +0.1 V SCE in 0.1 M Na_2SO_4.

	component				
	n.1 main peak	**n.1 satellite**	**n.2 main peak**	**n.2 satellite**	**Polari_ zation time (h)**
BE (eV)	853.0_0	860.3_2	856.9_8	863.1_9	1
	853.2_1	860.5_5	857.0_0	863.2_1	3
	853.2_0	860.5_0	857.0_0	863.2_1	14
Δ (BE$_{sat.}$ – - BE$_{main\ peak}$) (eV)	7.3_2		6.2_1		1
	7.3_4		6.2_1		3
	7.3_0		6.2_1		14
FWHM (eV)	1.2	3.1	1.8	4.3	1
					3
					14
line shape	GL(97) T(1.3)	GL(0)	GL(89) T(1)	GL(0)	1
					3
					14
A$_{sat.}$ / / A$_{main\ peak}$	0.09		0.42		1
	0.09		0.42		3
	0.09		0.42		14
A$_{tot}^{(comp.\ n.2)}$ / / A$_{tot}^{(comp.\ n.1)}$	0.04				1
	0.03				3
	0.03				14

After polarization at +0.1 V SCE in 0.1 M Na_2SO_4, the $Ni2p_{3/2}$ region of the NiP alloys shows two components (Figure 5.13). The most intense is located at ca. 853 eV with its satellite at ca. 860 eV . The other component is located at ca. 857 eV with one satellite at ca. 863 eV . No significant difference was observed between spectra acquired after 1, 3 and 14 hours polarization, either in peak position or relative intensity. Table 5.3 shows the peak fitting parameters for all three spectra, together with the intensity ratio between all the satellites and the corresponding main peaks. The table also gives the ratio between total intensity (i.e. main peak intensity plus satellite intensity) of the two components, for all three polarization times.

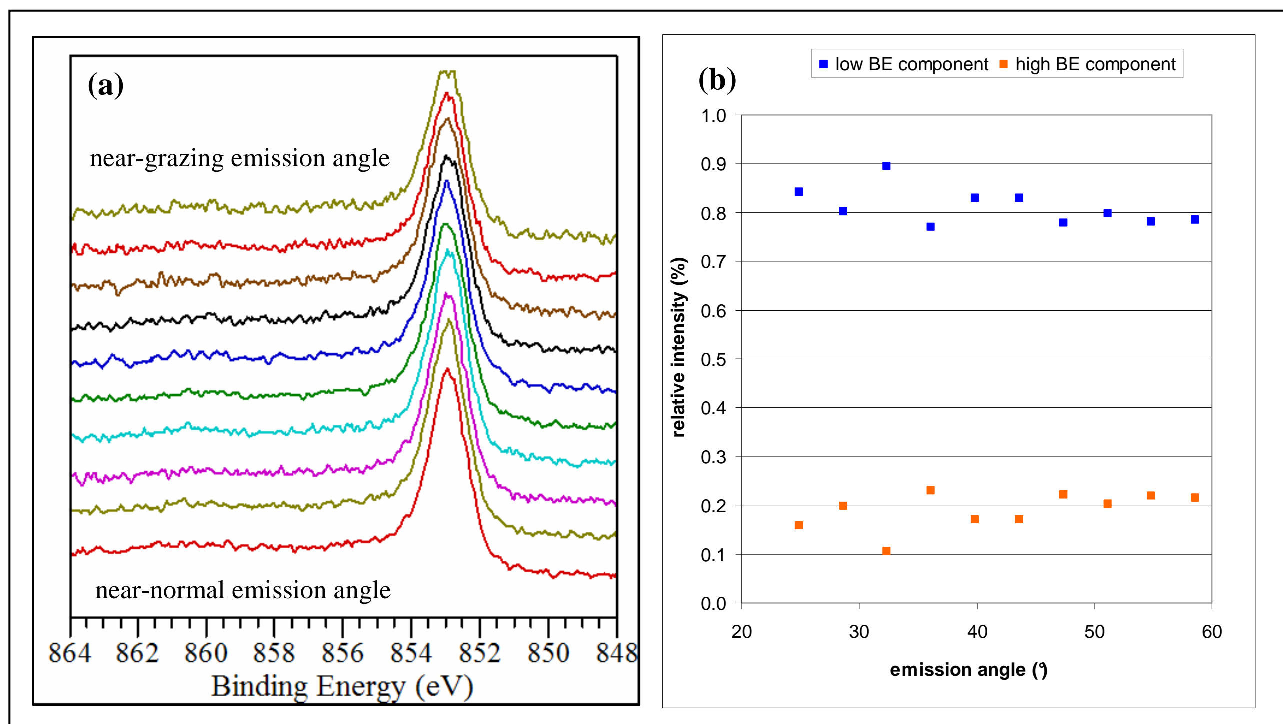

*Figure 5.14 : **(a)** high resolution Ni2p$_{3/2}$ spectra acquired Theta Probe in ARXPS acquisition mode from NiP specimen polarized at +0.1 V SCE in 0.1 M Na_2SO_4 for 1 hour. **(b)** Relative intensities vs. emission angle.*

Figure 5.14 (a) shows the angle-resolved high resolution spectra of the Ni2p$_{3/2}$ region acquired with the Theta Probe on a NiP sample polarized at +0.1 V SCE in a 0.1 M Na_2SO_4 solution for 1 hour. The relative intensity of the component at ca. 857 eV and of its satellite at ca. 863 eV were found to increase with emission angle (Figure 5.14 b). On the contrary, the relative intensity of the component at ca. 853 eV and of its satellite at ca. 860 eV were found to decrease with increasing emission angle (Figure 5.14 b). Exactly the same trend was observed for the spectra acquired on samples after 3 and 14 hours polarization. Curve fitting parameters are given in appendix B.

5.4.2.3 HIGH-RESOLUTION SPECTRA OF THE P2p AND THE PKLL REGIONS

After polarization at +0.1 V SCE in 0.1 M Na_2SO_4, the P2p region of the NiP alloys shows three components i.e. three doublets (Figure 5.15). Each doublet is due to the spin-orbit coupling: the most intense peak of the doublet corresponds to the quantic number of the total angular momentum j = 3/2 and is located at a lower BE than the least intense peak of the doublet, which corresponds to j = 1/2. The area of the least intense peak of each P2p doublet was always constrained to be 1/2 of the most intense one, as stated by theoretical multiplicity of a generic p-doublet.

After polarization at +0.1 V SCE in 0.1 M Na_2SO_4, the PKLL region of the NiP alloys also shows three components i.e. three singlets (Figure 5.16). No significant difference in peak position or relative intensity was observed between spectra acquired after 1, 3 and 14 hours polarization.

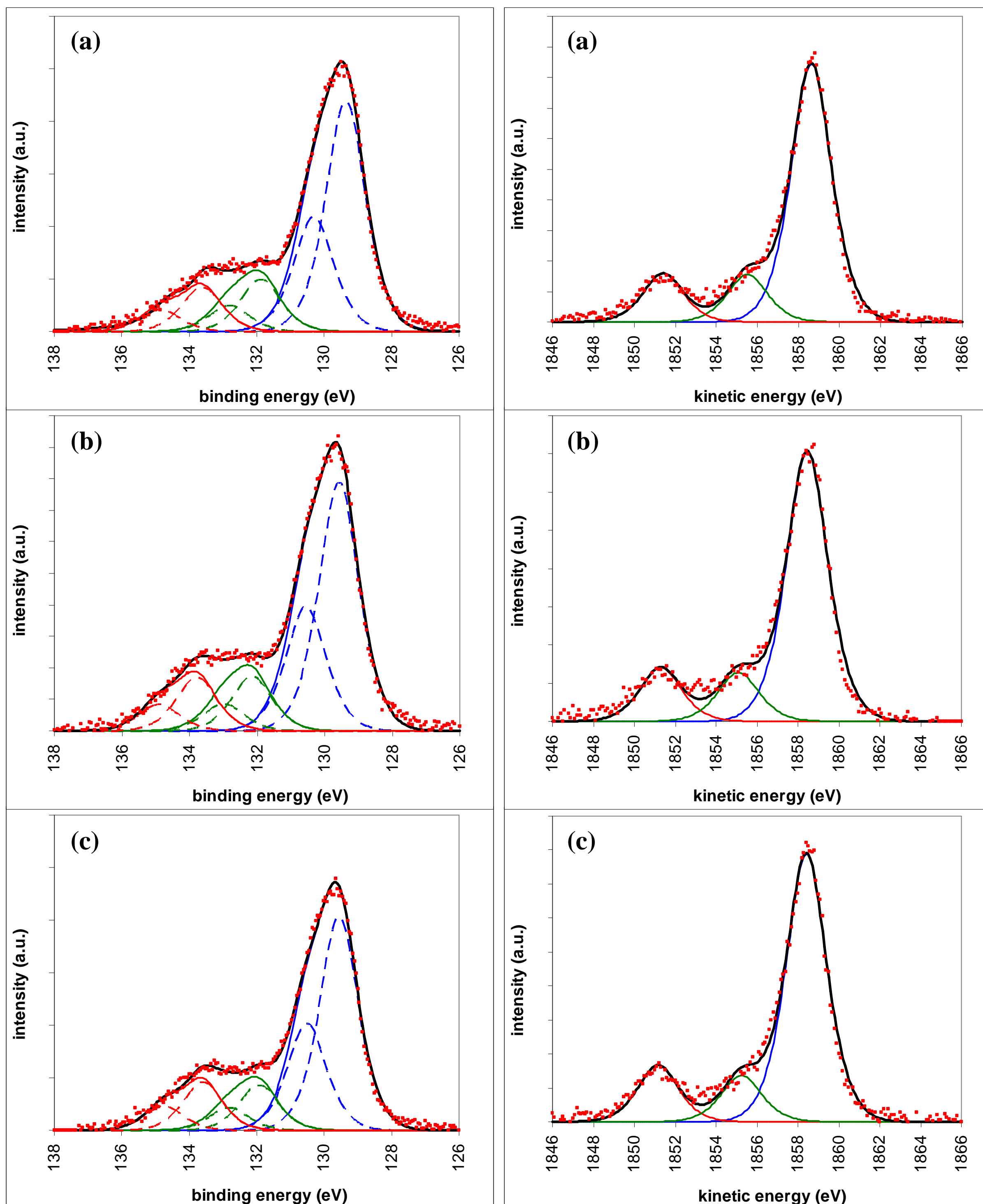

*Figure 5.15 : high resolution P2p spectra acquired with ESCALAB 200 from NiP specimen polarized at +0.1 V SCE in 0.1 M Na_2SO_4 for **(a)** 1, **(b)** 3 and **(c)** 14 hours.*

*Figure 5.16 : high resolution PKLL spectra acquired with ESCALAB 200 from NiP specimen polarized at +0.1 V SCE in 0.1 M Na_2SO_4 for **(a)** 1, **(b)** 3 and **(c)** 14 hours.*

Table 5.4 gives the peak-fitting parameters of both the P2p and the PKLL regions acquired with the ESCALAB 200 from the NiP alloys after 1, 3 and 14 hours polarization. The line shape of all the peaks was a product of the Gaussian and the Lorentzian function with a mixing ratio of 60. Table 5.4 also reports the calculated modified Auger parameters.

Table 5.4 : Peak-fitting parameters of the P2p and the PKLL region acquired with the ESCALAB 200 from the NiP alloys after 1, 3 and 14 hours polarization at +0.1 V SCE in 0.1 M Na_2SO_4, together with the calculated modified Auger parameters.

	P2p spectrum						**polarization time (h)**
	component n.1		**component n.2**		**component n.3**		
	$P2p_{3/2}$	**$P2p_{1/2}$**	**$P2p_{3/2}$**	**$P2p_{1/2}$**	**$P2p_{3/2}$**	**$P2p_{1/2}$**	
BE (eV)	129.3_5	130.3_0	131.8_6	132.7_6	133.5_7	134.7_4	1
	129.5_8	130.5_6	132.1_6	133.0_0	133.7_9	134.9_0	3
	129.5_6	130.5_1	131.9_4	132.8_2	133.6_0	134.7_5	14
KE (eV)	1357.3_2	1356.3_7	1354.8_1	1353.9_1	1353.1_0	1351.9_3	1
	1357.0_9	1356.1_1	1354.5_1	1353.6_7	1352.8_8	1351.7_7	3
	1357.1_1	1356.1_6	1354.7_3	1353.8_5	1353.0_7	1351.9_2	14
Δ BE ($P2p_{1/2}$ - $P2p_{3/2}$) (eV)	0.9_5		0.9_0		1.1_7		1
	0.9_8		0.8_4		1.1_1		3
	0.9_5		0.8_8		1.1_5		14
FWHM (eV)	1.4	1.4	1.4	1.4	1.4	1.4	1
							3
							14
$A(P2p_{1/2})$ / / $A(P2p_{3/2})$	0.50		0.50		0.50		1
	0.50		0.50		0.50		3
	0.50		0.50		0.50		14
component (doublet) relative area	0.71		0.15		0.13		1
	0.70		0.15		0.15		3
	0.70		0.15		0.16		14

	PKLL spectrum			**polarization time (h)**
	component n.1	**component n.2**	**component n.3**	
BE (eV)	-372.0_4	-368.9_1	-364.8_0	1
	-371.8_6	-368.4_9	-364.6_9	3
	-371.8_2	-368.6_4	-364.5_6	14
KE (eV)	1858.7_1	1855.5_8	1851.4_7	1
	1858.5_3	1855.1_6	1851.3_6	3
	1858.4_9	1855.3_1	1851.2_3	14
FWHM (eV)	2.3	2.3	2.3	1
				3
				14
component relative area	0.73	0.13	0.14	1
	0.72	0.13	0.14	3
	0.72	0.13	0.15	14

	modified Auger parameter (eV)			polarization time (h)
	component n.1	**component n.2**	**component n.3**	
	1988.1	*1987.4*	*1985.0*	*1*
	1988.1	*1987.3*	*1985.2*	*3*
	1988.1	*1987.3*	*1984.8*	*14*

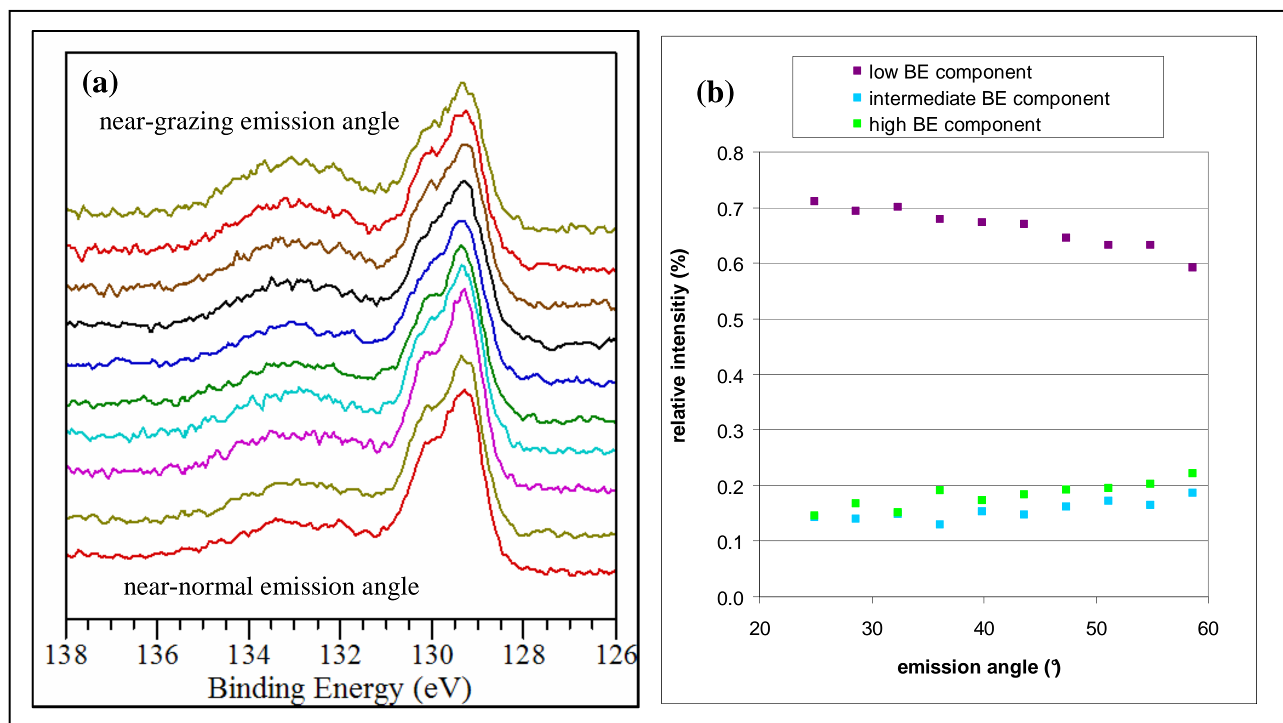

*Figure 5.17 : (**a**) P2p high resolution spectra acquired with the Theta Probe in the ARXPS acquisition mode from NiP specimen polarized at +0.1 V SCE in 0.1 M Na_2SO_4 for 1 hour. (**b**) Relative intensity vs. emission angle.*

Figure 5.17 (a) shows the angle-resolved high resolution spectra of the P2p region recorded with the Theta Probe for a NiP sample polarized at +0.1 V SCE in a 0.1 M Na_2SO_4 solution for 1 hour. The relative intensity of the doublet at the lower binding energy (ca. 130 eV) was found to decrease with increasing emission angle (Figure 5.17 b). On the contrary, relative intensity of the doublet at the higher binding energy (ca. 134 eV) was found to increase with emission angle (Figure 5.17 b). Finally, the relative intensity of the doublet at the intermediate binding energy (ca. 132 eV) was found to increase slightly with increasing emission angle (Figure 5.17 b). Exactly the same trend was observed for the spectra acquired from samples after 3 and 14 hours polarization. Curve fitting parameter are given in appendix B.

5.4.2.4 HIGH-RESOLUTION SPECTRA OF THE O1S REGION

After polarization at +0.1 V SCE in 0.1 M Na_2SO_4, the O1s region of the NiP alloys shows three components i.e. three singlets (Figure 5.18). No significant difference in peak position or their relative intensity was observed between spectra acquired after 1 and 3 hours polarization. After 14 hours polarization, relative intensity of the most intense peak at ca. 531 eV was found to increase significantly, while the peak at ca. 533 eV was found to decrease. Table 5.5 gives the peak-fitting parameters for all three components acquired with the ESCALAB 200 after 1, 3 and 14 hours polarization. Line shape was always GL(60).

Table 5.5 : Peak-fitting parameters of the O1s region acquired with the ESCALAB 200 from NiP alloys after 1, 3 and 14 hours polarization at +0.1 V SCE in 0.1 M Na_2SO_4.

	component of the O1s spectrum			**polari_ zation time(h)**
	n.1	**n.2**	**n.3**	
BE (eV)	*531.3_4*	*532.7_4*	*535.0_0*	*1*
	531.6_0	*533.1_0*	*535.0_0*	*3*
	531.5_4	*532.8_6*	*535.0_0*	*14*
KE (eV)	*955.3_3*	*953.9_3*	*951.6_7*	*1*
	955.0_7	*953.5_7*	*951.6_7*	*3*
	955.1_3	*953.8_1*	*951.6_7*	*14*
FWHM (eV)	*2.2*	*2.2*	*2.4*	*1*
				3
				14
relative area	*0.55*	*0.40*	*0.05*	*1*
	0.51	*0.41*	*0.08*	*3*
	0.60	*0.31*	*0.09*	*14*

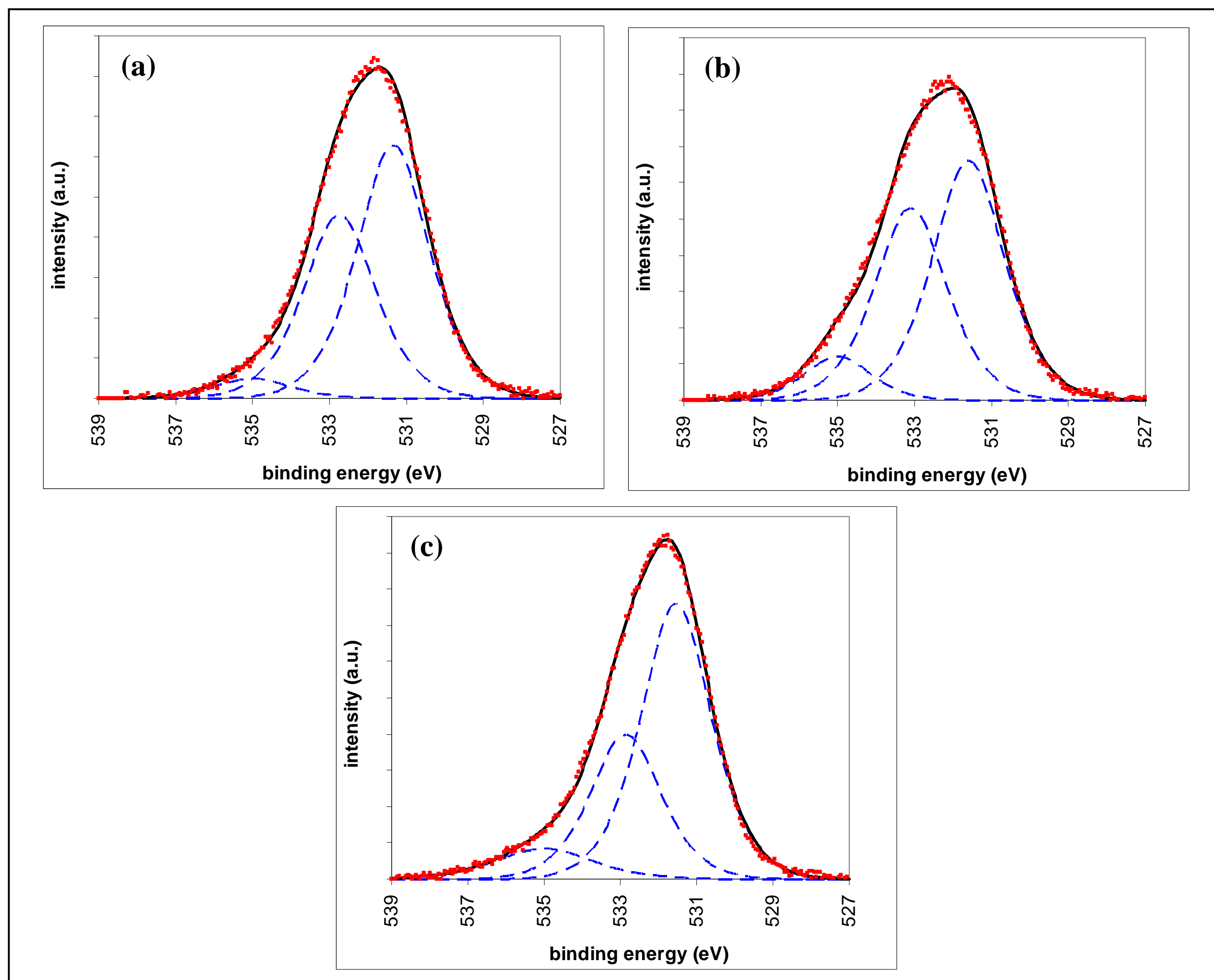

*Figure 5.18 : high resolution O1s spectra acquired with ESCALAB 200 from NiP specimen polarized at +0.1 V SCE in 0.1 M Na_2SO_4 for **(a)** 1, **(b)** 3 and **(c)** 14 hours.*

Figure 5.19 (a) shows the angle-resolved high resolution spectra of the O1s region recorded with the Theta Probe for a NiP sample polarized at +0.1 V SCE in a 0.1 M Na_2SO_4 solution for 1 hour. The relative intensity of the component at the lower binding energy (ca. 531 eV) was found to decrease slightly with increasing emission angle (Figure 5.19 b), while the relative intensity of the component at the intermediate binding energy (ca. 533 eV) was found to increase slightly with emission angle (Figure 5.19 b). Finally, the relative intensity of the component at the higher binding energy (ca. 535 eV) was found to increase with emission angle (Figure 5.19 b). Exactly the same trend was observed for the spectra acquired from samples after 3 and 14 hours polarization. Curve fitting parameters are given in appendix B.

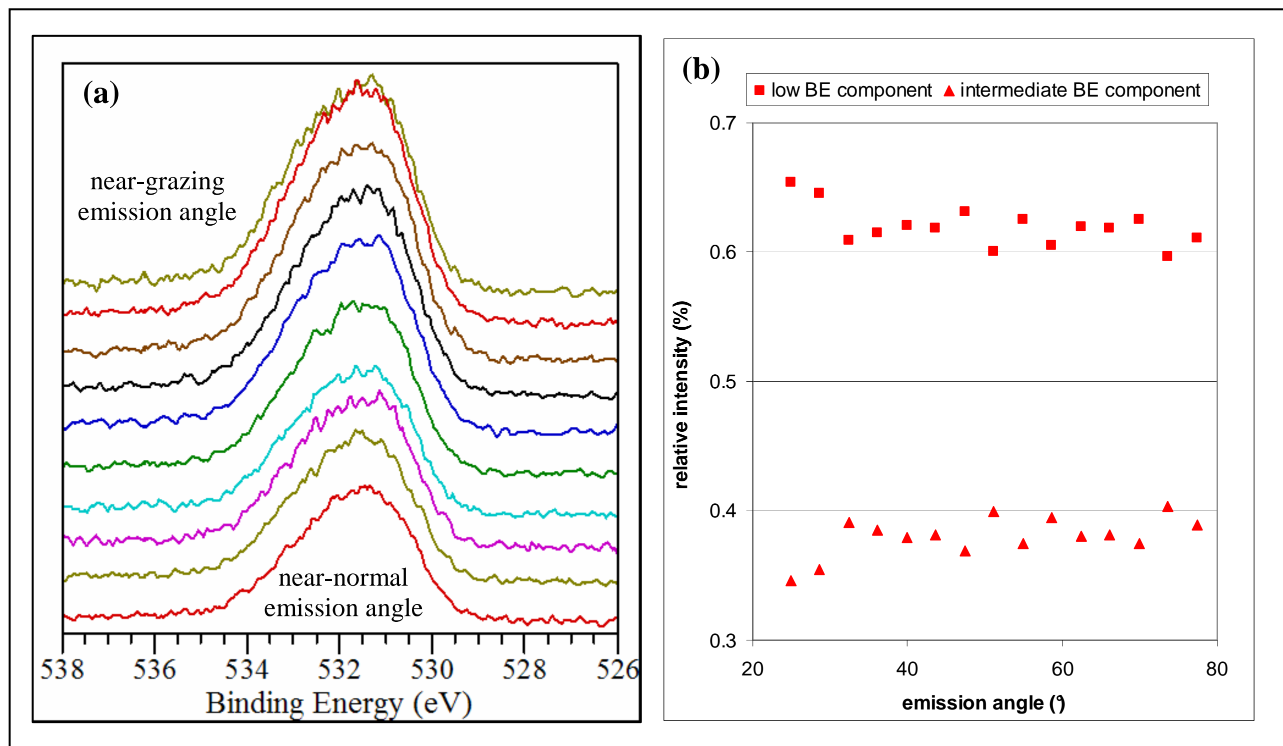

*Figure 5.19 : **(a)** O1s high resolution spectra acquired with the Theta Probe in the ARXPS acquisition mode on a NiP specimen polarized at +0.1 V SCE in 0.1 M Na_2SO_4 for 1 hour. **(b)** Relative intensity vs. emission angle.*

5.4.2.5 HIGH-RESOLUTION SPECTRA OF C1S REGION

After polarization at +0.1 V SCE in 0.1 M Na_2SO_4, the C1s region of the NiP alloys shows three components i.e. three singlets (Figure 5.20). Table 5.6 gives the peak-fitting parameters for all three peaks acquired with the ESCALAB 200 after 1, 3 and 14 hours polarization. Line shape was always a Gaussian and Lorentzian product function with mixing ratio of 60. No significant difference in peak position or relative intensity was observed between spectra acquired after 1, 3 and 14 hours polarization.

Table 5.6 : Peak-fitting parameters of C1s region acquired with the ESCALAB 200 from NiP alloys after 1, 3 and 14 hours polarization at +0.1 V SCE in 0.1 M Na_2SO_4.

	component of the C1s spectrum			polarization time (h)
	n.1	**n.2**	**n.3**	
BE (eV)	284.6_4	286.4_5	288.5_8	1
	284.9_9	286.8_1	288.7_9	3
	284.8_2	286.4_2	288.4_7	14
KE (eV)	1202.0_3	1200.2_2	1198.0_9	1
	1201.6_8	1199.8_6	1197.8_8	3
	1201.8_5	1200.2_5	1198.2_0	14
FWHM (eV)	1.8	1.8	1.8	1
				3
				14
relative area	0.76	0.15	0.09	1
	0.74	0.18	0.08	3
	0.76	0.16	0.08	14

*Figure 5.20 : high resolution C1s spectra acquired with ESCALAB 200 from a NiP specimen polarized at +0.1 V SCE in 0.1 M Na_2SO_4 for **(a)** 1, **(b)** 3 and **(c)** 14 hours.*

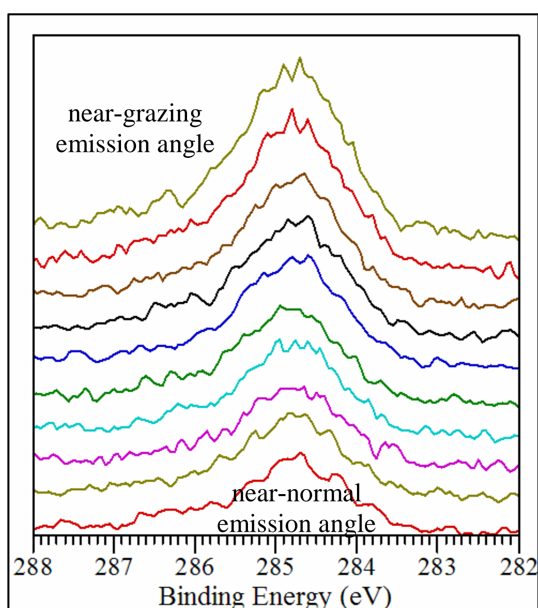

Figure 5.21 : high resolution C1s spectra acquired with Theta Probe in ARXPS acquisition mode from NiP specimen polarized at +0.1 V SCE in 0.1 M Na_2SO_4 for 1 hour.

Figure 5.21 shows the angle-resolved high resolution spectra of the C1s region recorded with the Theta Probe for a NiP sample polarized at +0.1 V SCE in a 0.1 M Na_2SO_4 solution for 1 hour. The relative intensity of the three components did not vary significantly with increasing emission angle. Exactly the same trend was observed for the spectra recorded for samples after 3 and 14 hours polarization. Curve fitting parameters are given in appendix B.

5.4.3 ION ETCHING KINETICS

5.4.3.1 KINETICS 1

An electrodeposited Ni-29P specimen was mechanically polished and immediately transferred to the Theta Probe analysis chamber. Ion etching was performed for a total of 300 s. Survey and high-resolution spectra of Ni2p3/2 , P2p , O1s and C1s were recorded at etching time intervals of 30 s. After the first step (30 s etching), the high BE component of the $Ni2p_{3/2}$ region was completely removed (Figure 5.22) and low BE component intensity increased; the highest and intermediate BE components of the P2p region were completely removed (Figure 5.23) intensity of the lowest BE component increasing. All the components of C1s and O1s regions were also completely removed.

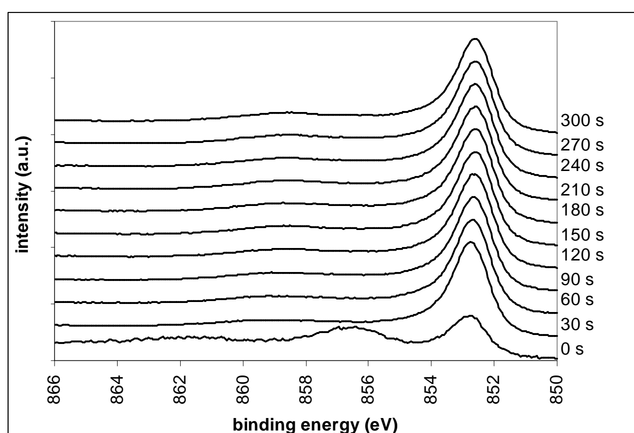

Figure 5.22 : high-resolution $Ni2p_{3/2}$ spectra from Ni-29P alloy for 30 s etching time steps, from 0 to 300 s, at 3 kV and 1 μA.

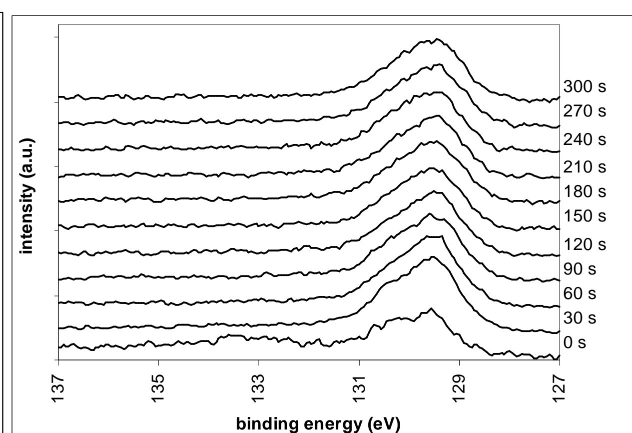

Figure 5.23 : high-resolution P2p spectra from Ni-29P alloy for 30 s etching time steps, from 0 to 300 s, at 3 kV and 1 μA.

Figure 5.24 shows $Ni2p_{3/2}$ and P2p intensity versus etching time. From 30 to ca. 120 s, $Ni2p_{3/2}$ intensity increases with etching time; on the contrary, P2p intensity decreases during the same etching interval. At longer etching times, intensity of both $Ni2p_{3/2}$ and P2p reaches a plateau. Application of the First principles method of quantification to these data shows that the surface alloy composition changes with increasing etching time (Figure 5.25). P content of the alloy decreases with increasing etching time, until surface alloy composition becomes stationary at ca. 120 s. However, P content is equal to 23.7 at.% at 30 s, yielding a relative error of ca. 18% with respect to the expected value of 29 at.%.

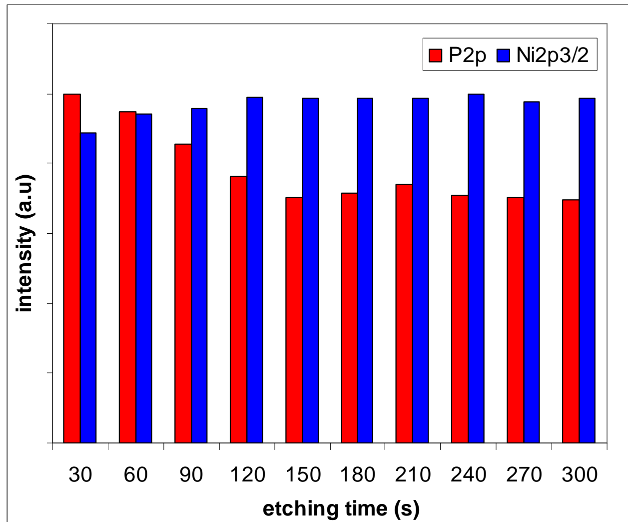

Figure 5.24 : Ni2p$_{3/2}$ and P2p intensity of Ni-29P alloy vs. etching time (30÷300 s) , at 3 kV and 1 μA.

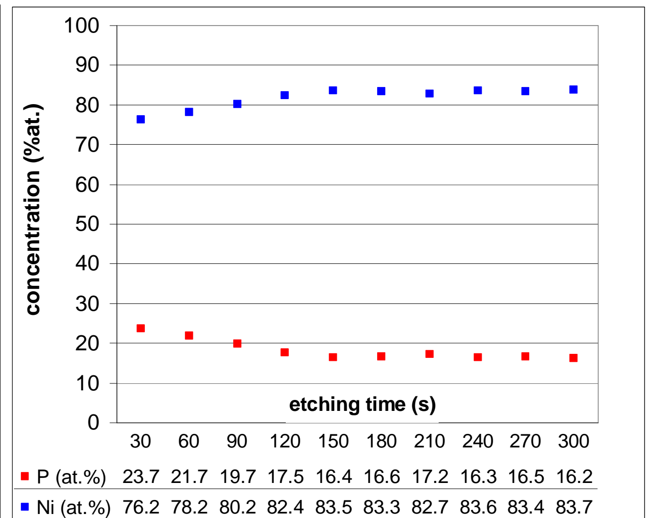

Figure 5.25 : Ni-29P alloy surface composition vs. etching time (30÷300 s) , at 3 kV and 1 μA.

5.4.3.2 KINETICS 2

A second surface point was chosen on the same specimen used for the first kinetics run. This second point was chosen at an appropriate distance from the first so as to perform the second run on a fresh surface area. Ion etching was performed for a total of 30 s. Survey and high-resolution spectra of Ni2p$_{3/2}$, P2p , O1s and C1s were recorded after every 5 s sputtering. After the first step (5 s etching), the high BE component of the Ni2p$_{3/2}$ region was completely removed (Figure 5.26) and the intensity of the low BE component increased. The components at ca. 132 eV and at ca. 134 eV of the P2p region were completely removed (Figure 5.27) while the intensity of the component at ca. 130 eV increased. After the first step (5 s etching), C was completely removed. After the second step (10 s etching), O was completely removed too.

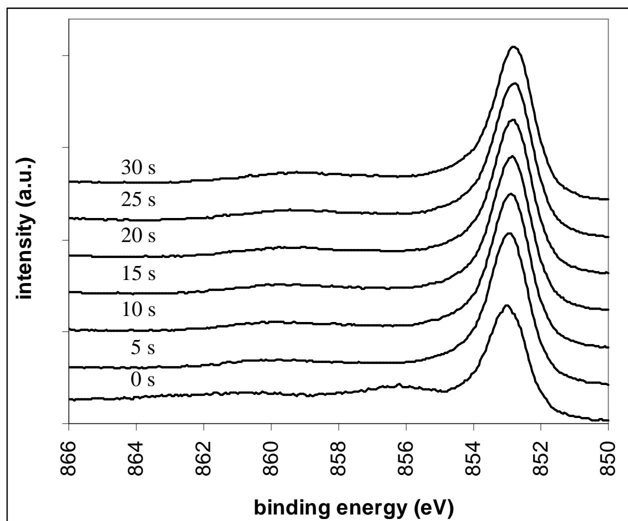

Figure 5.26 : high-resolution Ni2p$_{3/2}$ spectra from Ni-29P alloy for 5 s etching time steps, from 0 to 30 s, at 3 kV and 1 μA.

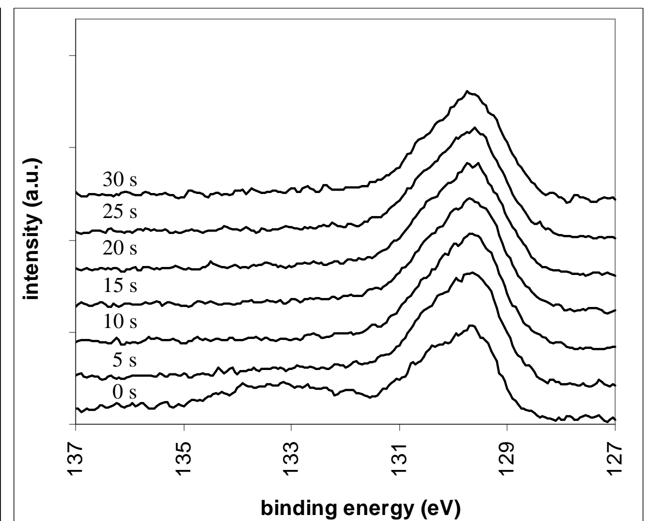

Figure 5.27 : high-resolution P2p spectra from a Ni-29P alloy for 5 s etching time steps, from 0 to 30 s, at 3 kV and 1 μA.

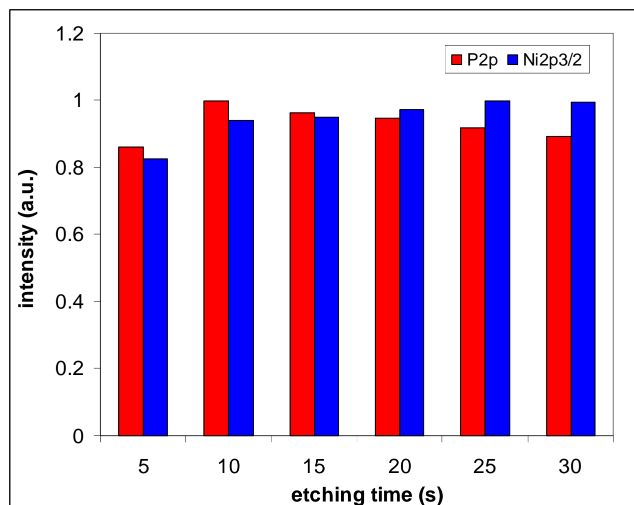

Figure 5.28 : Ni2p$_{3/2}$ and P2p intensity of Ni-29P alloy vs. etching time (5÷30 s) , at 3 kV and 1 μA.

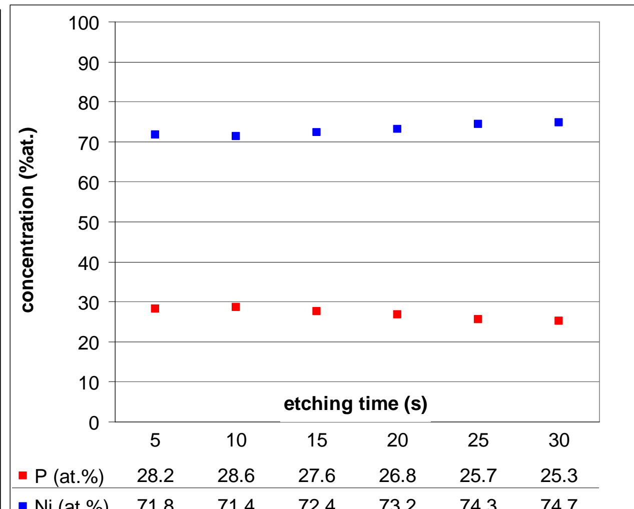

Figure 5.29 : Ni-29P alloy surface composition vs. etching time (5÷30 s) , at 3 kV and 1 μA.

Figure 5.28 shows Ni2p$_{3/2}$ and P2p intensity versus etching time. From 5 to 10 s, P2p intensity increases, while it decreases at longer etching times. On the other hand, Ni2p$_{3/2}$ intensity increases with etching time over the entire range examined. Application of the first principles method for the quantification of these data shows that surface alloy composition changes with increasing etching time (Figure 5.29). P content of the alloy reached a maximum after 10 s etching, equal to 28.6 at.%. Relative error is $< 2\%$ with respect to the expected value of 29 at.%.

5.4.3.3 KINETICS 3

Another electrodeposited Ni-29P specimen was mechanically polished and immediately transferred to the Theta Probe analysis chamber. Ion etching kinetics run 3 was performed in exactly the same way as for kinetics run 2. The results of the third run were in a very good agreement with the second one. After 10 s etching, carbon and oxygen were completely removed from the sample surface and the high BE components of both the Ni2p$_{3/2}$ and P2p spectra also disappeared. The lowest BE P2p component reached a maximum intensity after 10 s etching time corresponding to a P content of 29.1 at.%. This result is in excellent agreement with the expected value.

5.4.4 FIRST PRINCIPLES METHOD OF QUANTIFICATION

The first principles method for quantification was applied to determine the surface composition of the electroless deposited NiP alloys after ion etching. P content was 18 ± 2 at.% , where concentration uncertainty was calculated as three times the standard deviation of three independent determinations.

5.4.5 TOUGAARD'S METHOD OF QUANTIFICATION AND IN-DEPTH PROFILING

5.4.5.1 THE ANALYZE APPROACH

The "Analyze" approach was used to analyze etched NiP survey spectra for determining surface composition of the electroless deposited NiP alloys. Figure 5.30 (a) shows the Ni2p region of a pure metallic nickel survey spectrum. The Ni2p region is shown together with its inelastic background and the spectrum resulting from inelastic background subtraction, i.e. the reference spectrum for Tougaard's analyze approach to the same spectral region acquired from the etched NiP specimens. Inelastic background was calculated using the depth profile model shown in Figure 5.30 (b), which represents a pure Ni sample.

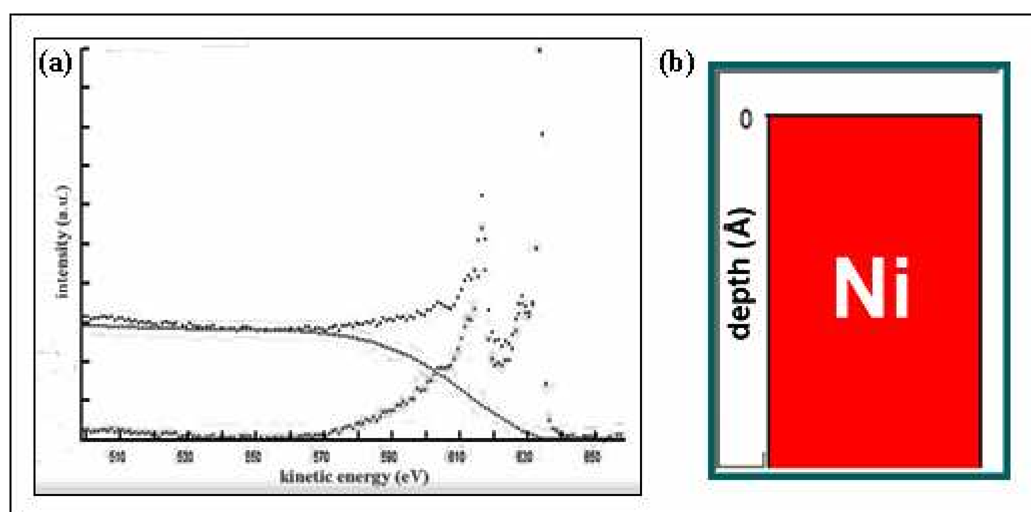

*Figure 5.30 : (**a**) Inelastic background analysis of Ni2p region, isolated from survey spectra from pure Ni foil. (**b**) Depth profile model of pure Ni sample.*

Then, the resulting Ni2p spectrum was used as reference for applying Tougaard's analyze approach to the Ni2p region of the etched NiP specimen survey spectra. Figure 5.31 (a) shows an example. After background removal, the Ni2p region of the etched NiP alloy is superimposed on the reference spectrum. They are in very good agreement. The inelastic background of the Ni2p region of etched NiP alloy, was calculated using the depth profile model shown in Figure 5.31 (b), which represents a surface region where Ni is homogeneously distributed down to a depth greater than XPS sampling depth, but Ni content is not 100 at.%. Phosphorus was calculated as the difference. P content of the electroless deposited NiP alloys surface was 13 ± 8 at.% , where concentration uncertainty was calculated as three times the standard deviation of three independent determinations.

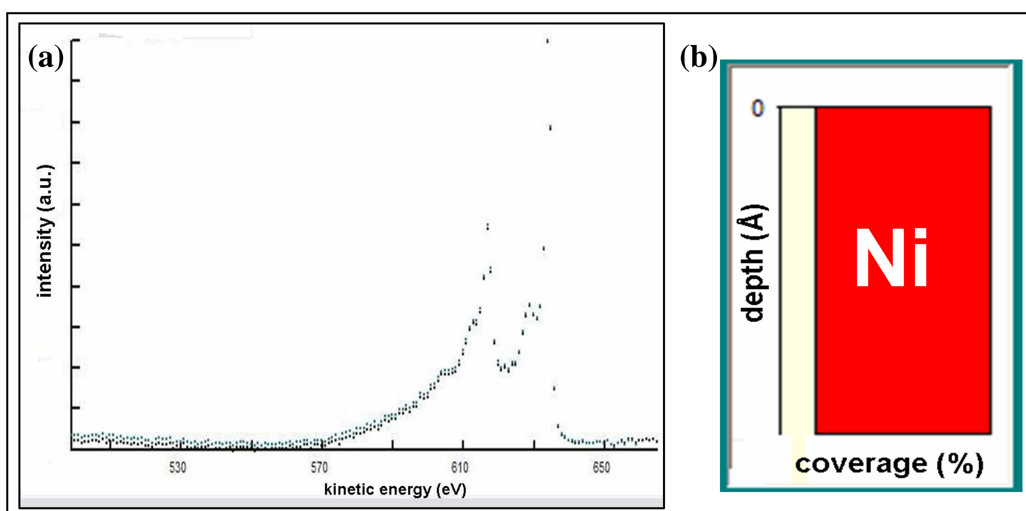

*Figure 5.31 : (**a**) Inelastic background analysis of Ni2p region, isolated from survey spectra from an electroless NiP specimen after ion etching. (**b**) Depth profile model.*

5.4.5.2 THE GENERATE APPROACH

Tougaard's "Generate" approach was applied to the non-destructive reconstruction of the polarized electroless NiP specimens depth profile after polarization. Figure 5.32 (a) shows an example of the NiP alloy survey spectra simulation, together with the three reference spectra. The simulated and experimental spectra are superimposed and are in good agreement. The simulated spectrum was obtained by modelling the inelastic background of the three reference spectra using the depth profile model shown in Figure 5.32 (b).

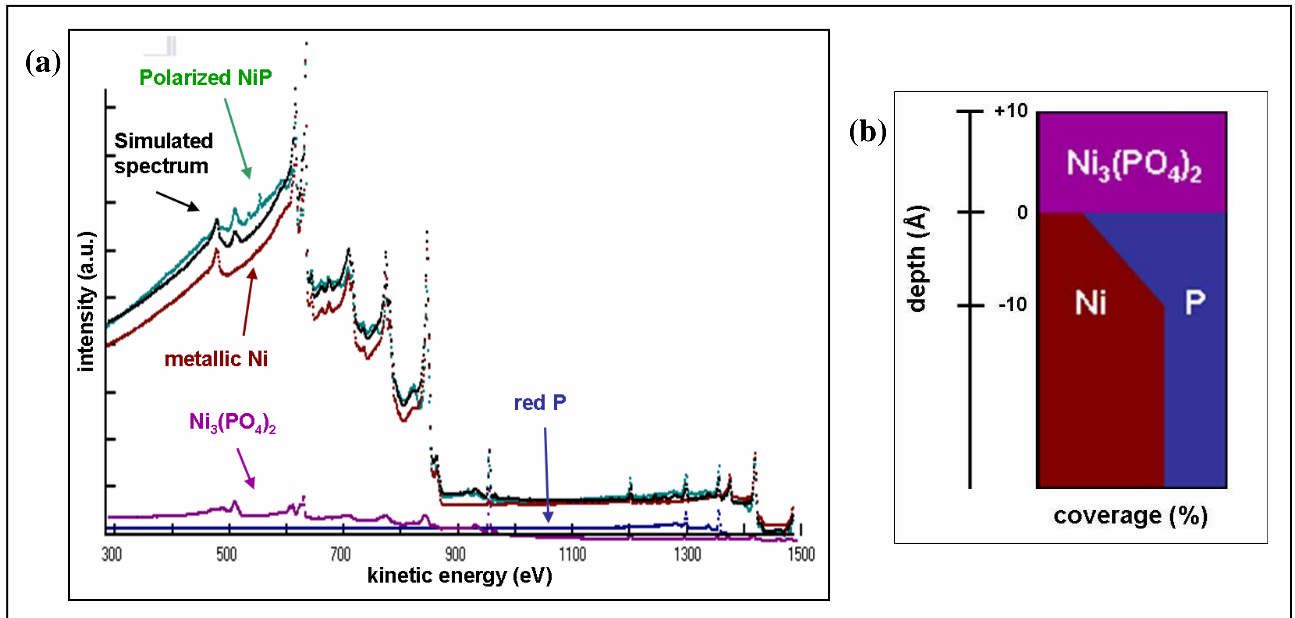

*Figure 5.32 : **(a)** Polarized NiP alloy spectrum simulation by Tougaard's "Generate" approach; **(b)** Depth profile model of polarized NiP alloy surface.*

Table 5.7 : Tougaard's "Generate" results. NiP depth profile at three different polarization times.

polarization time (h)	*1*	*3*	*14*
phosphate layer thickness (Å)	*10*	*8*	*10*
P- enriched interface thickness (Å)	*10*	*10*	*10*
P- enriched interface P content (at.%)	*55*	*70*	*70*
bulk alloy	*Ni-18P*		

After 1 hour polarization, the depth profile of the NiP alloy surface region was composed of an outer phosphate layer, estimated to be 10 Å thick, and an intermediate 10 Å thick P-enriched layer, located at the interface between the outer phosphate layer and the bulk of the alloy. P content of the bulk alloy was restricted to 18 at.%. P content of the P-enriched interface was equal to 55 at.%. The only significant difference between the depth profiles at 1, 3 and 14 hours polarization, is the P-content of this P-enriched interface: it increases up to 3 hours, becoming "constant" at longer polarization times. Table 5.7 gives the depth profiles of the NiP alloy surface at the three different polarization times.

5.4.6 MAXIMUM ENTROPY METHOD

5.4.6.1 NUMERICAL EXPERIMENTS

A series of numerical experiments was carried out to evaluate the performance and accuracy of the algorithms protocol for the MEM application. These numerical experiments were performed on various synthetic (i.e. numerical) structures composed of 3 to 8 components labelled A, B, C, D, E, F, G and H. The IMFP values of these components were chosen arbitrarily as 40, 30, 20, 10, 45, 35, 25 and 27 Å respectively. Before examining the results of the numerical experiments, let us consider the difference between the reconstruction of the depth profile of a real sample using the MEM and a numerical experiment.

The aim of surface analysis of a real sample is the quantitative determination of the depth profile, while numerical experiments take the quantitative depth profile as the starting point.

Surface analysis of a real sample starts with the angle-resolved acquisition of the high resolution spectra of the sample. ARXPS peak intensities are then corrected for photoionization cross section, asymmetry function and intensity/energy response function of the spectrometer. The thus corrected peak intensities are normalized for each of the emission angles examined. Thus, the normalized and corrected intensities of all the XPS peaks considered are plotted versus the emission angle to construct the apparent concentrations diagrams (ACD).

On the other hand, the so called *relative depth* is calculated for each of the components as the ratio between the normalized and corrected intensity at near-grazing and at near-normal emission angle. The relative depth is proportional to the mean depth at which the component is located within the surface region of the sample. The greater the relative depth, the closer to the surface the component is located, and vice versa. The relative depth plot (RDP) histogram can then be constructed using the relative depth value of each component.

Thus, the starting point of the depth profile reconstruction of a real sample are the ACD and the RDP obtained from the experimental ARXPS data. The aim of the MEM is to convert the ARXPS data into the quantitative depth profile of the sample by fitting the recalculated data with the experimental points of the apparent concentrations diagram.

On the contrary, in a numerical experiment, the ACD and the corresponding RDP are calculated on the basis of a given synthetic structure (i.e.: a predefined depth profile) and the above mentioned IMFP values are set. In the following, these ACD and RDP are referred to as real-ACD and real-RDP respectively, simply to indicate that they were used as starting point for the MEM application in that they were real experimental data. Thus, the MEM

protocol was applied to these real-ACD data to verify whether it was able to reconstruct the depth profile used to calculate the real-ACD itself.

Lastly, for an identical synthetic structure, the apparent concentrations diagrams (ACD) and the corresponding relative depth plots (RDP) were recalculated using only one IMFP value for all the components, in order to examine the influence of the IMFP on ACD and RDP. In the following, these recalculated diagrams are referred to as trial-ACD and trial-RDP respectively, simply to indicate that they were not used in the MEM protocol application but only to evaluate the influence of the IMFP on ACD and RDP data.

In the following, only the results of the most significant numerical experiments will be presented. All the other numerical results can be found in Appendix A.

SYNTHETIC STRUCTURE ***3_1+1+1***

This structure simulates a layered sample where the overlayer or the contamination consists of just one component (A) and the bulk is a pure elemental solid (C). Between the overlayer and the bulk there is an intermediate layer which has just one component (B).

Figure 5.33 shows the depth profile of the synthetic structure 3_1+1+1, together with its MEM simulation (dotted lines). Figure 5.34 shows the real-ACD calculated on the basis of the synthetic structure 3_1+1+1 (circles) and using IMFP values of 40, 30 and 20 Å for components A, B and C respectively, together with the MEM recalculated curves (dotted lines).

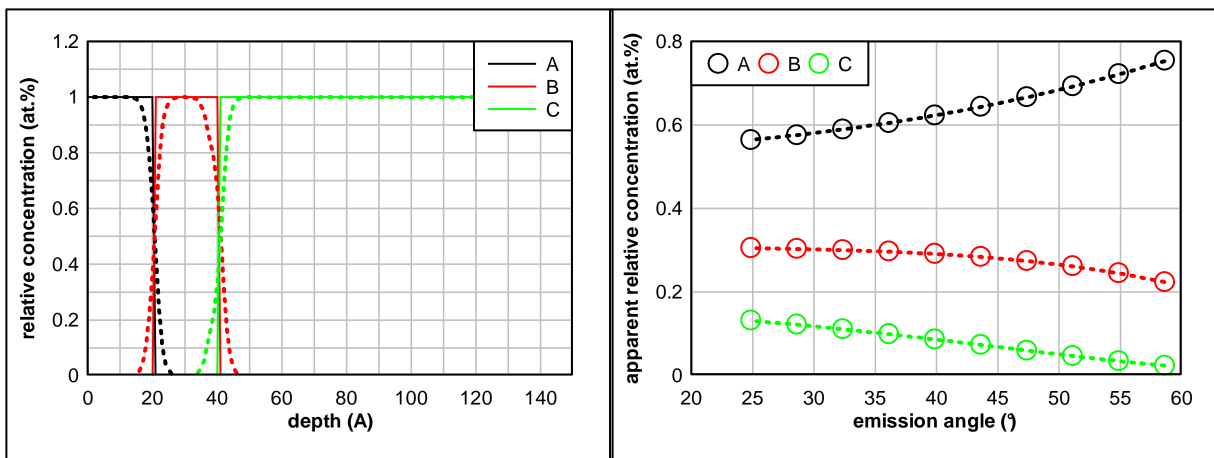

Figure 5.33 : Depth profile of the synthetic structure 3_1+1+1 and its MEM simulation (dotted lines).

Figure 5.34 : Apparent concentration diagram of the synthetic structure 3_1+1+1 (circles) and recalculated MEM data (dotted lines).

For this numerical experiment the depth profile was known but, as mentioned above, when the MEM protocol is applied to the experimental ARXPS data acquired for a real sample, the object of the analysis is to reconstruct the depth profile. Thus, assumptions about the depth profile have to be introduced and some indications can be gleaned from the ACD data. Actually, observing the ACD points in Figure 5.34, the overlayer would appear to be composed of A coating a binary B-C alloy or compound, but we know that this is not the case. Figure 5.35(a) shows the real-RDP, while figure 5.35(b) shows the trial-RDP, of the synthetic structure 3_1+1+1.

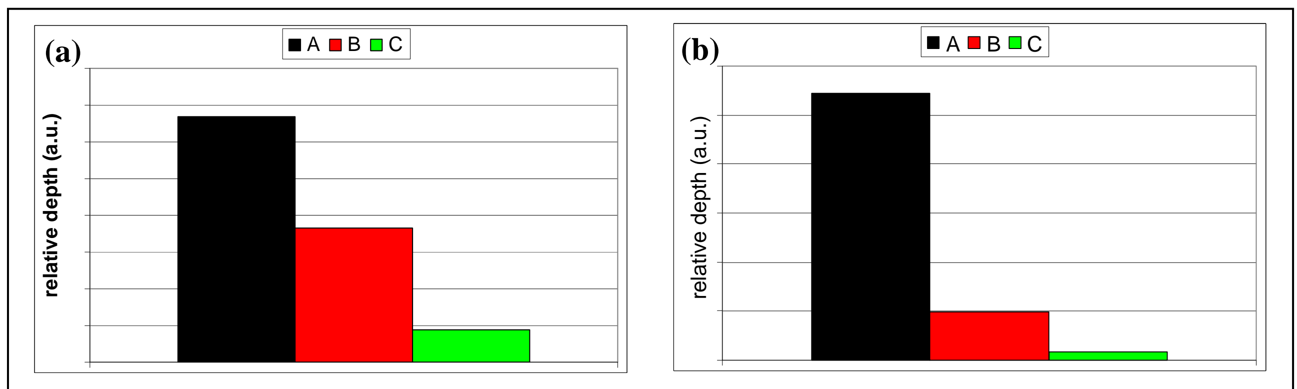

Figure 5.35 : Relative depth plot of synthetic structure 3_1+1+1. ***(a)*** *real-RDP and* ***(b)*** *trial-RDP.*

While erroneous assumptions were possible using the real-ACD, the corresponding real-RDP confirm the presence of the A component in the overlayer, clarifying that the bulk is composed of C alone, B constituting an intermediate layer. The y-axis of the RDP shows the relative depth of the components and does not have a specific dimension. The greater the bar, the closer to the surface the component is located. So there is no difference between the real and trial RDP in Figure 5.35, as both indicate the presence of an overlayer composed of A, an intermediate layer composed of B and the bulk composed of C.

Table 5.8 shows layer thickness of both the model and MEM simulated depth profiles.

Table 5.8 : Depth profile parameters of synthetic structure 3_1+1+1 and results of MEM simulation.

layer	thickness (Å)		|deviation| (Å)
	model	simulation	
overlayer	*21.0*	*21.0*	*0.0*
intermediate layer	*20.0*	*19.1*	*0.9*

SYNTHETIC STRUCTURE ***3_1+2***

In the case reported above (i.e. synthetic structure 3_1+1+1), it has been seen that observing the real-ACD, an erroneous assumption about the actual depth profile could be made: a profile 3_1+2. Thus, it was decided to show here the results of a numerical experiment actually performed on the synthetic structure 3_1+2 which simulates a layered sample where the overlayer or contaminated layer is composed of only one component (A) and the bulk is a binary alloy or compound (B and C).

Figure 5.36 shows the depth profile of the synthetic structure 3_1+2, together with its MEM simulation (dotted lines). Figure 5.37 shows the real-ACD calculated using the synthetic structure 3_1+2 (circles) and IMFP values of 40, 30 and 20 Å for components A, B and C respectively, together with the recalculated MEM curves (dotted lines).

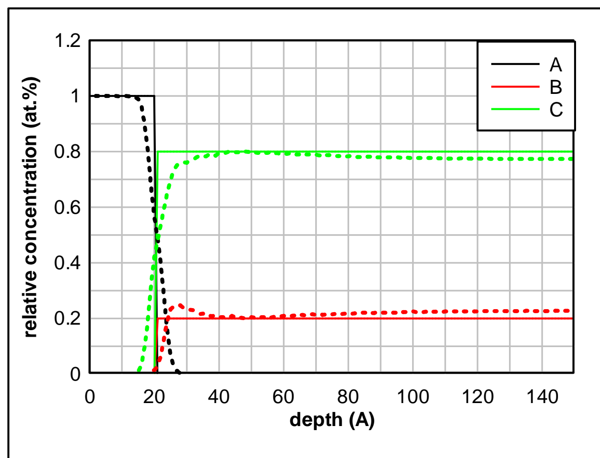

Figure 5.36 : Depth profile of the synthetic structure 3_1+2 and its MEM simulation (dotted lines).

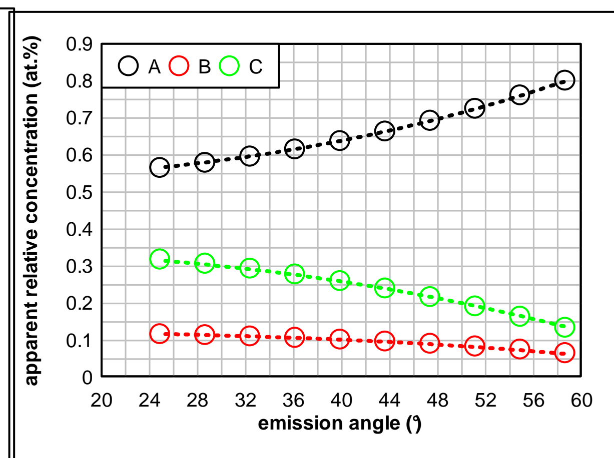

Figure 5.37 : Apparent concentration diagram of the synthetic structure 3_1+2 (circles) and recalculated MEM data (dotted lines).

Observing the ACD points in Figure 5.37, imagining that the depth profile is unknown, it could be correctly hypothesized that the A component constitutes the overlayer on a binary B-C alloy or compound. Otherwise, it could be wrongly assumed that there is an intermediate layer composed of B alone, located between the overlayer composed of A and the bulk composed of C.

Figure 5.38(a) shows the real-RDP, while Figure 5.38(b) shows the trial-RDP, for the synthetic structure 3_1+2.

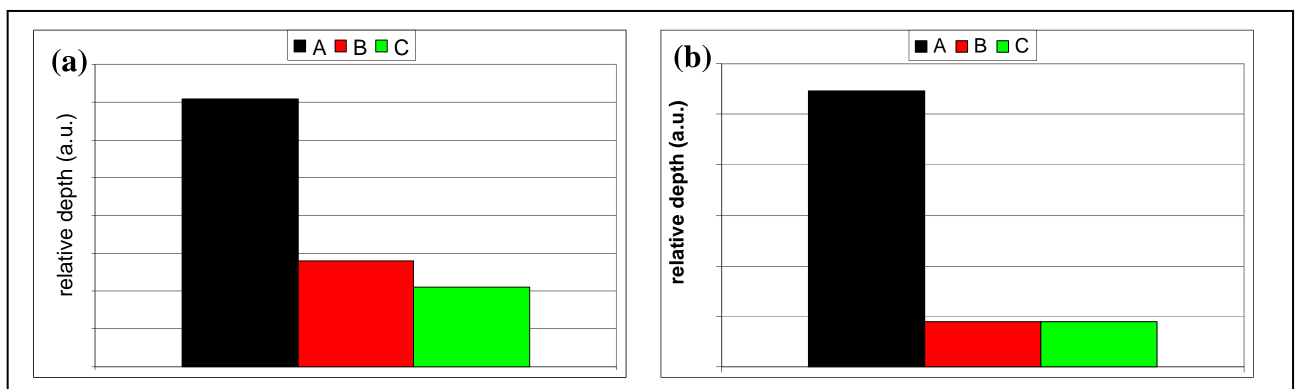

*Figure 5.38 : Relative depth plot for synthetic structure 3_1+2. **(a)** real-RDP and **(b)** trial-RDP.*

Also in this case, the real-RDP (Figure 5.38a) indicate the actual relative component depths. However, the relative depth of C in the real-RDP is lower than B, even if they are actually located within the bulk beneath the same overlayer. On the other hand we have to consider that also the IMFP of C is lower than B. In fact, this difference in the relative depth does not exist in the trial-RDP (Figure 5.38b) which was calculated on the basis of the same depth profile shown in Figure 5.36 but using the same IMFP value for all three species. Note that the RDP only provides qualitative information about the relative depth at which the different components are located but it does not give any information about layer thickness, that can only be evaluated at the end of the MEM protocol routine.

Table 5.9 shows layer thickness of both the model and MEM simulated depth profiles together with component concentrations.

Table 5.9 : Depth profile parameters for synthetic structure 3_1+2 and results of MEM simulation.

layer	thickness (Å)		|deviation| (Å)
	model	simulation	
overlayer	*21.0*	*21.3*	*0.3*

layer	species	concetration (at.%)		relative error (%)
		model	simulation	
bulk	*B*	*20*	*22*	*10*
	C	*80*	*78*	*-3*

SYNTHETIC STRUCTURE ***3_2+1***

Lastly, the results of the numerical experiment performed on the last 3-component structure, the profile 3_2+1, are shown. This synthetic structure simulates, as an example, the adventitious contamination (A and B) formed on a noble metal like gold (C).

Figure 5.39 shows the depth profile of the synthetic structure 3_2+1, together with its MEM simulation (dotted lines). Figure 5.40 shows the real-ACD calculated using the synthetic structure 3_2+1 (circles) setting IMFP as 40, 30 and 20 Å for components A, B and C respectively, together with the recalculated MEM curves (dotted lines).

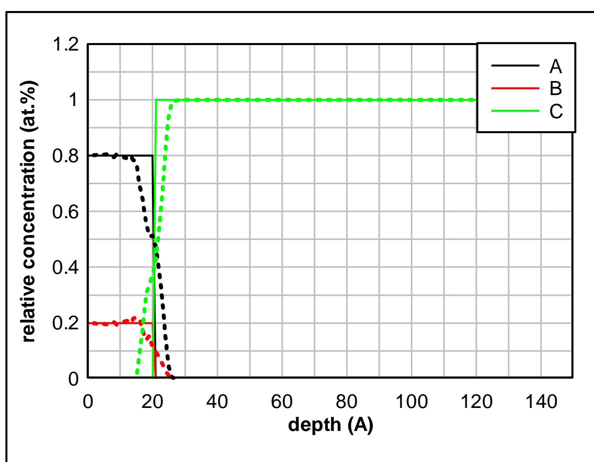

Figure 5.39 : In-depth profile of the synthetic structure 3_2+1 and its MEM simulation (dotted lines).

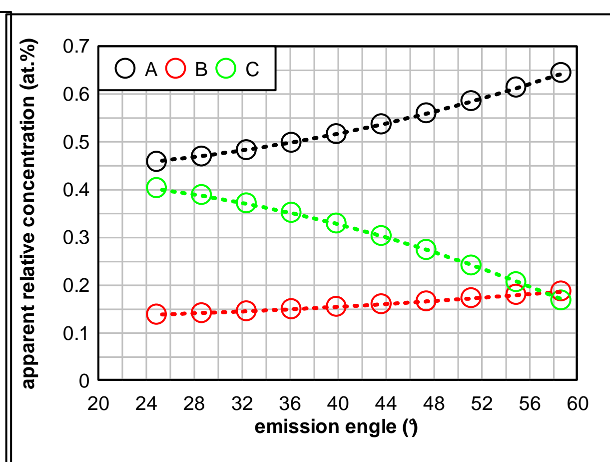

Figure 5.40 : Apparent Concentration Diagram of the synthetic structure 3_2+1 (circles) and MEM recalculated data (dotted lines).

In this case, observation of the real-ACD spots leads to the correct assumption about the depth profile. This hypothesis is further confirmed by the real-RDP, as is shown in Figure 5.41(a).

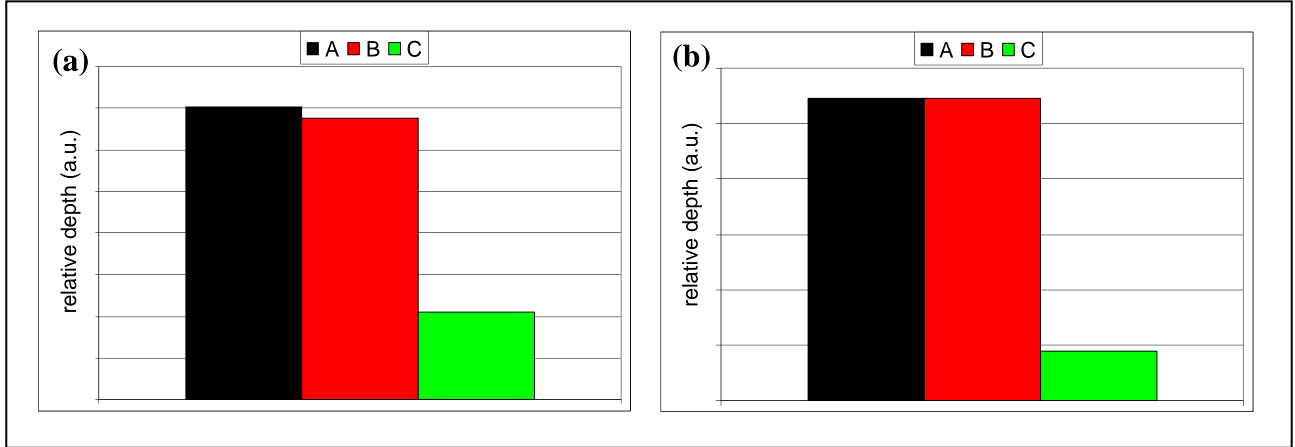

*Figure 5.41 : Relative depth plot for synthetic structure 3_2+1. (**a**) real-RDP and (**b**) trial-RDP.*

However, the minor difference in relative depth between components A and B can be attributed to the difference in their IMFP values (40 and 30 Å respectively). In fact, this difference in relative depth does not exist in the trial-RDP (Figure 5.41b) which was calculated using the same depth profile shown in Figure 5.39 but the same IMFP value for all three species.

Table 5.10 gives layer thickness of both the model and MEM simulated depth profiles, together with component concentrations.

Table 5.10 : Depth profile parameters for synthetic structure 3_2+1 and results of MEM simulation.

layer	**thickness (Å) model**	**thickness (Å) simulation**	**|deviation| (Å)**
overlayer	*21.0*	*22.0*	*1.0*

layer	**species**	**concentration (at.%) model**	**concentration (at.%) simulation**	**relative error (%)**
overlayer	*A*	*80*	*80*	*0*
	B	*20*	*20*	*0*

SYNTHETIC STRUCTURE ***4_1+1+1+1***

One of the doubts about the MEM protocol performance was the depth resolution obtainable. To resolve this, we performed some numerical experiments on particular synthetic structures formed of mono-component layers alone. One example is the above reported 3_1+1+1 in which layer thickness was taken as 20 Å. Here the results are shown of the numerical experiment performed for the synthetic structure 4_1+1+1+1 which has one more component than the 3_1+1+1 structure, taking a smaller layer thickness of 10 Å. In the following, the results of the numerical experiments performed on the 5_1+1+1+1+1 and the 6_1+1+1+1+1+1 structures are also described, setting layer thickness as 7 and 5 Å respectively.

Figure 5.42 shows the depth profile of the synthetic structure 4_1+1+1+1, together with its MEM simulation (dotted lines). Figure 5.43 shows the real-ACD calculated using the synthetic structure 4_1+1+1+1 (circles) and IMFP values of 40, 30, 20 and 10 Å for the components A, B, C and D respectively, together with the recalculated MEM curves (dotted lines).

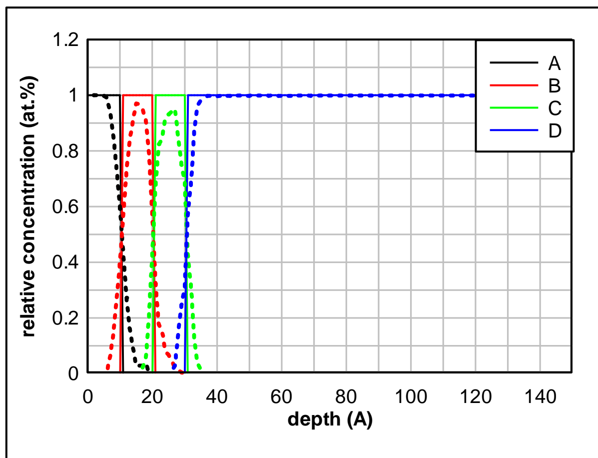

Figure 5.42 : In-depth profile of the synthetic structure 4_1+1+1+1 and its MEM simulation (dotted lines).

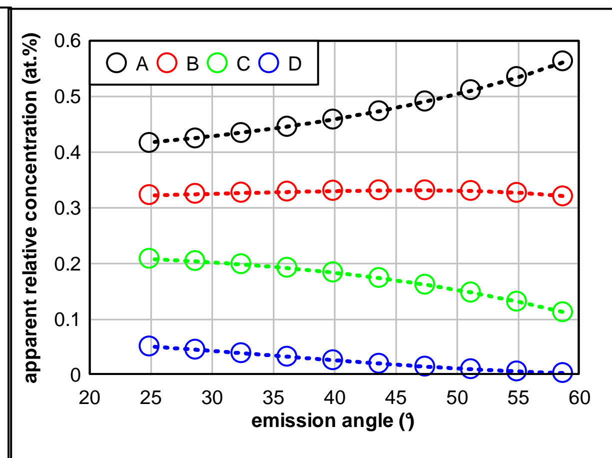

Figure 5.43 : Apparent Concentration Diagram of the synthetic structure 4_1+1+1+1 (circles) and MEM recalculated data (dotted lines).

In this case, the real ACD could lead to an erroneous assumption: an overlayer of A, an intermediate layer of B, and a bulk composed of a binary C-D compound. But again, the real-RDP (Figure 5.44a) clarifies the actual depth profile. Similarly to the synthetic structure 3_1+1+1, there is no difference between real- and trial-RDPs (Figure 5.44).

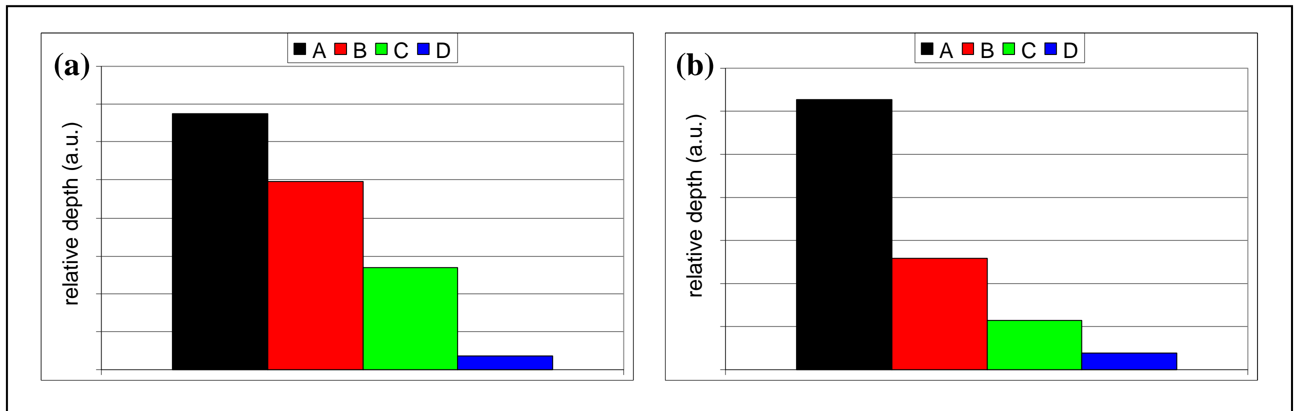

Figure 5.44 : Relative depth plot of synthetic structure 4_1+1+1+1. ***(a)*** *real-RDP and* ***(b)*** *trial-RDP.*

Table 5.11 gives layer thickness of both the model and MEM simulated depth profiles, together with the area under the curves for all components.

Table 5.11 : Depth profile parameters of synthetic structure 4_1+1+1+1 and results of MEM simulation.

layer	**thickness (Å)**		**|deviation| (Å)**
	model	**simulation**	
overlayer	*11.0*	*10.8*	*0.2*
1st intermediate layer	*10.0*	*10.2*	*0.2*
2nd intermediate layer	*10.0*	*10.9*	*0.9*
species	**curve area (a.u.)**		**relative error (%)**
	model	**simulation**	
A	*11.0*	*10.7*	*-2.7*
B	*10.0*	*10.1*	*1.0*
C	*10.0*	*10.0*	*0.0*

SYNTHETIC STRUCTURE ***4_1+2+1***

This structure simulates, as an example, a binary oxide (B and C components) formed on the surface of an elemental material (D) with a mono-component contaminated overlayer (A). Figure 5.45 shows the depth profile of the synthetic structure 4_1+2+1, together with its MEM simulation (dotted lines). Figure 5.46 shows the real-ACD calculated using the synthetic structure 4_1+2+1 (circles) and IMFP values of 40, 30, 20 and 10 Å for components A, B, C and D respectively, together with the recalculated MEM curves (dotted lines).

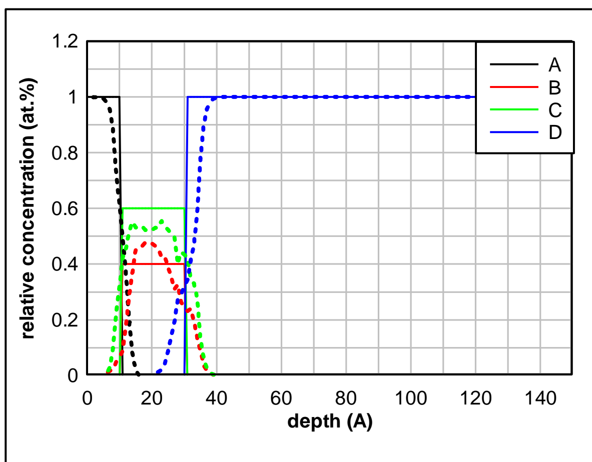

Figure 5.45 : In-depth profile of the synthetic structure 4_1+2+1 and its MEM simulation (dotted lines).

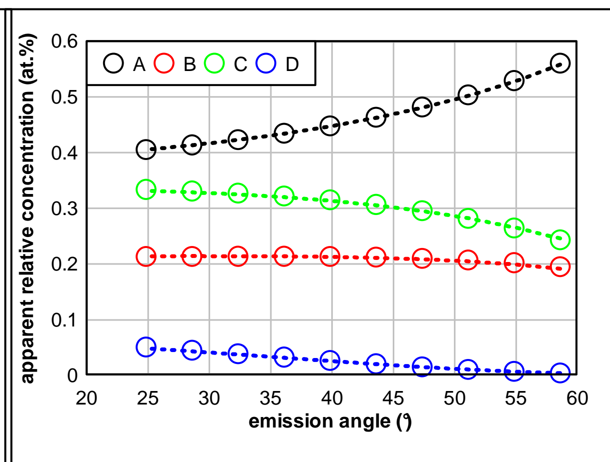

Figure 5.46 : Apparent Concentration Diagram of the synthetic structure 4_1+2+1 (circles) and MEM recalculated data (dotted lines).

In this case, the trend of the real-ACD points should yield the right assumption about the depth profile, even if the exact location of the component D may be quite uncertain. However, here again, the real-RDP (Figure 5.47 a) clarifies the doubt, especially if the differences in IMFP for the four species are taken into account.

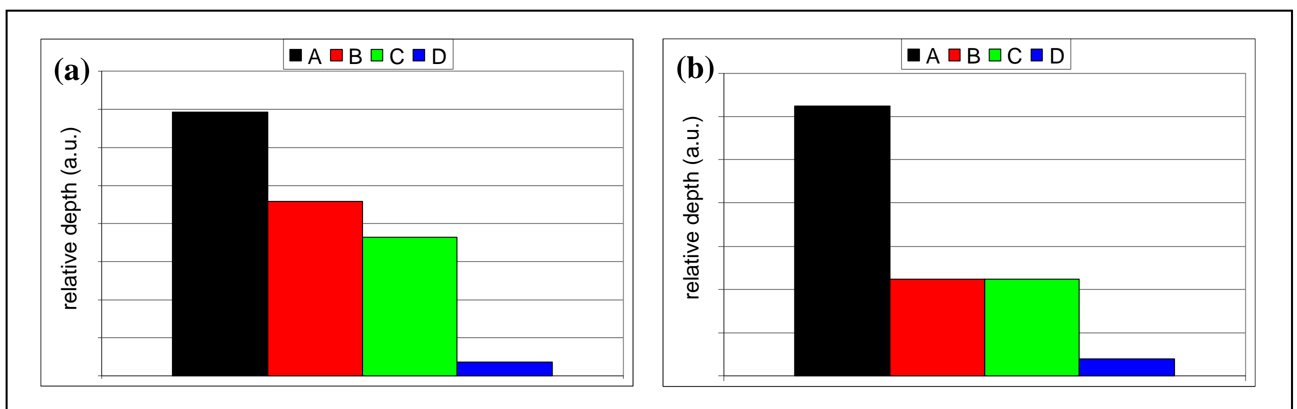

*Figure 5.47 : Relative depth plot of synthetic structure 4_1+2+1. **(a)** real-RDP and **(b)** trial-RDP.*

Again, the difference in relative depth between B and C (Figure 5.47 a) disappears if B and C have exactly the same IMFP, as it is forced to calculate the trial-RDP (Figure 5.47 b) for exactly the same depth profile.

Table 5.12 shows layer thickness of both the model and MEM simulated depth profile, together with the component concentrations.

Table 5.12 : Depth profile parameters of synthetic structure 4_1+2+1 and results of MEM simulation.

layer	**thickness (Å)**		**|deviation| (Å)**
	model	**simulation**	
overlayer	*10.0*	*10.2*	*0.2*
intermediate layer	*20.0*	*21.6*	*1.6*

layer	**species**	**concentration (at.%)**		**relative error (%)**
		model	**simulation**	
intermediate layer	*B*	*40*	*41*	*2*
	C	*60*	*59*	*-1*

SYNTHETIC STRUCTURE ***5_1+1+1+1+1***

As mentioned above, this structure was chosen in order to determine the depth resolution obtainable with our MEM protocol. The structure consists of four mono-component 7 Å thick layers, overlying an elemental bulk material composed of E alone.

Figure 5.48 shows the depth profile of the synthetic structure 5_1+1+1+1+1, together with its MEM simulation (dotted lines). Figure 5.49 shows the real-ACD calculated using the synthetic structure 5_1+1+1+1+1 (circles) and IMFP of 40, 30, 20, 10 and 45 Å for components A, B, C, D and E respectively, together with the recalculated MEM curves (dotted lines).

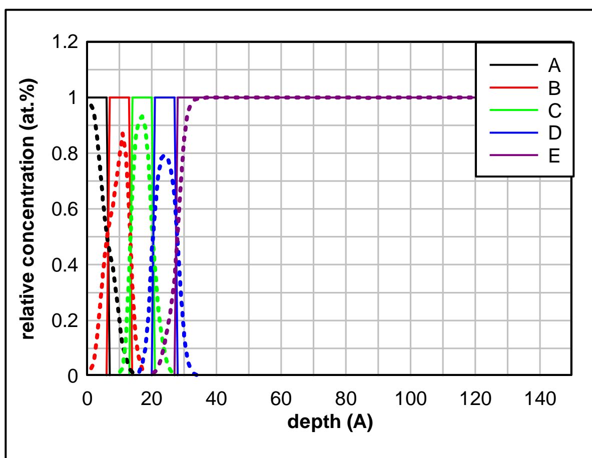

Figure 5.48 : Depth profile of synthetic structure 5_1+1+1+1+1 and MEM simulation (dotted lines).

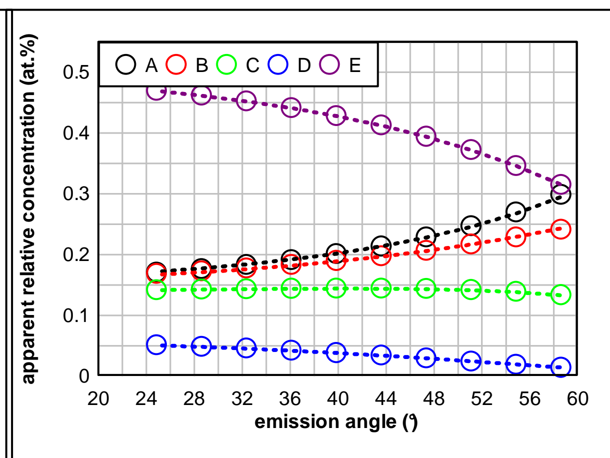

Figure 5.49 : Apparent concentration diagram of synthetic structure 5_1+1+1+1+1 (circles) and recalculated MEM data (dotted lines).

Based on the real-ACD points alone, several different hypotheses on the depth profile may be advanced. However, some of these can be ruled out observing the real-RDP (Figure 5.50 a) and taking into account the different IMFP of the components. In the real-RDP, the relative depth of E is too great since it corresponds to the highest IMFP. In fact, when relative depths are recalculated using only one IMFP for all the components to provide the trial-RDP (Figure 5.50 b), this discrepancy is eliminated and the trial-RDP gives a perfect representation of the layered structure.

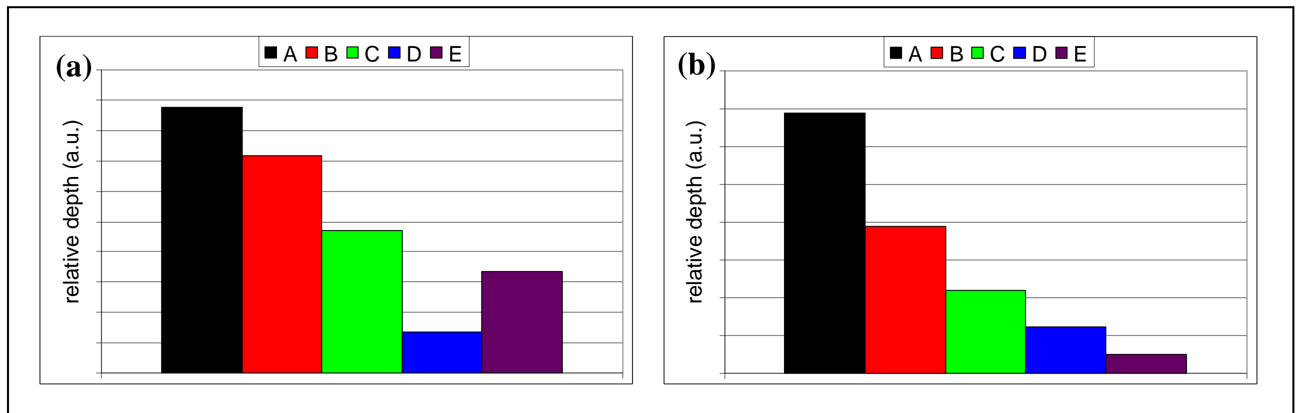

*Figure 5.50 : Relative depth plot of synthetic structure 5_1+1+1+1+1. **(a)** real-RDP and **(b)** trial-RDP.*

Table 5.13 gives layer thickness of both the model and MEM simulated depth profiles, together with the area under the curves of all components.

Table 5.13 : Depth profile parameters of synthetic structure 5_1+1+1+1+1 and results of MEM simulation.

layer	thickness (Å)		|deviation| (Å)
	model	simulation	
overlayer	*7.0*	*7.0*	*0.0*
1st intermediate layer	*7.0*	*6.9*	*0.1*
2nd intermediate layer	*7.0*	*6.5*	*0.5*
3rd intermediate layer	*7.0*	*8.8*	*1.8*
species	**curve integral (u.a.)**		**relative error (%)**
	model	**simulation**	
A	*7.0*	*6.7*	*-4.3*
B	*7.0*	*6.8*	*-2.9*
C	*7.0*	*7.1*	*1.4*
D	*7.0*	*6.9*	*-1.4*

SYNTHETIC STRUCTURE ***5_3+2***

This synthetic structure was chosen to simulate the case of a three-component layer formed on a binary alloy, such as an orthophosphate layer formed on the surface of a NiP alloy.

Figure 5.51 shows the depth profile of the synthetic structure 5_3+2, together with its MEM simulation (dotted lines). Figure 5.52 shows the real-ACD calculated using the synthetic structure 5_3+2 (circles) and IMFP values of 40, 30, 20, 10 and 45 Å for components A, B, C, D and E respectively, together with the recalculated MEM curves (dotted lines).

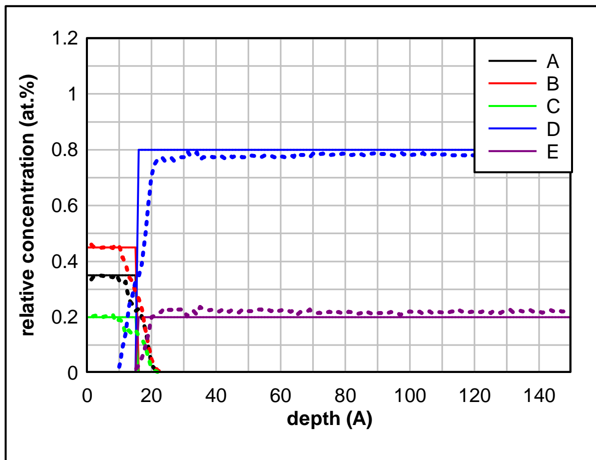

Figure 5.51 : In-depth profile of the synthetic structure 5_3+2 and its MEM simulation (dotted lines).

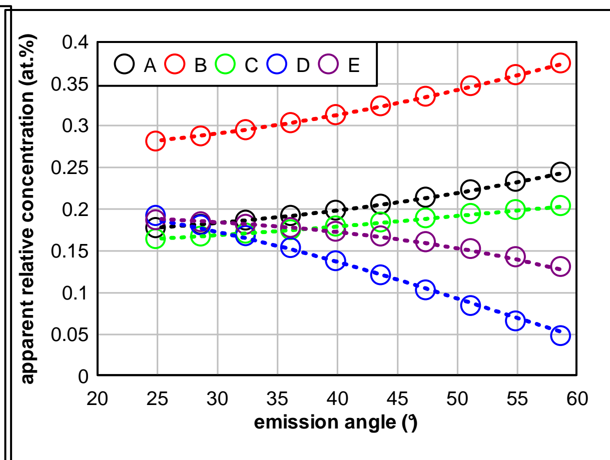

Figure 5.52 : Apparent Concentration Diagram of synthetic structure 5_3+2 (circles) and recalculated MEM data (dotted lines).

In this case, the real-ACD provides fairly clear evidence of the actual depth profile.

Figure 5.53 shows both the real- and trial-RDP. Again, a correct interpretation of the real-RDP requires the difference in the IMFP values to be taken into account, as shown by the trial-RDP which, on the contrary, gives a perfect representation of the depth profile of this synthetic structure.

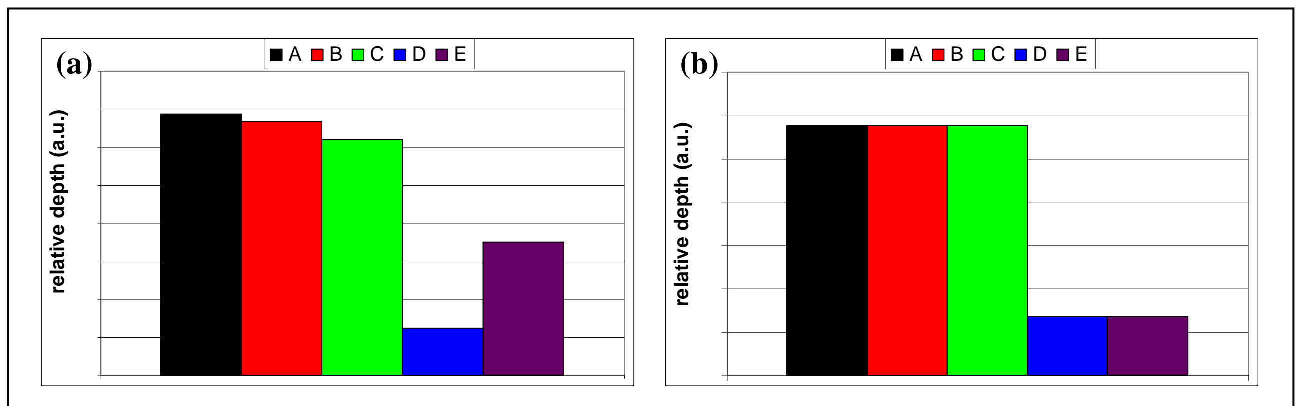

*Figure 5.53 : Relative depth plot of synthetic structure 5_3+2. **(a)** real-RDP and **(b)** trial-RDP.*

Table 5.14 gives layers thickness of both the model and the MEM simulated depth profiles, together with the component concentrations.

Table 5.14 : Depth profile parameters of synthetic structure 5_3+2 and results of MEM simulation.

layer	thickness (Å)		|deviation| (Å)
	model	simulation	
overlayer	*16.0*	*15.3*	*0.7*

layer	species	concentration (at.%)		relative error (%)
		model	simulation	
overlayer	*A*	*35*	*35*	*0*
	B	*45*	*45*	*0*
	C	*20*	*20*	*0*
bulk	*D*	*80*	*78*	*-3*
	E	*20*	*22*	*10*

SYNTHETIC STRUCTURE ***6_1+1+1+1+1+1***

This synthetic structure was chosen, similarly to 5_1+1+1+1+1, 4_1+1+1+1 and 3_1+1+1, to determine the depth resolution obtainable with our MEM protocol.

Figure 5.54 shows the depth profile of this synthetic structure, together with its MEM simulation (dotted lines). Figure 5.55 shows the real-ACD calculated using the synthetic structure 6_1+1+1+1+1+1 (circles) and IMFP values of 40, 30, 20, 10, 45 and 35 Å for components A, B, C, D, E and F respectively, together with the recalculated MEM curves (dotted lines).

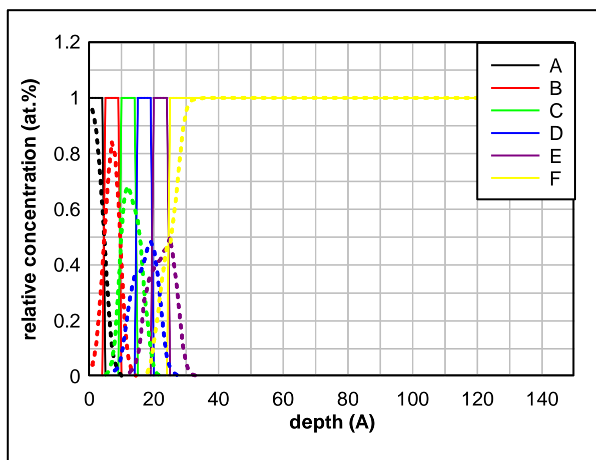

Figure 5.54 : Depth profile of synthetic structure 6_1+1+1+1+1+1 and MEM simulation (dotted lines).

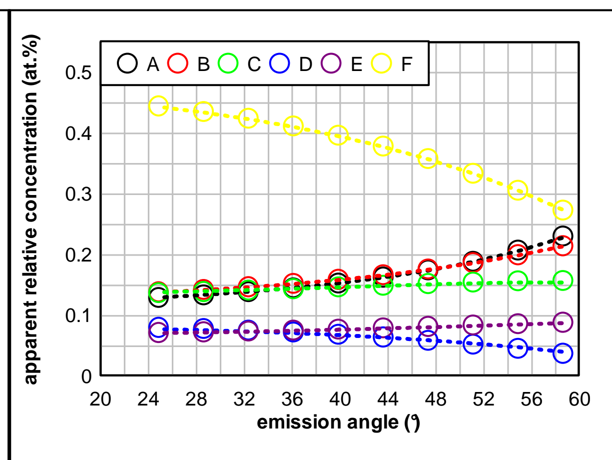

Figure 5.55 : Apparent concentration diagram of synthetic structure 6_1+1+1+1+1+1 (circles) and recalculated MEM data (dotted lines).

Firstly, note that even if the maximum of the simulated concentration vs. depth curves in Figure 5.54 is too low with respect to the depth profile model, the area under each of the simulated curves is comparable with the corresponding curve in the depth profile model to within a maximum error of 8 %, as shown in Table 5.15.
Then, observing both the real-ACD and the real-RDP (Figure 5.56 a), several hypotheses can be advanced about the depth profile. However, here too, the different IMFP of the components play a fundamental role in determining both the trend of the ACD points and the relative depth of the components in the RDP and must be taken into account. In fact, as shown in Figure 5.56 b, the trial-RDP perfectly represent the actual depth profile of the system.

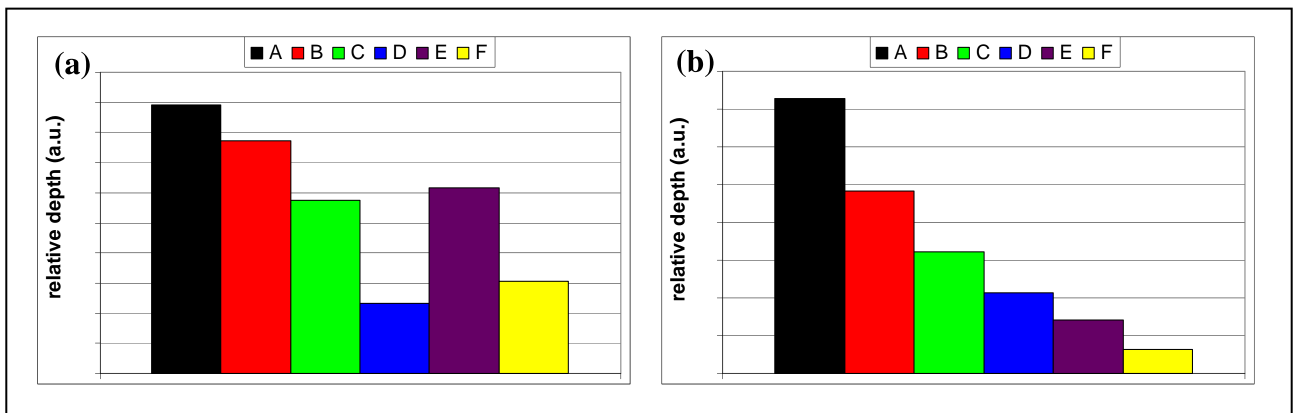

*Figure 5.56 : Relative depth plot of synthetic structure 6_1+1+1+1+1+1. **(a)** real-RDP and **(b)** trial-RDP.*

Table 5.13 shows layer thickness of both the model and MEM simulated depth profiles, together with the area under the curves of all components.

Table 5.15 : Depth profile parameters of synthetic structure 6_1+1+1+1+1+1 and results of MEM simulation.

layer	thickness (Å)		|deviation| (Å)
	model	simulation	
overlayer	*5.0*	*5.0*	*0.0*
1st intermediate layer	*5.0*	*4.9*	*0.1*
2nd intermediate layer	*5.0*	*5.5*	*0.5*
3rd intermediate layer	*5.0*	*7.1*	*2.1*
4th intermediate layer	*5.0*	*6.0*	*1.0*
species	**curve intergral (a.u.)**		**relative error (%)**
	model	**simulation**	
A	*5.0*	*4.6*	*-8.0*
B	*5.0*	*5.0*	*0.0*
C	*5.0*	*5.3*	*6.0*
D	*5.0*	*4.7*	*-6.0*
E	*5.0*	*5.0*	*0.0*

SYNTHETIC STRUCTURE ***6_1+2+1+2***

This synthetic structure was chosen to simulate the case of a two-component layer formed on a binary alloy, such as a nickel oxide layer formed on the surface of a NiP alloy. To increase the complexity of the system, a layer of pure D was introduced at the interface between the "oxide" layer and the "alloy", as well as an pure A outer contamination layer.

Figure 5.57 shows the depth profile of this synthetic structure 6_1+2+1+2, together with its MEM simulation (dotted lines). Figure 5.58 shows the real-ACD calculated using this synthetic structure (circles) and IMFP of 40, 30, 20, 10, 45 and 35 Å for components A, B, C, D, E and F respectively, together with the recalculated MEM curves (dotted lines).

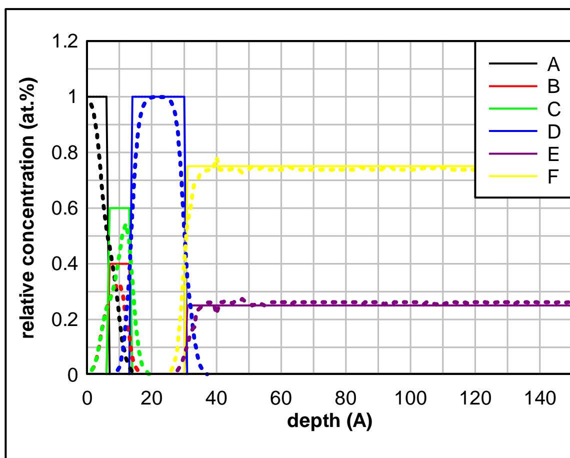

Figure 5.57 : Depth profile of synthetic structure 6_1+2+1+2 and MEM simulation (dotted lines).

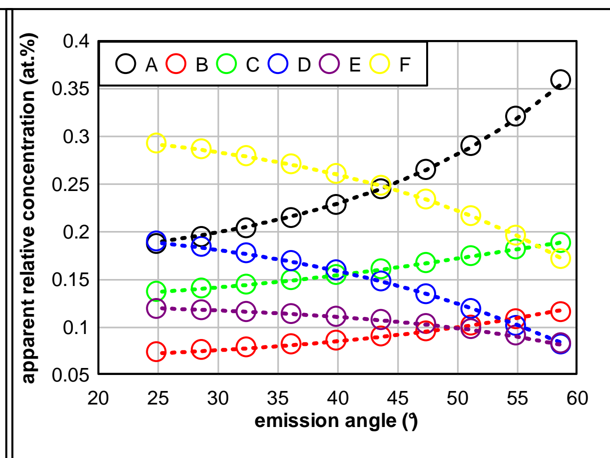

Figure 5.58 : Apparent Concentration Diagram of synthetic structure 6_1+2+1+2 (circles) and recalculated MEM data (dotted lines).

As before, observing both the real-ACD and the real-RDP (Figure 5.59 a), several hypotheses can be advanced about the depth profile. Again, note how the trial-RDP perfectly represents the actual depth profile of this complex synthetic structure, stressing the fundamental role played by IMFP values in determining the trend of ACD points and the relative depths of all components.

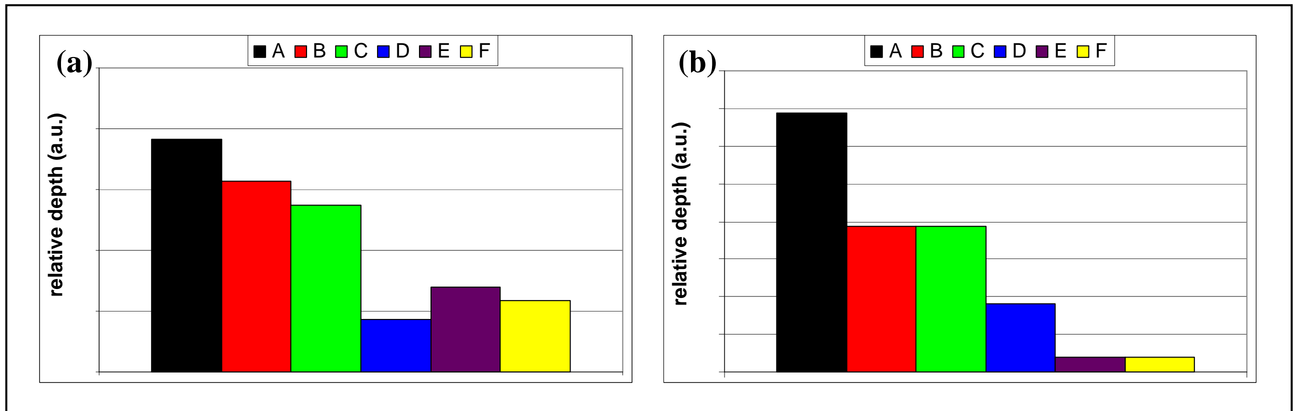

*Figure 5.59 : Relative depth plot of synthetic structure 6_1+2+1+2. **(a)** real-RDP and **(b)** trial-RDP.*

Table 5.16 shows layer thickness of both the model and MEM simulated depth profiles, together with component concentrations.

Table 5.16 : Depth profile parameters of synthetic structure 6_1+2+1+2 and results of MEM simulation.

layer		**thickness (Å)**		**|deviation| (Å)**
		model	**simulation**	
overlayer		*7.0*	*6.3*	*0.7*
1st intermediate layer		*7.0*	*8.5*	*1.5*
2nd intermediate layer		*17.0*	*16.1*	*0.9*
layer	**species**	**concentration (at.%)**		**relative error (%)**
		model	**simulation**	
1st intermediate layer	*B*	*40*	*38*	*-5*
	C	*60*	*62*	*3*
bulk	*E*	*25*	*26*	*4*
	F	*75*	*74*	*-1*

SYNTHETIC STRUCTURE ***6_1+3+2***

This synthetic structure was chosen to increase the complexity of the structure 5_3+2 described above which represented the case of an orthophosphate layer formed on the surface of a NiP alloy. Here, a pure A contamination layer was added to that system.

Figure 5.60 shows the depth profile of the synthetic structure 6_1+3+2, together with its MEM simulation (dotted lines). Figure 5.61 shows the real-ACD calculated using this synthetic structure (circles) and IMFP of 40, 30, 20, 10, 45 and 35 Å for components A, B, C, D, E and F respectively, together with the recalculated MEM curves (dotted lines).

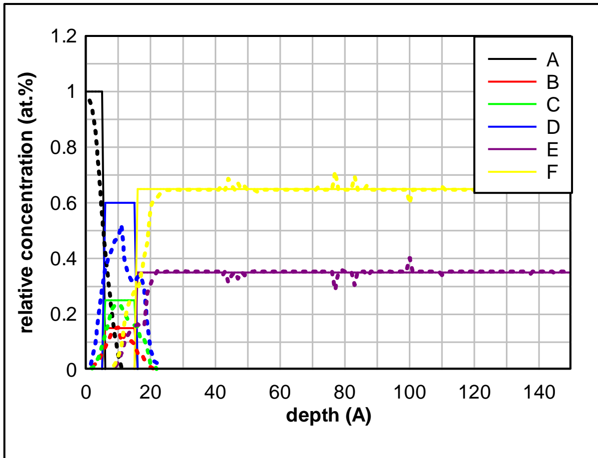

Figure 5.60 : Depth profile of synthetic structure 6_1+3+2 and MEM simulation (dotted lines).

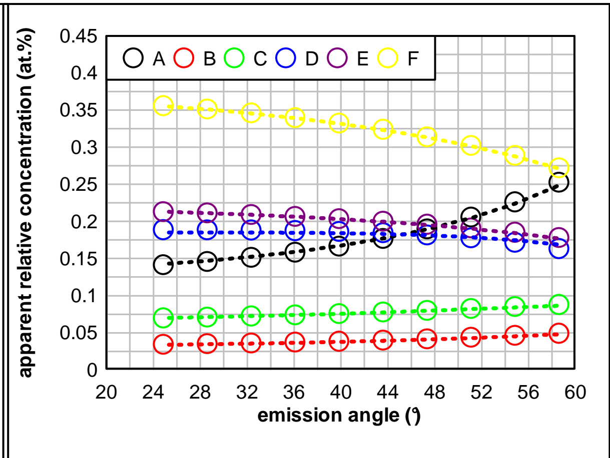

Figure 5.61 : Apparent Concentration Diagram of synthetic structure 6_1+3+2 (circles) and recalculated MEM data (dotted lines).

In this case observation of both the real-ACD and the real-RDP (figure 5.62 a), should lead to the incorrect hypothesis about a depth profile such as 6_1+2+3. However, taking into account the fact that the D component has the lowest IMFP, alternatively the correct 6_1+3+2 profile can also be hypothesized. Note, once again, how the trial-RDP (Figure 5.62 b) perfectly represents the actual relative depth of all the components.

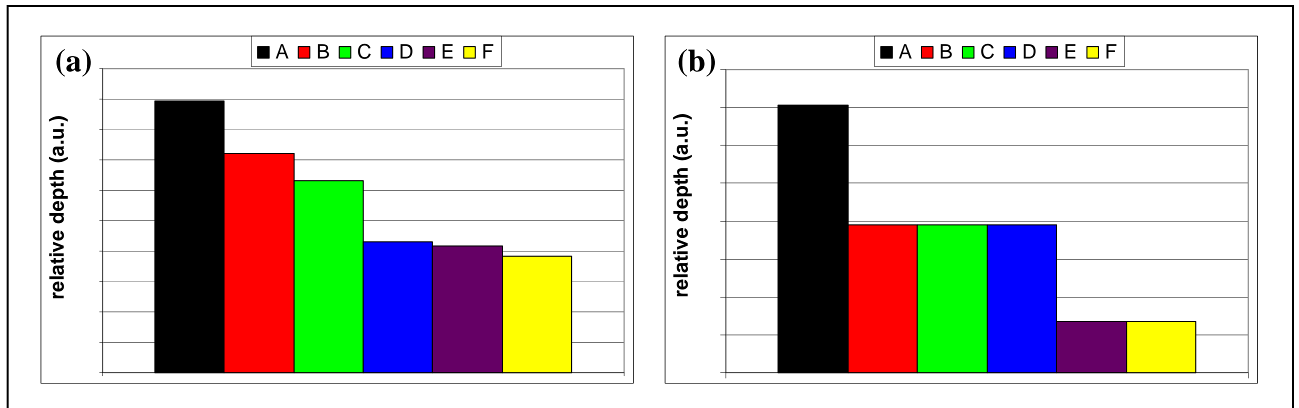

Figure 5.62 : Relative depth plot of synthetic structure 6_1+3+2. ***(a)*** *real-RDP and* ***(b)*** *trial-RDP.*

Table 5.17 shows layer thickness of both the model and MEM simulated depth profiles, together with component concentrations.

Table 5.17 : Depth profile parameters of synthetic structure 6_1+3+2 and results of MEM simulation.

layer	thickness (Å)		|deviation| (Å)
	model	simulation	
overlayer	*6.0*	*5.6*	*0.4*
intermediate layer	*10.0*	*11.4*	*1.4*

layer	species	concentration (at.%)		relative error (%)
		model	simulation	
intermediate layer	*B*	*15*	*15*	*0*
	C	*25*	*26*	*4*
	D	*60*	*59*	*-2*
bulk	*E*	*35*	*35*	*0*
	F	*65*	*65*	*0*

SYNTHETIC STRUCTURE ***6_3+1+2***

This synthetic structure was chosen to increase the complexity of the structure 5_3+2 described above which represented the case of an orthophosphate layer formed on the surface of a NiP alloy. Here, a pure D intermediate layer was added to that system at the interface between the "phosphate" layer and the "alloy".

Figure 5.63 shows the depth profile of this synthetic structure 6_3+1+2, together with its MEM simulation (dotted lines). Figure 5.64 shows the real-ACD calculated using this synthetic structure (circles) and IMFP of 40, 30, 20, 10, 45 and 35 Å for components A, B, C, D, E and F respectively, together with the recalculated MEM curves (dotted lines).

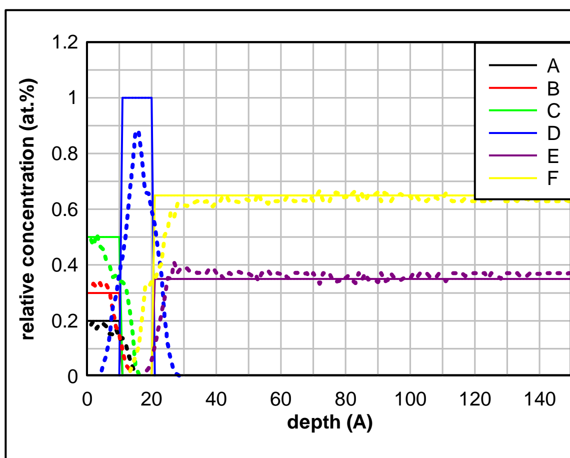

Figure 5.63 : Depth profile of synthetic structure 6_3+1+2 and MEM simulation (dotted lines).

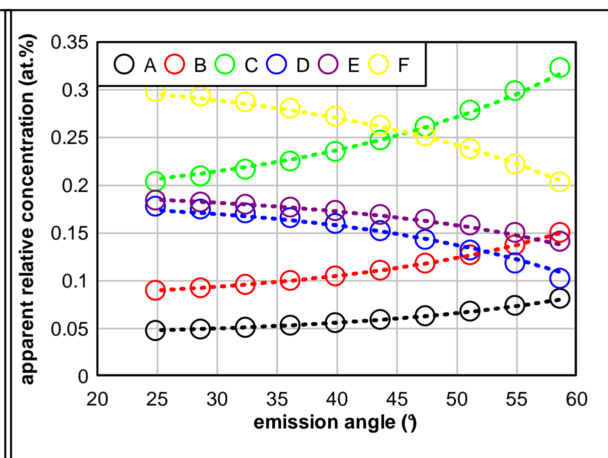

Figure 5.64 : Apparent concentration diagram of synthetic structure 6_3+1+2 (circles) and recalculated MEM data (dotted lines).

Similarly to the previous numerical experiment, observation of both the real-ACD and the real-RDP (figure 5.65 a), should lead to the incorrect hypothesis about a depth profile such as 6_3+3. However, taking into account the fact that the D component has the lowest IMFP, alternatively the correct 6_3+1+2 profile can also be hypothesized. Note, once again, how the trial-RDP (Figure 5.65 b) perfectly represents the actual relative depth of all components.

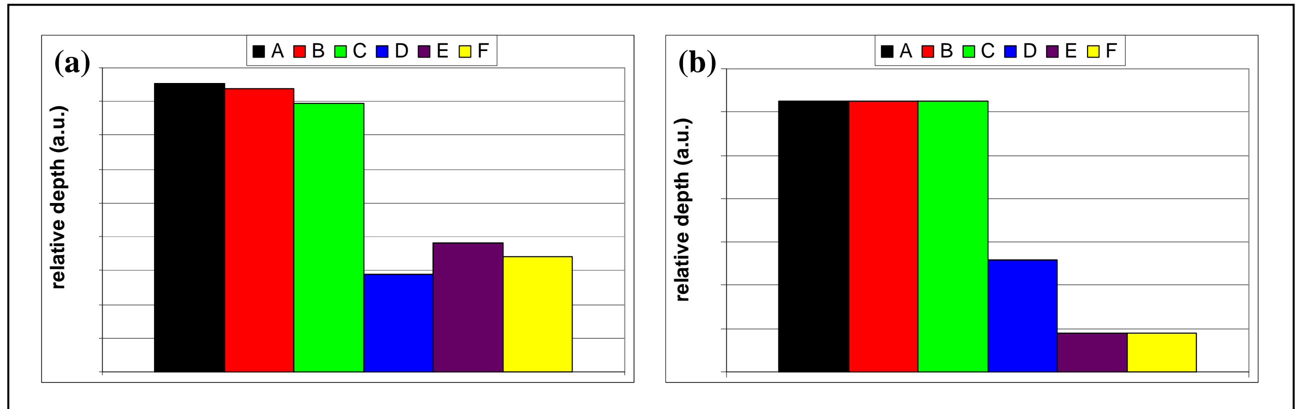

*Figure 5.65 : Relative depth plot of synthetic structure 6_3+1+2. **(a)** real-RDP and **(b)** trial-RDP.*

Table 5.18 shows layer thickness of both the model and MEM simulated depth profiles, together with component concentrations.

Table 5.18 : Depth profile parameters of synthetic structure 6_3+1+2 and results of MEM simulation.

layer	**thickness (Å)**		**|deviation| (Å)**
	model	**simulation**	
overlayer	*11.0*	*10.9*	*0.1*
intermediate layer	*10.0*	*10.3*	*0.3*

layer	**species**	**concentration (at.%)**		**relative error (%)**
		model	**simulation**	
overlayer	*A*	*20*	*20*	*0*
	B	*30*	*29*	*-3*
	C	*50*	*51*	*2*
bulk	*E*	*35*	*36*	*3*
	F	*65*	*64*	*-2*

SYNTHETIC STRUCTURE *6_3+3*

Since in the results described above, it was shown how the observation of both the real-ACD and the real-RDP could lead to the erroneous hypothesis of a 6_3+3 profile, this profile was chosen to here to emphasize how often two, or even more, structures can be misunderstood. Figure 5.66 shows the depth profile of the synthetic structure 6_3+3, together with its MEM simulation (dotted lines). Figure 5.67 shows the real-ACD calculated using this synthetic structure (circles) and IMFP of 40, 30, 20, 10, 45 and 35 Å for components A, B, C, D, E and F respectively, together with the recalculated MEM curves (dotted lines).

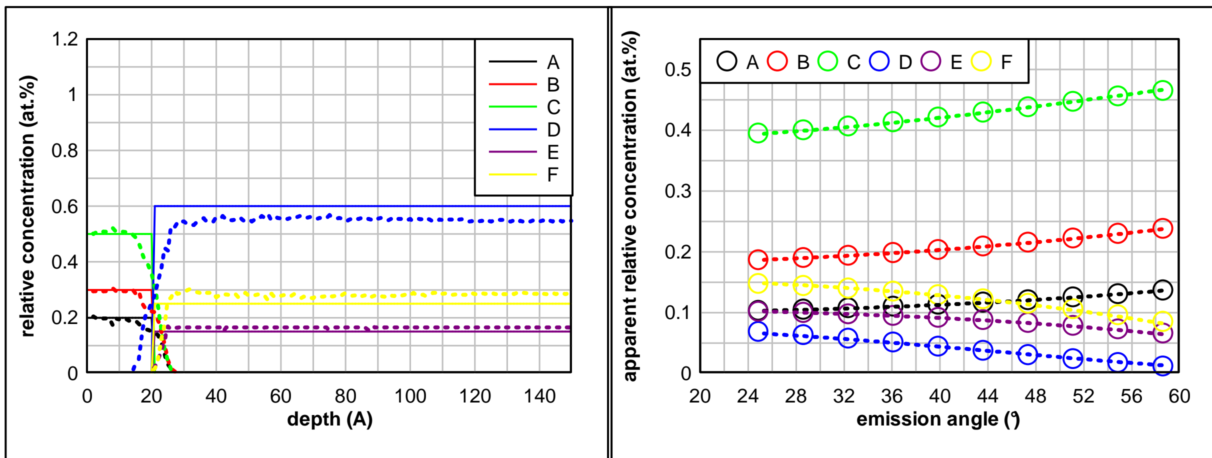

Figure 5.66 : Depth profile of synthetic structure 6_3+3 and MEM simulation (dotted lines).

Figure 5.67 : Apparent concentration diagram of synthetic structure 6_3+3 (circles) and recalculated MEM data (dotted lines).

In this case, based on the real-ACD and the real-RDP (Figure 5.68 a), and taking into account that the D component has the lowest IMFP, it is possible to obtain the correct hypothesis for the depth profile of this synthetic structure. Again, note that the difference in relative depth between components located within the same layer (e.g. A, B and C in Figure 5.68 (a) are not present in the trial-RDP (Figure 5.68 b).

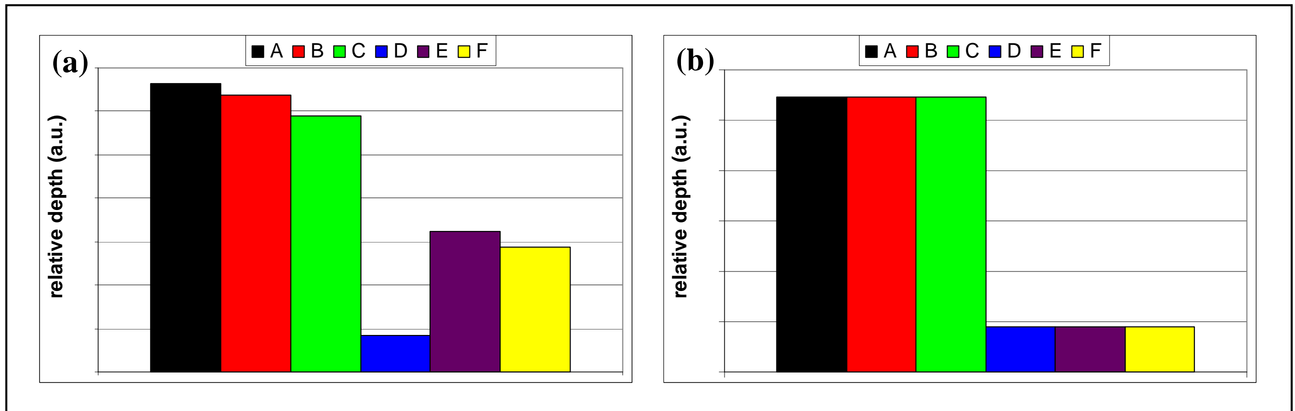

*Figure 5.68 : Relative depth plot of synthetic structure 6_3+3. (**a**) real-RDP and (**b**) trial-RDP.*

Table 5.19 shows layer thickness of both the model and MEM simulated depth profiles, together with component concentrations.

Table 5.19 : Depth profile parameters of the synthetic structure 6_3+3 and results of MEM simulation.

layer		**thickness (Å)**		**|deviation| (Å)**
		model	**simulation**	
overlayer		*21.0*	*21.3*	*0.3*
layer	**species**	**concentration (at.%)**		**relative error (%)**
		model	**simulation**	
overlayer	*A*	*20*	*20*	*0*
	B	*30*	*30*	*0*
	C	*50*	*50*	*0*
bulk	*D*	*60*	*56*	*-7*
	E	*15*	*16*	*7*
	F	*25*	*28*	*12*

SYNTHETIC STRUCTURE ***7_a*** AND ***7_a$_{error}$***

This synthetic structure was chosen to simulate the corrosion film of a Ni-18P alloy. As shown in Table 5.20, this synthetic structure is composed of a B-G contamination layer to simulate carbon-oxygen adventitious contamination, a D-F-G intermediate layer to simulate the presence of an orthophosphate layer, a pure A layer at the interface between the "phosphate" and the C-E bulk which simulates a Ni-18P alloy. Note that here the complexity of the system is not only the result of adding the 7th component, but also of the fact that this 7th component is present in both the contamination and phosphate layers.

As mentioned above, as well as in Chapter 4, our MEM protocol was applied to this synthetic structure in order to determine whether it was able to reconstruct the depth profiles used to calculate the ACD data to be fitted during the routine.

Figure 5.69 shows the depth profile of this synthetic structure 7_a, together with its MEM simulation (dotted lines). Figure 5.70 shows the real-ACD calculated using this synthetic structure (circles) and IMFP of 40, 30, 20, 10, 45, 35 and 25 Å for components A, B, C, D, E, F and G respectively, together with the recalculated MEM curves (dotted lines). The results obtained and their relative errors (with respect to the depth profile model) are given in Table 5.20.

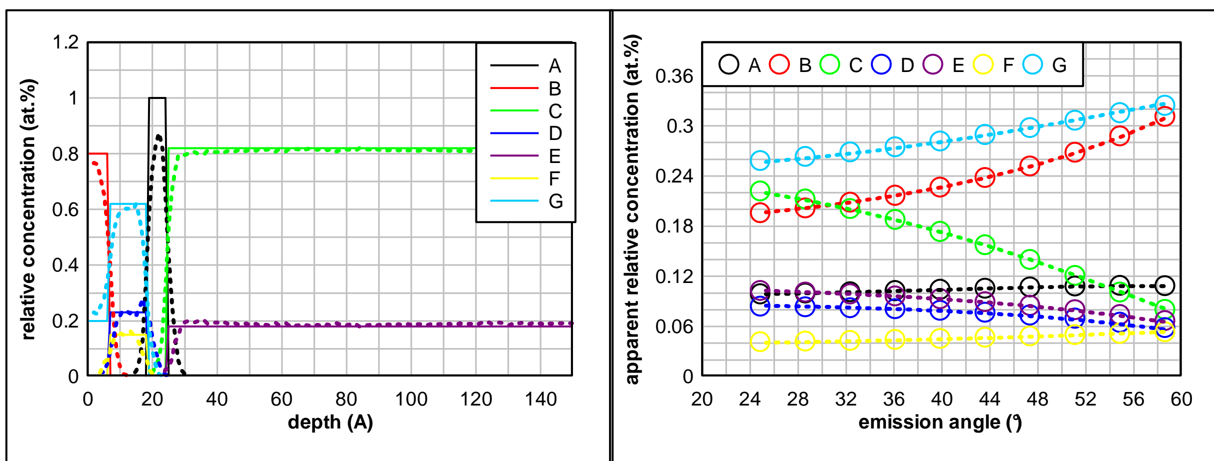

Figure 5.69 : Depth profile of synthetic structure 7_a and MEM simulation (dotted lines).

Figure 5.70 : Apparent concentration diagram of synthetic structure 7_a (circles) and recalculated MEM data (dotted lines).

However, even if a very good agreement was obtained with the depth profile model (Figure 5.69), experimental ACD data (i.e. corrected and normalized ARXPS peak intensities) are always affected to some degree by error. Experimental ACD "curves" are not so smooth as the theoretical ones plotted in Figure 5.70. Therefore, to assess the performance and accuracy of our MEM protocol when applied to experimental ACD data, a random error of ±10 % was added to each of the ACD points in Figure 5.70. Introduction of a random error, led to a new set of ACD data and, thus, to a new numerical experiment, referred to as 7_a_{error}. Our MEM protocol was applied to this new set and a new simulated depth profile was correspondingly reconstructed (Figure 5.71). The fit of the recalculated data with the error-affected ACD data is shown in Figure 5.72.

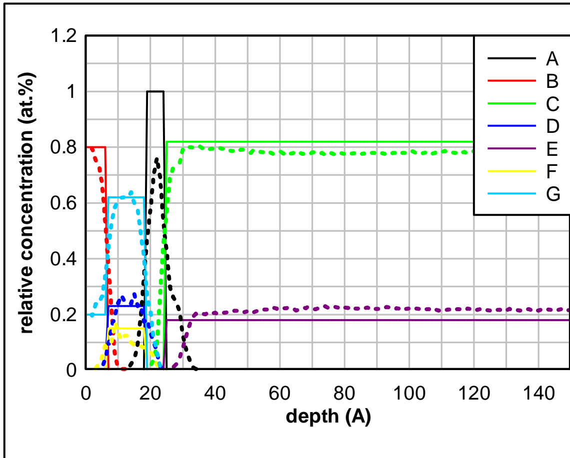

Figure 5.71 : Depth profile of synthetic structure 7_a_{error} and MEM simulation (dotted lines).

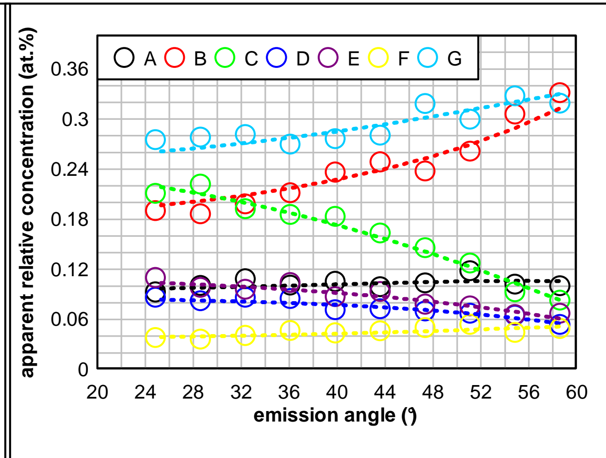

Figure 5.72 : Apparent Concentration Diagram of synthetic structure 7_a_{error} (circles) and recalculated MEM data (dotted lines).

Table 5.20 shows the results, and their relative errors, obtained in this 7_a_{error} numerical experiment.

Table 5.20 : Depth profile parameters of synthetic structure 7_a and results of MEM simulation, both with and without random error in the ACD data.

layer	model	simulation with error-free ACD data		simulation with error-affected ACD data	
	thickness (Å)	thickness (Å)	|deviation| (Å)	thickness (Å)	|deviation| (Å)
overlayer	*7*	*6.5*	*0.5*	*6.1*	*0.9*
1st intermediate layer	*12*	*11.9*	*0.1*	*12.5*	*0.5*
2nd intermediate layer	*6*	*7.9*	*1.9*	*9.2*	*3.2*

layer	species	model	simulation with error-free ACD data		simulation with error-affected ACD data	
		concentration (at%)	concentration (at%)	relative error (%)	concentration (at%)	relative error (%)
overlayer	*B*	*80*	*78*	*-3*	*79*	*-1*
	G	*20*	*22*	*10*	*21*	*5*
1st intermediate layer	*D*	*23*	*27*	*17*	*25*	*9*
	F	*15*	*14*	*-7*	*14*	*-7*
	G	*62*	*59*	*-5*	*61*	*-2*
bulk	*C*	*82*	*81*	*-1*	*79*	*-4*
	E	*18*	*19*	*6*	*21*	*17*

SYNTHETIC STRUCTURE ***7_b*** AND ***7_b$_{error}$***

This synthetic structure is exactly the same as 7_a reported above, but here an E-enriched layer was added in order to simulate the presence of an enriched P layer between the corrosion film and the NiP alloy.

As before, the MEM protocol was first applied to the theoretical ACD data. The reconstructed depth profile is shown in Figure 5.73 (dotted lines) together with the depth profile model, while Figure 5.74 shows the theoretical ACD data and their MEM curve fitting (dotted lines).

Then a random error of ±10 % was added to the theoretical ACD data in order to simulate a set of experimental data. Thus a new numerical experiment was performed on this new data set, referred to as 7_b$_{error}$. Figure 5.75 shows the reconstructed depth profile (dotted lines) together with the same depth profile model of the 7_b experiment, while Figure 5.76 shows these new ACD data and their MEM curve fitting (dotted lines).

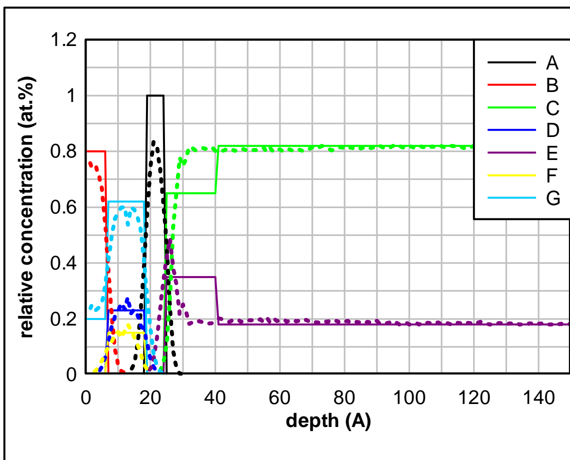

Figure 5.73 : In-depth profile of synthetic structure 7_b and MEM simulation (dotted lines).

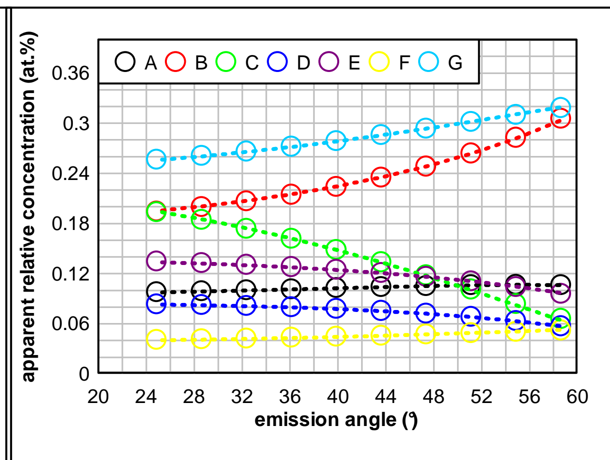

Figure 5.74 : Apparent Concentration Diagram of synthetic structure 7_b (circles) and recalculated MEM data (dotted lines).

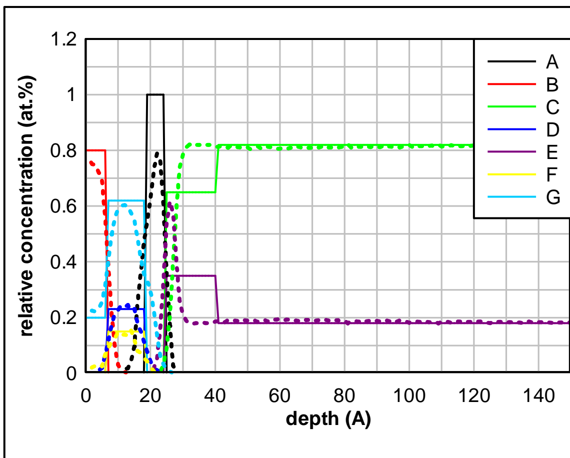

Figure 5.75 : In-depth profile of synthetic structure 7_b$_{error}$ and MEM simulation (dotted lines).

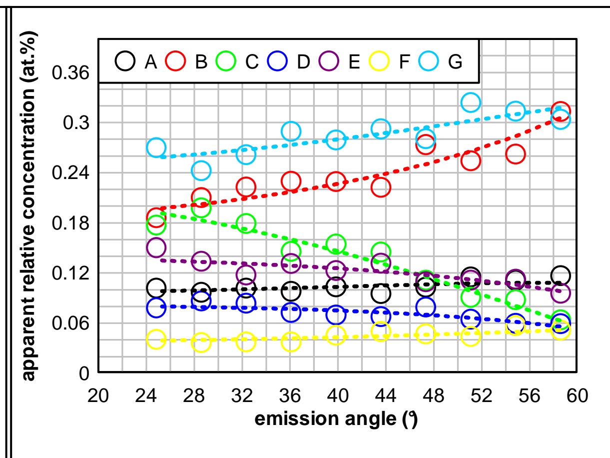

Figure 5.76 : Apparent Concentration Diagram of synthetic structure 7_b$_{error}$ (circles) and recalculated MEM data (dotted lines).

Table 5.21 shows the results obtained for both the 7_b and 7_b$_{error}$ numerical experiments, together with their relative errors.

Table 5.21 : Depth profile parameters of synthetic structure 7_b and results of MEM simulation, both with and without random error in ACD data.

layer	**model**	**simulation with error-free ACD data**		**simulation with error-affected ACD data**	
	thickness (Å)	**thickness (Å)**	**|deviation| (Å)**	**thickness (Å)**	**|deviation| (Å)**
overlayer	*7.0*	*6.4*	*0.6*	*6.6*	*0.4*
1st intermediate layer	*12.0*	*11.8*	*0.2*	*12.3*	*0.3*
2nd intermediate layer	*6.0*	*7.2*	*1.2*	*7.1*	*1.1*
E- enriched bulk layer	*16.0*	*8.7*	*7.3*	*8.0*	*8.0*

layer	**species**	**model**	**simulation with error-free ACD data**		**simulation with error-affected ACD data**	
		concentration (at.%)	**concentration (at.%)**	**relative error (%)**	**concentration (at.%)**	**relative error (%)**
overlayer	*B*	*80*	*78*	*-3*	*79*	*-1*
	G	*20*	*22*	*10*	*21*	*5*
1st intermediate layer	*D*	*23*	*24*	*4*	*22*	*-4*
	F	*15*	*15*	*0*	*14*	*-7*
	G	*62*	*61*	*-2*	*64*	*3*
E-enriched bulk layer	*C*	*65*	*65*	*0*	*62*	*-5*
	E	*35*	*35*	*0*	*38*	*9*
bulk	*C*	*82*	*constrained*	*/*	*constrained*	*/*
	E	*18*	*constrained*	*/*	*constrained*	*/*

SYNTHETIC STRUCTURE ***8*** AND ***8$_{error}$***

This synthetic structure, referred to as 8, was also chosen to simulate the corrosion film of a Ni-18P alloy. As shown in Table 5.22, this synthetic structure consists of a B-H contamination layer to simulate carbon-oxygen adventitious contamination and a D-F-G intermediate layer to simulate the presence of an orthophosphate layer. Between this

"phosphate" layer and the C-E bulk simulating the Ni-18P alloy, there is a complex interface where the A component is mixed with an E-enriched phase of the bulk.

Figure 5.77 shows the depth profile of this synthetic structure 8, together with its MEM simulation (dotted lines). Figure 5.78 shows the real-ACD calculated using this synthetic structure (circles) and IMFP of 40, 30, 20, 10, 45, 35, 25 and 27 Å for components A, B, C, D, E, F, G and H respectively, together with the recalculated MEM curves (dotted lines).

Here too, a random error of ± 10% was introduced for each of the theoretical ACD data to simulate the random error which always affects any experimental data set and a new numerical experiment was performed, referred to as 8_{error}. Figure 5.79 shows the reconstructed depth profile (dotted lines) together with the same in-depth profile model of the 8 experiment, while figure 5.80 shows these new ACD data and their MEM curve fitting (dotted lines).

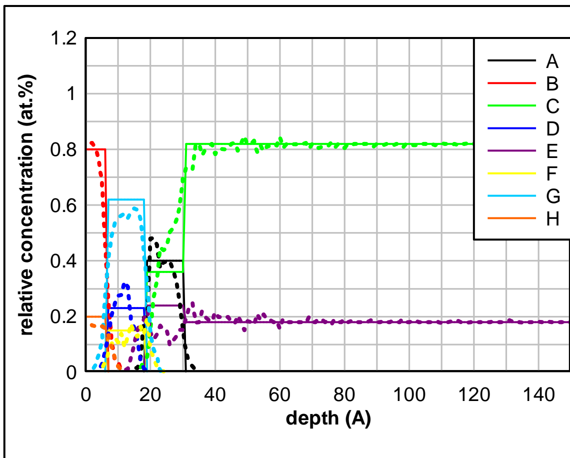

Figure 5.77 : Depth profile of synthetic structure 8 and MEM simulation (dotted lines).

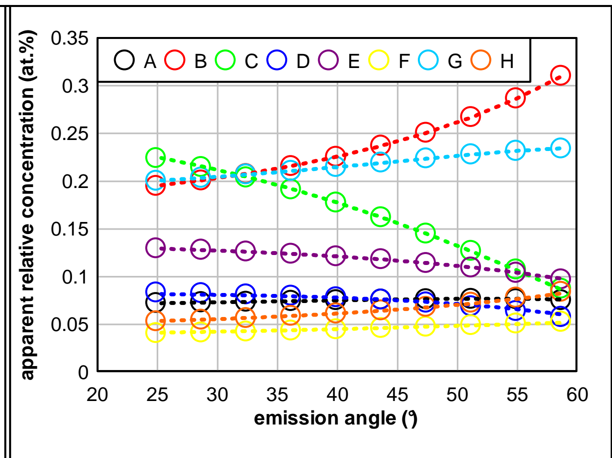

Figure 5.78 : Apparent concentration diagram of synthetic structure 8 (circles) and recalculated MEM data (dotted lines).

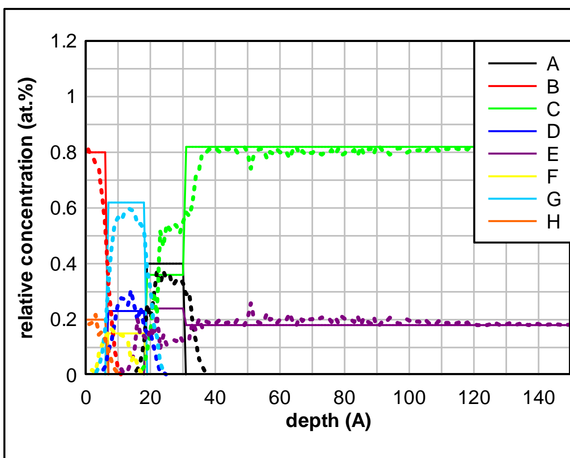

Figure 5.79 : Depth profile of synthetic structure 8_{error} and MEM simulation (dotted lines).

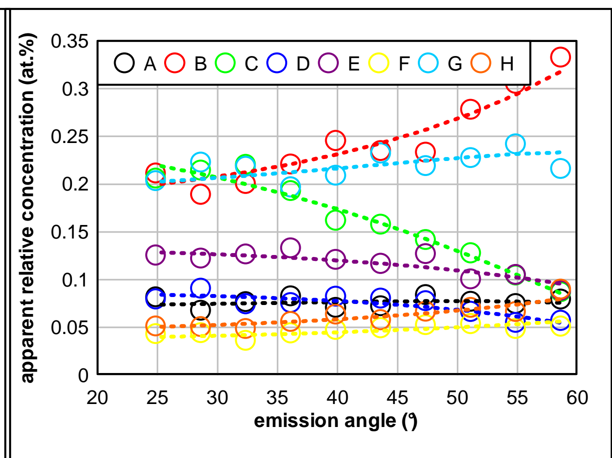

Figure 5.80 : Apparent concentration diagram of synthetic structure 8_{error} (circles) and recalculated MEM data (dotted lines).

Table 5.21 shows the results obtained for both the 7_b and 7_b$_{error}$ numerical experiments, together with their relative errors with respect to the depth profile model.

Table 5.22 : Depth profile parameters of synthetic structure 8 and results of MEM simulation, both with and without random error in the ACD data.

layer	model	simulation with error-free ACD data		simulation with error-affected ACD data	
	thickness (Å)	thickness (Å)	|deviation| (Å)	thickness (Å)	|deviation| (Å)
overlayer	*7.0*	*6.6*	*0.4*	*6.8*	*0.2*
intermediate layer	*12.0*	*12.1*	*0.1*	*12.7*	*0.7*
E-enriched bulk + A layer	*12.0*	*11.8*	*0.2*	*15.0*	*3.0*

layer	species	model	simulation with error-free ACD data		simulation with error-affected ACD data	
		concentration (at.%)	concentration (at.%)	relative error (%)	concentration (at.%)	relative error (%)
overlayer	*B*	*80*	*78*	*-3*	*81*	*1*
	H	*20*	*22*	*10*	*19*	*-5*
intermediate layer	*D*	*23*	*27*	*17*	*25*	*9*
	F	*15*	*14*	*-7*	*13*	*-13*
	G	*62*	*59*	*-5*	*62*	*0*
E-enriched bulk + A layer	*A*	*40*	*40*	*0*	*34*	*-15*
	C	*36*	*40*	*11*	*47*	*31*
	E	*24*	*20*	*-17*	*19*	*-21*
bulk	*C*	*82*	*constrained*	*/*	*constrained*	*/*
	E	*18*	*constrained*	*/*	*constrained*	*/*

5.4.6.2 APPLICATION TO REAL SAMPLES

Our MEM algorithms protocol was applied to ARXPS data, recorded for the NiP alloys after 1, 3 and 14 hours polarization in Na_2SO_4 0.1 M at +0.1 V SCE. Spectra were recorded at 16 different emission angles ranging from 24.88° to 81.13°. However, spectra at emission angles above 60° were not considered owing to the increasing effect of elastic scattering [1,2]. Data processing was performed with CASA XPS software (Casasoftware Ltd., UK) as previously

described (§ 4.4.6). Then, the high resolution angle-resolved spectra of C1s, O1s, $Ni2p_{3/2}$ and P2p regions were resolved into their components and intensity was determined. Intensities were then corrected for photoionization cross-section [3], angular asymmetry function (§ 4.5.2) and Theta Probe IERF (§ 4.4.4). Regarding angular asymmetry function, note that for the Theta Probe ARXPS acquisition mode, γ angle was not constant since data collection was done without tilting the specimen. Lastly, corrected intensities were normalized to 1 for each emission angle. Corrected and normalized intensities were plotted against emission angle to construct the ACD.

IMFP were calculated using the G-1 predictive equation [4]. The G-1 equation was implemented with NIST "Standard Reference Database 71" software [5]. IMFP values were plotted versus electron KE, ranging from 200 to 2000 eV, considering an electron travelling through four different materials:

mat. 6) ill-defined homogeneous material composed of O (α at.%) and C (β at.%) with density of 1 g cm^{-3} to simulate adventitious surface contamination

mat. 7) $Ni_3(PO_4)_2$ with density 1.6 g cm^{-3} determined by the immersion method

mat. 8) pure red phosphorus [4]

mat. 9) NiP alloy with phosphorus content of 18 at.% and density of 7.75 g cm^{-3} [6]

Then the electron IMFP values were calculated for all the chemical species contained in the NiP polarized specimens (i.e. for the photoelectrons which generated the corresponding components of the XPS signals) as the photoelectrons travelled through each of the materials considered separately (i.e. four different IMFP values for each of the signal electrons). Starting from these values, the actual IMFP values were determined with the simulator routine, as described above (§ 4.5.4.8). Figure 5.81

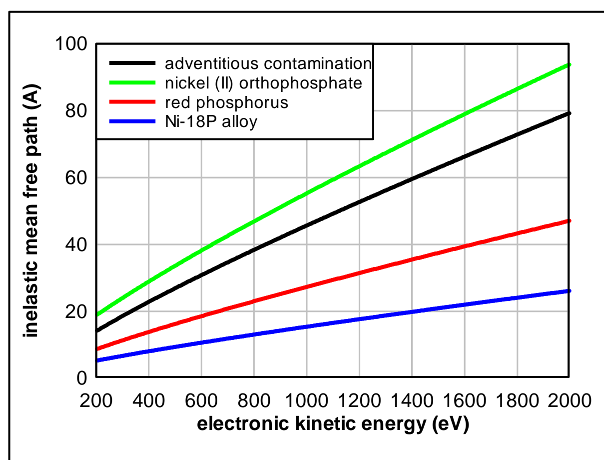

Figure 5.81 : Inelastic mean free path versus kinetic energy of photoelectrons travelling through the adventitious contamination layer, nickel (II) orthophosphate, red phosphorus and a Ni-18P alloy.

shows the IMFP vs. KE plot for the four materials (for *mat.1*, the first hypothesized composition of 80 at.% C and 20 at.% O is shown).

1 HOUR POLARIZATION

Figure 5.82 shows the ACD and corresponding RDP, calculated from the ARXPS data acquired from a Ni-18P alloy after 1 hour polarization at +0.1 V SCE in 0.1 M Na_2SO_4.

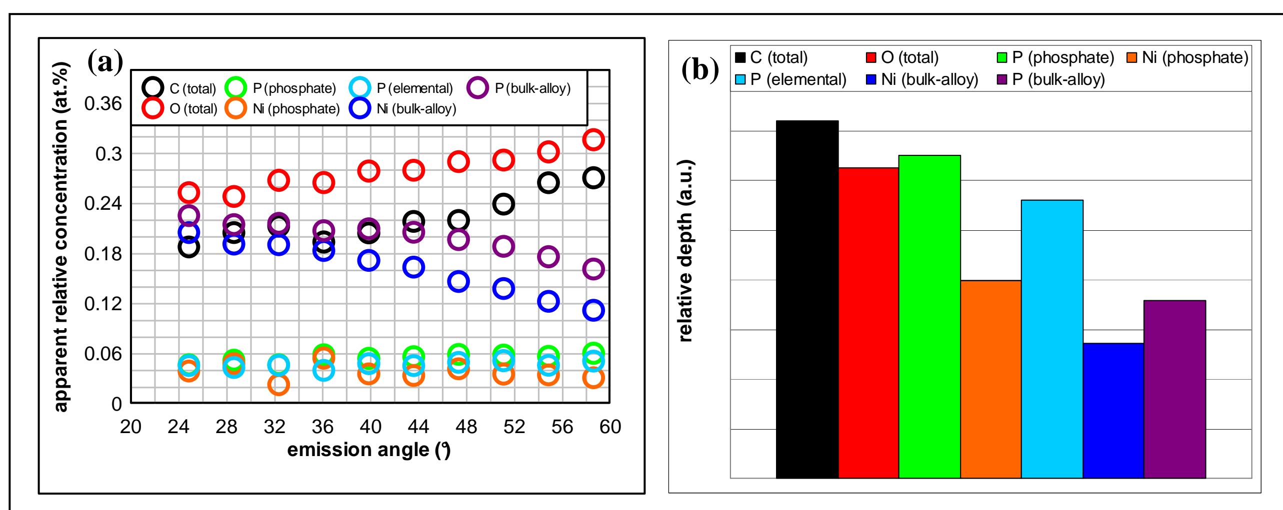

*Figure 5.82 : (**a**) ACD and (**b**) RDP of a Ni-18P alloy after 1 hour polarization at +0.1 V SCE in 0.1 M Na_2SO_4.*

Considering that the IMFP of a photoelectron travelling through a generic material is proportional to its kinetic energy, the series $P2p_{3/2}$ > C1s > O1s > $Ni2p_{3/2}$ can be identified. So, observing the ACD and RDP, and taking into account the results of Tougaard's method (§ 5.4.5.2), a nickel (II) phosphate layer was initially hypothesized to have formed on the alloy surface. A carbon-oxygen contamination film was located on the phosphate film as the overlayer, while the elemental phosphorus could be located at the interface between the phosphate layer and bulk alloy.

Using our simulator routine, the best layered structure was determined (Figure 5.83 a) and a suitable IMFP set was found correspondingly (total C1s = 65.08 Å ; total O1s = 54.07 Å ; phosphate $P2p_{3/2}$ = 70.22 Å ; phosphate $Ni2p_{3/2}$ = 39.98 Å ; elemental $P2p_{3/2}$ = 53.19 Å ; bulk-alloy $Ni2p_{3/2}$ = 14.63 Å ; bulk-alloy $P2p_{3/2}$ = 25.69 Å). The ACD curves of this layered

structure were calculated and are shown in Figure 5.83 b, together with the experimental ACD data.

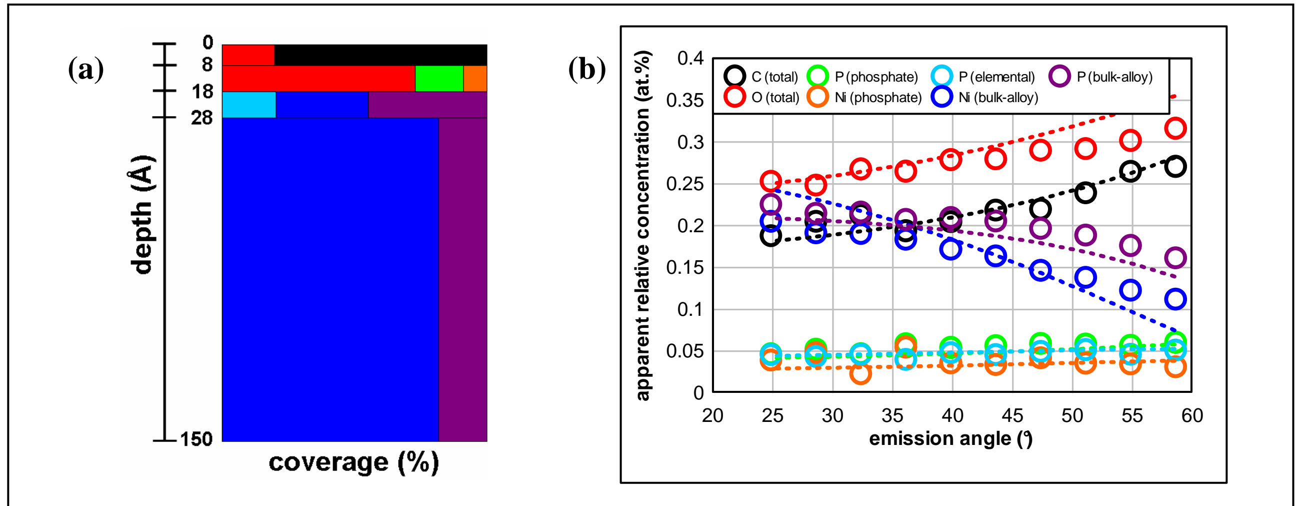

*Figure 5.83 : **(a)** Best layered structure for depth profile of a Ni-18P alloy after 1 hour polarization and **(b)** ACD curves calculated correspondingly (dotted lines); experimental ACD data are also shown (circles).*

Then, the simulator routine was used to find the starting parameters, i.e. layer thickness and a suitable IMFP set, for applying our MEM algorithms protocol to the experimental ACD data. Lastly, Figure 5.84 shows the reconstructed depth profile of the sample, Figure 5.85 the corresponding ACD data fit.

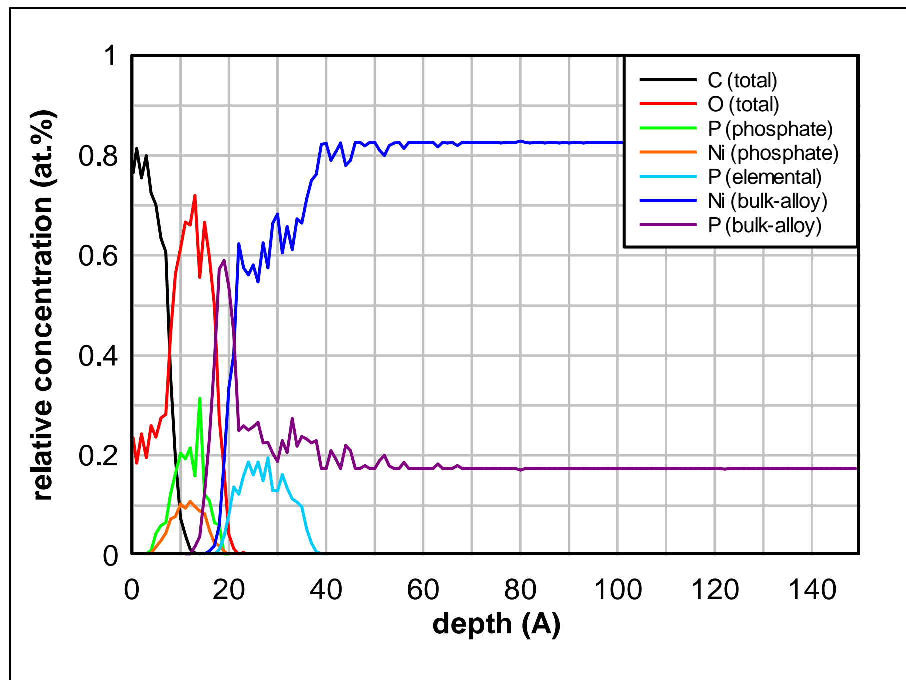

Figure 5.84 : Depth profile of a Ni-18P alloy after 1 hour polarization at +0.1 V SCE in 0.1 M Na_2SO_4.

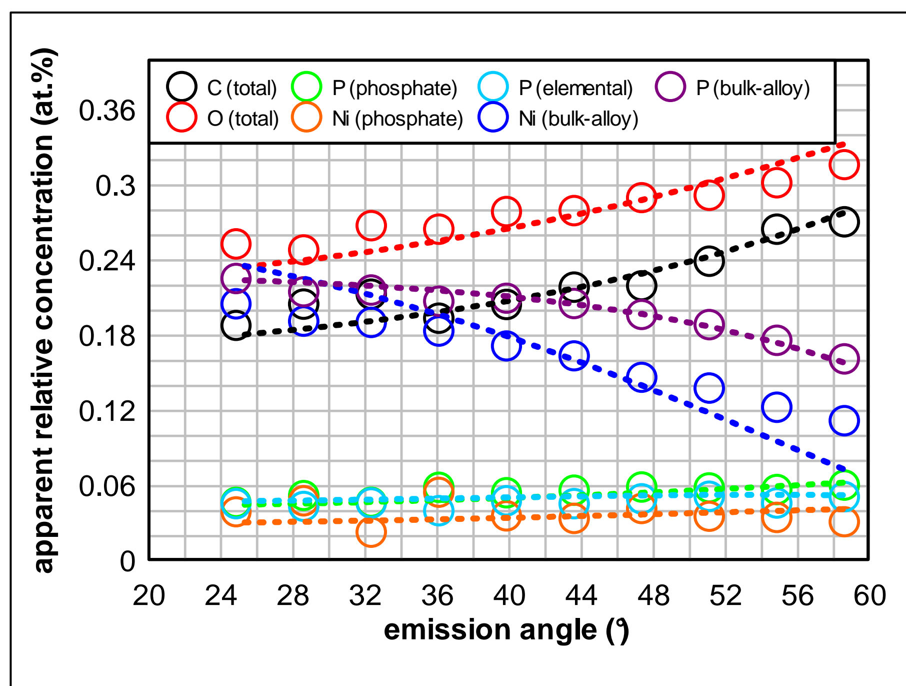

Figure 5.85 : Apparent concentration diagram of a Ni-18P alloy after 1 hour polarization at +0.1 V SCE in 0.1 M Na_2SO_4 (circles) and recalculated MEM data (dotted lines).

Table 5.23 shows layer thickness and species concentration together with their uncertainty, which was calculated as three times the standard deviation between three independent determinations.

Table 5.23 : Depth profile parameters of a Ni-18P alloy after 1 hour polarization at +0.1 V SCE in 0.1 M Na_2SO_4.

layer	thickness (Å)	species	concentration (at.%)
adventitious contamination	*10 ± 9*	*C*	*78 ± 12*
		O	*22 ± 12*
nickel phosphate	*12 ± 6*	*Ni*	*11 ± 3*
		P	*23 ± 9*
		O	*66 ± 12*
P-enriched	*20 ± 6*	*Ni*	*54 ± 6*
		P (bulk-alloy)	*33 ± 3*
		P (elemental)	*13 ± 3*
bulk	*/*	*Ni*	*82 (constrained)*
		P	*18 (constrained)*

P/Ni ratio in the bulk alloy is equal to 0.22, while, total P/Ni ratio for the P-enriched layer is 0.85.

3 HOURS POLARIZATION

Figure 5.86 shows the ACD and corresponding RDP, calculated from the ARXPS data acquired from a NiP specimen after 3 hours polarization at +0.1 V SCE in 0.1 M Na_2SO_4.

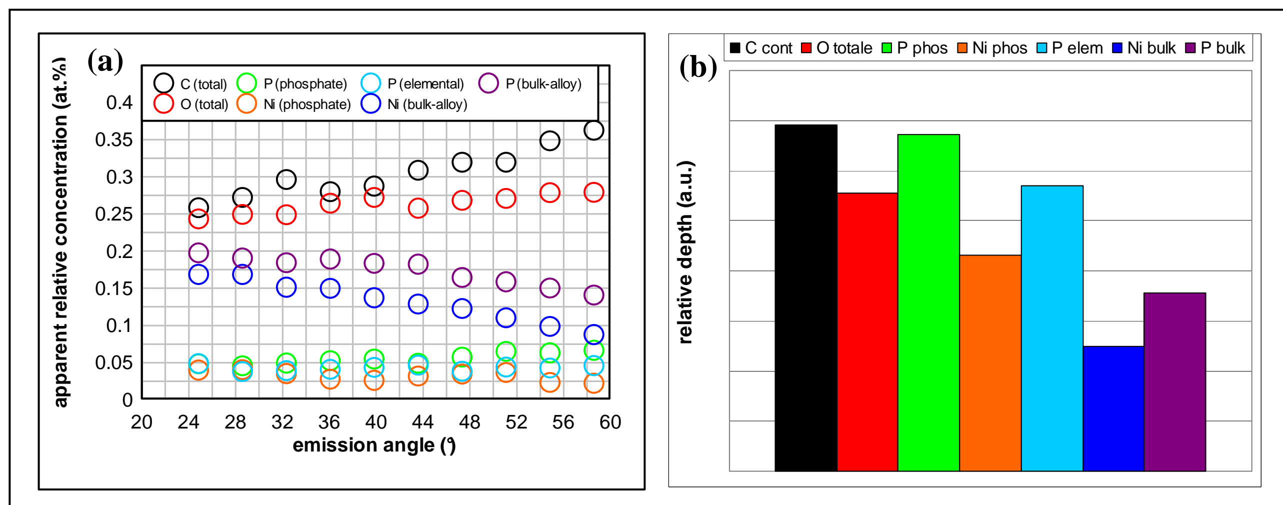

*Figure 5.86 : (**a**) ACD and (**b**) RDP of a Ni-18P alloy after 3 hours polarization at +0.1 V SCE in 0.1 M Na_2SO_4.*

Using our simulator routine, the best layered structure was determined (Figure 5.87 a) and a suitable IMFP set was found correspondingly (total C1s = 65.08 Å ; total O1s = 54.21 Å ; phosphate $P2p_{3/2}$ = 70.41 Å ; phosphate $Ni2p_{3/2}$ = 40.09 Å ; elemental $P2p_{3/2}$ = 52.28 Å ; bulk-alloy $Ni2p_{3/2}$ = 15.04 Å ; bulk-alloy $P2p_{3/2}$ = 26.39 Å). The ACD curves of this layered structure were calculated and are shown in Figure 5.87 b, together with the experimental ACD data.

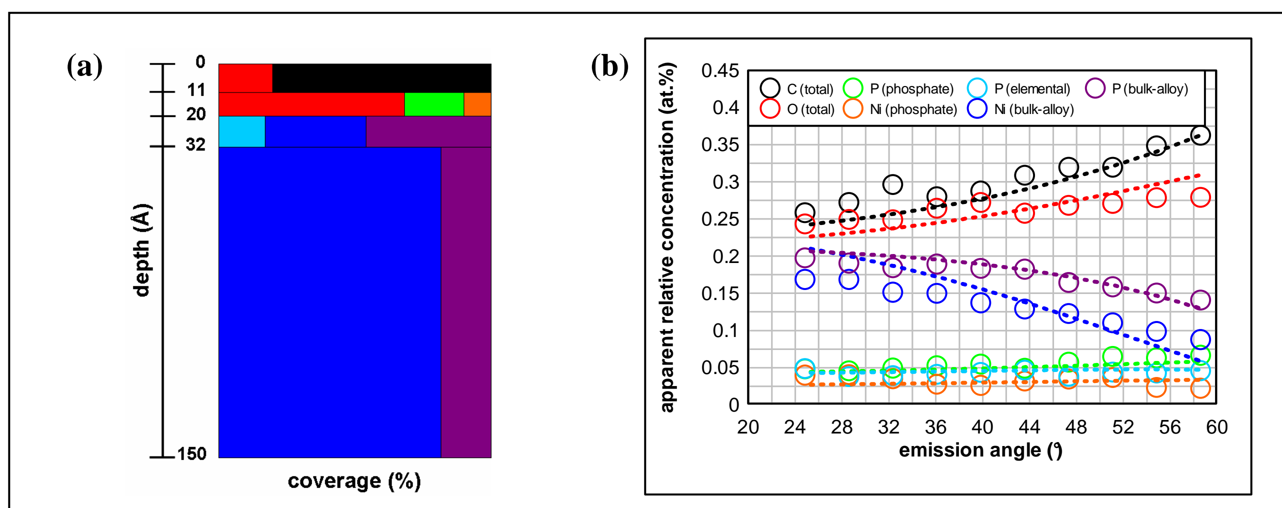

*Figure 5.87 : (**a**) Best layered structure for-depth profile of a Ni-18P alloy after 3 hours polarization and (**b**) ACD curves calculated correspondingly (dotted lines); experimental ACD data are also shown (circles).*

Lastly, Figure 5.88 shows the reconstructed depth profile of the sample, Figure 5.89 the corresponding ACD data fit.

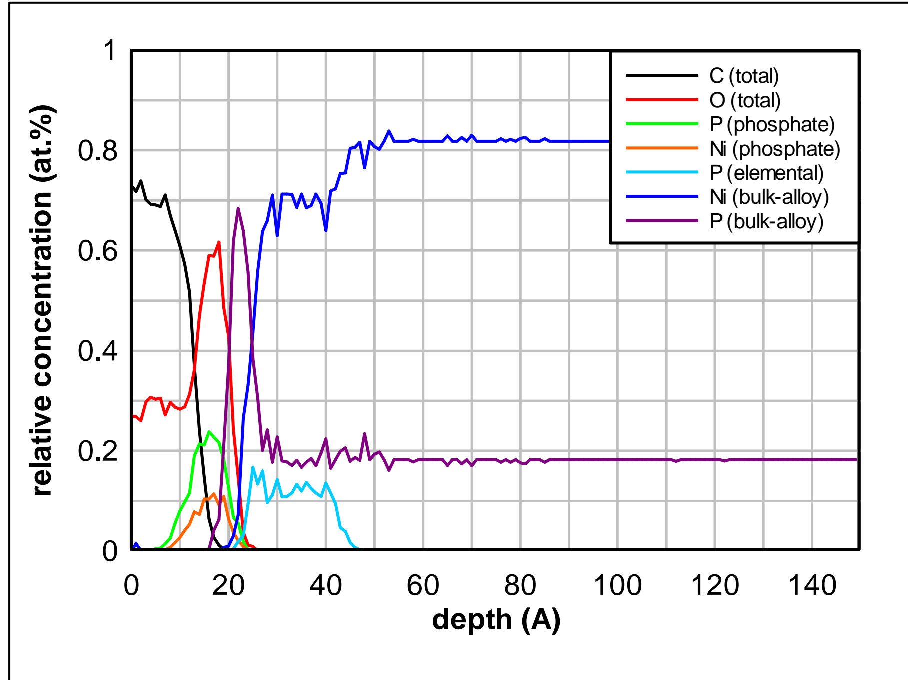

Figure 5.88 : Depth profile of a Ni-18P alloy after 3 hours polarization at +0.1 V SCE in 0.1 M Na_2SO_4.

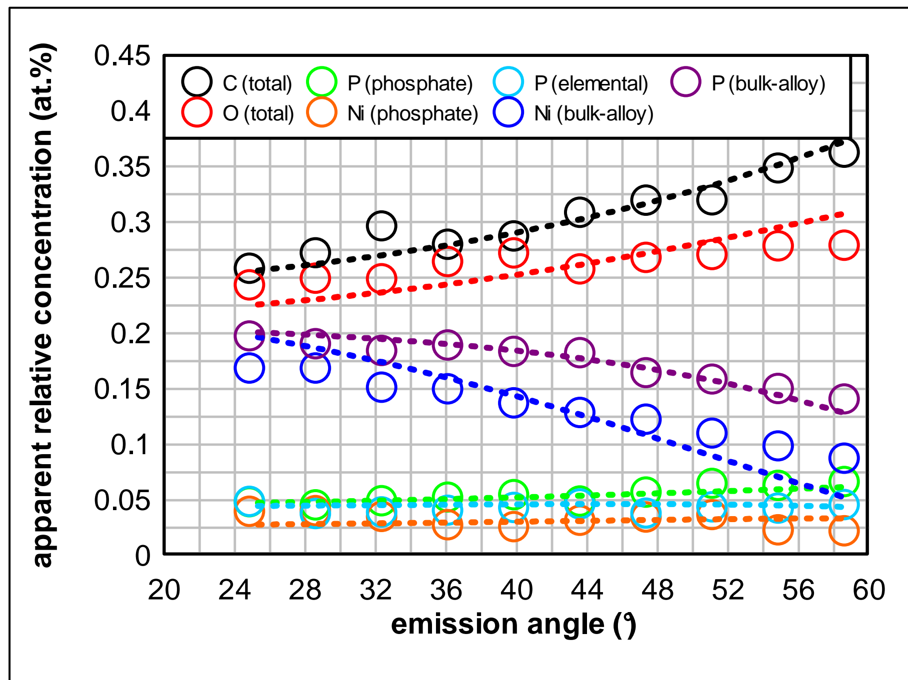

Figure 5.89 : Apparent concentration diagram of a Ni-18P alloy after 3 hours polarization at +0.1 V SCE in 0.1 M Na_2SO_4 (circles) and recalculated MEM data (dotted lines).

Table 5.24 shows layer thickness and species concentration together with their uncertainty, which was calculated as three times the standard deviation between three independent determinations.

Table 5.24 : Depth profile parameters of a Ni-18P alloy after 3 hours polarization at +0.1 V SCE in 0.1 M Na_2SO_4.

layer	thickness (Å)	species	concentration (at.%)
adventitious contamination	*11 ± 6*	*C*	*74 ± 9*
		O	*26 ± 9*
nickel phosphate	*11 ± 6*	*Ni*	*11 ± 3*
		P	*27 ± 12*
		O	*62 ± 12*
P-enriched	*21 ± 6*	*Ni*	*56 ± 9*
		P (bulk-alloy)	*32 ± 6*
		P (elemental)	*12 ± 3*
bulk	*/*	*Ni*	*82 (constrained)*
		P	*18 (constrained)*

P/Ni ratio in the bulk alloy is equal to 0.22, while, total P/Ni ratio of the P-enriched layer is 0.79.

14 HOUR S POLARIZATION

Figure 5.90 shows the ACD and corresponding RDP, calculated from the ARXPS data acquired from a NiP specimen after 14 hours polarization at +0.1 V SCE in 0.1 M Na_2SO_4.

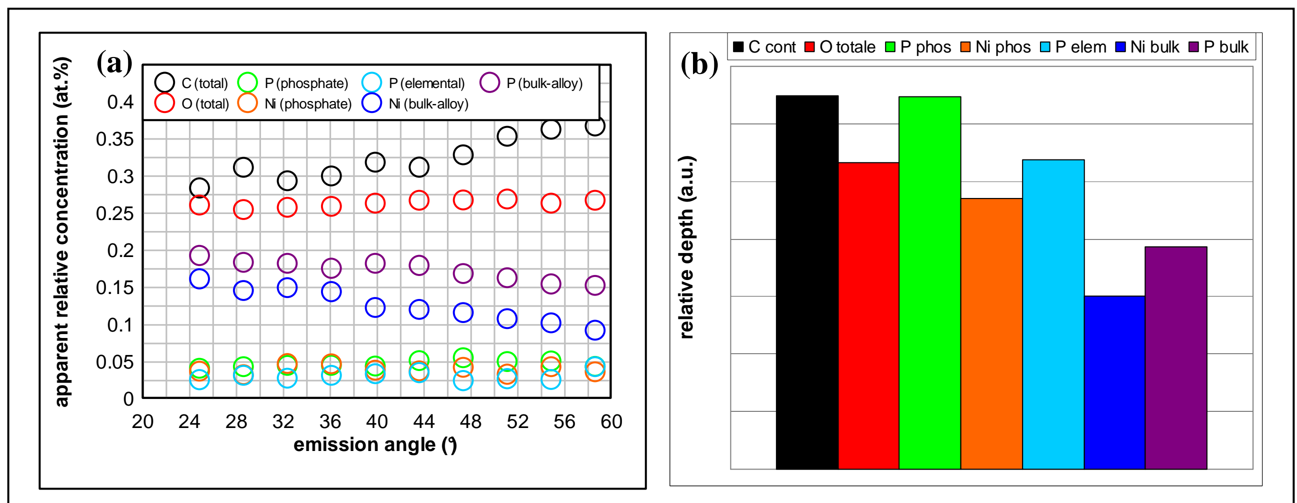

*Figure 5.90 : (**a**) ACD and (**b**) RDP of a Ni-18P alloy after 14 hours polarization at +0.1 V SCE in 0.1 M Na_2SO_4.*

Using our simulator routine, the best layered structure was determined (Figure 5.91 a) and a suitable IMFP set was found correspondingly (total C1s = 65.08 Å ; total O1s = 54.27 Å ; phosphate $P2p_{3/2}$ = 70.48 Å ; phosphate $Ni2p_{3/2}$ = 40.13 Å ; elemental $P2p_{3/2}$ = 53.18 Å ; bulk-alloy $Ni2p_{3/2}$ = 15.40 Å ; bulk-alloy $P2p_{3/2}$ = 27.04 Å). The ACD curves of this layered structure were calculated and are shown in Figure 5.91 b, together with the experimental ACD data.

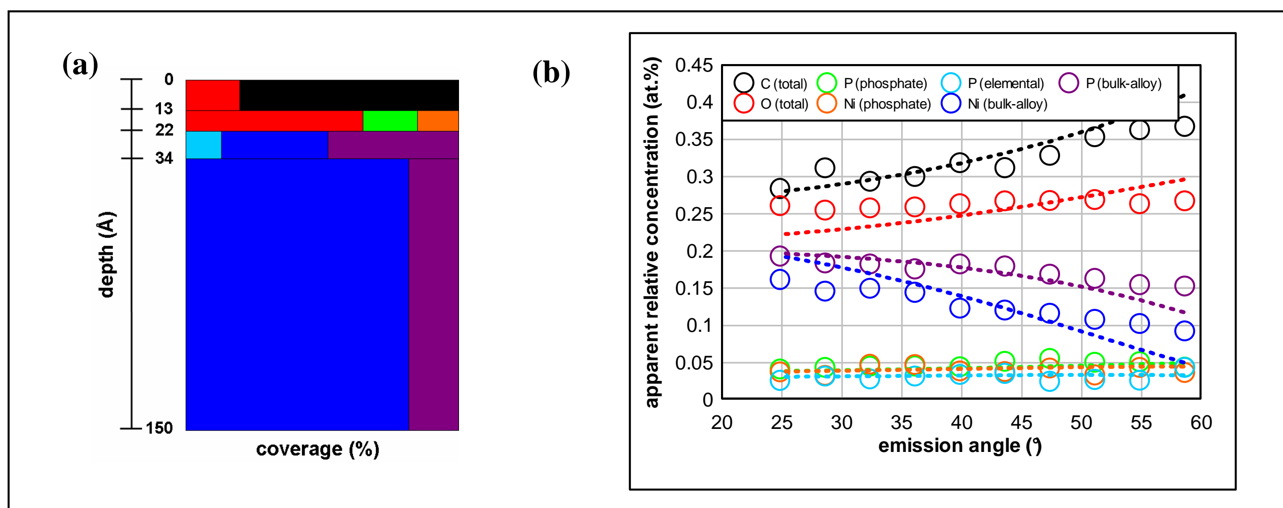

*Figure 5.91 : **(a)** Best layered structure for depth profile of a Ni-18P alloy after 14 hours polarization and **(b)** ACD curves calculated correspondingly (dotted lines); experimental ACD data are also shown (circles).*

Lastly, Figure 5.92 shows the reconstructed depth profile of the sample, Figure 5.93 the corresponding ACD data fit.

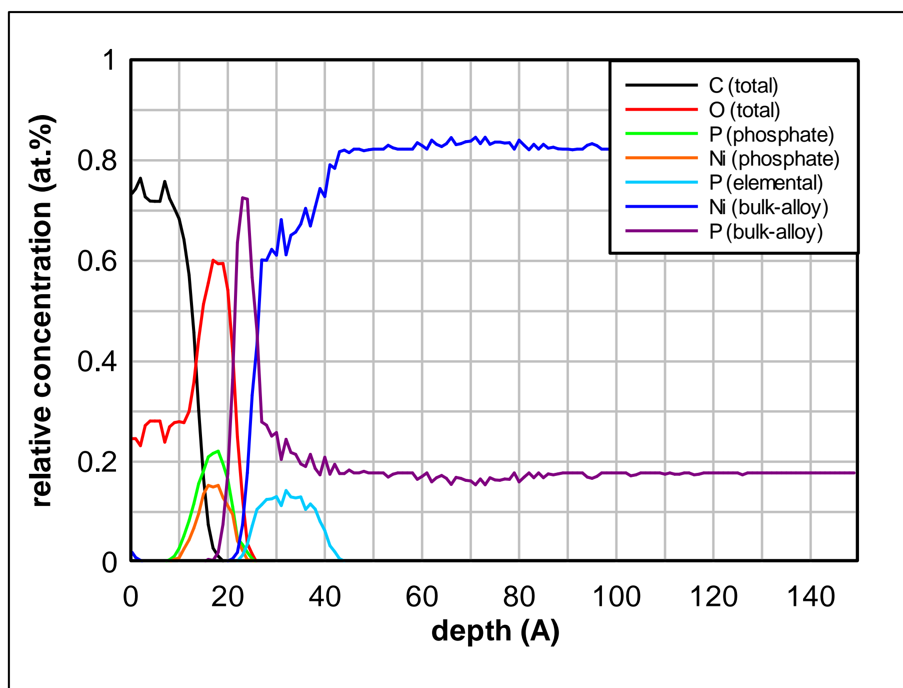

Figure 5.92 : Depth profile of a Ni-18P alloy after 14 hours polarization at +0.1 V SCE in 0.1 M Na_2SO_4.

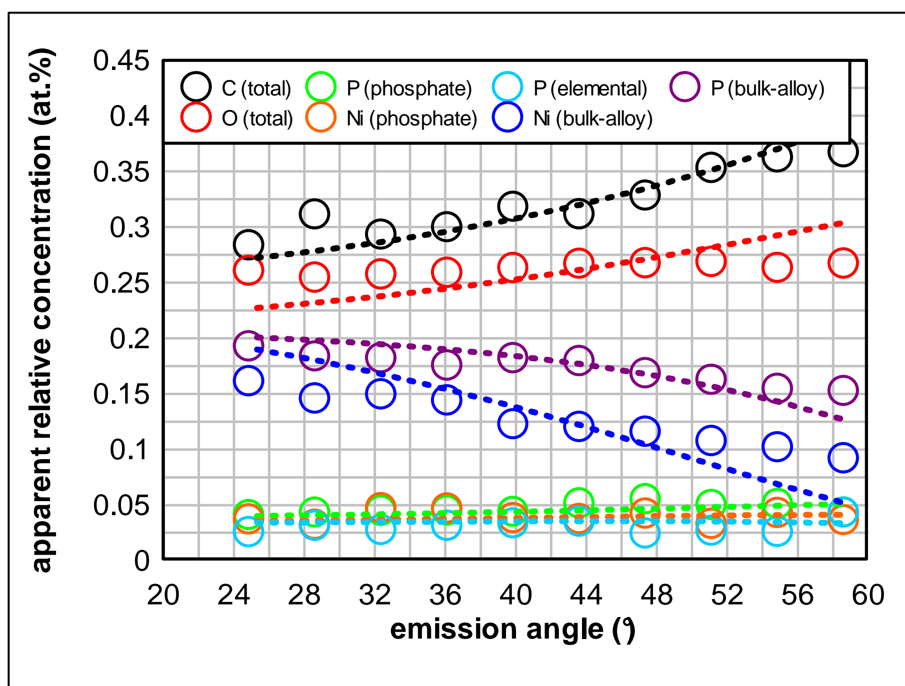

Figure 5.93 : Apparent concentration diagram of a Ni-18P alloy after 14 hours polarization at +0.1 V SCE in 0.1 M Na_2SO_4 (circles) and recalculated MEM data (dotted lines).

Table 5.25 shows layer thickness and species concentration together with their uncertainty, which was calculated as three times the standard deviation between three independent determinations.

Table 5.25 : Depth profile parameters of a Ni-18P alloy after 14 hours polarization at +0.1 V SCE in 0.1 M Na_2SO_4.

layer	thickness (Å)	species	concentration (at.%)
adventitious contamination	*12 ± 6*	*C*	*77 ± 6*
		O	*23 ± 6*
nickel phosphate	*11 ± 3*	*Ni*	*15 ± 6*
		P	*21 ± 3*
		O	*64 ± 6*
P-enriched	*18 ± 3*	*Ni*	*53 ± 3*
		P (bulk-alloy)	*36 ± 3*
		P (elemental)	*11 ± 3*
bulk	*/*	*Ni*	*82 (constrained)*
		P	*18 (constrained)*

P/Ni ratio in the bulk alloy is equal to 0.22, total P/Ni ratio of the P-enriched layer is 0.89.

5.4.6.3 SUMMARY OF THE MEM RESULTS OBTAINED ON THE POLARIZED SAMPLES

Table 5.26 summarizes the MEM results of the depth profile of a Ni-18P alloy, examined after polarization for the three times investigated in this work, i.e. 1, 3 and 14 hours at +0.1 V SCE in 0.1 M Na_2SO_4.

Table 5.26 : Depth profile parameters of a Ni-18P alloy after 1, 3 and 14 hours polarization at +0.1 V SCE in 0.1 M Na_2SO_4.

layer	thickness (Å)			species	concentration (at.%)		
	1 hour	3 hours	14 hours		1 hour	3 hours	14 hours
adventitious contamination	*10 ± 9*	*11 ± 6*	*12 ± 6*	***C***	*78 ± 12*	*74 ± 9*	*77 ± 6*
				O	*22 ± 12*	*26 ± 9*	*23 ± 6*
nickel phosphate	*12 ± 6*	*11 ± 6*	*11 ± 3*	***Ni***	*11 ± 3*	*11 ± 3*	*15 ± 6*
				P	*23 ± 9*	*27 ± 12*	*21 ± 3*
				O	*66 ± 12*	*62 ± 12*	*64 ± 6*
P-enriched	*20 ± 6*	*21 ± 6*	*18 ± 3*	***Ni***	*54 ± 6*	*56 ± 9*	*53 ± 3*
				P (bulk-alloy)	*33 ± 3*	*32 ± 6*	*36 ± 3*
				P (elemental)	*13 ± 3*	*12 ± 3*	*11 ± 3*

REFERENCES

1. P. J. Cumpson, in *Angle-resolved X-Ray Photoelectron Spectroscopy* in *Surface Analysis by Auger and X-Ray Photoelectron Spectroscopy* - Briggs D, Grant JT (eds) - Surface Spectra and IM Publications - Manchester, NH; p.651 (2003)
2. P. J. Cumpson, M. P. Seah, *Surface and Interface Analysis* 25, 430 (1997)
3. J. H. Scofield, *J. of Electron Spectroscopy* 8, 129 (1976)
4. W. H. Gries, *Surface and Interface Analyisis* 24, 38-50 (1996)
5. C. J. Powell, A. Jablonski, NIST Electron Inelastic-Mean-Free-Path Database v.1.1 (2000)
6. PhD thesis of R. Taheri, *Evaluation of Electroless Nickel-Phosphorus (EN) Coatings*, University of Saskatchevan, Saskatoon, CDN (2002)

CHAPTER 6

DISCUSSION

In this chapter the experimental results are discussed comparing them with each other and with those found in the literature. The electrochemical results are discussed in section 6.1. Then, in section 6.2, the XPS spectra acquired both in the standard and the angle-resolved mode are compared to those acquired on the reference compounds analyzed in this work and to those reported in the literature. The spectra acquired in the standard mode are discussed in order to clarify the chemical state of the elements present in the surface films formed on the Ni18P alloy. . Section 6.3 discusses the results of the ion sputtering kinetics performed on the Ni29P and Ni18P alloys: a procedure to monitor the changes induced by the ion sputtering is proposed: changes of the intensity of the P2p signal appears to be a suitable method to avoid the alteration of the surface composition of the NiP alloy due to the preferential sputtering of phosphorus.

The results of the XPS quantitative analysis of the sputtered NiP alloys obtained with the First Principles method and the Tougaard's method are compared with each other and with the results of the EDX analysis. The spectra acquired in the angle-resolved mode are discussed to illustrate the starting point for the non-destructive determination of the concentration in-depth profile. In section 6.4 the results of the concentrations in-depth profile of the polarized NiP alloys obtained with both the Tougaard's method and the MEM protocol are discussed and compared with each other. To validate the MEM protocol and to assess its performances and accuracy the results obtained on model arxps data are discussed. Finally in section 6.5, a new model for the film formation mechanism and for explaining the corrosion resistance of the Ni18P in contact with solution is put forward.

6.1 ELECTROCHEMICAL BEHAVIOUR

The corrosion performance of NiP alloys is one of the major reasons for their wide application in a variety of industrial fields. However, despite being widely studied, no conclusive explanation for their corrosion resistance has yet been provided.

It is well known [1-7] that amorphous/nanocrystalline NiP alloys show high corrosion resistance both in acidic and neutral solutions and that the anodic behaviour of amorphous alloys differs from that of pure crystalline nickel [2,8-10].

6.1.1 CURRENT ARREST

NiP alloys passivate at potentials at which Ni dissolves actively, while at more anodic potentials the alloy undergoes transpassive dissolution in a potential region where nickel passivates. Furthermore, the anodic behaviour of NiP alloys is unaffected by the presence or concentration of chloride ions, while pure Ni is severely pitted [2,8-10]. The results of this work confirmed these observations (§ 5.3.1). Ni-18P alloys exhibit a current density arrest, in the potentiodynamic polarization curves, both in acidic and near neutral solutions, in the potential range from ca. -0.2 V to +0.2 V SCE (Figure 5.5), where active-passive transition takes place for pure nickel [2,11-14]. This current arrest as well as the current increase at potentials higher than +0.2 V SCE, were found to be practically independent of solution pH. The same results have been reported for electrodeposited NiP alloys with 23 and 29 at.% P in a pH range from 1 to 6 [14]. In addition, this current arrest was found to be independent of chloride presence and, as previously reported [12,13], of chloride concentration too. These results rule out the classical passivation mechanism by oxy-hydroxide film formation that is known for pure nickel [15-17], in agreement with XPS surface analytical results (see below), no nickel oxide being found on samples potentiostatically polarized in the current arrest region (Figure 5.12).

6.1.2 PASSIVATION VS. DIFFUSION LIMITATION

Results of potentiostatic experiments in the current arrest region (§ 5.3.2) provide additional important information. Whereas the current decay for pure nickel follows a power law with exponent -1 (i.e. slope in logi/logt plots), NiP alloys show a power law decay with an exponent of about -0.5, thus a square root law (Figure 5.6). This behaviour has been reported for electrodeposited NiP alloys in neutral chloride-containing solutions [13], sulphuric acid [2,9,11] and hydrochloric acid [2]. The electrochemical results can be interpreted in terms of diffusion of the faster dissolving component of the alloy (nickel) through the developing

surface layer enriched in the slower dissolving component (phosphorus) [11-13,18,19]. Preferential dissolution of nickel from the NiP alloys is well documented and electrochemical results provide evidence of a diffusion controlled process. Thus, the observed current decay may be due to the slowing down of nickel diffusion through a thickening P-enriched surface layer. However, the chemical state of this phosphorus species is not yet clear.

6.1.3 LOCALIZED CORROSION OF NiP ALLOYS

After prolonged potentiostatic polarization in the current arrest region ($-0.2 < E < +0.2$ v SCE), very small localized corrosion features (“black spots”) were observed on the surface of NiP alloys in earlier works [3,10] and also found in this work (Figure 5.7). These features cannot be considered as chloride induced pitting corrosion because NiP alloys are not protected by a passive oxide film and because the “black spots” were found to occur both in 0.1 M NaCl and in 0.1 M Na_2SO_4. Whereas on mechanically polished samples the starting point of these localized attacks is difficult to establish, on the unpolished samples, the “black spots” do not seem to be preferentially located at morphological features such as grain boundaries, but more randomly distributed. The reasons for and identification of the initiation of these localized attacks requires further investigation.

6.2 CHEMICAL STATE OF ELEMENTS PRESENT ON SURFACE FILMS

6.2.1 $Ni2p_{3/2}$

$Ni2p_{3/2}$ spectra, acquired from the polarized NiP alloys, showed the presence of two components associated with at least two different chemical environments of nickel. Two components of the $Ni2p_{3/2}$ region were also reported in earlier surface analytical studies of NiP alloys after anodic polarization [1,20]. Peak maxima and their relative intensity s were found to be independent of polarization potential and time. The binding energy values of the spectra acquired after polarization were also found to be equal to those recorded for the unpolished and mechanically polished sample. Using the reference compounds reported in the literature [1,9,20] and analyzed in this work (Table 5.1), the peak at 853.1 eV and its satellite at 860.5 eV were assigned to the nickel in the bulk alloy, while the second peak at 857.0 eV and its satellite at 863.2 eV were assigned to Ni^{2+} as in nickel phosphate or polyphosphates. These findings are in agreement with those reported in the literature (Table 2.1) and with those found in this work (Table 5.3). Since the difference between phosphate and pyrophosphate is only 0.3 eV, no attempt is made here to distinguish between these two

chemical states. The presence of nickel hydroxide may be excluded because its binding energy is reported to be 856.3 eV accompanied by the multiplet splitting signal at 857.3 eV [49]. Furthermore it should be pointed out that the $Ni2p_{3/2}$ region does not exhibit a component at 854.5 eV, thus it can be concluded that no NiO is present in the surface film of polarized NiP alloys in neutral de-aerated solutions.

The binding energy difference between the main peak and the satellite of the nickel in the bulk alloy (7.3 eV), as well as the ratio of the satellite and the main peak area (0.09), is in good agreement with an earlier work [21] about the effect of the phosphorus concentration on the electronic structure of NiP alloys.

On the basis of these results, an “oxide” passive film similar to the one formed on pure nickel [15-17] can be ruled out: the surface film very likely contains a mixture of nickel phosphates which have very low solubility in water at 25°C ($K_{ps} \approx 10^{-36}$).

6.2.2 P2p

Three doublets, due to the spin-orbit coupling are detected in the spectra of the P2p region acquired from the polarized NiP samples. They are associated to three different chemical state of phosphorus. Three peaks in the P2p spectral region were also reported in earlier surface analytical studies on amorphous melt-spun NiP alloys after mechanical polishing and after anodic polarization [1,18,20]. The $P2p_{3/2}$, $P2p_{1/2}$ binding energy values and the PKLL kinetic energy of these three phosphorus species, as well as their relative intensities, were found to remain unchanged within the experimental uncertainty with the polarization potential and the polarization time as reported in an earlier work [9]. The $P2p_{3/2}$ BE and PKLL KE values reported in the literature for polarized samples are in good agreement with those found in this work (Table 5.4). Using the values recorded for reference compounds taken from the literature [1,9,18,20] and obtained in this work (Table 5.2), it was possible to assign the peak at 129.5 eV to the phosphorus in the bulk alloy. The other peak found at 133.7 eV was slightly shifted (0.3-0.4 eV) at higher binding energies with respect to the same peak acquired for the NiP sample both in the unpolished and polished states (133.3 eV). The same binding energy difference was observed between the reference pyrophosphate (133.6 eV) and the orthophosphate (133.3 eV) analyzed here. Furthermore, the O1s curve-fitting results, that after polarization exhibit a component at 532.9 eV (§ 5.4.2.4 – Figs 5.18, 5.19), as well as the quantitative data obtained applying the MEM to the angle-resolved spectra (§ 5.4.6.2), suggest that this component may be assigned to (poly)phosphates. The mechanism of film formation, its growth and stability are discussed in the following (§ 6.5).

Regarding the component at 132.0 eV, its identification is not straightforward. The binding energy value is higher than that of elemental phosphorus (ca. 130.0 eV) [this work,9,18], but slightly lower than that derived from P(+1) compounds (NaH_2PO_2 at 132.3 eV) [this work,7,18]. Some authors proposed assigning the intermediate P species to P(+1) or P(+3) even if they were not able to identify the compound [20]; others suggested the formation of hypophosphite [18]. Alternatively, this phosphorus species was assigned to elemental phosphorus P^0 [9,22].

6.2.3 CHEMICAL STATE OF INTERMEDIATE P

More precise information on the chemical environment of an element can be obtained from the concept of the (modified) Auger parameter α, calculated by means of:

$$\alpha = BE(P2p_{3/2})+KE(PKLL)$$

and using the two dimensional "chemical state plot" [9, 23, 24].

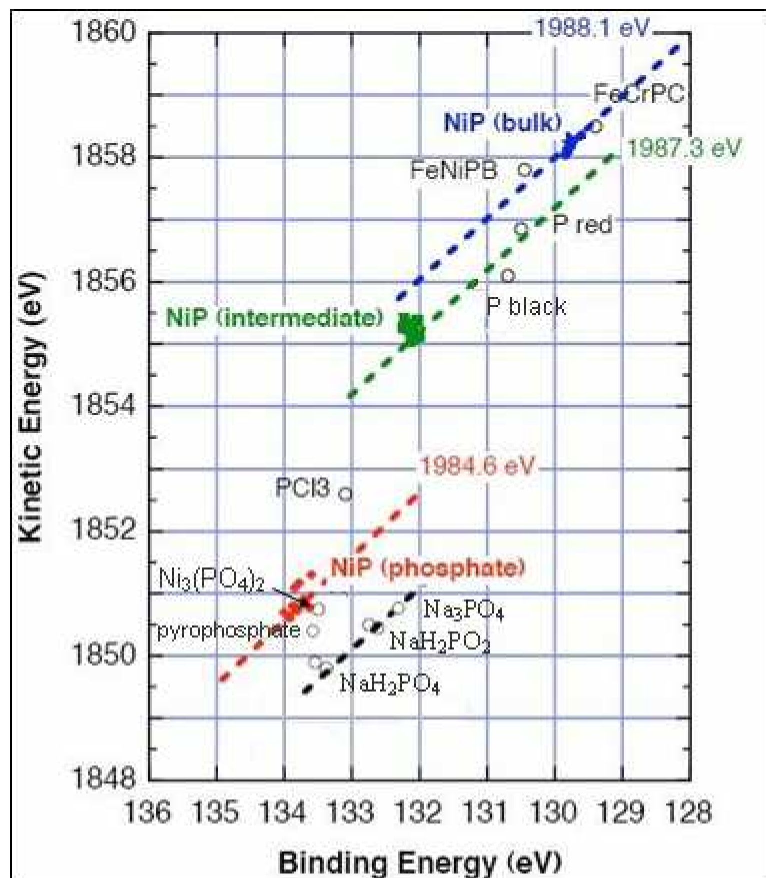

Figure 6.1 : Wagner chemical state plot of phosphorus, showing the different P species present on the surface of electroless deposited NiP alloys after 1, 3 and 14 hours polarization at +0.1 V SCE in 0.1 M Na_2SO_4 (full symbols). P-containing reference compounds analyzed in this work and others from the literature are given for comparison (open circles).

The three phosphorus species are found in three distinct regions of the chemical state plot (Figure 6.1). The group in the lower left region of the plot ($P2p_{3/2}$ 133.7 eV, PKLL 1851.4 eV) corresponds to P(+5) in phosphates, close to transition metal phosphates [22,25]. The group in the upper right region of the plot ($P2p_{3/2}$ 129.5 eV, PKLL 1858.5 eV) corresponds to P in the bulk alloy as for melt spun FeNiPB or $FeCr_{10}P_{13}C_7$ [9,22]. The intermediate P ($P2p_{3/2}$ 132.0 eV, PKLL 1855.3 eV) occupies the region in the chemical state plot nearest to

elemental phosphorus (red or black) with Auger parameter 1987.3 eV [9,22]. Thus, it can be concluded that P in the bulk alloy cannot be assigned to phosphorus with an oxidation number equal to zero. Actually the P in NiP alloys showed a slightly negative formal charge compared to elemental red P. The binding energy of phosphorus atoms in the alloy $P2p_{3/2}$ was about 0.3-0.4 eV lower than elemental red P. Comparing these results with those found in the literature, it can be concluded that a slight charge transfer (about 0.3-0.4 electrons per P atom) from Ni to P occurred in the NiP alloys [26] leading to a partially covalent bond [27]. This charge transfer corresponds to 0.1 electron per Ni atom [26] as shown by the small shift of the $Ni2p_{3/2}$ peak compared to pure nickel. The chemical state of the intermediate P is attributed to a phosphorus in the same chemical state of P^0 (in agreement with previous results for FeCrPC alloys [22]), while the attribution to P(+1) or P(+3) found in the literature [18,20] can be ruled out.

6.2.4 O1s

Three components were detected in the O1s spectra of NiP alloys acquired after anodic polarization (§ 5.4.2.4). The binding energy values at 531.5 , 532.9 and 535.0 eV respectively were found to be independent of polarization potential and time (Table 5.5). On the contrary, only two components at 531.5 and 533.4 eV respectively (Figure 6.2), were found in the O1s spectra acquired from unpolished and mechanically polished NiP alloys.

On the basis of the binding energy values reported in the literature [1,18,20,28,29] and of those found for the reference compounds analyzed in this work, it was possible to assign the peak at 531.5 eV to non-bridging oxygen as in phosphates [1]. This signal includes the contribution of the oxygen from carbonates (531.6 eV) [29,30], whose presence on the surface of the polarized samples is confirmed by the C1s signal at 288.6 eV (§ 5.4.2.5). The peak at 532.9 eV was only detected following

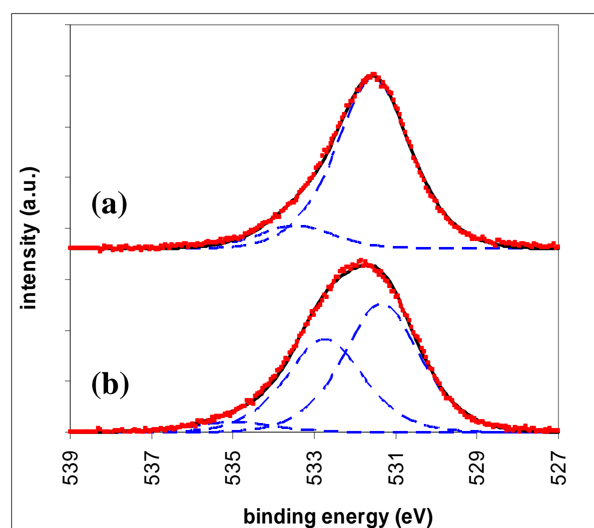

*Figure 6.2 : Comparison of high resolution spectra for O1s region acquired from NiP alloy **(a)** unpolished **(b)** after 1 hour polarization at +0.1 V SCE in 0.1 M Na_2SO_4.*

potentiostatic polarization and it might be assigned to the bridging oxygen in polyphosphates. However, this component includes the contributions of the oxygen from adsorbed water (533.4 eV) [18], which was clearly observed on the unpolished NiP alloy surface.
The higher binding energy peak at 535.0 eV was attributed to the NaKLL Auger signal.

6.2.5 C1s

The C1s spectra belongs to the surface film formed on the Ni-18P alloy acquired after anodic polarization (§ 5.4.2.5). It is the convolution of three signals and their relative intensity was found to be independent of polarization potential and time (Table 5.6). On the basis of the binding energy values reported in the literature for the reference compounds [29,31,32] it was possible to assign the peak at 284.8 eV to the aliphatic carbon from adventitious contamination. The peak at 288.6 eV was attributed to the carbonates formed as a consequence of the adsorption of CO_2 on top of the surface film [29,30]. The intermediate binding energy peak at 286.6 eV might be identified as a carbon atom bonded to a single oxygen atom, such as in adsorbed ethanol: this solvent was used as lubricant during mechanical polishing.

6.2.6 NON-DESTRUCTIVE DEPTH PROFILE

In the present work, the distribution of the elements and their chemical states as a function of depth is reported for the first time for NiP alloys. The angle-resolved XP-spectra of the $Ni2p_{3/2}$ region (Fig. 5.14) reveal that the phosphates are located in the outer part of the sample surface. This is confirmed by the ARXPS spectra of the P2p region (Fig. 5.17) that also suggest that elemental phosphorus is present at the interface between the polyphosphates and the bulk alloy. The ARXPS spectra for the O1s region (Fig. 19) show that the non-bridging / bridging oxygen ratio decreases slightly with increasing emission angle. This might also be ascribed to the contribution of the adsorbed water to the bridging oxygen peak. Since this species is adsorbed on the top of the surface film, its contribution to the bridging oxygen peak increases with increasing emission angle. However, at near-normal emission angles, where the contribution of the adsorbed species is attenuated by the greater sampling depth, the O1s ARXPS spectra acquired from the Ni-18P alloys after both 1 and 3 hours polarization, show a non-bridging / bridging oxygen ratio equal to ca. 1.8, typical of a long-chain phosphate. After 14 hours polarization the non-bridging / bridging oxygen ratio was found at near-normal emission angles to increase to ca. 3.0. This may be attributed to the breakdown or to a rearrangement of the phosphate chains, since the intensity of the non-bridging oxygen

increases with increasing polarization time. This hypothesis is further confirmed by the observation that after 14 hours polarization, the non-bridging O to “phosphate” P intensity ratio is higher (+ 40%) than after 1 or 3 hours of polarization.

6.3 XPS QUANTITATIVE ANALYSIS OF SPUTTERED NiP ALLOYS SURFACE

6.3.1 PREFERENTIAL ION SPUTTERING OF PHOSPHORUS

In order to obtain a pristine NiP surface as a reference for testing the different quantitative approaches, it was decided to sputter clean the samples in situ before acquiring the spectra. On the other hand, since it is well known that ion sputtering process modify the surface chemical composition of multi-component materials as a result of preferential sputtering [33,34] it was necessary to set up a procedure for monitoring the sputtering-induced surface changes. This work is not intended to contribute to the understanding of the sputtering process, but simply provides a phenomenological description of the compositional changes occurring in NiP alloy surfaces under our experimental sputtering conditions (§ 4.4.2). Ion bombardment generally leads to surface enrichment of the component having the lower sputtering yield [33]. The sputtering yield is a phenomenological coefficient that actually depends on many factors such as ion beam energy, angle of incidence, target/ion mass ratio, and target binding energy [33,35].

The results of the ion sputtering kinetic runs performed in this work (§ 5.4.3) reveal that the relative intensity of both Ni and P peaks increases with increasing etching time, up until the contamination films is completely removed from the alloy surface. The P2p peak intensity reached its maximum for the etching time (10 s under the experimental conditions applied in this work) where both O1s and C1s signal intensity became indistinguishable from the spectral background noise. At longer etching times, P2p intensity decreased with increasing etching time, while $Ni2p_{3/2}$ intensity continued to increase. Finally, after a certain etching time (ca. 120÷150 s under the experimental conditions adopted here) the relative intensity of $Ni2p_{3/2}$ and P2p peaks remained stable.

These results are interpreted in terms of preferential ion sputtering. Until such time as the contamination layer is not completely removed from the alloy surface, the ion beam etches all the chemical species within the contamination layer itself. The contamination layer becomes increasingly thinner and its contribution to the attenuation of photoelectronic signals generated in the bulk is thus progressively reduced. As a consequence, the intensity of both the Ni and P bulk-lines increases. Once the surface contamination layer has been completely

removed, preferential sputtering of phosphorus occurs, leading to a surface enrichment of nickel, which is then thought to have a lower sputtering yield [33]. The preferential sputtering of phosphorus continues up to a given etching time (ca. 120÷150 s under the present experimental conditions). At longer etching times, the reduced phosphorus concentration at the surface alloy, possibly tends to offset its higher sputtering yield, thus, the surface composition then appears to be insensitive to sputtering. Under the experimental conditions adopted here, preferential sputtering of phosphorus ceased, thus it was concluded that Ni and P sputtering yields became comparable at that etching time. In other words, at ca. 120÷150 s, the system reached an equilibrium sputter rate.

6.3.2 COMPARISON OF DIFFERENT METHODS FOR QUANTITATIVE XPS ANALYSIS

In order to avoid preferential sputtering induced compositional changes of the NiP samples surface, ion sputtering was performed as described for the kinetics run n.2 (§ 5.4.3). The bulk component of the P2p region was monitored versus etching time and the Ar^+ flow was interrupted as soon as P2p bulk intensity reached the maximum. The "complete" removal of the contamination layer was denoted by the disappearance of the C1s and O1s lines and the First Principles method for quantification was applied (§ 5.4.4) using the areas of the $Ni2p_{3/2}$ and P2p signals. Tougaard's method was also applied (§ 5.4.5.1). The results obtained with the different methods are compared with those obtained with EDX analysis (§ 5.2) in Table 6.1.

Table 6.1 : XPS and EDX results of quantitative surface analysis of the NiP alloys studied in this work.

	XPS First Principle method	**XPS Tougaard's method (analyze approach)**	**EDX**
P content (at.%)	*18 ± 2*	*13 ± 8*	*18.7 ± 0.3*

These results are comparable within the experimental error, showing that the P2p intensity monitoring procedure has been effective in limiting the preferential sputtering of the NiP alloy surface within the accuracy of the XPS technique. Tougaard's analyze approach was found to be the least precise and accurate of all three quantification methods tested here. However, it should be pointed out that Tougaard's method is applied using the survey rather than high-resolution spectra [36], thus it is usually faster and simpler than the First Principles

method, since it requires shorter acquisition times for both spectra recording and data processing [37].

6.4 POLARIZED NiP ALLOYS IN-DEPTH PROFILING

6.4.1 TOUGAARD'S GENERATE APPROACH

Using Tougaard's generate approach (§ 5.4.5.2), the thickness of the phosphates overlayer was estimated to be 9 ± 1 Å after anodic polarization at +0.1 V SCE in 0.1 M Na_2SO_4 solution. Here, only the thickness is significant since the composition of this overlayer is constrained by the reference survey spectra use for the application of Tougaard's method (Figure 6.3). These results also suggest the formation of a P-enriched interface between the "phosphate" layer and the bulk alloy, as shown schematically in Figure 6.3.

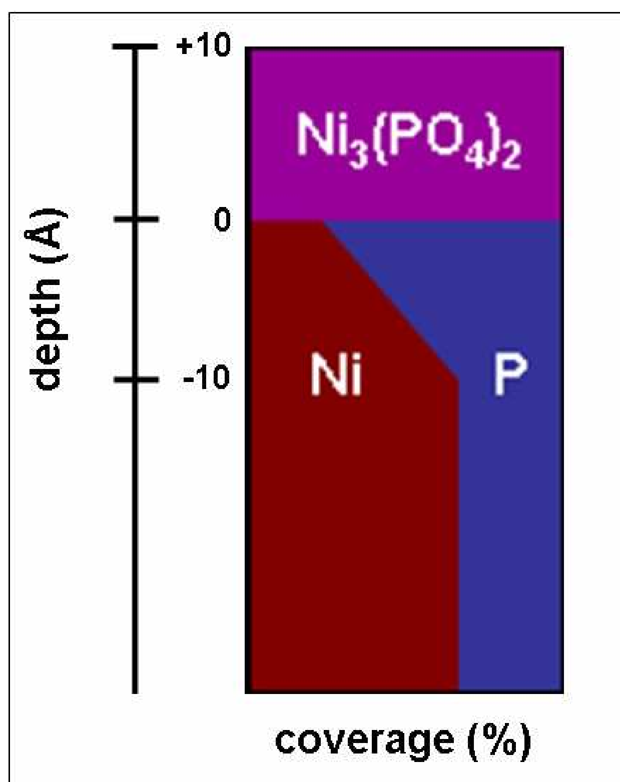

Figure 6.3 : Schematic diagram of depth profile of a polarized Ni-18P alloy, reconstructed with Tougaard's generate approach.

The thickness of this P-enriched interface was calculated as 10 Å. The presence of a P-enriched layer at the alloy surface has been hypothesized by many authors [1,4,7,9-11,18,20,38-40] and its presence has also been confirmed with both glow discharge optical spectroscopy [8] and Auger Electron Spectroscopy (AES) depth-profiling [2]. However, some authors maintain that the phosphorus atoms in this phosphorus enriched layer should occur as phosphate [1,11] or as hypophosphite [2,7,18] without allowing for the possibility that the phosphorus could be present in different chemical states [9]. The results obtained with Tougaard's generate approach revealed, after polarization, phosphorus enrichment at the NiP alloy surface and allowed to distinguish between an outer phosphate layer and an P-enriched interface. However, with Tougaard's depth-profiling it is possible to use a maximum of only three components for simulating the experimental spectrum [36]. Thus the elemental P (i.e. the intermediate P chemical state (§ 6.2.3) [9]) could not be taken into "explicit" account, since only two P-containing reference compound spectra could be used: one to simulate the

phosphates overlayer and the other to simulate the P in the bulk alloy together with the P in the elemental chemical state.

Table 6.2 summarizes the layer thickness and species concentration of the depth profile of the Ni-18P alloy after 1, 3 and 14 hours potentiostatic polarization. Thickness of both the phosphate layer and the P-enriched interface were found to be independent of polarization time. Regarding P concentration at the P-enriched interface, after 3 hours polarization, it was found to increase from 55 at.% (1 hour) to 70 at% (3 hours). At longer polarization times, the phosphorus concentration at the interface seems to be independent of the polarization time. However, as far as the accuracy of these results is concerned, depth profile structural parameters should be divided into two groups [41]: three primary and a maximum of three secondary structural parameters. More than six structural parameters cannot normally be determined with any degree of accuracy [41]. The primary parameters are the three most important parameters for describing the depth profile within a depth of 5-10 λ (170-350 Å in this case) [41]. The three primary parameters of the depth profile of the polarized Ni-18P alloys (Figure 6.3) are: phosphates layer thickness (ca. 10 Å), phosphates layer coverage (100%) and Ni (or P) bulk coverage (82%). Uncertainty in the three primary parameters is typically 5-10% [41]. The secondary parameters are parameters that characterize the finer details of the depth profile in the outermost 5-10 λ of the surface region [41]. The depth profile of the polarized Ni-18P alloys (Figure 6.3) has only two secondary parameters: P-enriched interface thickness (ca. 10 Å) and maximum P (or minimum Ni) content (55-70%) within the P-enriched interface. Uncertainty in the secondary parameters is always greater than in the primary parameters, and typically amounts to ≥ 35% [41].

Table 6.2 : In-depth profile parameters of a Ni-18P alloy after 1, 3 and 14 hours polarization in 0.1 M Na_2SO_4 at +0.1 V SCE, determined with Tougaard's generate approach.

polarization time (h)	***1***	***3***	***14***
phosphates layer thickness (Å)	*10*	*8*	*10*
P-enriched interface thickness (Å)	*10*	*10*	*10*
P-enriched interface P content (at.%)	*55*	*70*	*70*
bulk alloy	*Ni-18P*		

It can be concluded that the depth profile of the polarized Ni-18P alloys is actually independent of polarization time, since the difference between the maximum P concentration in the P-enriched interface (Table 6.2) determined at 1 hour (55 at.%) and at longer polarization times (70 at.%) are actually comparable within Tougaard method accuracy [41]. These results are consistent indeed with the fact that the relative intensities of the components

of the P2p spectral region (Table 5.4) were found to be independent of polarization time (§ 6.2.2).

6.4.2 MEM PERFORMANCE AND ACCURACY : NUMERICAL EXPERIMENTS

As mentioned in the previous chapters, in order to transform the intensity vs. angle profiles into the concentration vs. depth distribution of the elements in the different chemical environments, a maximum entropy method has been developed. This paragraph discusses the results of the MEM numerical experiments performed to demonstrate the ability of our algorithms protocol to resolve the depth profile of a sample with varying number of components. Here, examples with 3 to 8 components, that can be differently distributed within the layers, (§ 5.4.6.1) are discussed. However, it is also clear that any information about the sample, such as chemical state of the elements and a starting estimation of the depth profile (e.g. obtained with Tougaard's method), or gleaned from the literature, is essential for solving the ill-posed problem of the non-destructive reconstruction of a depth profile from ARXPS data [42].

6.4.2.1 APPARENT CONCENTRATION DIAGRAMS AND RELATIVE DEPTH PLOTS : INFLUENCE OF IMFP

Results of the numerical experiments (§ 5.4.6.1) show that the apparent concentration diagram provides very important clues about the relative depth of the different chemical species, since it is well known [31,32] that the relative intensity of a photoelectronic peak of an overlayer species increases with increasing emission angle. Vice versa, the relative intensity of a photoelectronic peak of an inner-layer species decreases with increasing emission angle [31,32]. As an example, Figure 6.4 shows the ACD of the synthetic structure 3_2+1. The corrected intensity of both the species A and B increases with increasing emission angle, as expected for two species located in the outer layers of the surface region. Vice versa, the corrected intensity of the species C decreases with increasing

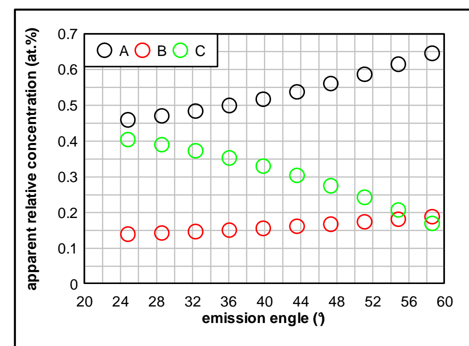

Figure 6.4 : ACD of synthetic structure 3_2+1.

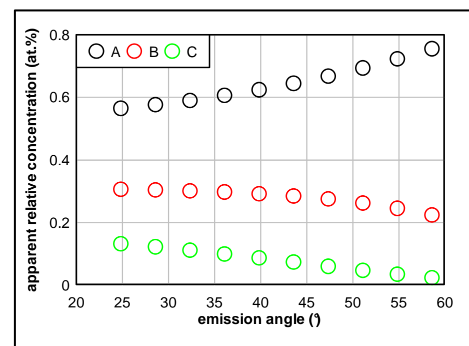

Figure 6.5 : ACD of synthetic structure 3_1+1+1.

emission angle as expected for a species located in the inner layers of the surface region. However, misleading conclusions can often be drawn about the relative depth of the different chemical species from the trend of the ACD points as the example in Figure 6.5 illustrates. This graph shows the ACD of the synthetic structure 3_1+1+1. Observing the ACD points, one could mistakenly deduce that the sample depth profile is characterized by an overlayer of pure A and a binary sublayer composed of B and C. Our numerical experiments (§ 5.4.6.1) show that even a trend reversal of the ACD points is possible, leading to completely mistaken conclusions about the relative depth of the chemical species.

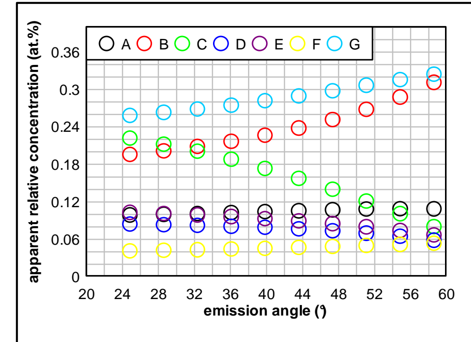

Figure 6.6 : ACD of synthetic structure 7_a.

Another example that elucidates the possible problems encountered in data interpretation is illustrated in Figure 6.6 which shows the ACD of the synthetic structure 7_a. The species A is actually located deeper than the species D, but it can be seen that while the corrected intensity of D decreases with increasing emission angle, the corrected intensity of A slightly increases. The species D and F are located within the same layer (i.e. at the same depth), but as can be seen, while the corrected intensity of D decreases with increasing emission angle, the corrected intensity of F slightly increases. On the other hand, the ACD points for the species A and F exhibit almost the same trend, even if they are not located within the same layer. The data can be more conveniently displayed using the relative depth plots (RDP) (§ 5.4.6.1). which display corrected intensities from ARXPS data better than the ACD. Let us take as an example, the ACD of the synthetic profile 3_1+1+1 (Figure 6.5). This profile can be mistaken

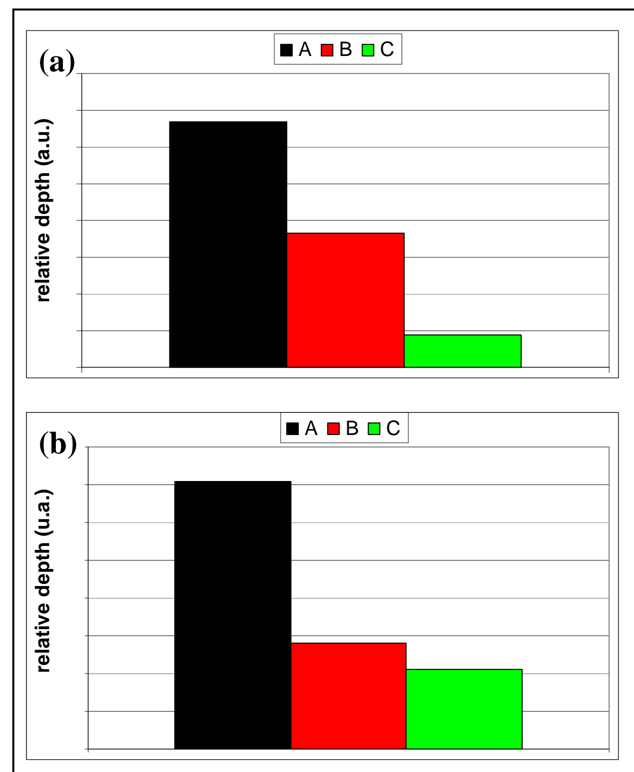

*Figure 6.7 : RDP of synthetic structure **(a)** 3_1+1+1 and **(b)** 3_1+2.*

for the ACD of structure 3_1+2 (see discussion above). On the contrary, these two structures can be clearly distinguished examining their RDP (Figure 6.7).

Another example with a more complex structure is: 4_1+2+1. Figure 6.8 shows both its ACD and the corresponding RDP.

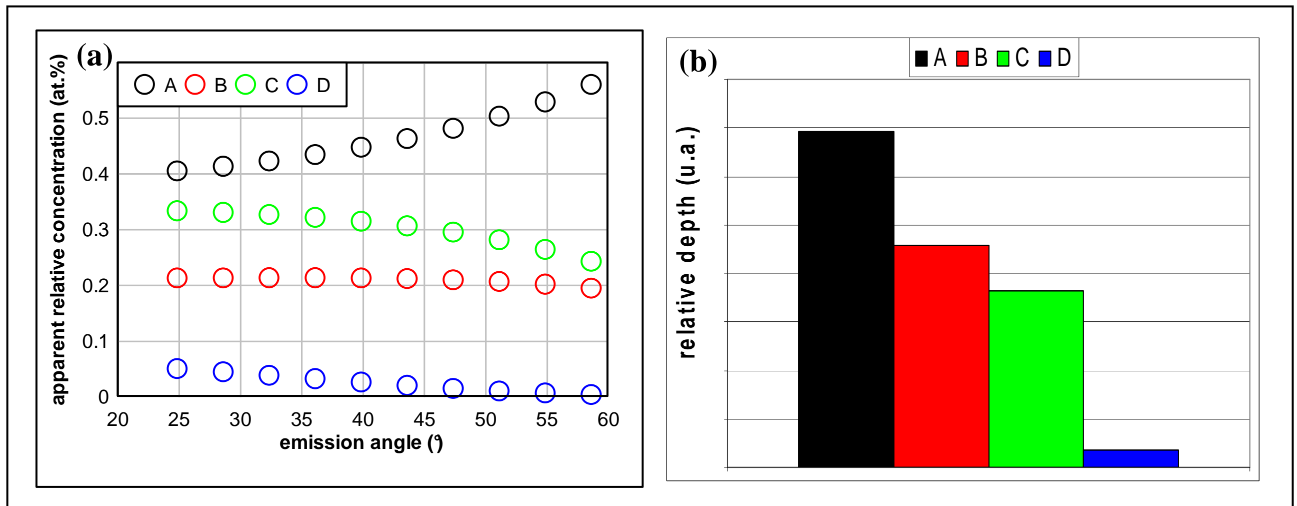

*Figure 6.8 : (**a**) ACD and (**b**) RDP of synthetic structure 4_1+2+1.*

The apparent relative concentration of species A increases with increasing emission angle, as expected for a species located in the overlayer. On the contrary, the apparent relative concentration of species C and D decreases with increasing emission angle, as expected for a species located in the sublayer. The trend of ACD points for species B is intermediate, thus it could be hypothesized that this species is located in an intermediate layer or at the interface between the overlayer, composed of pure A, and a binary bulk, composed of C and D. Thus, the ACD leads to the erroneous structure: 4_1+1+2. On the other hand, the RDP clearly show the actual relative depth of all four species. The majority of synthetic structures examined here could be misunderstood relying simply on their ACD.

However, when performing the numerical experiments several cases arose where the RDP could also lead to misinterpretation of the actual depth profile (§ 5.4.6.1). It can be concluded that both these diagrams are very useful tools for restricting depth profile starting hypotheses to two or three structures at the most. Thus, depth profile reconstruction of a sample surface becomes very difficult in the absence of other information except for ACD and RDP. As mentioned above, it is essential that all available information about the sample be taken into

account. In particular, Tougaard's method is thought to be a very good and quite simple way for obtaining an optimum starting point for the MEM simulation.

Finally, the most important result of the numerical experiments are discussed. The numerical experiments reveal that every time two or more species are located in the same layer (i.e. within the same depth range), they never show exactly the same relative depth in the RDP. The difference in RDP relative depths was found to increase with increasing difference in IMFP of the two species. Linear proportionality was checked but ruled out.

Let us consider again the RDP in Figure 6.8. The relative depth of B and C is not identical, even if they are actually located in the same layer. The IMFP of B (30 Å) is higher than C (20 Å), thus the "photoelectrons" emitted from C undergo greater attenuation than those emitted from B [31,32,43]. Thus, the fact that the C species appears to be located deeper than B (Figure 6.8 b), was attributed to the difference in their IMFP, and hence to the difference in the attenuation of their "photoelectrons". From a rigorous physical standpoint, this interpretation is correct only if we assume that the escape path of B and C photoelectrons is exactly the same [42]. Elastic scattering events can cause the escape path of B and C photoelectrons to deviate from an initially identical pathway [42]. However elastic scattering can be neglected at emission angles ≤ 60° [42,44-46].

Actually, the RDP relative depth is calculated as the ratio of the corrected intensity of a photoelectronic peak acquired at a near grazing emission angle to the corrected intensity of the same photoelectronic peak acquired at a near incident emission angle. Then, it has to be expected that the RDP relative depths depend upon the atomic concentration of the photoemitting species, besides its IMFP, since the corrected intensity of a peak depends on both IMFP and atomic concentration of the photoemitting species [31,32]. As an example, let us consider again the ACD and the RDP in Figure 6.8, calculated for the synthetic structure 4_1+2+1, where the intermediate layer was composed of 40 at.% B and 60 at.% C. The ACD and the RDP were recalculated for the same synthetic structure, but taking the intermediate layer to be compoesd of 50 at.% of both B and C. The results are shown in Figure 6.9.

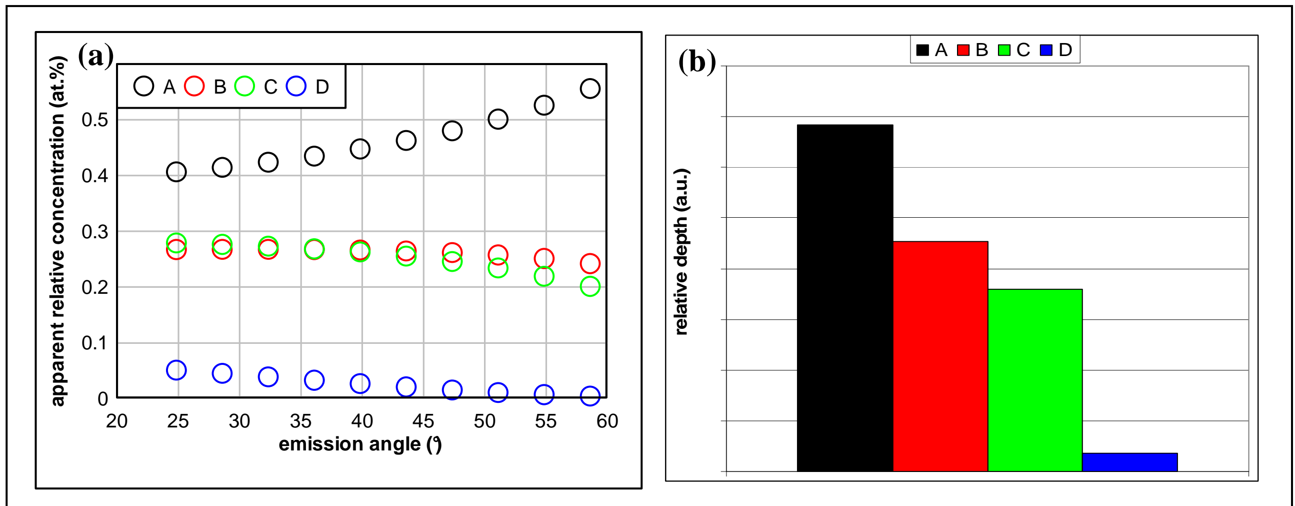

*Figure 6.9 : (**a**) ACD and (**b**) RDP of modified synthetic structure 4_1+2+1. Intermediate layer composed of 50 at.% B and C, instead of 40 and 60 at.% respectively.*

The ACD can equally lead to the same erroneous interpretations discussed above. On the other hand, the RDP is almost identical to that shown in Figure 6.8.

The ACD, and the corresponding RDP, of all the synthetic structures examined in this work, were re-calculated using only one IMFP value for all the species involved (§ 5.4.6.1) and these were referred to as "trial" diagrams (e.g. the trial-RDP). The trial-ACD and the trial-RDP calculated for the synthetic structure 4_1+2+1 are shown in Figure 6.10. The IMFP was taken as 10 Å for all four species.

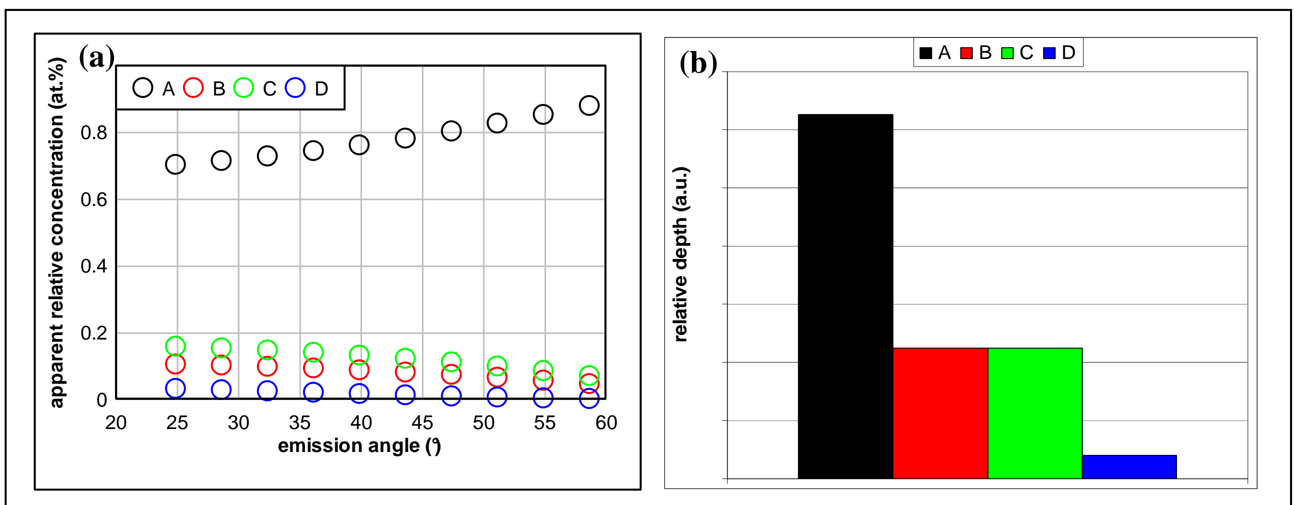

*Figure 6.10 : (**a**) trial-ACD and (**b**) trial-RDP of synthetic structure 4_1+2+1.*

The ACD can again lead to a totally erroneous hypothesis, e.g. the structure 4_1+3, while the RDP reproduces perfectly the actual relative depth of all the species. In particular, B and C

exhibit exactly the same relative depth, as expected for two species located within the same layer. Actually, the trial-RDP of all the numerical structures examined in this work (§ 5.4.6.1 and Appendix A), perfectly reproduce the expected relative depth of all the species involved, no differences existing between species located within the same layer.

In conclusion, these numerical experiments reveal that the difference between the RDP relative depth of two or more species, located within the same depth range (i.e. the same layer), is due solely to their IMFP difference, and thus, can be interpreted in terms of the difference in photoelectron attenuation [42].

6.4.2.2 ACCURACY OF ALGORITHMS PROTOCOL FOR MEM APPLICATION

Results of the numerical experiments clearly show the ability of our algorithms protocol to resolve the depth profile of a sample, composed of between 3 and 8 components (§ 5.4.6.1).

Deviation of layer interface depth from the expected values was found to increase with increasing depth (Figure 6.11). Within the investigated range, the relative error was found to be $\leq 10\%$ for the majority of the examined interfaces. A relative error of $10\text{-}20\%$ was only found for a few interfaces, all of which can be considered “secondary structural parameters” [41]. The introduction of a random error in the ACD data, equal to 10%, caused deviation of layer interface depth to increase by around 1 Å (Figure 6.11). The relative error of species concentration did not exhibit any particular trend (Figure 6.12).

Within the investigated range, the relative error was found to be $\leq 10\%$ for most of the cases examined. A relative error of $10\text{-}30\%$ was found only for a few species concentration, all of which can be considered “secondary structural parameters” [41].

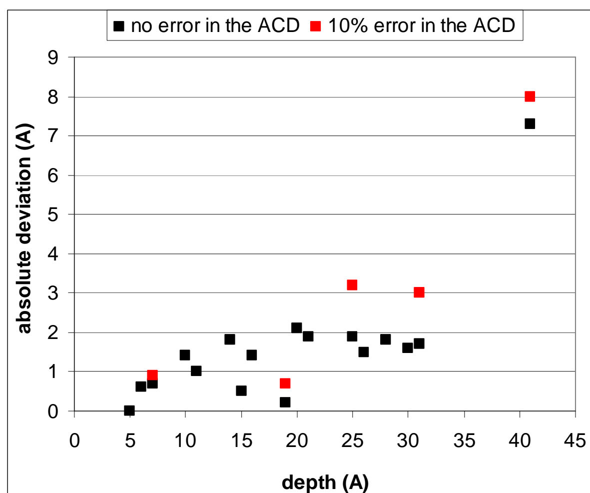

Figure 6.11 : Maximum absolute deviation of layer interface depth vs. depth.

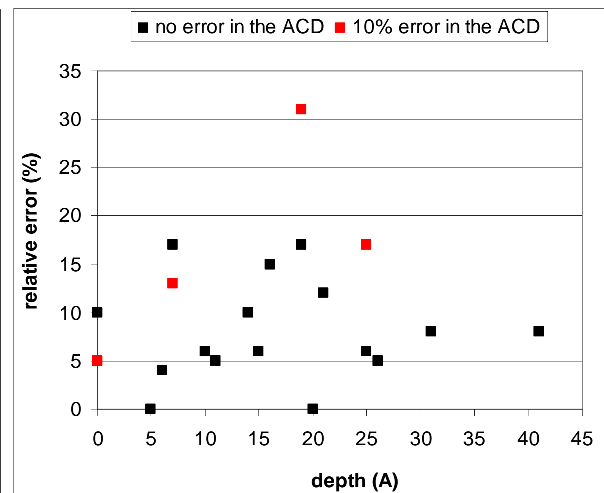

Figure 6.12 : Maximum relative error of species concentration vs. depth.

Thus, summarizing the results, accuracy of the MEM protocol was found, in general, to decrease with increasing depth, similarly to Tougaard's method too [41]. Accuracy of the MEM protocol was found to decrease with increasing number of species in the sample (Figure 6.13). But this is not surprising, as the complexity of the structure increases with the number of the species contained therein.

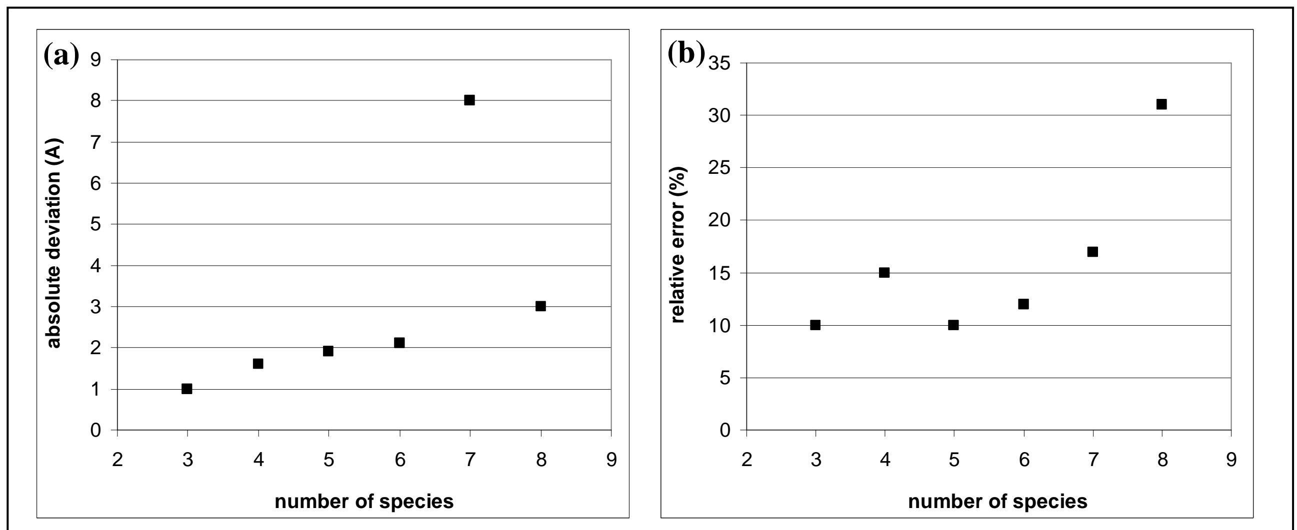

*Figure 6.13 : Maximum **(a)** absolute deviation of layer interface depth and **(b)** relative error of species concentration vs. number of the species involved in the structure.*

6.4.3 APPLICATION OF MEM TO REAL SAMPLES : POLARIZED Ni-18P ALLOYS

Results of the MEM protocol (§ 5.4.6.2), reveal that after anodic polarization at +0.1 V SCE in 0.1 M Na_2SO_4, an overlayer of nickel phosphates forms on the NiP alloy surface. The thickness of this phosphates layer was calculated as11 ± 1 Å. The MEM results also reveal the formation of a P-enriched interface between this phosphates layer and the bulk alloy, as shown schematically in Figure 6.14. The thickness of this P-enriched interface was calculated as 20 ± 2 Å. The results of the MEM not only revealed, after polarization,

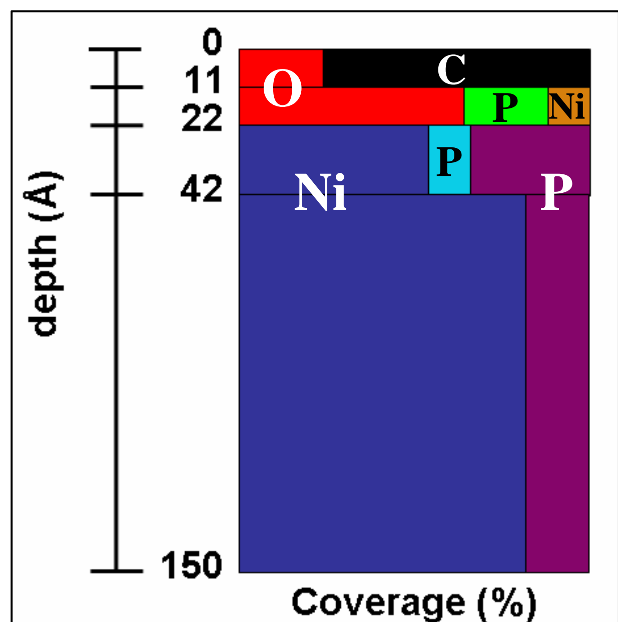

Figure 6.14 : Schematic diagram of the depth profile of polarized Ni-18P alloy, reconstructed with MEM protocol.

phosphorus enrichment at the NiP alloy surface but also allowed to distinguish between an outer phosphates layer and a P-enriched interface where the phosphorus is present both in the NiP alloy and in the elemental chemical state taking into account the adventitious contamination as well. A carbon-oxygen layer was detected overlaying the nickel long-chain phosphates layer. The thickness of this contamination layer was calculated as 11 ± 1 Å.
Table 6.3 summarizes the layer thickness and species concentration, of the depth profile of the Ni-18P alloy after 1, 3 and 14 hours polarization.

Table 6.3 : Depth profile parameters of Ni-18P alloy after 1, 3 and 14 hours polarization at +0.1 V SCE in 0.1 M Na_2SO_4, determined with MEM protocol.

layer	thickness (Å)			species	concentration (at.%)		
	1 hour	3 hours	14 hours		1 hour	3 hours	14 hours
adventitious contamination	*10 ± 9*	*11 ± 6*	*12 ± 6*	***C***	*78 ± 12*	*74 ± 9*	*77 ± 6*
				O	*22 ± 12*	*26 ± 9*	*23 ± 6*
nickel phosphate	*12 ± 6*	*11 ± 6*	*11 ± 3*	***Ni***	*11 ± 3*	*11 ± 3*	*15 ± 6*
				P	*23 ± 9*	*27 ± 12*	*21 ± 3*
				O	*66 ± 12*	*62 ± 12*	*64 ± 6*
P-enriched	*20 ± 6*	*21 ± 6*	*18 ± 3*	***Ni***	*54 ± 6*	*56 ± 9*	*53 ± 3*
				P (bulk-alloy)	*33 ± 3*	*32 ± 6*	*36 ± 3*
				P (elemental)	*13 ± 3*	*12 ± 3*	*11 ± 3*

This depth profile was found to be independent of polarization time, within the MEM protocol accuracy (§ 6.4.2). These results are consistent with the fact that the relative intensities of the components of the P2p spectral region (Table 5.4) were found to be independent of polarization time (§ 6.2.2). These results also show that the phosphorus in the P-enriched interface has a concentration of ca. 46 at.%. The phosphorus in the P-enriched interface is present indeed in two different chemical states: ca. 34 at% of alloy-P and ca. 12 at.% of elemental-P.
As far as the phosphates layer is concerned, the Ni:P:O concentration ratios were 1:2:5 which are consistent with the hypothesis of a polyphosphates layer suggested here. Since total O1s intensity was used in the MEM protocol application to the ARXPS spectra of the polarized Ni-18P alloys, no-bridging/bridging oxygen ratio could be determined. However, on the basis of the raw ARXPS intensity data of the components of the O1s region (§ 6.2.6), the no-bridging/bridging oxygen ratio was estimated to be equal to ca. 1.8 after 1 and 3 hours polarization, and ca. 3.5 after 14 hours polarization.

Thus, taking into account the accuracy of the MEM protocol (§ 6.4.2), the hypothesis of a nickel (II) orthophosphate layer [11] can be ruled out, as already mentioned above comparing the P2p and O1s spectra acquired from the NiP alloys after electrochemical polarization and the same regions acquired from the unpolarized NiP alloy (§ 6.2.2 ; 6.2.4). On the basis of the chemical state plot of phosphorus (§ 6.2.3), the hypothesis of a hypophosphite [18] or a phosphide layer [3] can also be dismissed. Based on the results of the present investigation, the formation of a polyphosphate-like layer could be proposed.

6.4.4 COMPARISON OF TOUGAARD'S AND MAXIMUM ENTROPY METHOD

Both the Tougaard (§ 6.4.1) and the MEM method (§ 6.4.3) show the depth profile of the Ni-18P alloy to be independent of polarization time. Both in-depth profiling methods reveal the formation of a phosphate layer on the alloy surface whose thickness was estimated to be ca. 1 nm. However, to apply Tougaard's method, the survey spectra of the $Ni_3(PO_4)_2$ were used to simulate the phosphate layer, while with the MEM protocol it was possible to determine the composition of this phosphate layer without any constraints.

Both Tougaard's (§ 6.4.1) and the MEM method (§ 6.4.3) reveal the formation of a P-enriched interface between the phosphate layer and the bulk alloy, whose thickness was estimated to be ca. 1 nm and ca. 2 nm respectively. The discrepancy between the two in-depth profiling methods can be explained by the presence of the adventitious contamination overlayer. XPS lines generated from the inner layers (i.e. phosphates layer, P-enriched layer and bulk alloy) are attenuated by the presence of this overlayer [31,32,42,43]. The deeper the layer, the greater the attenuation of the intensity of the corresponding XPS lines [42,43]. Tougaard's method does not take into account the contamination layer [36] while the MEM indicates the formation of a carbon-oxygen contamination layer, over the polyphosphate layer, whose thickness was estimated to be ca. 1 nm (§ 6.4.3). Consequently, the P-enriched layer indicated by Tougaard's method is thinner than the one indicated by the MEM.

Regarding the composition of this P-enriched interface, Tougaard's method only determines total P content (§ 6.4.1). On the other hand, the MEM protocol enabled to distinguish two different contributions to the P content due to two different chemical states: elemental-P and the alloy-P (§ 6.4.3). However Tougaard's [41] and the MEM method (§ 6.4.2) results for total P content in the P-enriched interface, are comparable within the accuracy of the two in-depth profiling methods.

Note that neither method accounts for surface roughness, i.e. they both assume an ideally flat surface.

Summarizing:

- The accuracy of the MEM protocol applied in this work is comparable with Tougaard's method [41] namely ≤ 10% for the primary structural parameters and 30% at the most for the secondary ones;
- Tougaard's in-depth profiling method is faster and simpler to implement than the MEM protocol developed in this work but provides less detail;
- Tougaard's method is based upon a subjective graphical comparison of experimental and reference low-resolution survey spectra [36]. On the contrary, the MEM protocol is based on a mathematical fit of corrected intensity data of high-resolution ARXPS spectra versus emission angle [47];
- Tougaard's method is restricted to a maximum of three components [36], while the numerical experiments performed in this work have shown that MEM allows to reconstruct depth profiles of materials having up to 8 components (§ 6.4.2). However this "limit" may be extended to 9 or more components by further numerical experiments.

It should be pointed out that Tougaard's method is very effective for obtaining a starting depth profile for application of the MEM. Thus, it can be concluded that these two in-depth profiling methods should be considered as complementary.

6.5 DISSOLUTION MECHANISM OF NICKEL-PHOSPHORUS ALLOY

Summarizing, based on the results of this work, the following model is proposed to explain the high corrosion resistance of the amorphous/nanocrystalline NiP alloys.

1) As soon as the Ni-18P alloy is immersed in the solution at pH 6.3 , both nickel and phosphorus tend to dissolve in the electrolyte solution, according to the equilibria [48]:

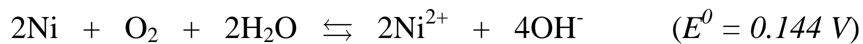

$$2Ni + O_2 + 2H_2O \leftrightarrows 2Ni^{2+} + 4OH^- \qquad (E^0 = 0.144\ V)$$

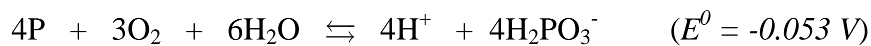

$$4P + 3O_2 + 6H_2O \leftrightarrows 4H^+ + 4H_2PO_3^- \qquad (E^0 = -0.053\ V)$$

However, nickel dissolves faster than phosphorus [11-13,18,19] (Figure 6.15), resulting in an enrichment of P at the alloy surface.

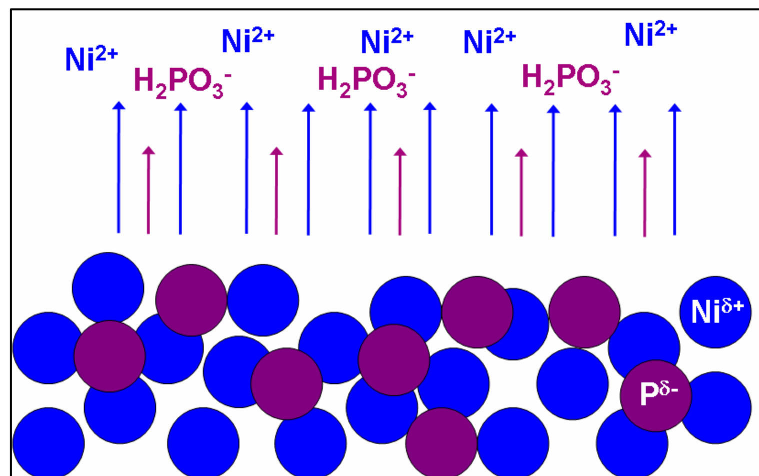

Figure 6.15 : Schematic diagram of dissolution mechanism of NiP alloy upon immersion in the electrolyte solution.

2) At lower polarization times (< 1 hour), nickel continues to dissolve faster than phosphorus. This causes the P-enriched layer to thicken. The phosphorus in this P-enriched layer is present in two different chemical states: an alloy-P, which is still coordinated with Ni atoms, and the elemental-P, which has lost its nickel coordination sphere and has other P atoms as nearest neighbors. As this P-enriched layer thickens both

Ni and P dissolution are suppressed. Thus, further dissolution of the alloy is first controlled by nickel diffusion through the thickening P-enriched layer as shown by the electrochemical results of this work.

The dihydrogenated phosphite anions can undergo further oxidation, according to the equilibrium:

$$2H_2PO_3^- + O_2 \leftrightarrows 2H_2PO_4^- \qquad (E^0 = 0.125\ V)$$

The dihydrogenated phosphate anions may be retained as well as adsorbed at the alloy surface forming polyphosphates chains which have a lower solubility in water. Thus, a polyphosphates layer is formed on the P-enriched layer. This polyphosphate layer may act as a further barrier between the alloy surface and the electrolyte solution. Oxygen is prevented from reaching the alloy surface, and at the same time, the diffusion of nickel atoms is further suppressed (Figure 6.16).

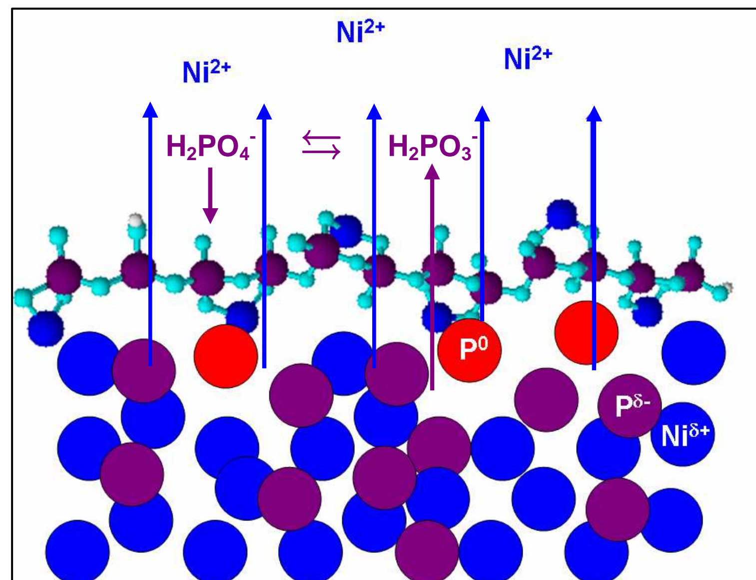

Figure 6.16 : Schematic diagram of dissolution mechanism of NiP alloy at lower polarization times.

3) At polarization times of over an hour, the depth profile of the NiP alloy surface remains unchanged, both in layer thickness and composition. However, several “black spots” appear on the alloy surface though it has been shown that they do not initiate from any particular morphological feature.

Current density increases slightly with increasing polarization time, but the only spectral variation revealed by XPS, is the intensity ratio of the two O1s peaks assigned to the polyphosphates: bridging and non-bridging oxygen respectively. The non-bridging / bridging oxygen as well as the non-bridging oxygen / phosphate P intensity ratio at near-normal emission angles, were found to increase with increasing polarization time.

These observations may be interpreted in terms of a breakdown of the polyphosphates layer. In several points of the surface film, the long-chain phosphates are re-transformed into soluble dihydrogenated orthophosphate which is readily dissolved. Thus, several “channels” are formed on the surface film destroying the protective barrier and allowing the oxygen to reach the alloy surface as well as the nickel to readily diffuse from the alloy to the solution. However, since the depth profile does not change with polarization time, the dissolution rate of the alloy has to be equal to the rate at which the surface film is restored. This sort of stationary state of dissolution may explain why the depth profile of the corrosion film does not change with increasing polarization time while the current increases. The formation of these “channels” has already been suggested by other authors to explain the breakdown of the protective surface film of NiP alloys [10].

REFERENCES

1. A.Kawashima, K.Asami, K.Hashimoto, *Corrosion Science 24(9)*, 807 (1984)
2. R.B.Diegle, N.R.Sorensen, G.C.Nelson, *Journal of the Electrochemical Society 133(9)*, 1769 (1986)
3. G.Salvago, G.Fumagalli, *Metal Finishing 85*, 31 (1987)
4. R.L.Zeller, *Corrosion 47(9)*, 692 (1991)
5. A.Krolikowski, P.Butkiewicz, *Electrochimica Acta 38(14)*, 1979 (1993)
6. M.M.V.Parente, O.R.Mattos, S.L.Diaz, P.Lima Neto, F.J.Fabri Miranda, *Journal of Apllied Electrochemistry 31*, 677 (2001)
7. P.Lo, W.Tsai, J.Lee, M.Hung, *Surface and Coatings Technology 67*, 27 (1994)
8. E.T.Van der Kouwe, *Electrochimica Acta 38(14)*, 2093 (1993)
9. A.Rossi, D.Atzei, B.Elsener, A.Krolikowski, *EUROCORR (on CD)*, (2001)
10. B.Bozzini, C.Lenardi, M.Serra, A.Fanigliulo, *British Corrosion Journal 37(3)*, 173 (2002)
11. H.Habazaki, S.Ding, A.Kawashima, K.Asami, K.Hashimoto, A.Inoue, T.Masumoto, *Corrosion Science 29(11/12)*, 1319 (1989)
12. A.Krolikowski, *"Passive Characteristics of Amorphous NiP alloys"*, in *Modification of Passive Films*, ed. P.Marcus, B.Baroux and M.Keddam, The Institute of Materials, London (1994)
13. A.Krolikowski, *Material Science Forum 799*, 185 (1995)
14. A.Krolikowski, B.Karbownicka, O.Jaklewics, *Electrochimica Acta 51*, 6120 (2006)
15. B.MacDougall, D.F.Mitchell, M.J.Graham, *Corrosion 38*, 85 (1982)
16. E.Sikara, D.D.MacDonald, *Electrochimica Acta 48*, 69 (2002)
17. H.W.Hoppe, H.H.Strehblow, *Surface and Interface Analysis 16*, 271 (1990)
18. R.B.Diegle, N.R.Sorensen, C.R.Clayton, M.A.Helfand, Y.C.Yu, *Journal of the Electrochemical Society 135(5)*, 1085 (1988)
19. M.Crobu, M.A.Scorciapino, B.Elsener, A.Rossi, *The corrosion resistance of electroless deposited nano-crystalline NiP alloys*, accepted for publication on *Electrochimica Acta* (2007)
20. S.J.Splinter, R.Rofagha, N.S.McIntyre, U.Erb, *Surface and Interface Analysis 24*, 181 (1996)
21. B.Elsener, A.Krolikowski, D.Atzei, A.Rossi, "*Effect of phosphorus concentration on the electronic structure of NiP nanocrystalline electrodeposited alloys: an XPS and*

X-AES investigation", accepted for publication on *Surface and Interface Analysis* (2007)

22. A.Rossi, B.Elsener, *"Characterization of surface films on FeCrPC alloys by XPS and X-ray excited Auger peaks", Surface Modification of Passive Films,* ed. P.Marcus, B.Baroux and M.Keddam, EFC Pubblication No.12, The Institute of Materials, London (1994)
23. C.D.Wagner, A.Joshi, *Journal of Electron Spectroscopy and Related Phenomena 47*, 283 (1991)
24. G.Moretti, *Journal of Electron Spectroscopy and Related Phenomena 95*, 95 (1998)
25. P.Peeters, G.Hoorn, T.Daenen, A.Kurowski, G.Staikov, *Electrochimica Acta 47*, 161 (2001)
26. J.Kojnok, A.Szasz, W.Krasser, G.Mark, V.S.Stepanjuk, A.A.Katsnelson, *Journal of Physics of Condensed Matter 4*, 2487 (1992)
27. E.Belin, A.Traverse, A.Szàsz, F.Machizaud, *J. Phys. F.: Met. Phys. 17*, 1913 (1987)
28. D.J.Siconolfi, R.P.Frankenthal, *Journal of the Electrochemical Society 136(9)*, 2475 (1989)
29. H.J.Freund, M.W.Roberts, *Surface Science Reports 25*, 225 (1996)
30. L.Zhang, J.Zhu, X.Jiang, D.G.Evans, F.Li, *Journal of Physics and Chemistry of Solids 67*, 1678 (2006)
31. J.F.Watts, J.Wolstenholme, *"An Introduction to Surface Anlysis by XPS and AES"*, ed. J.Wiley & Sons Ltd. (2003)
32. D.Briggs, M.Seah, *"Pratical Surface Analysis – vol.1"*, ed. J.Wiley & Sons Ltd. (1992)
33. Z.W.Kowalski, *Journal of Vacuum Science and Technology 1(2)*, 494 (1983)
34. M.A.Makeev, A.L.Barbasi, *Applied Physics Letters 71(19)*, 2800 (1997)
35. D.Briggs, M.Seah, *"Pratical Surface Analysis – vol.2"*, ed. J.Wiley & Sons Ltd. (1992)
36. http://www.quases.com/Downloads/QUASES-Tougaard/QUASESTougaard%20Ver5%20Manual.zip
37. S.Tougaard, *Surface and Interface Analysis 11*, 453 (1988)
38. U.Hofmann, K.G.Weil, *Corrosion Science 34(3)*, 423 (1993)
39. L.Peter, G.Lang, L.Kiss, J.Szalma, *Journal of Applied Electrochemistry 26*, 403 (1996)

40. J.N.Balaraju, T.S.N.Sankara Nayanan, S.K.Seshadri, *Journal of Solid State Electrochemistry 5*, 334 (2001)
41. S.Tougaard, *Surface and interface Analysis 26*, 249 (1998)
42. P.J.Cumpson, *"Angle-Resolved X-Ray Photoelectron Spectroscopy"* in *Surface Analysis by Auger and X-Ray Photoelectron Spectroscopy*, ed. D.Briggs and J.T.Grant, Surface Spectra and IM Pubblications (2003)
43. S.Tougaard, *Journal of Vacuum Science and Technology A14(3)*, 1415 (1996)
44. W.S.M.Werner, W.H.Gries, H.Störi, *Journal of Vacuum Science Technology 9*, 21 (1991)
45. A.Jablonski, J.Zemek, *Surface Science 387*, 288 (1997)
46. P.J.Cumpson, M.P.Seah, *Surface and Interface Analysis 25*, 430 (1997)
47. M.Olla, G.Navarra, B.Elsener, A.Rossi, *Surface and Interface Analysis 38*, 964 (2006)
48. M.Pourbaix, *Atlas of Electrochemical Equilibria in Aqueous Solutions,* Pergamon Press Ltd. (1966)
49. D.Addari and A.Rossi, unpublished data

CHAPTER 7

CONCLUSIONS AND OUTLOOK

In the final chapter of this thesis the most important conclusions that can be drawn from this work are summarized. Open questions and proposes experiments for their clarification are also addressed, as well as ideas for the further development of the MEM protocol.

7.1 CONCLUSIONS

In this work an efficient new protocol has been developed and validated for the non-destructive reconstruction of compositional depth profiles for the outermost surface region of layered samples, using the Maximum Entropy Method from ARXPS data. It has been demonstrated that the MEM protocol allows to reconstruct the depth profile of a sample composed of between 3 and 8 components, a larger number than that envisaged by Tougaard's method. The accuracy of the MEM protocol is comparable with that reported for Tougaard's method ($\leq$ 10% for the primary structural parameter and 10-30% for the secondary ones) and deteriorates with increasing depth. However, though the compositional depth profiles reconstructed using the MEM protocol are more detailed than those obtained with Tougaard's method, it is concluded that these two in-depth profiling methods should be considered as complementary. Tougaard's method is a fairly simple and fast method for obtaining a rough approximation of the compositional depth-profile, which can be described in greater detail with the MEM protocol.

The MEM protocol was implemented for reconstructing the compositional depth-profiles of technologically important electroless deposited Ni-P alloys, known to exhibit outstanding corrosion resistance. Indeed, the anodic polarization behaviour was found to be the same in neutral and in acid solutions, a current density arrest occurring in the potential range from ca. -0.2 to +0.2 V SCE, as reported in the literature. Current decay during potentiostatic polarization obeys, in this potential range, a square root law with time, indicating a diffusion controlled dissolution process. As XPS/XAES data did not reveal any nickel oxide on the polarized Ni-18P alloys, the formation of an oxide passive film, as happens for pure nickel, can be ruled out. Application of the new MEM protocol developed in this work, combined with Tougaard's method allowed to non-destructively reconstruct the compositional depth profile of Ni-18P alloys after 1, 3 and 14 hours polarization at +0.1 V SCE in 0.1 M Na_2SO_4 solution. A carbon/oxygen contamination layer (ca. 1 nm) was detected overlying the corrosion film formed on the Ni-18P alloy. This corrosion film is composed of a (poly)phosphates layer (ca. 1 nm) separated from the bulk alloy by a P-rich interface (ca. 2 nm) containing ca. 50 at.%. phosphorus. This P-enriched layer may explain the diffusion controlled dissolution of the alloy. Based on XPS/XAES surface analysis, the concept of Auger parameter and the chemical state plot, two different chemical states of phosphorus were identified: P as in the bulk of the Ni-18P alloy and P in the elemental

chemical state. Thus, both the hypotheses advanced in the literature, namely a hypophosphite and a phosphide layer, can be ruled out.
This is the first time the occurrence of localized corrosion after prolonged potentiostatic polarization in the potential range of the current arrest in chloride-free solutions has been reported. Corrosion attack does not preferentially occur at morphological features, but is more randomly distributed. The thickness of the NiP coating, ranging from 10 to 20 μm, does not influence the electrochemical and corrosion properties of the electroless deposited Ni-18P alloys.

Finally, based on the findings of this study, a model is proposed for explaining the high corrosion resistance of NiP alloys in near neutral solutions. As soon as the Ni-P alloy is immersed in the solution, both nickel and phosphorus tend to dissolve in the electrolyte solution as Ni^{2+} and $H_2PO_3^-$ respectively. Nickel dissolves faster than phosphorus, resulting in an enrichment of P at the alloy surface. At polarization times < 1 hour, further dissolution of the alloy is controlled by nickel diffusion through the thickening P-enriched layer. Part of the phosphite anions produced by phosphorus oxidation, may be further oxidized to phosphate anions, which, in turn, may condense and be adsorbed at the P-enriched alloy surface, forming a (poly)phosphates layer. This phosphates layer may act as a further barrier between the alloy surface and the electrolyte solution. At longer polarization times (> 1 hour), the phosphates layer breaks down and "channels" may form penetrating the corrosion film and allowing oxygen to reach the alloy surface and nickel to diffuse towards the solution. However, no changes in depth profile of the corrosion film were detected in this study, suggesting that further dissolution of the alloy is counterbalanced by restoration of the corrosion films.

7.2 OUTLOOK

The new MEM protocol developed in this work is certainly applicable to a very large variety of real samples but now needs to be fully implemented. The input/output linkage between the two algorithms involved need to be computer coded as well as the input/output linkage between the simulator routine and the protocol. Furthermore, it is possible to also implement the G-1 predictive formula for calculating the appropriate IMFP set during protocol runs instead of working with a fixed values set. These improvements will make the overall simulator-protocol routine enormously less time-consuming and should also improve accuracy of the results. Once this code has been implemented, it could be incorporated into a software package for XPS spectra analysis such as CasaXPS used in this work, so as to

simplify the passage from ARXPS spectra curve-fitting to their intensity correction for sensitivity factors and their input into the MEM simulator-protocol code.
In this work, the new MEM protocol was numerically tested on structures with up to 8 components but this “limit” could be extended to 9 or more components performing new suitable numerical experiments.
The numerical experiments performed here show, for the relative depth plots, that the difference in relative depths of two or more species located within the same depth range (i.e. within the same layer) is due solely to their different IMFP, thus a correction factor needs to be devised that make these plots more reliable.

As far as the hypothesis about the formation and breakdown mechanisms of the corrosion protection of Ni-P alloys is concerned, further insight could be gained “sampling” the potentiostatic polarization curve a greater number of times in an attempt to reconstruct the evolution of corrosion film formation during the first hour of immersion. An accurate surface study of different kinds of nickel phosphates, poly- and ultra-phosphates as well as phosphites, would certainly provide further insight into the actual nature of the phosphates film detected in this work.
Lastly, the localized attacks detected at longer polarization time do not seem to initiate in any particular morphological feature. Increasing the polarization time, the only spectral variation revealed by XPS was the intensity ratio of the two O1s peaks attributed to bridging and non-bridging oxygen of (poly)phosphates. Thus, the appearance of “black spots” warrants further investigation to determine whether these are related to chemical/structural modifications within the (poly)phosphates layer or in the alloy.

ACKNOWLEDGMENTS

First of all, I would like to thank prof. Antonella Rossi who gave me the opportunity to carry out my Ph.D thesis in her laboratory, doing really a great job in supervising my work. I would like to thank prof. Bernhard Elsener for his great contribute to the present thesis. The motivating discussions with them and their encouraging support were an important factor for the success of my work.

I also thank prof. Gabriele Navarra for his fundamental help in implementing the algorithms and in adjusting and optimizing the MEM protocol.

Prof. Anna Musinu and Dr. Carla Cannas are greatly acknowledged for their help in synthesizing the pyrophosphate glass.

I would also to thank Maura Crobu for his help in performing the electrochemical measurements and Gaby Peschke for EDX analysis.

Finally, I would like to thank Dr. Danilo Addari and Dr. Marzia Fantauzzi because they are the best colleague that a Ph.D student can desire.

MIUR is acknowledged for the financial support.

APPENDIX A : OTHER MEM NUMERICAL EXPERIMENTS RESULTS

In this appendix, the MEM numerical experiments results, which were omitted in the chapter 5, are reported. Numerical experiments were performed on various synthetic (i.e. numerical) structures which were composed by 3 to 8 components which were labeled A, B, C, D, E, F, G and H. Components IMFP values were chosen arbitrary to be 40, 30, 20, 10, 45, 35, 25 and 27 Å respectively. The ACD and the corresponding RDP, calculated on the basis of this IMFP set, are referred to as "real" (e.g. the real-RDP).

The ACD and the corresponding RDP, were also re-calculated by using only one IMFP value for all the species, in order to examine the effects of the differences between the species IMFP. These diagrams are referred to as "trial" (e.g. the trial-RDP).

For each of the numerical experiments, the model in-depth profile and its MEM simulation are reported. Furthermore, both the real-ACD and the MEM recalculated curves, and one double figure to show both the real- and the trial-RDP, are reported too. Finally, a table resumes all the layers thickness and the species concentration of both the model and the MEM simulated in-depth profile. Results are reported with their deviation from the model profile.

SYNTHETIC STRUCTURE ***4_1+1+2***

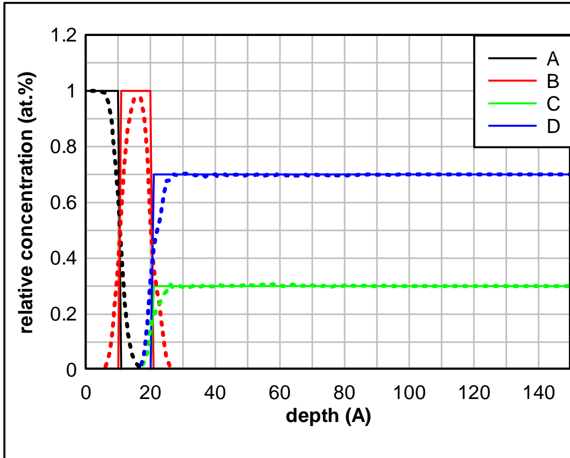

Figure A.1 : Depth profile of synthetic structure 4_1+1+2 and MEM simulation (dotted lines).

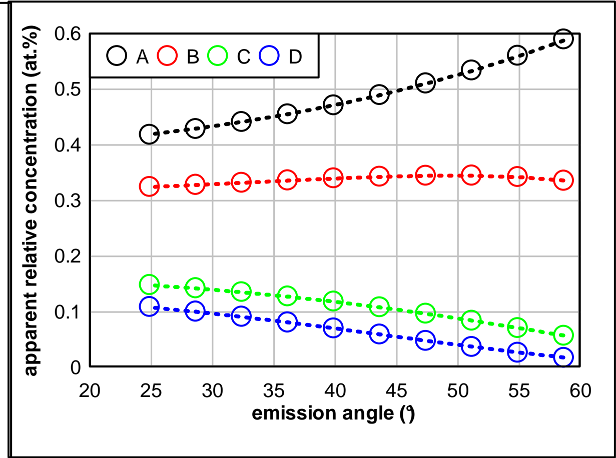

Figure A.2 : Apparent Concentration Diagram of synthetic structure 4_1+1+2 (circles) and recalculated MEM data (dotted lines).

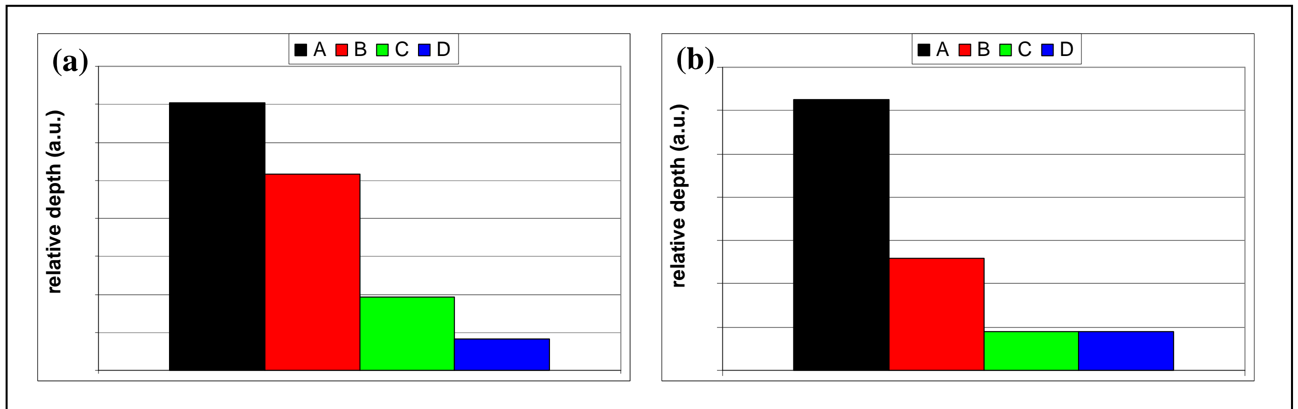

Figure A.3 : Relative Depth Plot of synthetic structure 4_1+1+2. ***(a)*** *real-RDP and* ***(b)*** *trial-RDP.*

Table A.1 : In-depth profile parameters of synthetic structure 4_1+1+2 and results of MEM simulation.

layer	**thickness (Å)**		**|deviation| (Å)**
	model	**simulation**	
overlayer	*11.0*	*10.5*	*0.5*
intermediate layer	*10.0*	*11.1*	*1.1*

layer	**species**	**concentration (at.%)**		**relative error (%)**
		model	**simulation**	
bulk	*C*	*30*	*30*	*0*
	D	*70*	*70*	*0*

SYNTHETIC STRUCTURE ***4_2+1+1***

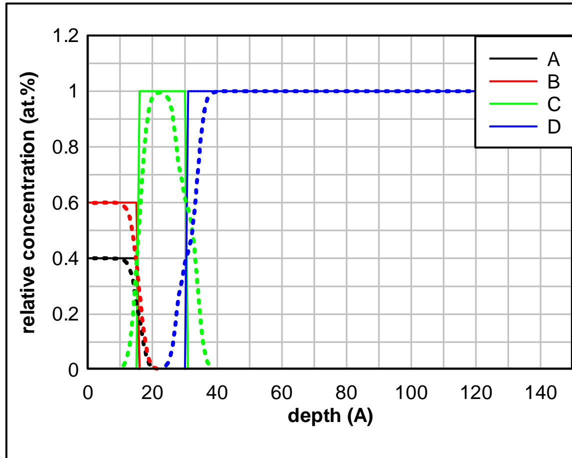

Figure A.4 : Depth profile of synthetic structure 4_2+1+1 and MEM simulation (dotted lines).

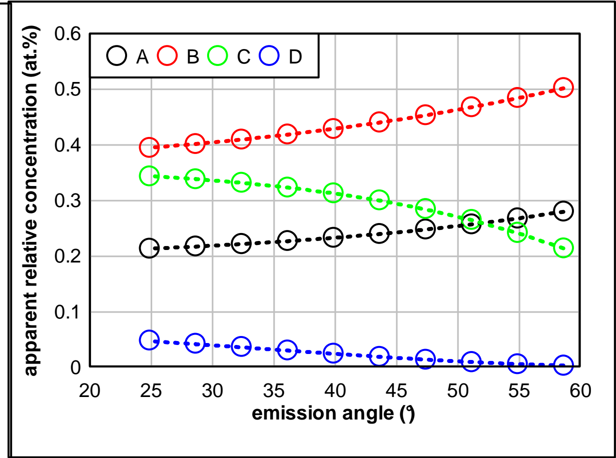

Figure A.5 : Apparent Concentration Diagram of synthetic structure 4_2+1+1 (circles) and recalculated MEM data (dotted lines).

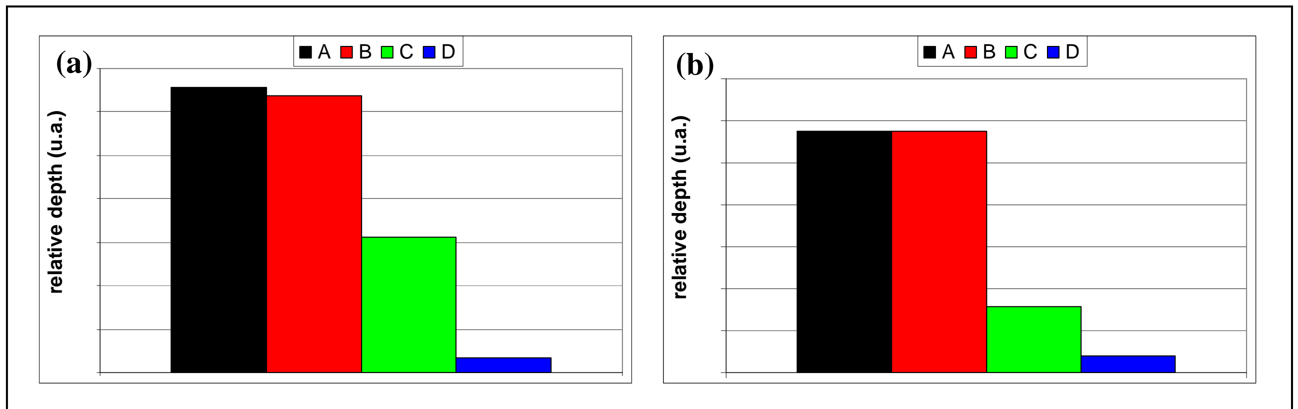

*Figure A.6 : Relative Depth Plot of synthetic structure 4_2+1+1. (**a**) real-RDP and (**b**) trial-RDP.*

Table A.2 : In-depth profile parameters of synthetic structure 4_2+1+1 and results of MEM simulation.

layer	**thickness (Å)**		**|deviation| (Å)**
	model	**simulation**	
overlayer	*16.0*	*16.5*	*0.5*
intermediate layer	*15.0*	*15.2*	*0.2*

layer	**species**	**concentration (at.%)**		**relative error (%)**
		model	**simulation**	
overlayer	*A*	*40*	*40*	*0*
	B	*60*	*60*	*0*

SYNTHETIC STRUCTURE ***4_1+3***

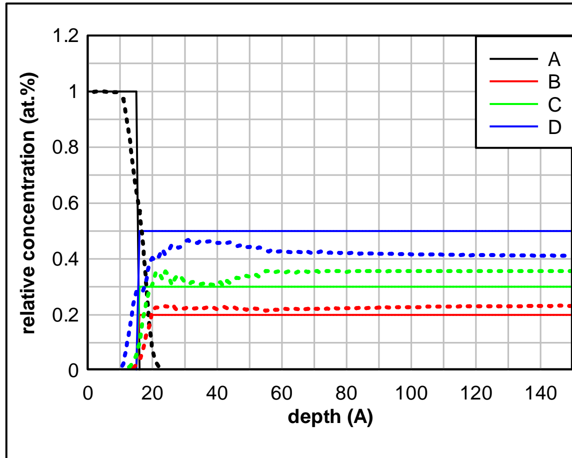

Figure A.7 : Depth profile of synthetic structure 4_1+3 and MEM simulation (dotted lines).

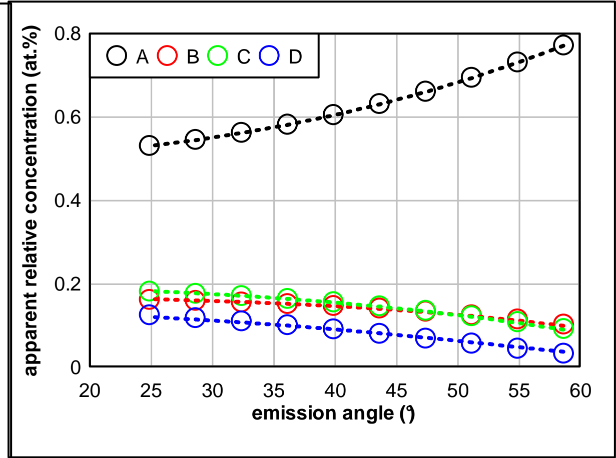

Figure A.8 : Apparent Concentration Diagram of synthetic structure 4_1+3 (circles) and recalculated MEM data (dotted lines).

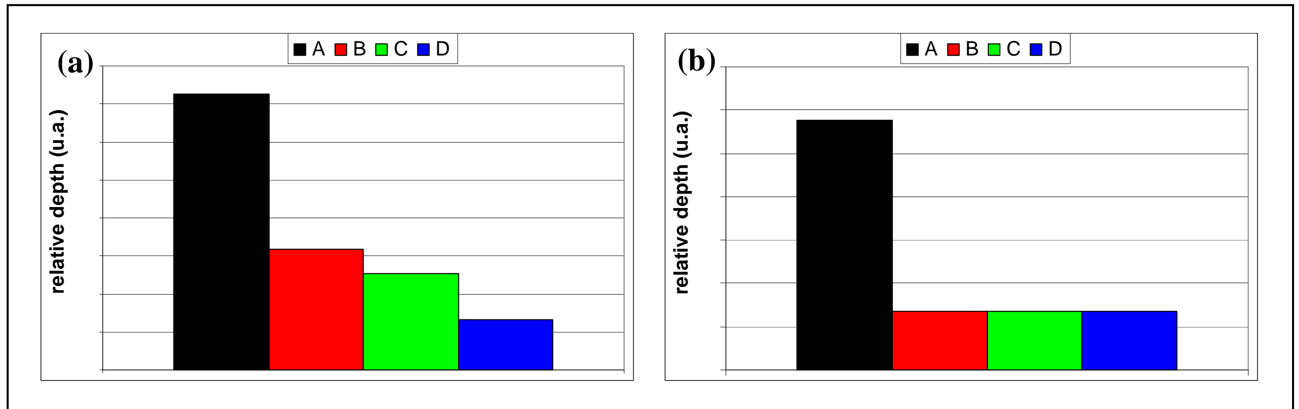

*Figure A.9 : Relative Depth Plot of synthetic structure 4_1+3. (**a**) real-RDP and (**b**) trial-RDP.*

Table A.3 : In-depth profile parameters of synthetic structure 4_1+3 and results of MEM simulation.

layer		thickness (Å)		|deviation| (Å)
		model	simulation	
overlayer		*16.0*	*15.7*	*0.3*
layer	**species**	**concentration (at.%)**		**relative error (%)**
		model	**simulation**	
bulk	*B*	*20*	*22*	*12*
	C	*30*	*35*	*15*
	D	*50*	*43*	*-14*

SYNTHETIC STRUCTURE ***4_3+1***

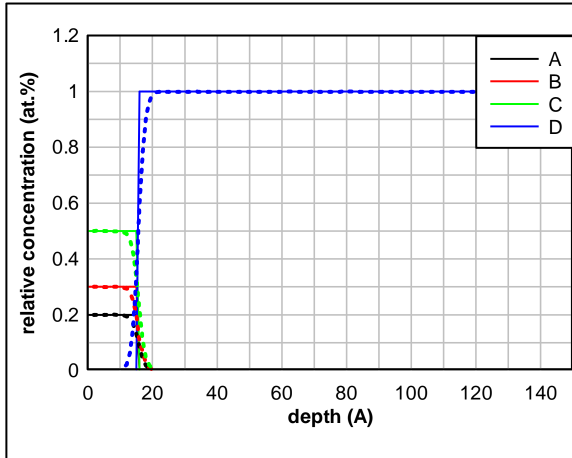

Figure A.10 : Depth profile of synthetic structure 4_3+1 and MEM simulation (dotted lines).

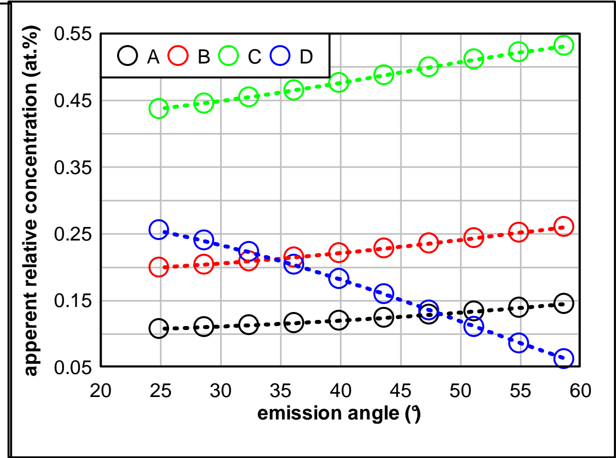

Figure A.11 : Apparent Concentration Diagram of synthetic structure 4_3+1 (circles) and recalculated MEM data (dotted lines).

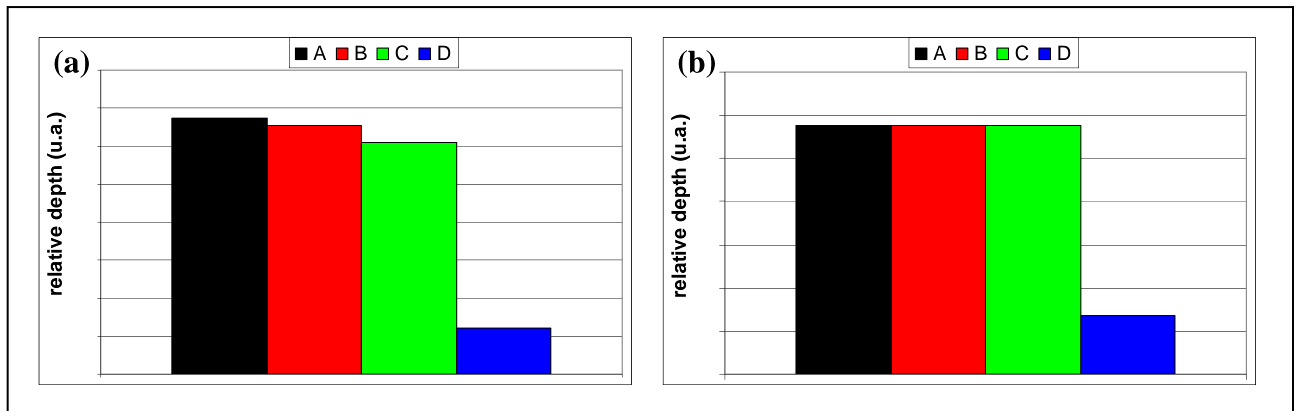

Figure A.12 : Relative Depth Plot of synthetic structure 4_3+1. ***(a)*** *real-RDP and* ***(b)*** *trial-RDP.*

Table A.4 : In-depth profile parameters of synthetic structure 4_3+1 and results of MEM simulation.

layer	**thickness (Å)**		**|deviation| (Å)**
	model	**simulation**	
overlayer	*16.0*	*16.6*	*0.6*

layer	**species**	**concentration (at.%)**		**relative error (%)**
		model	**simulation**	
overlayer	*A*	*20*	*20*	*0*
	B	*30*	*30*	*0*
	C	*50*	*50*	*0*

SYNTHETIC STRUCTURE ***4_2+2***

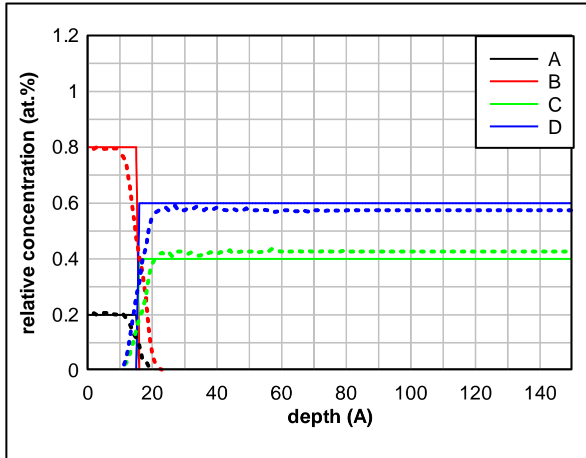

Figure A.13 : Depth profile of synthetic structure 4_2+2 and MEM simulation (dotted lines).

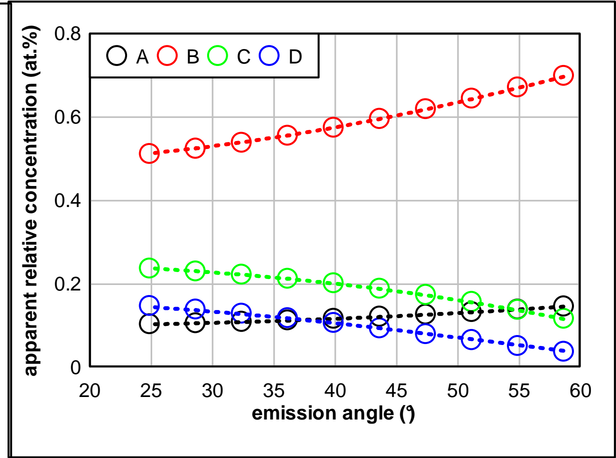

Figure A.14 : Apparent Concentration Diagram of synthetic structure 4_2+2 (circles) and recalculated MEM data (dotted lines).

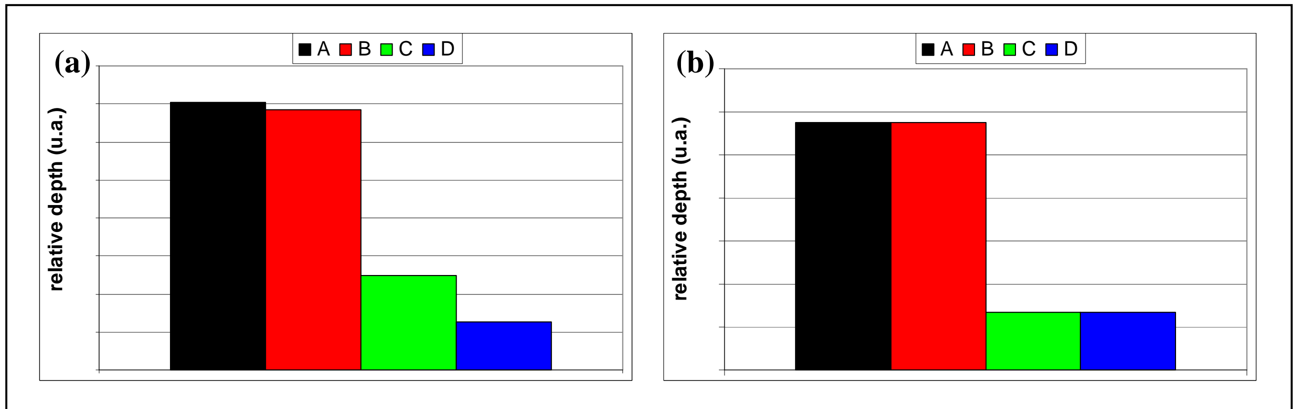

*Figure A.15 : Relative Depth Plot of synthetic structure 4_2+2. **(a)** real-RDP and **(b)** trial-RDP.*

Table A.5 : In-depth profile parameters of synthetic structure 4_2+2 and results of MEM simulation.

layer		**thickness (Å)**		**|deviation| (Å)**
		model	**simulation**	
overlayer		*16.0*	*15.9*	*0.1*
layer	**species**	**concentration (at.%)**		**relative error (%)**
		model	**simulation**	
overlayer	*A*	*20*	*20*	*0*
	B	*80*	*80*	*0*
bulk	*C*	*40*	*42*	*6*
	D	*60*	*58*	*-4*

SYNTHETIC STRUCTURE ***5_1+2+2***

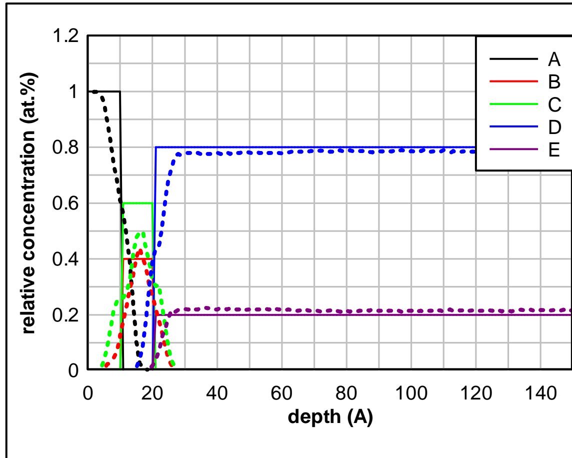

Figure A.16 : Depth profile of synthetic structure 5_1+2+2 and MEM simulation (dotted lines).

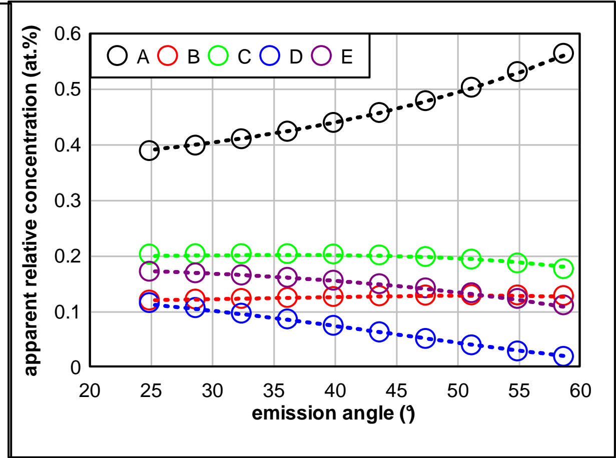

Figure A.17 : Apparent Concentration Diagram of synthetic structure 5_1+2+2 (circles) and recalculated MEM data (dotted lines).

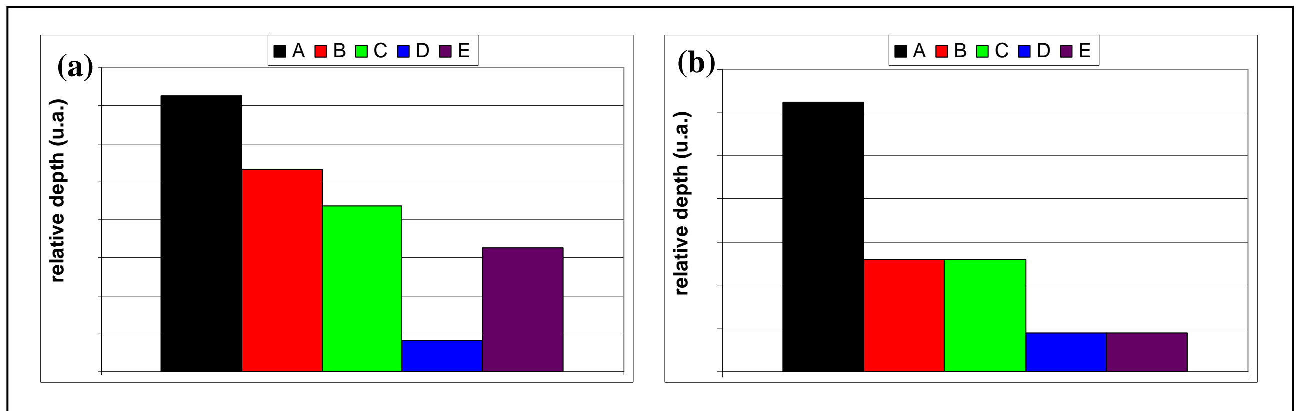

Figure A.18 : Relative Depth Plot of synthetic structure 5_1+2+2. ***(a)*** *real-RDP and* ***(b)*** *trial-RDP.*

Table A.6 : In-depth profile parameters of synthetic structure 5_1+2+2 and results of MEM simulation.

layer	**thickness (Å) model**	**thickness (Å) simulation**	**|deviation| (Å)**
overlayer	*11.0*	*10.1*	*0.9*
intermediate layer	*10.0*	*11.9*	*1.9*

layer	**species**	**concentration (at.%) model**	**concentration (at.%) simulation**	**relative error (%)**
intermediate layer	*B*	*40*	*41*	*3*
	C	*60*	*59*	*-2*
bulk	*D*	*80*	*79*	*-1*
	E	*20*	*21*	*5*

SYNTHETIC STRUCTURE ***5_2+1+2***

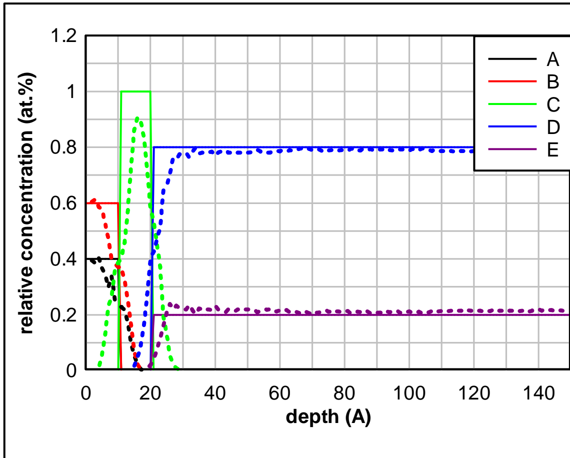

Figure A.19 : Depth profile of synthetic structure 5_2+1+2 and MEM simulation (dotted lines).

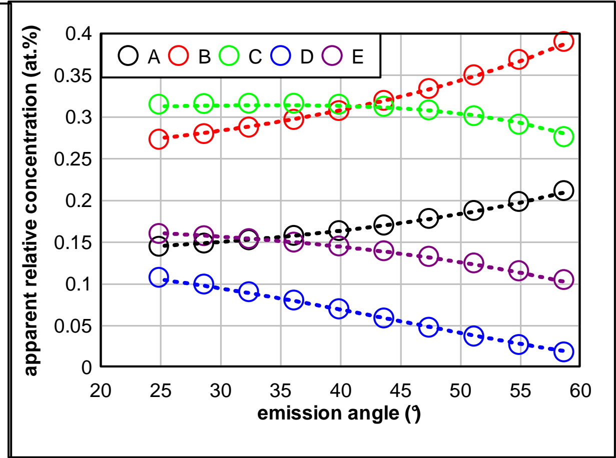

Figure A.20 : Apparent Concentration Diagram of synthetic structure 5_2+1+2 (circles) and recalculated MEM data (dotted lines).

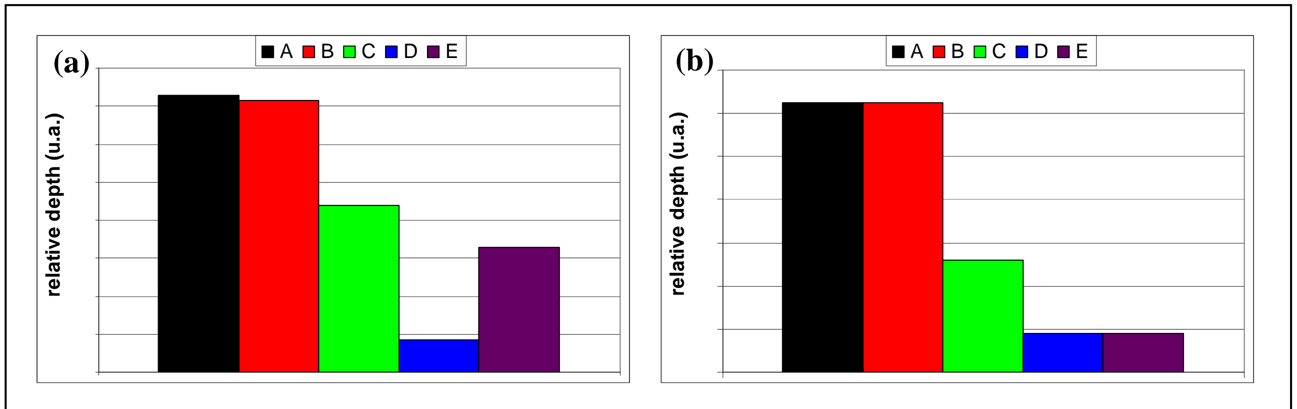

*Figure A.21 : Relative Depth Plot of synthetic structure 5_2+1+2. **(a)** real-RDP and **(b)** trial-RDP.*

Table A.7 : In-depth profile parameters of synthetic structure 5_2+1+2 and results of MEM simulation.

layer		thickness (Å) model	thickness (Å) simulation	|deviation| (Å)
overlayer		*11.0*	*12.0*	*1.0*
intermediate layer		*10.0*	*11.6*	*1.6*
layer	**species**	**concentration (at.%) model**	**concentration (at.%) simulation**	**relative error (%)**
overlayer	*A*	*40*	*40*	*0*
	B	*60*	*60*	*0*
bulk	*D*	*80*	*79*	*-1*
	E	*20*	*21*	*5*

SYNTHETIC STRUCTURE ***5_2+2+1***

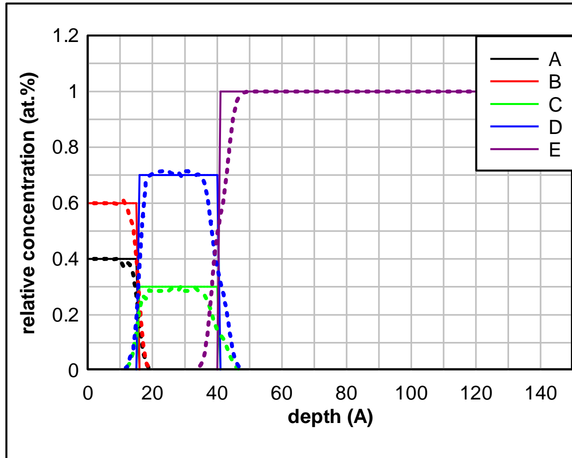

Figure A.22 : Depth profile of synthetic structure 5_2+2+1 and MEM simulation (dotted lines).

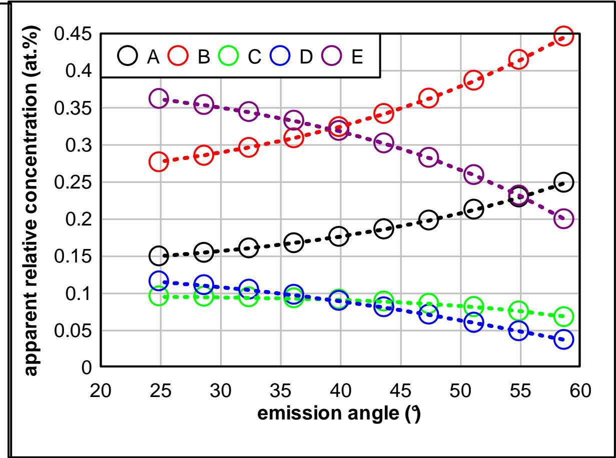

Figure A.23 : Apparent Concentration Diagram of synthetic structure 5_2+2+1 (circles) and recalculated MEM data (dotted lines).

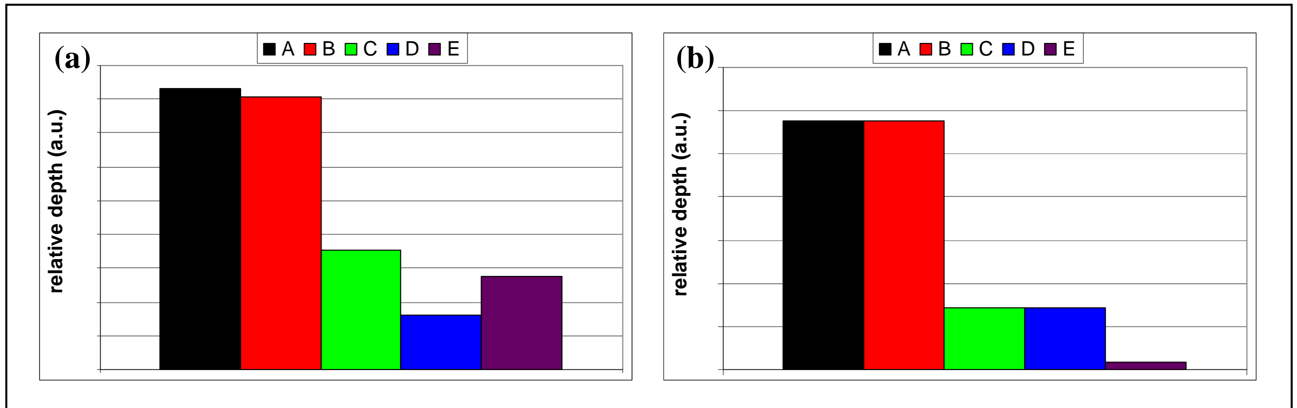

*Figure A.24 : Relative Depth Plot of synthetic structure 5_2+2+1. **(a)** real-RDP and **(b)** trial-RDP.*

Table A.8 : In-depth profile parameters of synthetic structure 5_2+2+1 and results of MEM simulation.

layer	thickness (Å)		|deviation| (Å)
	model	simulation	
overlayer	*16.0*	*16.1*	*0.1*
intermediate layer	*25.0*	*25.5*	*0.5*

layer	species	concentration (at.%)		relative error (%)
		model	simulation	
overlayer	*A*	*40*	*40*	*0*
	B	*60*	*60*	*0*
intermediate layer	*C*	*30*	*29*	*-3*
	D	*70*	*71*	*1*

SYNTHETIC STRUCTURE ***5_1+3+1***

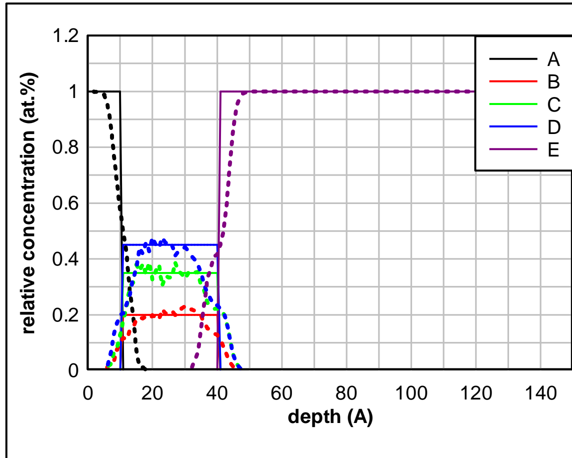

Figure A.25 : Depth profile of synthetic structure 5_1+3+1 and MEM simulation (dotted lines).

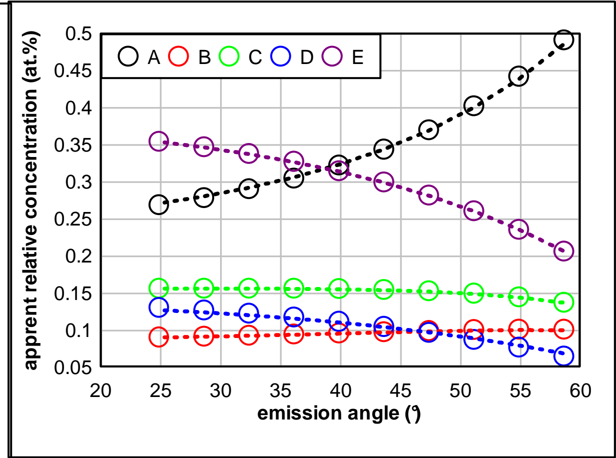

Figure A.26 : Apparent Concentration Diagram of synthetic structure 5_1+3+1 (circles) and recalculated MEM data (dotted lines).

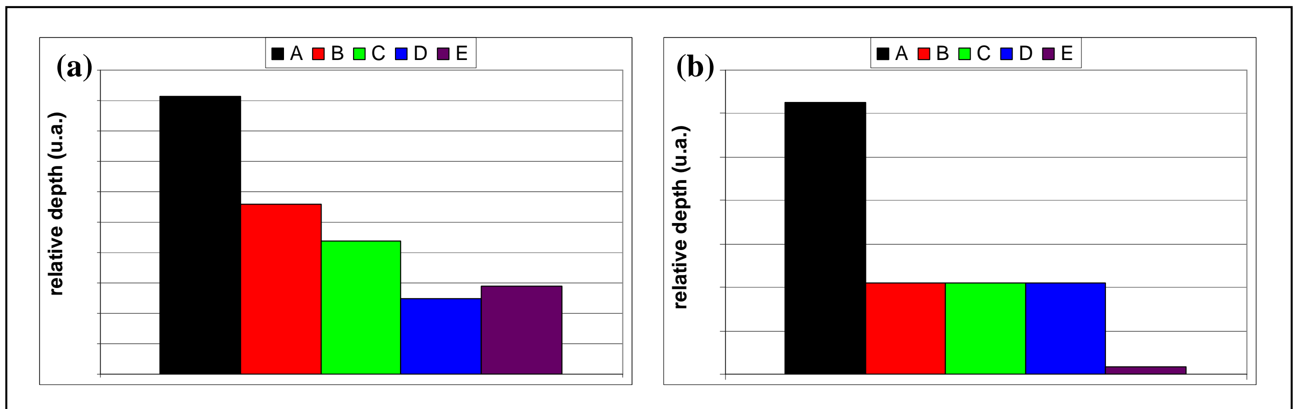

*Figure A.27 : Relative Depth Plot of synthetic structure 5_1+3+1. (**a**) real-RDP and (**b**) trial-RDP.*

Table A.9 : In-depth profile parameters of synthetic structure 5_1+3+1 and results of MEM simulation.

layer	**thickness (Å)**		**|deviation| (Å)**
	model	**simulation**	
overlayer	*11.0*	*10.6*	*0.4*
intermediate layer	*30.0*	*29.9*	*0.1*

layer	**species**	**concentration (at.%)**		**relative error (%)**
		model	**simulation**	
intermediate layer	*B*	*20*	*21*	*5*
	C	*35*	*36*	*3*
	D	*45*	*43*	*-4*

SYNTHETIC STRUCTURE ***5_3+1+1***

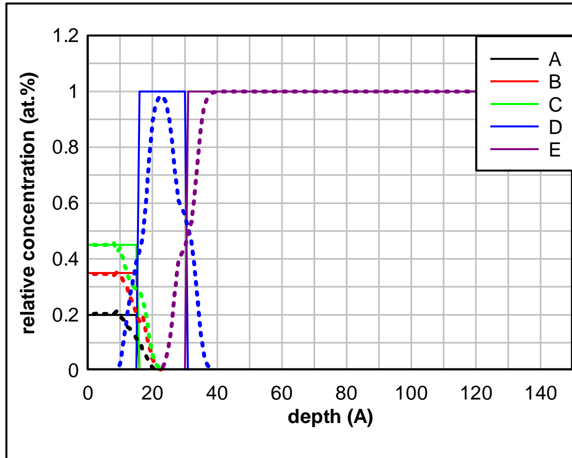

Figure A.28 : Depth profile of synthetic structure 5_3+1+1 and MEM simulation (dotted lines).

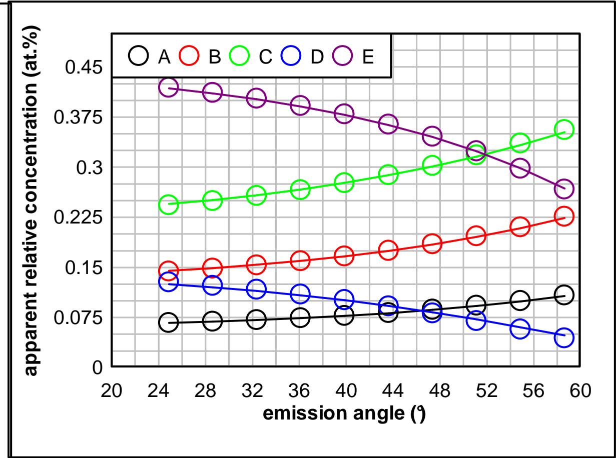

Figure A.29 : Apparent Concentration Diagram of synthetic structure 5_3+1+1 (circles) and recalculated MEM data (dotted lines).

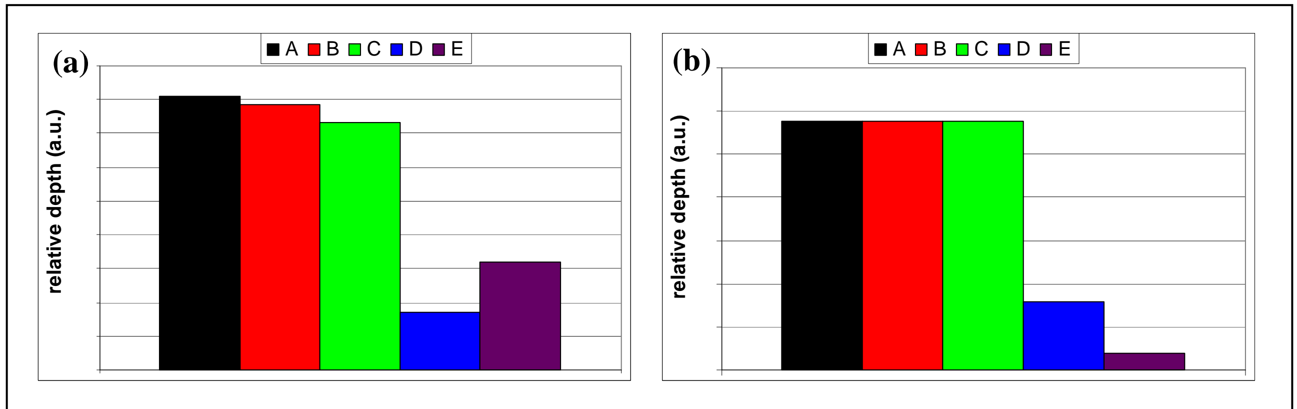

*Figure A.30 : Relative Depth Plot of synthetic structure 5_3+1+1. **(a)** real-RDP and **(b)** trial-RDP.*

Table A.10 : In-depth profile parameters of synthetic structure 5_3+1+1 and results of MEM simulation.

layer	**thickness (Å)**		**|deviation| (Å)**
	model	**simulation**	
overlayer	*16.0*	*15.9*	*0.1*
intermediate layer	*15.0*	*15.2*	*0.2*

layer	**species**	**concentration (at.%)**		**relative error (%)**
		model	**simulation**	
overlayer	*A*	*20*	*20*	*0*
	B	*35*	*35*	*0*
	C	*45*	*45*	*0*

SYNTHETIC STRUCTURE ***5_2+3***

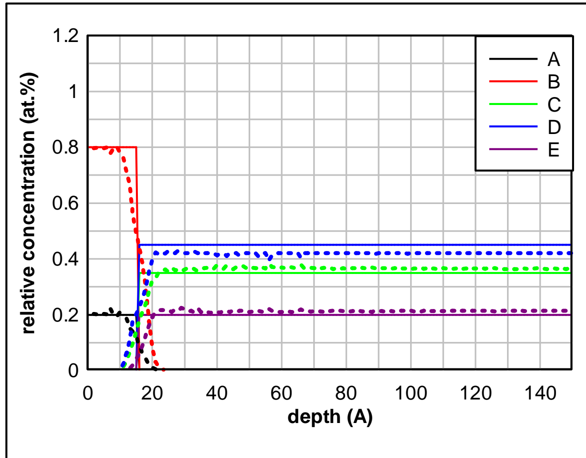

Figure A.31 : Depth profile of synthetic structure 5_2+3 and MEM simulation (dotted lines).

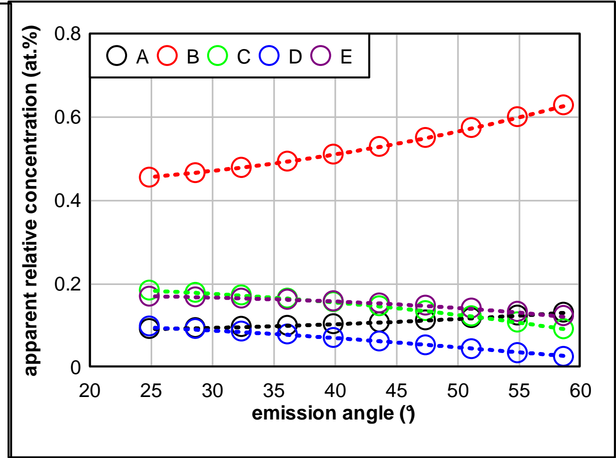

Figure A.32 : Apparent Concentration Diagram of synthetic structure 5_2+3 (circles) and recalculated MEM data (dotted lines).

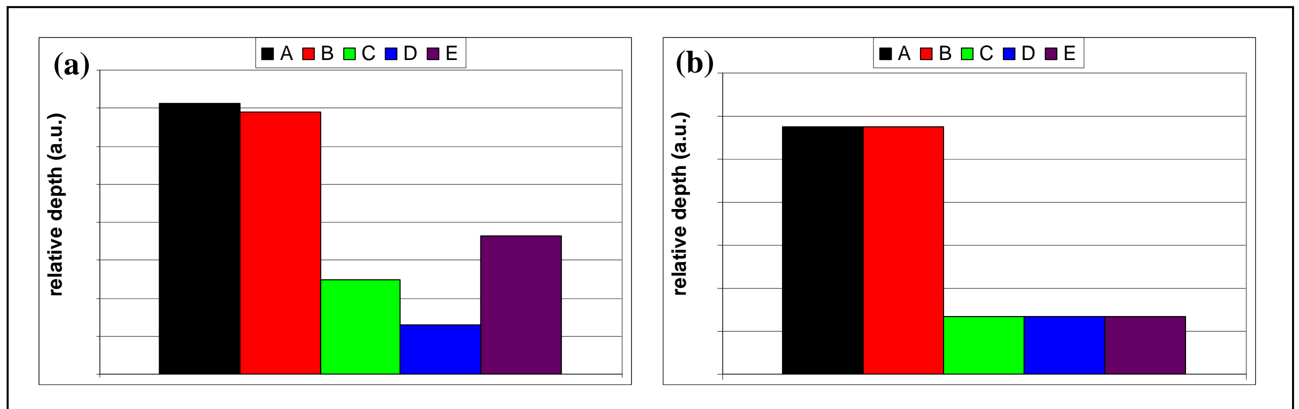

Figure A.33 : Relative Depth Plot of synthetic structure 5_2+3. ***(a)*** *real-RDP and* ***(b)*** *trial-RDP.*

Table A.11 : In-depth profile parameters of synthetic structure 5_2+3 and results of MEM simulation.

layer		**thickness (Å)** **model**	**simulation**	**|deviation| (Å)**
overlayer		*16.0*	*16.8*	*0.8*
layer	**species**	**concentration (at.%)** **model**	**simulation**	**relative error (%)**
overlayer	*A*	*20*	*20*	*0*
	B	*80*	*80*	*0*
bulk	*C*	*35*	*37*	*6*
	D	*45*	*42*	*-7*
	E	*20*	*21*	*5*

SYNTHETIC STRUCTURE ***6_1+1+2+2***

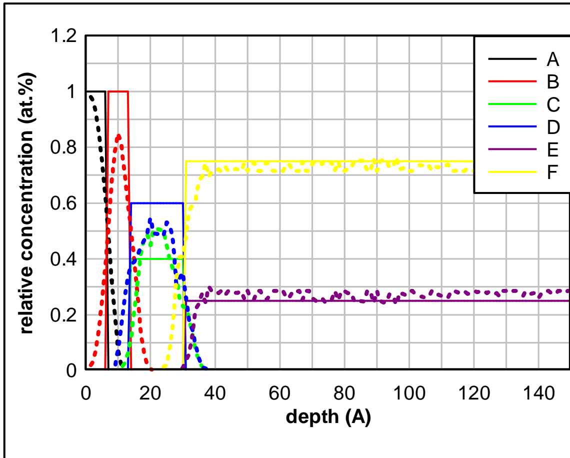

Figure A.34 : Depth profile of synthetic structure 6_1+1+2+2 and MEM simulation (dotted lines).

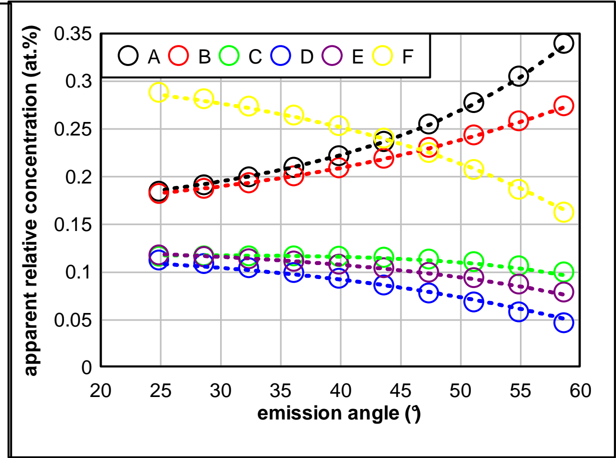

Figure A.35 : Apparent Concentration Diagram of synthetic structure 6_1+1+2+2 (circles) and recalculated MEM data (dotted lines).

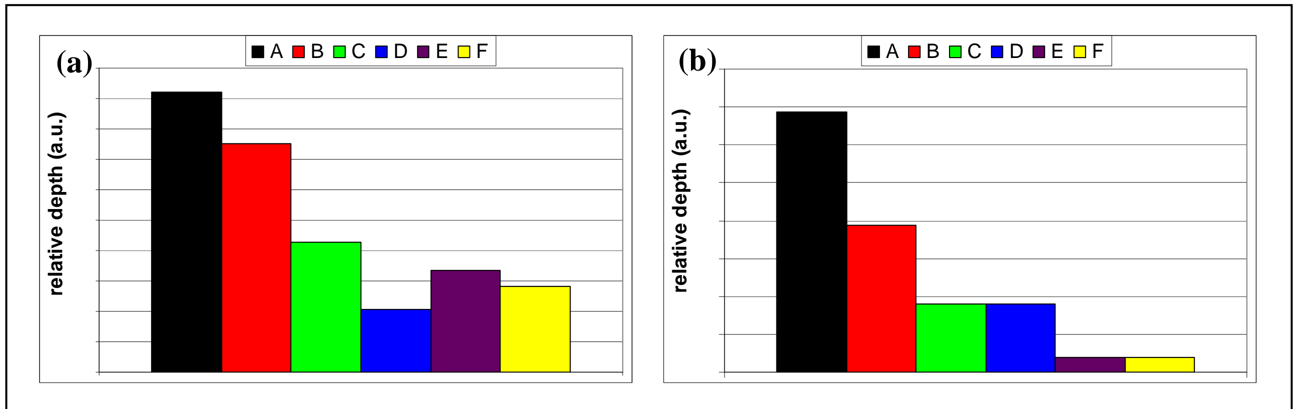

*Figure A.36 : Relative Depth Plot of synthetic structure 6_1+1+2+2. **(a)** real-RDP and **(b)** trial-RDP.*

Table 5.12 : In-depth profile parameters of synthetic structure 6_1+1+2+2 and results of MEM simulation.

layer	thickness (Å) model	thickness (Å) simulation	|deviation| (Å)
overlayer	*7.0*	*6.5*	*0.5*
1st intermediate layer	*7.0*	*8.8*	*1.8*
2nd intermediate layer	*17.0*	*15.3*	*1.7*

layer	species	concentration (at.%) model	concentration (at.%) simulation	relative error (%)
2nd intermediate layer	*C*	*40*	*44*	*10*
	D	*60*	*56*	*-7*
bulk	*E*	*25*	*27*	*8*
	F	*75*	*73*	*-3*

SYNTHETIC STRUCTURE ***6_1+2+2+1***

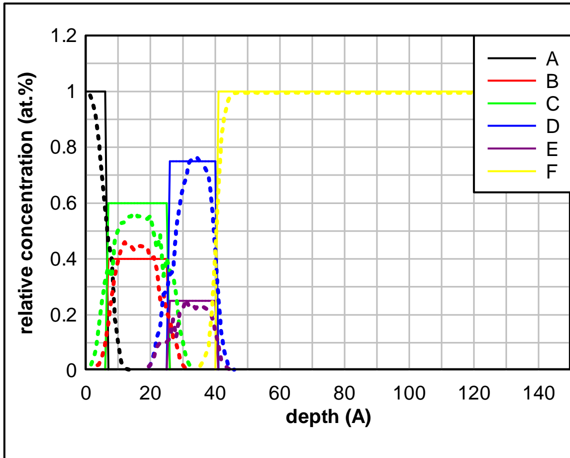

Figure A.37 : Depth profile of synthetic structure 6_1+2+2+1 and MEM simulation (dotted lines).

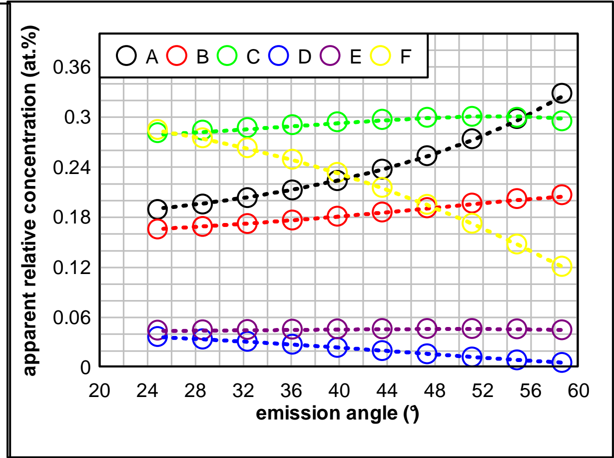

Figure A.38 : Apparent Concentration Diagram of synthetic structure 6_1+2+2+1 (circles) and recalculated MEM data (dotted lines).

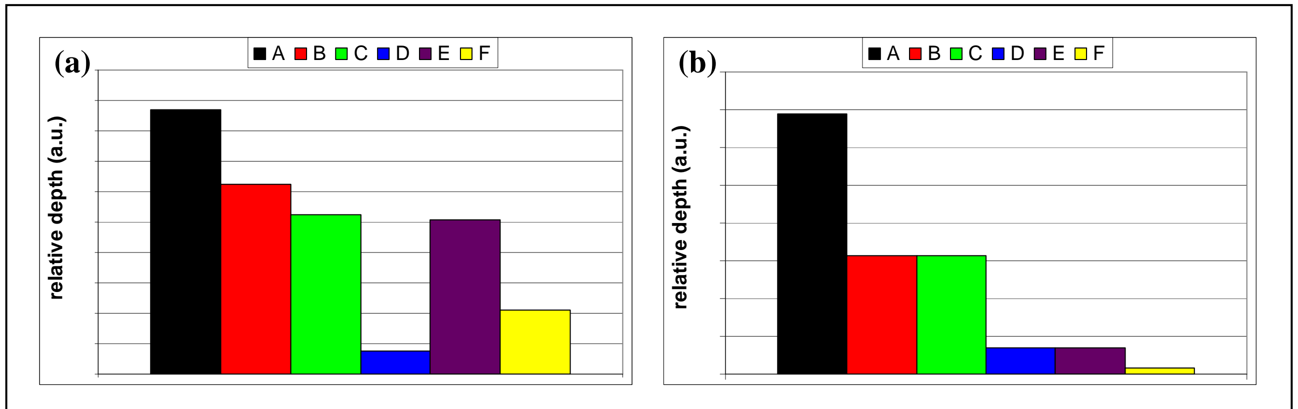

Figure A.39 : Relative Depth Plot of synthetic structure 6_1+2+2+1. ***(a)*** *real-RDP and* ***(b)*** *trial-RDP.*

Table 5.13 : In-depth profile parameters of synthetic structure 6_1+2+2+1 and results of MEM simulation.

layer	thickness (Å) model	thickness (Å) simulation	|deviation| (Å)
overlayer	*7.0*	*7.1*	*0.1*
1st intermediate layer	*19.0*	*18.5*	*0.5*
2nd intermediate layer	*15.0*	*16.8*	*1.8*

layer	species	concentration (at.%) model	concentration (at.%) simulation	relative error (%)
1st intermediate layer	*B*	*40*	*40*	*0*
	C	*60*	*60*	*0*
2nd intermediate layer	*D*	*75*	*75*	*0*
	E	*25*	*25*	*0*

SYNTHETIC STRUCTURE ***6_2+1+1+2***

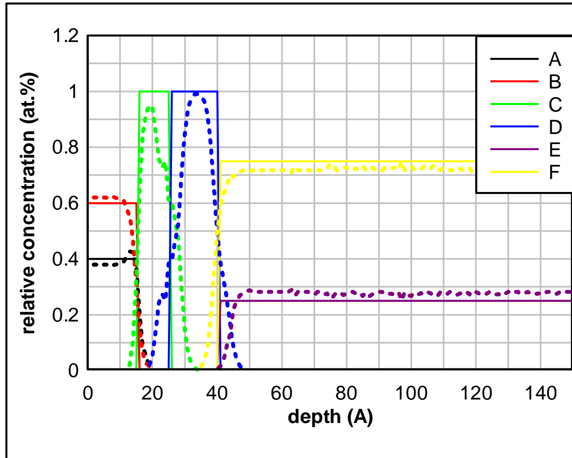

Figure A.40 : Depth profile of synthetic structure 6_2+1+1+2 and MEM simulation (dotted lines).

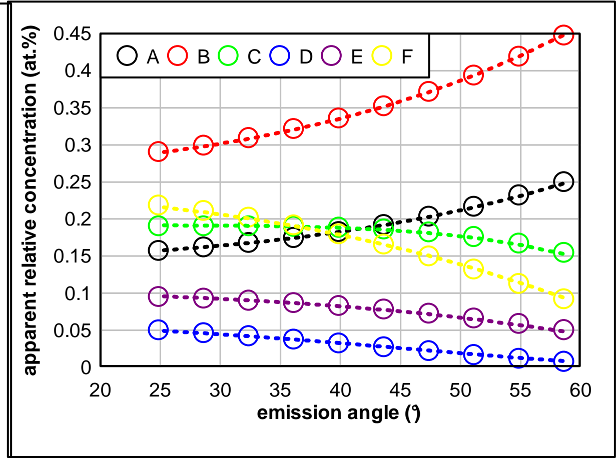

Figure A.41 : Apparent Concentration Diagram of synthetic structure 6_2+1+1+2 (circles) and recalculated MEM data (dotted lines).

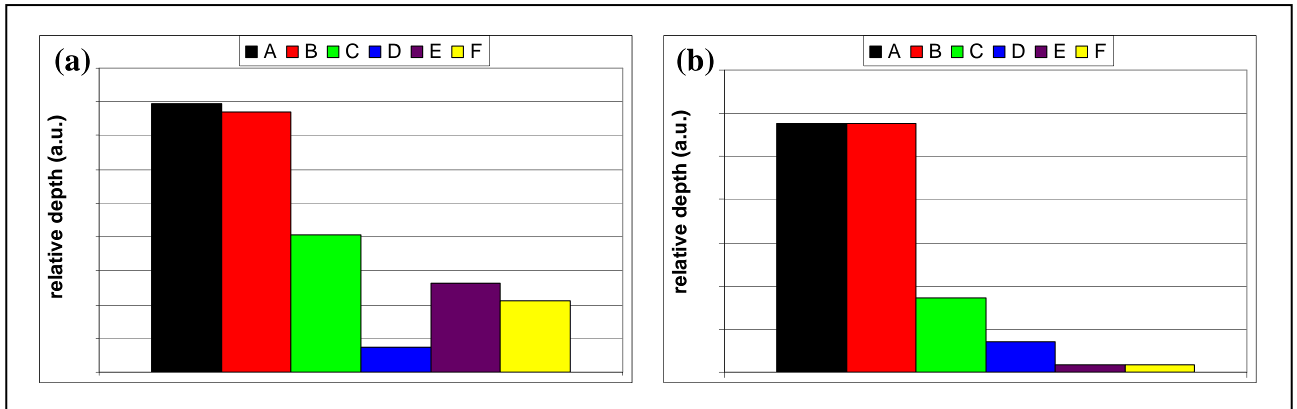

*Figure A.42 : Relative Depth Plot of synthetic structure 6_2+1+1+2. **(a)** real-RDP and **(b)** trial-RDP.*

Table 5.14 : In-depth profile parameters of synthetic structure 6_2+1+1+2 and results of MEM simulation.

layer	**thickness (Å)**		**|deviation| (Å)**
	model	**simulation**	
overlayer	*16.0*	*16.0*	*0.0*
1st intermediate layer	*10.0*	*10.1*	*0.1*
2nd intermediate layer	*15.0*	*15.5*	*0.5*

layer	**species**	**concentration (at.%)**		**relative error (%)**
		model	**simulation**	
overlayer	*A*	*40*	*41*	*3*
	B	*60*	*59*	*-2*
bulk	*E*	*25*	*27*	*8*
	F	*75*	*73*	*-3*

SYNTHETIC STRUCTURE ***6_2+1+2+1***

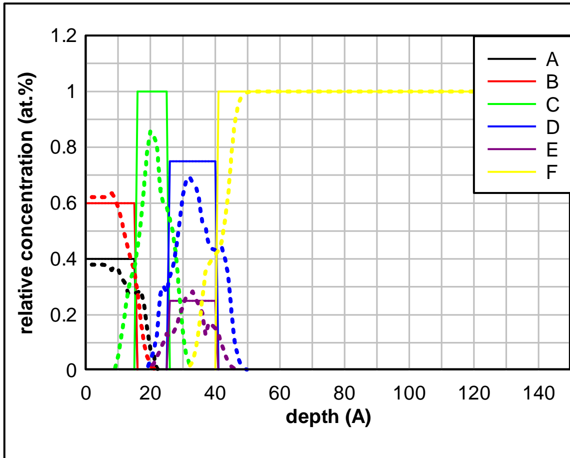

Figure A.43 : Depth profile of synthetic structure 6_2+1+2+1 and MEM simulation (dotted lines).

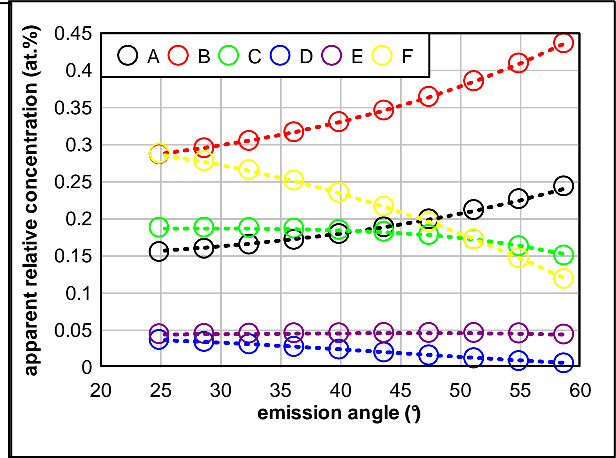

Figure A.44 : Apparent Concentration Diagram of synthetic structure 6_2+1+2+1 (circles) and recalculated MEM data (dotted lines).

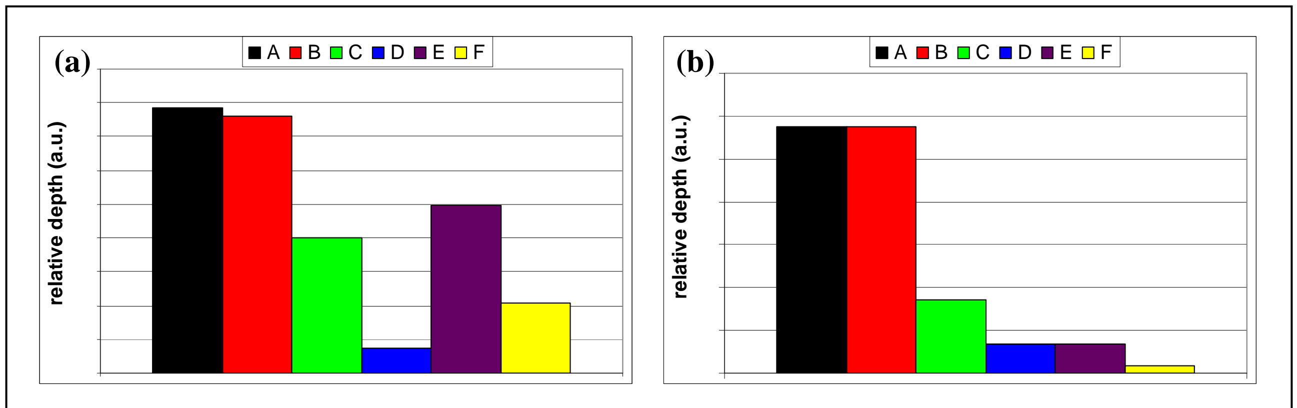

Figure A.45 : Relative Depth Plot of synthetic structure 6_2+1+1+2. ***(a)*** *real-RDP and* ***(b)*** *trial-RDP.*

Table 5.15 : In-depth profile parameters of synthetic structure 6_2+1+2+1 and results of MEM simulation.

layer	thickness (Å) model	thickness (Å) simulation	|deviation| (Å)
overlayer	*16.0*	*15.3*	*0.7*
1st intermediate layer	*10.0*	*11.5*	*1.5*
2nd intermediate layer	*15.0*	*15.2*	*0.2*

layer	species	concentration (at.%) model	concentration (at.%) simulation	relative error (%)
overlayer	*A*	*40*	*41*	*3*
	B	*60*	*59*	*-2*
2nd intermediate layer	*D*	*75*	*75*	*0*
	E	*25*	*25*	*0*

SYNTHETIC STRUCTURE ***6_1+2+3***

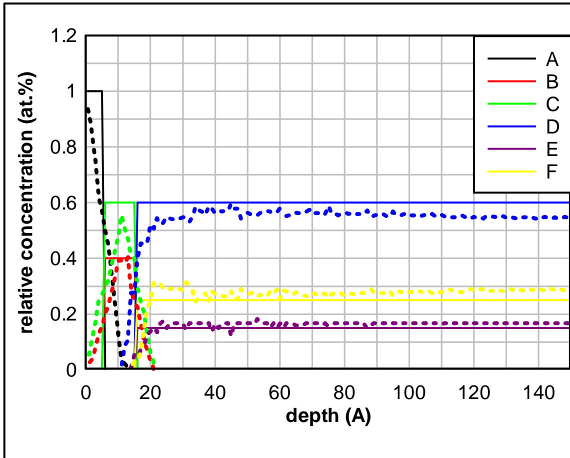

Figure A.46 : Depth profile of synthetic structure 6_1+2+3 and MEM simulation (dotted lines).

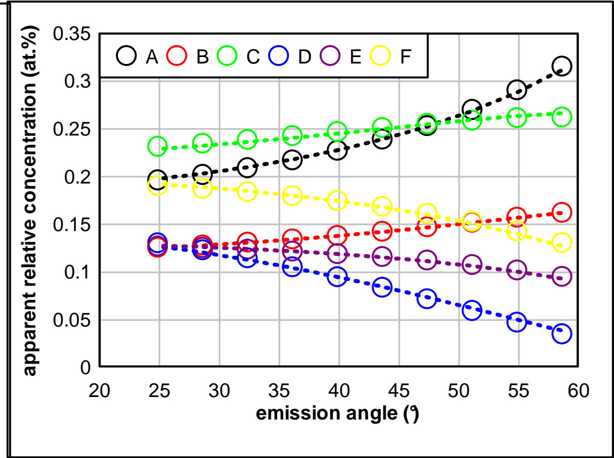

Figure A.47 : Apparent Concentration Diagram of synthetic structure 6_1+2+3 (circles) and recalculated MEM data (dotted lines).

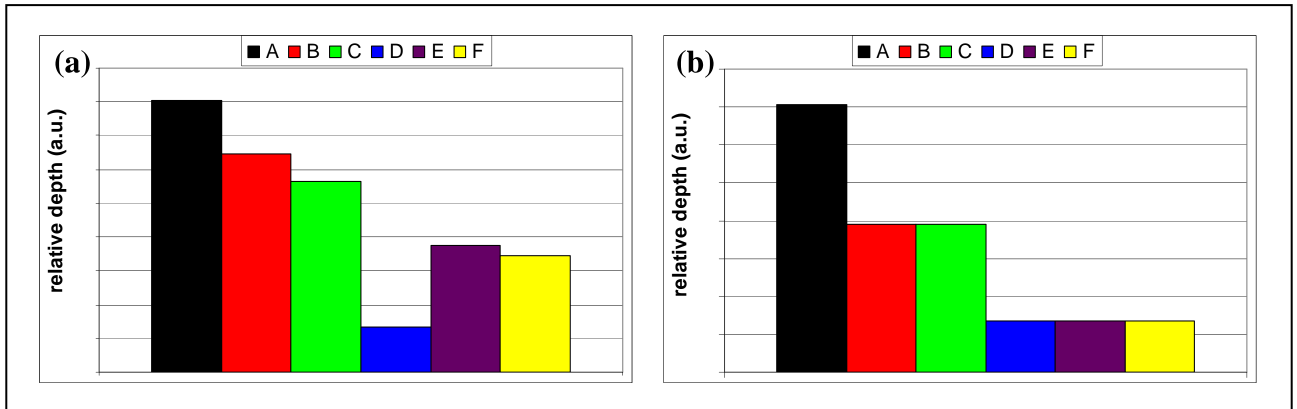

*Figure A.48 : Relative Depth Plot of synthetic structure 6_1+2+3. (**a**) real-RDP and (**b**) trial-RDP.*

Table 5.16 : In-depth profile parameters of synthetic structure 6_1+2+3 and results of MEM simulation.

layer	thickness (Å)		|deviation| (Å)
	model	simulation	
overlayer	*6.0*	*5.8*	*0.2*
intermediate layer	*10.0*	*11.0*	*1.0*

layer	species	concentration (at.%)		relative error (%)
		model	simulation	
intermediate layer	*B*	*40*	*41*	*3*
	C	*60*	*59*	*-2*
bulk	*D*	*60*	*56*	*-7*
	E	*15*	*16*	*7*
	F	*25*	*28*	*12*

SYNTHETIC STRUCTURE ***6_2+1+3***

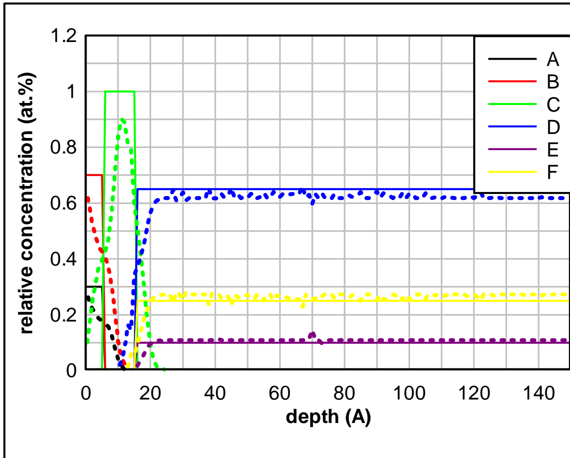

Figure A.49 : Depth profile of synthetic structure 6_2+1+3 and MEM simulation (dotted lines).

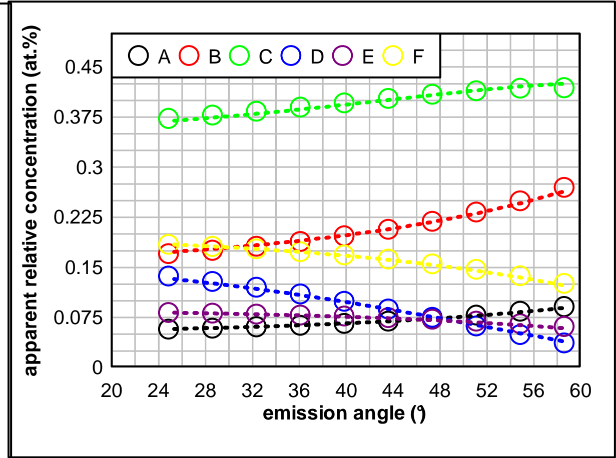

Figure A.50 : Apparent Concentration Diagram of synthetic structure 6_2+1+3 (circles) and recalculated MEM data (dotted lines).

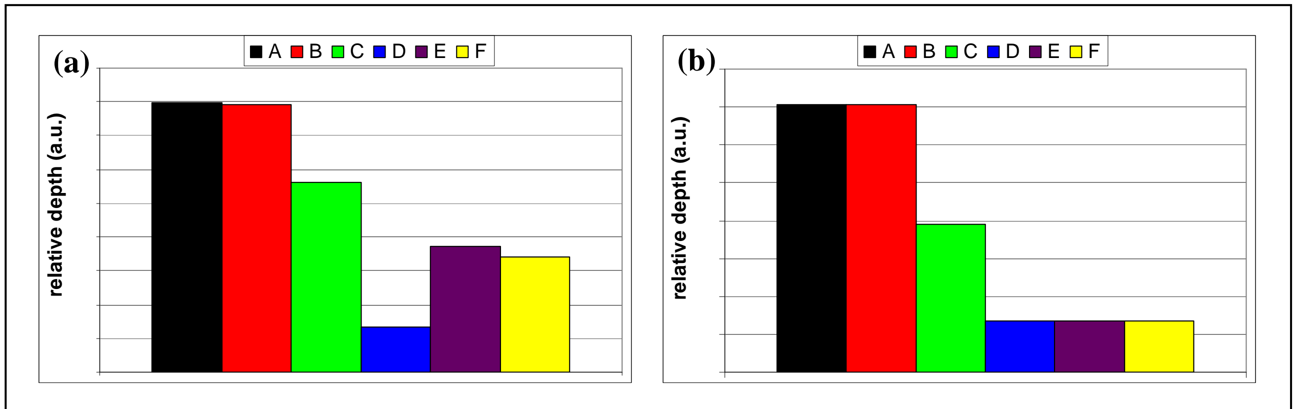

*Figure A.51 : Relative Depth Plot of synthetic structure 6_2+1+3. **(a)** real-RDP and **(b)** trial-RDP.*

Table 5.17 : In-depth profile parameters of synthetic structure 6_2+1+3 and results of MEM simulation.

layer	thickness (Å)		|deviation| (Å)
	model	simulation	
overlayer	*6.0*	*5.4*	*0.6*
intermediate layer	*10.0*	*11.2*	*0.0*

layer	species	concentration (at.%)		relative error (%)
		model	simulation	
overlayer	*A*	*30*	*30*	*0*
	B	*70*	*70*	*0*
bulk	*D*	*65*	*63*	*-3*
	E	*10*	*11*	*10*
	F	*25*	*26*	*4*

SYNTHETIC STRUCTURE ***6_2+3+1***

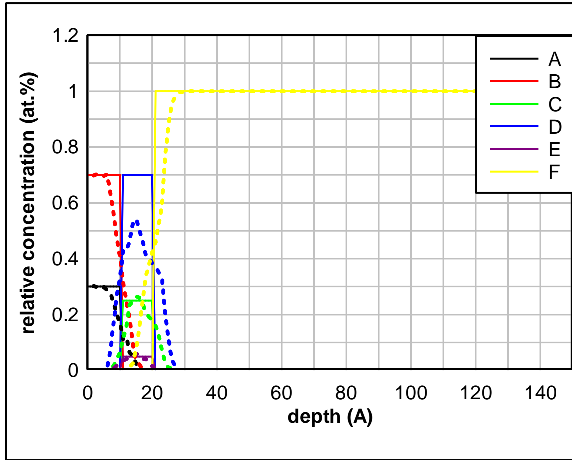

Figure A.52 : Depth profile of synthetic structure 6_2+3+1 and MEM simulation (dotted lines).

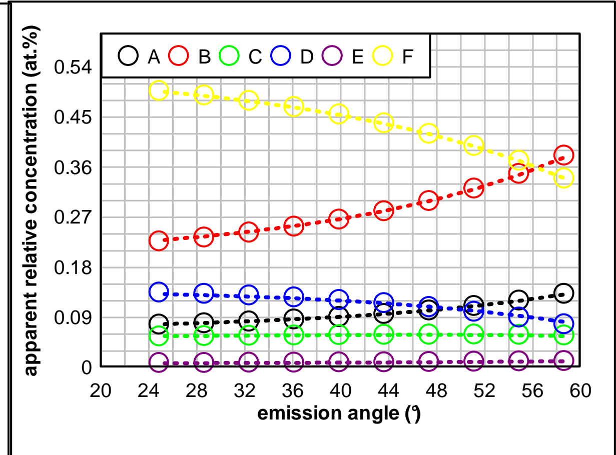

Figure A.53 : Apparent Concentration Diagram of synthetic structure 6_2+3+1 (circles) and recalculated MEM data (dotted lines).

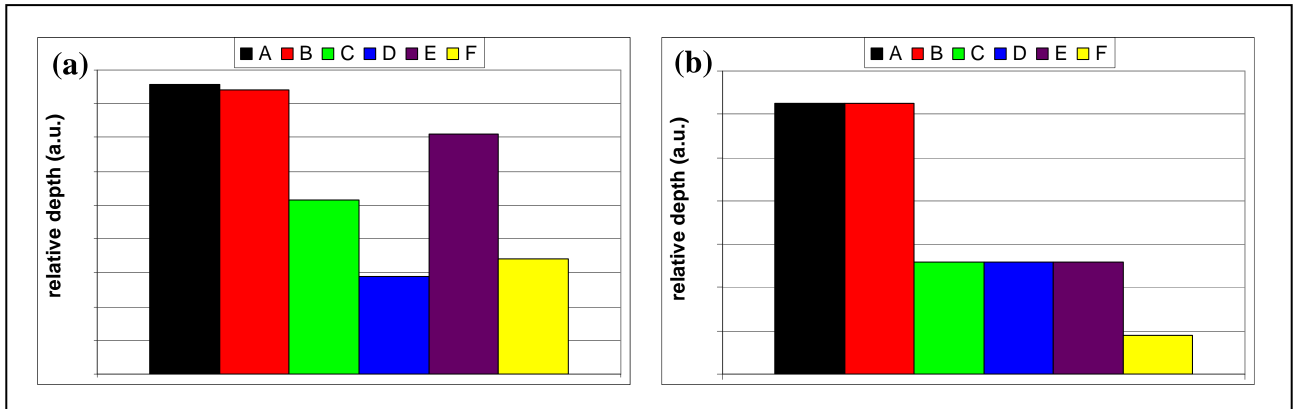

Figure A.54 : Relative Depth Plot of synthetic structure 6_2+3+1. ***(a)*** *real-RDP and* ***(b)*** *trial-RDP.*

Table 5.18 : In-depth profile parameters of synthetic structure 6_2+3+1 and results of MEM simulation.

layer	thickness (Å)		
	model	**simulation**	**|deviation| (Å)**
overlayer	*11.0*	*10.5*	*0.5*
intermediate layer	*10.0*	*11.5*	*1.5*

layer	species	concentration (at.%)		relative error (%)
		model	**simulation**	
overlayer	*A*	*30*	*30*	*0*
	B	*70*	*70*	*0*
intermediate layer	*D*	*25*	*26*	*4*
	E	*70*	*69*	*-1*
	F	*5*	*5*	*0*

SYNTHETIC STRUCTURE ***6_3+2+1***

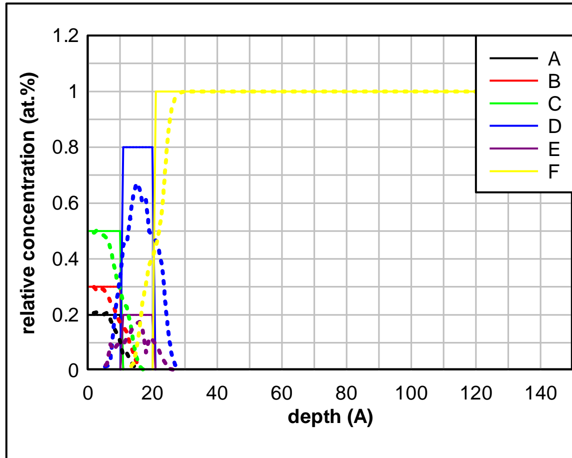

Figure A.55 : Depth profile of synthetic structure 6_3+2+1 and MEM simulation (dotted lines).

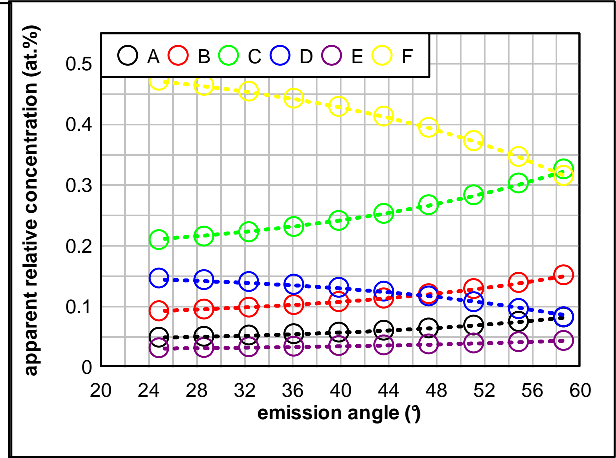

Figure A.56 : Apparent Concentration Diagram of synthetic structure 6_3+2+1 (circles) and recalculated MEM data (dotted lines).

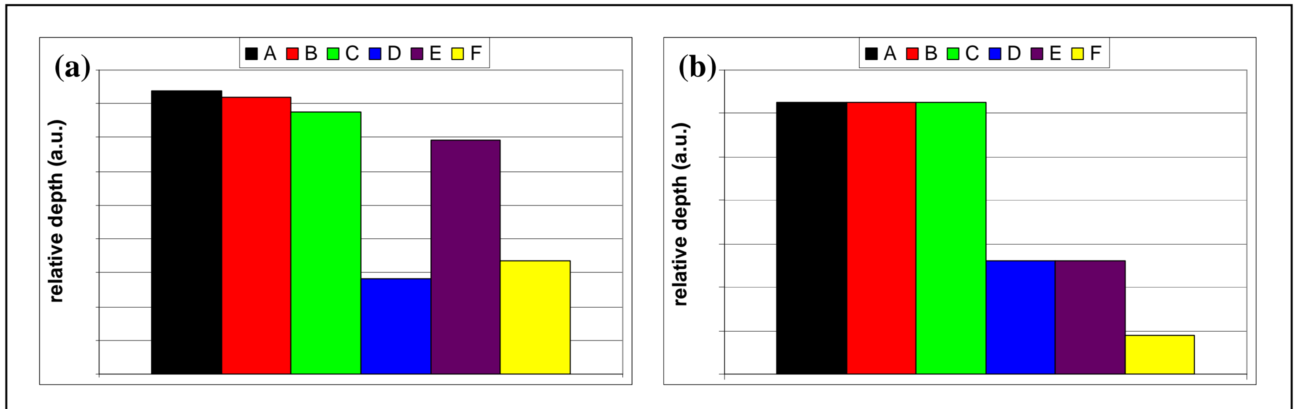

*Figure A.57 : Relative Depth Plot of synthetic structure 6_3+2+1. (**a**) real-RDP and (**b**) trial-RDP.*

Table 5.19 : In-depth profile parameters of synthetic structure 6_3+2+1 and results of MEM simulation.

layer	**thickness (Å)**		**|deviation| (Å)**
	model	**simulation**	
overlayer	*11.0*	*10.9*	*0.1*
intermediate layer	*10.0*	*11.4*	*1.4*

layer	**species**	**concentration (at.%)**		**relative error (%)**
		model	**simulation**	
overlayer	*A*	*20*	*19*	*-5*
	B	*30*	*30*	*0*
	C	*50*	*51*	*2*
intermediate layer	*D*	*80*	*81*	*1*
	E	*20*	*19*	*-5*

SYNTHETIC STRUCTURE ***6_2+2+2***

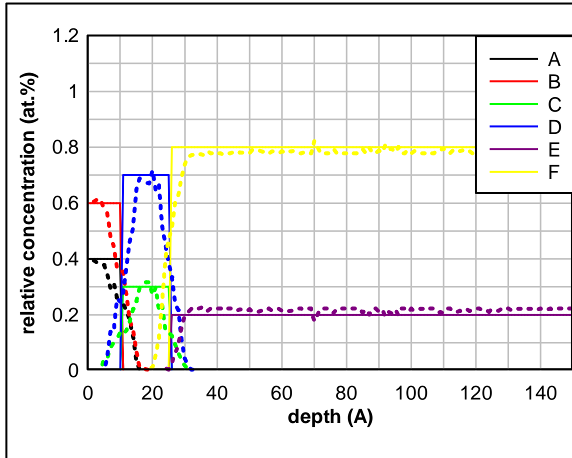

Figure A.58 : Depth profile of synthetic structure 6_2+2+2 and MEM simulation (dotted lines).

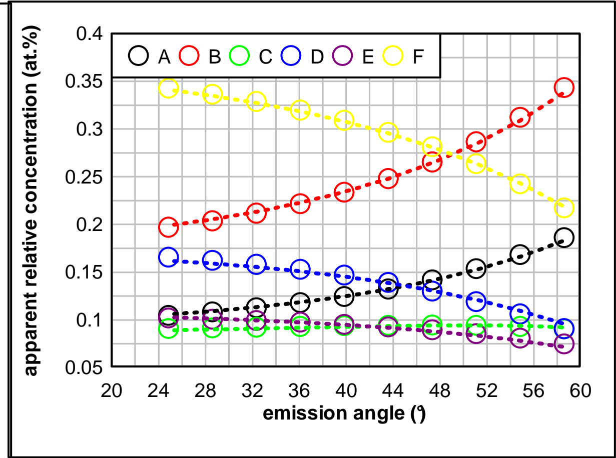

Figure A.59 : Apparent Concentration Diagram of synthetic structure 6_2+2+2 (circles) and recalculated MEM data (dotted lines).

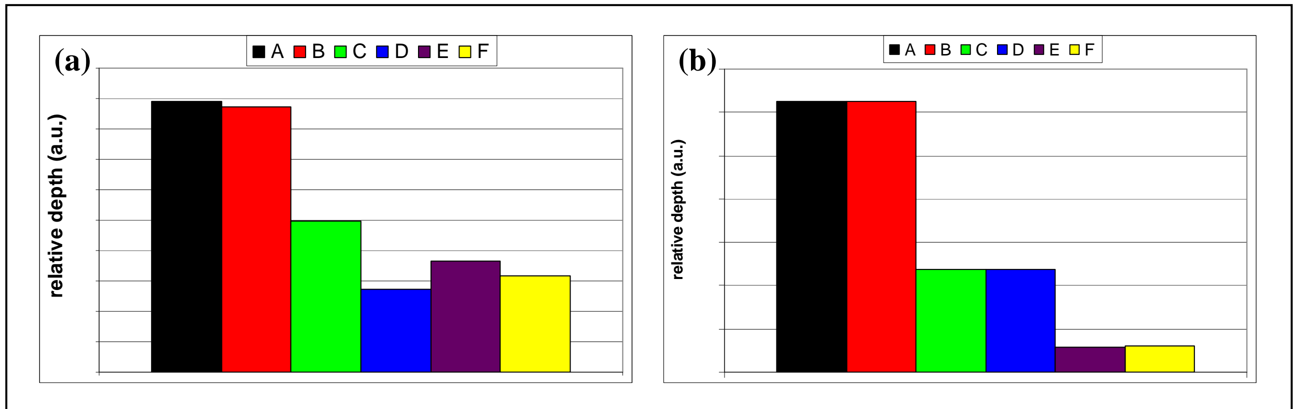

*Figure A.60 : Relative Depth Plot of synthetic structure 6_2+2+2. (**a**) real-RDP and (**b**) trial-RDP.*

Table 5.20 : In-depth profile parameters of synthetic structure 6_2+2+2 and results of MEM simulation.

layer	**thickness (Å)**		**|deviation| (Å)**
	model	**simulation**	
overlayer	*11.0*	*11.0*	*0.0*
intermediate layer	*15.0*	*15.4*	*0.4*

layer	**species**	**concentration (at.%)**		**relative error (%)**
		model	**simulation**	
overlayer	*A*	*40*	*40*	*0*
	B	*60*	*60*	*0*
intermediate layer	*C*	*30*	*30*	*0*
	D	*70*	*70*	*0*
bulk	*E*	*20*	*21*	*5*
	F	*80*	*79*	*-1*

APPENDIX B : CURVE FITTING PARAMETERS FOR SPECTRA ACQUIRED WITH THETA PROBE

In this appendix, the curve fitting parameter used to process the angle resolved spectra, acquired with the Theta Probe on the NiP specimens studied in this work, are reported.

$Ni2p_{3/2}$ region

Table B.1 : Peak-fitting parameters of the $Ni2p_{3/2}$ region acquired with the Theta Probe on the NiP alloys after 1, 3 and 14 hours polarization at +0.1 V SCE in 0.1 M Na_2SO_4, in the angle-resolved mode.

	component				
	n.1 main peak	**n.1 satellite**	**n.2 main peak**	**n.2 satellite**	**Polarization time (h)**
BE (eV)	*852.8_7*	*860.1_8*	*856.1_1*	*862.7_9*	*1*
	852.8_9	*859.7_8*	*856.1_7*	*862.5_0*	*3*
	852.8_8	*859.9_3*	*856.1_0*	*862.4_1*	*14*
Δ ($BE_{sat.}$ – - $BE_{main\ peak}$) (eV)	*7.3_1*		*6.6_8*		*1*
	6.8_9		*6.3_3*		*3*
	7.0_5		*6.3_1*		*14*
FWHM (eV)	*1.0*	*2.5*	*2.0*	*2.5*	*1*
					3
					14
line shape	*GL(92) T(1.6)*	*GL(0)*	*GL(89) T(1)*	*GL(0)*	*1*
					3
					14
$A_{sat.}$ / / $A_{main\ peak}$	*0.07*		*0.40*		*1*
	0.07		*0.40*		*3*
	0.06		*0.40*		*14*
$A_{tot}^{(comp.\ n.2)}$ / / $A_{tot}^{(comp.\ n.1)}$	*0.14*				*1*
	0.21				*3*
	0.23				*14*

P2p region

Table B.2 : Peak-fitting parameters of the P2p region acquired with the Theta Probe on the NiP alloys after 1, 3 and 14 hours polarization at +0.1 V SCE in 0.1 M Na_2SO_4, in the angle-resolved mode.

	P2p spectrum						polarization time (h)
	component n.1		component n.2		component n.3		
	$P2p_{3/2}$	$P2p_{1/2}$	$P2p_{3/2}$	$P2p_{1/2}$	$P2p_{3/2}$	$P2p_{1/2}$	
BE (eV)	129.3_1	130.2_9	131.9_3	132.7_0	133.4_8	134.4_9	1
	129.3_8	130.3_3	131.9_2	132.6_8	133.4_8	134.5_3	3
	129.3_8	130.3_3	131.7_7	132.4_9	133.2_1	134.1_9	14
Δ BE ($P2p_{1/2}$ - $P2p_{3/2}$) (eV)	0.9_8		0.7_7		1.0_1		1
	0.9_5		0.7_6		1.0_5		3
	0.9_5		0.7_2		0.9_8		14
FWHM (eV)	1.1	1.1	1.1	1.1	1.1	1.1	1 / 3 / 14
line shape	GL(30)	GL(30)	GL(30)	GL(30)	GL(30)	GL(30)	1 / 3 / 14
A($P2p_{1/2}$) / / A($P2p_{3/2}$)	0.50		0.50		0.50		1
	0.50		0.50		0.50		3
	0.50		0.50		0.50		14
component (doublet) relative area	0.64		0.17		0.19		1
	0.62		0.16		0.22		3
	0.68		0.13		0.19		14

O1s region

Table B.3 : Peak-fitting parameters of the O1s region acquired with the Theta probe on the NiP alloys after 1, 3 and 14 hours polarization at +0.1 V SCE in 0.1 M Na_2SO_4, in the angle-resolved mode.

	component of the O1s spectrum			**polarization time(h)**
	n.1	**n.2**	**n.3**	
BE (eV)	*531.2_2*	*532.7_9*	*535.0_0*	*1*
	531.4_0	*532.9_3*	*535.0_0*	*3*
	531.1_9	*532.8_2*	*535.0_0*	*14*
FWHM (eV)	*2.0*	*2.0*	*2.3*	*1*
				3
				14
line shape	*GL(20)*	*GL(20)*	*GL(40)*	*1*
				3
				14
relative area	*0.60*	*0.36*	*0.04*	*1*
	0.60	*0.37*	*0.03*	*3*
	0.72	*0.26*	*0.02*	*14*

C1s region

Table B.4 : Peak-fitting parameters of the C1s region acquired with the Theta Probe on the NiP alloys after 1, 3 and 14 hours polarization at +0.1 V SCE in 0.1 M Na_2SO_4, in the angle-resolved mode.

	component of the C1s spectrum			**polarization time (h)**
	n.1	**n.2**	**n.3**	
BE (eV)	*284.7_9*	*286.5_7*	*288.6_4*	*1*
	284.7_6	*286.5_4*	*288.6_9*	*3*
	284.7_5	*286.3_3*	*288.3_4*	*14*
FWHM (eV)	*1.5*	*1.5*	*1.5*	*1*
				3
				14
line shape	*GL(30)*	*GL(30)*	*GL(30)*	*1*
				3
				14
relative area	*0.80*	*0.13*	*0.07*	*1*
	0.84	*0.10*	*0.06*	*3*
	0.81	*0.11*	*0.08*	*14*